HIBALL-II - An Improved Conceptual Heavy Ion Beam Driven Fusion Reactor Study

B. Badger, K. Beckert, R. Bock, D. Böhne, I. Bozsik, J. Brezina, M. Corradini, L. El-Guebaly, R. Engelstad, R. Fröhlich, B. Goel, D. Henderson, W. Höbel, I. Hofmann, A. Jahnke, R. Keller, G. Kessler, A. Klein, R. Kreutz, G. Kulcinski, E. Larsen, E. Lessmann, E. Lovell, U. von Möllendorff, N. Moritz, G. Moses, R. Müller, H. Nestle, R. Peterson, K. Plute, L. Pong, H. Runge, M. Sawan, K. Schretzmann, I. Sviatoslavsky, K. Symon, D. Sze, N. Tahir, W. Vogelsang, W. Wendel, A. White, and H. Wollnik

December 1984

UWFDM-625

Also KfK-3840, FPA-84-4.

FUSION TECHNOLOGY INSTITUTE

UNIVERSITY OF WISCONSIN

MADISON WISCONSIN

HIBALL-II - An Improved Conceptual Heavy Ion Beam Driven Fusion Reactor Study

B. Badger[a]
K. Beckert[b]
R. Bock[b]
D. Böhne[b]
I. Bozsik[c]
J. Brezina[d]
M. Corradini[a]
L. El-Guebaly[a]
R. Engelstad[a]
R. Fröhlich[e]
B. Goel[e]
D. Henderson[a]
W. Höbel[e]
I. Hofmann[b]
A. Jahnke[c]
R. Keller[b]
G. Kessler[e]
A. Klein[a]
R. Kreutz[f]
G. Kulcinski[a]
E. Larsen[a]
E. Lessmann[g]
E. Lovell[a]
U. von Möllendorff[e]
N. Moritz[e]
G. Moses[a]
R. Müller[b]
H. Nestle[d]
R. Peterson[a]
K. Plute[h]
L. Pong[a]
H. Runge[f]
M. Sawan[a]
K. Schretzmann[e]
I. Sviatoslavsky[a]
K. Symon[a]
D. Sze[i]
W. Vogelsang[a]
W. Wendel[d]
A. White[a]
L. Wittenberg[a]
H. Wollnik[d]

[a]Fusion Power Associates/University of Wisconsin
[b]Gesellschaft für Schwerionenforschung
[c]Institut für Plasmaphysik, Garching
[d]Universität Giessen, II. Physikalisches Institut
[e]KfK, Institut für Neutronenphysik und Reaktortechnik
[f]Interatom
[g]KfK, Abteilung für Angewandte Systemanalyse
[h]Now at Indiana University
[i]Now at Argonne National Laboratory

KfK-3840
FPA-84-4
UWFDM-625

December 1984

PREFACE

HIBALL (Heavy Ion Beams and Lithium Lead) is a conceptual reactor design study for inertial confinement fusion (ICF) with beams of heavy ions. The HIBALL study was started in January 1980 and resulted in the publication of a report in 1981 entitled "HIBALL - A Conceptual Heavy Ion Beam Driven Fusion Reactor Study," (KfK-3202/UWFDM-450). That report will sometimes be quoted as "HIBALL-I" in the present report. Subsequently, it was decided to optimize the HIBALL design and address some criticisms of the HIBALL-I driver concept. The present study was conducted by research groups of the

Kernforschungszentrum Karlsruhe (KfK)

Gesellschaft für Schwerionenforschung, Darmstadt (GSI)

Fusion Power Associates (FPA) and the University of Wisconsin, Fusion Technology Institute (UW)

Institut für Plasmaphysik, Garching (IPP), and

II. Physikalisches Institut, Universität Giessen.

The overall HIBALL study is part of a basic research program established by the German Federal Ministry of Research and Technology (BMFT). This program is aimed at the investigation of key problems in the fields of accelerator research, atomic physics, target physics and reactor design. Another main purpose is to examine the present conviction, generally accepted in the accelerator community, that no fundamental physics problems inhibit the use of heavy ions as a driver for ICF.

Acknowledgements

We wish to acknowledge R. Bangerter, K. Ehrlich, B. Franzke, D. Kaletta, Y. Kim and P. Spädtke for valuable technical discussions during this study.

The HIBALL-II study has been funded by the BMFT heavy-ion fusion research program. The FPA efforts were performed under a contract with KfK.

We also gratefully acknowledge the help of the secretarial staff at Fusion Power Associates -- Elizabeth Brown and Pat Caliva -- for their most professional efforts in typing this report. Special appreciation is extended to Mr. Dennis Bruggink who assembled, edited and coordinated the graphics for this publication.

TABLE OF CONTENTS

1. INTRODUCTION

1.1 General Perspectives

Inertial Confinement Fusion (ICF) is considered as an alternative to Magnetic Confinement Fusion, with the goal, in both cases, of exploiting the energy released from thermonuclear fusion reactions to produce electric energy. In the case of ICF, this is accomplished by imploding targets containing DT fuel to very high densities (1000 x liquid density) with the use of intense beams of photons or charged particles. The development of ICF started later (~ 1961) and with substantially less financial support than magnetic fusion. Because of this fact, as well as the emphasis on military rather than civilian applications in the United States, the ICF approach to electric power generation is not as well developed at this time as the magnetic fusion approach. However, inertial confinement fusion has many attractive features, including: the separation of the driver from the reactor cavity with its high level of radioactivity, and a relatively simple geometry for the nuclear system (compared with tokamak reactors) which gives greater design flexibility along with better maintenance accessibility of the reactor. On the other hand, new problems related to the pulsed release of energy (~ 10^{-8} s) require innovative protection schemes for the first wall and the final components that focus the driver beams onto the target.

The specific design and overall economics of an ICF reactor are mainly determined by the choice of driver and the target characteristics. Heavy ion beams, from accelerator systems similar to those widely used in high energy physics, have been considered since 1975-76 as an attractive driver choice for reactors. This is because they can deliver large amounts of energy per pulse at a high repetition frequency. However, on the way to commercial reactors, different criteria might favor other drivers for experimental proof-of-principle devices or for a single shot facility.

A major target physics requirement common to all drivers - whether lasers, light ions or heavy ions - is that a few megajoules of energy, at several hundreds of terawatts of power should be delivered onto a target of a few mm radius to achieve compression and ignition with high gain. Heavy ions are the only candidate which permit essentially ballistic beam transport to the target and classical deposition of energy in the target ablator shell. This is due to the fact that, based on the same classical penetration depth, the energy of very heavy ions (A > 200) can be on the order of 10 GeV, whereas

the equivalent energy of very light ions is below 10 MeV. As a consequence, the same demand for beam power has to be met with megaamperes of light ions (along with possible collective effects in both the cavity transport and the target deposition region) whereas heavy ion beam currents can remain in the kiloampere range. It is generally accepted now[1-7] that these requirements can be met -- at least in principle -- with existing accelerator technology. This technology has other significant advantages.

- A high efficiency of 20-25% is credited to high energy accelerators. This allows for "conservative" target design with allowable target gain of less than 100.
- A high driver repetition rate of 10 Hz or more is realizable for the RF accelerator based scenario. Such an accelerator can support several reactor cavities, the number of which is determined by the time needed to re-establish beam propagation conditions.
- High working reliability (70-80%) can be extrapolated from existing accelerators.
- The option of using quadrupole magnets to ballistically focus a beam on target -- as though in vacuum -- is available. This provides an independence from plasma channel transport schemes (as needed for light ion fusion) which cannot yet be assessed for a reactor with the present level of theoretical and experimental understanding.

On the other hand, it has become clear since the first Heavy Ion Fusion Study at Berkeley[7] in 1976 that the size and cost of a heavy ion driver will be considerable and such factors certainly have a major influence on the anticipated cost of electricity. This gives strong justification to a complete conceptual reactor design study at the present time.

1.2 Design Objectives of HIBALL-II Study

The early studies of Heavy Ion Fusion (HIF) concepts were focused on the accelerator scenarios only. It seemed justified to ignore the reactor because of the loose coupling between the driver and the reactor chamber. However, there are several important reasons to consider both components simultaneously and a few of these are listed below.

a) The physical interface between the "harsh" reactor environment and the "clean" accelerator environment must be defined in order to determine if they can both operate within the required parameters.

b) The impact of radiation leakage on the final focusing magnet train must be considered.

c) The use of ballistic focusing depends on the cavity environment and therefore questions about beam transmission and realistic repetition rates must be settled.

d) The cost of electricity depends on both the driver and nuclear systems and the effects of technology changes on the final economics must be weighed in relation to both systems.

The first study that put equal weight on both the driver and the reactor was the HIBALL study (hereafter referred to as HIBALL-I) conducted jointly in 1980 through 1981, by scientists in the Federal Republic of Germany and the United States.[1] While that study introduced several new concepts for both the driver and reactor cavity, some questions remained to be addressed. Therefore the HIBALL-II study was initiated, at a low level, in 1982. The main emphasis of HIBALL-II was to present a new and improved driver design and to correct some problems envisioned with the HIBALL-I final focusing train. This report documents those changes and includes several other improvements in the overall scenario as well.

Finally, it is important to appreciate the context in which the commercial HIBALL-II reactor should be perceived. There must be at least three major events leading up to the construction of a device like HIBALL-II.

1) A "scientific breakeven" device (energy out of target/energy into target = 1) will have to be built and operated.

2) An Engineering Test Facility will have to be built to show that the components of HIBALL-II can stand the temperature, stress, and neutron damage envisioned in a commercial system.

3) A Demonstration Plant will have to be built which produces significant amounts of net electricity and has a tritium breeding ratio greater than one.

HIBALL-II will then be the beneficiary of two to three decades of research and plant operation before it attempts to produce electricity in an economical fashion.

1.2.1 Driver Scenario

The task of the HIBALL driver is to produce a high beam intensity within a six-dimensional phase space volume (i.e., r, z, θ, P_r, P_z, P_θ) that is small enough to be focused onto a 7 mm diameter target, at a reactor standoff dis-

tance of 8.5 meters, and with a repetition rate of at least 20 Hz. We have chosen the RF accelerator and Bi ions at 10 GeV to accomplish that task in both HIBALL-I and HIBALL-II designs. The required energy per pulse is 5 MJ.

The +2 charge state of Bi was selected for the HIBALL-I design which required 150 mA of current to be injected into the 3 km long, 5 GV RF linac. This was followed by one transfer ring, 5 condenser rings and 10 storage rings to raise the total current to 2500 A by a series of stacking and bunching procedures. Finally, induction linacs supplied a ramped voltage of several hundred MV to achieve a final tenfold compression on the long path (2/3 of a kilometer) to the target. The final current to the cavity was 1250 A per beam or 25 kA in total. This amounts to 250 TW on target assuming that 100% of the ions hit the target. Two of the criticisms of the HIBALL-I driver design were (1) the long residence time in the storage rings (~ 35 ms) which might not be feasible because of instabilities, and (2) the large emittance which required unreasonably large and bulky final focusing magnets.

The criticisms of HIBALL-I were remedied in HIBALL-II by several major changes to the RF accelerator scenario:

1) Bi^{2+} was replaced by Bi^{1+} in order to reduce the space charge problems in the storage rings, but at the expense of additional linac length (total now 5 km).
2) The final beam emittances were reduced which resulted in much smaller beam ports in the reactor. In spite of the higher particle stiffness, the smaller emittance greatly favors the design of smaller lenses, which can also be made with unsaturated iron cores.
3) Recent progress[2,8,9] in the simulation of microwave instabilities suggests that, due to favorable nonlinear effects, the acceptable storage time can be made longer than anticipated from linearized theory. On this basis we have proposed a revised accelerator scenario with a 4 ms storage ring filling time.

A comparison of some major parameters of the HIBALL-I and HIBALL-II accelerator scenarios is given below. A conceptual ground plan of the HIBALL-II installation is shown in Fig. 1.2-1.

Parameter	HIBALL-I	HIBALL-II
Ion	Bi^{2+}	Bi^{1+}
RF linac		
Sum voltage - GV	5	10
Length - km	3	5
Combined circumferential length of all transfer, storage and buncher rings - km	15.7	22.2
Maximum storage time - ms	40	4
Combined induction voltage of all induction linac bunchers - GV	12	---
Max. field (at beam edge) in FF quadrupole magnets - T	5.4	1.8
Final pulse:		
Total energy - MJ	5	5
Effective width - ns	20	20
Number of beams	20	20
Electric current per beam - kA	2.5	1.25
Pulse repetition rate - Hz	20	20
Linac efficiency - %	33	33
Total driver efficiency - %	27	27

1.2.2 Target Design

The target (Fig. 1.2-2) is the central element of the reactor system on which the heavy ion beams are focused and where the fusion energy is released. Modest gain targets (fusion energy/input beam energy = 50-100) are required for a heavy ion beam ICF power reactor. The feasibility of such targets is inferred from theoretical analysis, but we are still far from actual experimental tests of such targets. For the time being, one has to rely on parameter models and numerical simulation.

The chosen working point for the HIBALL-I target (input beam energy - 4.8 MJ, released fusion energy - 400 MJ, and gain - 83) was well justified by parametric studies with reasonable assumptions concerning hydrodynamic efficiency, convergence ratio, cold fuel isentrope, ignition pressure and burn rate. The work at KfK correlated these parameters with the ion energy of the beam and maximum beam power as well as target geometry to allow for a general optimization. The physics of heavy ion stopping in hot dense plasma has been investigated, and actual ranges and deposition profiles have been calculated for a specific target configuration. As a first attempt, a cryogenic single

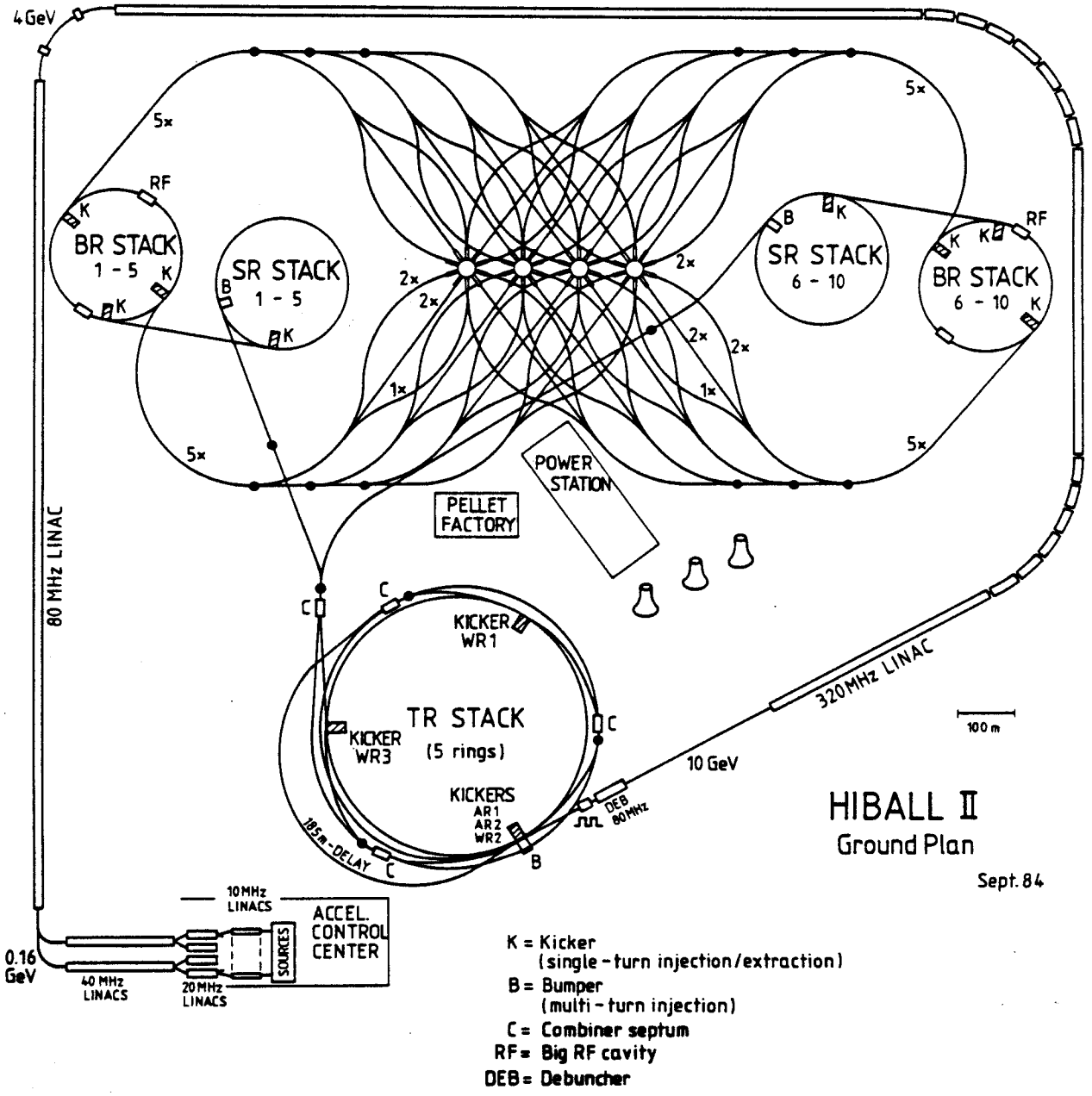

Fig. 1.2-1. HIBALL-II ground plan.

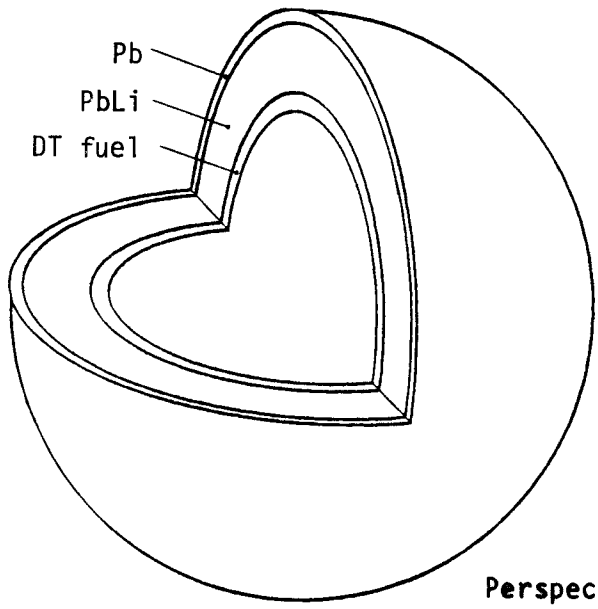

Fig. 1.2-2.
Perspective view of the HIBALL pellet (7.4 mm diameter).

shell design has been chosen, closely following a Livermore design for light ion beam fusion. The objective was to study one-dimensional implosions of this target to obtain a general insight and to identify critical issues rather than to present an optimal design which, at the moment, is beyond the capabilities of the groups involved. The spectra of X-rays and ions emerging from the burning target as well as the target neutronics have been calculated by both of the groups at FPA and KfK and their effect on the cavity design has been analyzed.

The reader should be aware that it was necessary to "freeze" the target output at an early stage of the HIBALL-I design in order that the rest of the analysis could proceed. Changes in the output neutron spectra[10] accompanied every improvement made in the modeling effort but no attempt was made to incorporate all of those adjustments as they would make only minor changes in coolant flow rates and temperatures. It was also decided that the HIBALL-I target parameters could be used for HIBALL-II because there has been no experimental information which would change those values from the original report. It is recognized that if significantly different target designs were used, the amount of liquid metal ablated from the first wall per shot might increase or decrease thus affecting the repetition rate. Such an analysis would be appropriate for future studies but was not included in this HIBALL-II report.

1.2.3 Reactor Chamber Concept

The reactor chamber is a cylindrical vessel with 20 ports for the beam entrance. A unique feature is its first wall protection concept. Using a eutectic of Pb (83%) and Li (17%) as coolant and breeder material, the vapor pressure at the time of beam and pellet injection can be kept as low as 10^{-5} torr. Through a system of porous SiC tubes the coolant is flowing down along the wall and can be fed around the beam ports. The repetition rate is 5 Hz for each chamber, the total plant consists of 4 chambers.

The same general chamber design described in the HIBALL-I report[1] was used in HIBALL-II. There was an improved design conducted for the roof of the chamber and the models which predict the time-dependent vapor pressure in the chamber were improved. A more detailed analysis of the flexible SiC tubes was conducted and some additional safety related issues were investigated in the HIBALL-II study. A minor change in the reactor shield thickness from 3.5 to 2.9 meters also should improve the economics.

Perhaps the biggest change in the HIBALL-II chamber and blanket concept is related to the final focusing magnet chain. In HIBALL-I, the final focusing lens was 4.6 meters in diameter. In HIBALL-II, because of the lower emittances along with advances in magnet design, the diameter of the final lens is 2.4 meters. The smaller diameter allows more flexibility in the angle in which the beams can enter the chamber and causes much less interference with the design. Figure 1.2-3 shows the conceptual layout of one reactor block.

1.2.4 Economic Performance

The adjustments to the driver design in HIBALL-I have added approximately 13% to the unit capital cost and 11% to the busbar cost of HIBALL-II when compared on an equal basis (HIBALL-I driver escalated at 3.6% to 1984 and converted at the 1984 DM/US$ exchange rate). Further, if the more recent unit costs used in the HIBALL-II driver are applied to the HIBALL-I driver, the difference is only 1.5% and 1.3% in the capital cost and busbar cost, respectively. The obtained unit capital cost of $2128/kWe is lower than the STARFIRE tokamak ($2304/kWe),[11] NUWMAK tokamak ($2410/kWe),[12] WITAMIR tandem mirror ($2454/kWe)[13] and the MARS tandem mirror ($2558/kWe)[14] reactors. The unit capital costs for these designs have been escalated at 3.6% to 1984. The calculated cost of electricity from HIBALL-II (47.9 mills/kWh) is 30-40% less than in the SOLASE[15] laser (66 mills/ kWh in 1977) and equal to the MARS[14] reactors. While it is risky to place too much emphasis on absolute cost estimates, it is clear that heavy ion beam driver fusion reactors compare very favorably with other magnetic and inertial confinement fusion devices and should be pursued further as our understanding of burning targets advances. New developments such as polarized fuel targets have the potential for reducing driver requirements and affecting the cost.

1.3 Assumptions on Level of Technology and on Utilization of HIBALL

The level of technology that has been assumed for HIBALL is what we think will be typical of the period between 2000-2020. This means that information developed over the next 20 years on accelerator design, superconducting magnets, liquid metal handling, radiation damage, and remote maintenance will be available. The target physics is assumed to have been established on a proof-of-principle device, the delivery of the target and repetitive operation of the system will have been demonstrated in an Engineering Test Facility, and the power handling, as well as indications of economic performance will have been established in a Demonstration Power Reactor. Since the HIBALL class of

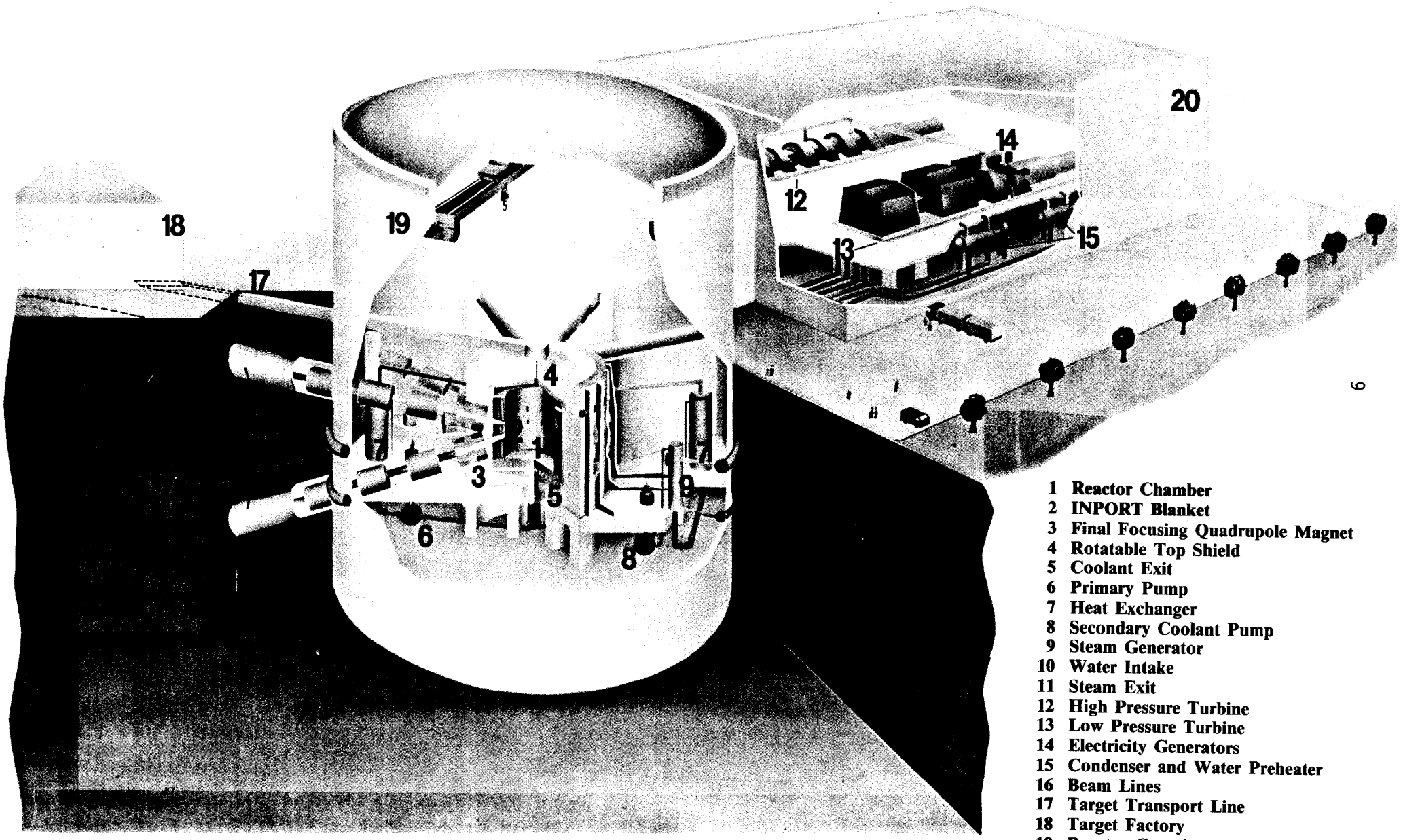

1 Reactor Chamber
2 INPORT Blanket
3 Final Focusing Quadrupole Magnet
4 Rotatable Top Shield
5 Coolant Exit
6 Primary Pump
7 Heat Exchanger
8 Secondary Coolant Pump
9 Steam Generator
10 Water Intake
11 Steam Exit
12 High Pressure Turbine
13 Low Pressure Turbine
14 Electricity Generators
15 Condenser and Water Preheater
16 Beam Lines
17 Target Transport Line
18 Target Factory
19 Reactor Containment
20 Machine Building

Fig. 1.2-3 One of the four reactor blocks of HIBALL plant.

reactors is designed to operate in perhaps the 2020-2030 period, the size of the electrical grids will be larger than at the present time, thus allowing larger units to be integrated into the utility without fear of overdependence on a single reactor. (The largest Light Water Reactor units have at present a power output of 1300 MWe. There are several sites already in Europe, Canada, and the USA where 4-8 units with as much as 7-8 GWe total output are operating at one site.)

Finally, we have chosen to examine the production of electricity first because we think that is where HIF reactor systems will have the most immediate impact. Other modes of operation, e.g., production of fissile fuel, synthetic fuels, or steam could also have been considered. At the present time, the relative economics of the various options are not readily apparent so there is no way to define the optimum form in which to derive energy from HIBALL. The large capital costs of a high energy accelerator driven reactor and the finite limits to waste heat disposal or electrical grid size, may require a combination of integrative (e.g., fissile or synthetic fuel production) and real time (e.g., electricity or process steam) systems for optimum performance.

References for Chapter 1

1. B. Badger et al., "HIBALL - A Conceptual Heavy Ion Beam Driven Fusion Reactor Study," KfK-3202/UWFDM-450, 1981.

2. Proceedings of 1984 INS Intern. Symp. on Heavy Ion Accelerators and Their Applications to Inertial Fusion, Institute for Nuclear Study, University of Tokyo (1984).

3. Proceedings of the Heavy Ion Fusion Workshop, Darmstadt, March 1982, GSI-82-8.

4. Proceedings of the Heavy Ion Fusion Workshop, Berkeley, September 1980, LBL-10301.

5. Proceedings of the Heavy Ion Fusion Workshop, Argonne, September 1978, ANL 79-41.

6. Proceedings of the Heavy Ion Fusion Workshop, Brookhaven, October 1977, BNL-50769.

7. ERDA Summer of Heavy Ions for Inertial Fusion Final Report, December 1976, LBL-5543.

8. I. Hofmann, I. Boszik and A. Jahnke, IEEE Trans. Nucl. Sci. NS-30, 2546 (1983).

9. I. Hofmann and I. Boszik, "Nonlinear Phenomena in Computer Simulation of the Microwave Instability," GSI-84-5 (1984), p. 33.

10. B. Goel and W. Hőbel, "The Role of Neutrons in the Performance of ICF Targets," 10th International Conference on Plasma Physics & Controlled Nuclear Fusion Research, London, U.K., 12-19 September 1984.

11. "STARFIRE - A Commercial Tokamak Fusion Power Plant Study," Argonne Report ANL/FPP-80-1, Sept. 1980.

12. B. Badger et al., "NUWMAK, A Tokamak Reactor Design Study," University of Wisconsin Fusion Technology Institute Report UWFDM-330 (March 1979).

13. B. Badger et al., "WITAMIR-I, A University of Wisconsin Tandem Mirror Reactor Design," University of Wisconsin Fusion Technology Institute Report UWFDM-400 (Sept. 1980).

14. "MARS - A Commercial Tandem Mirror Reactor Study," Lawrence Livermore National Laboratory Report UCRL-53480, July 1984.

15. R.W. Conn et al., "SOLASE - A Conceptual Laser Fusion Reactor Design," University of Wisconsin Fusion Technology Institute Report UWFDM-220 (Dec. 1977).

2. TARGET

2.1 Target Design

2.1.1 Target Design for HIBALL-II (By N.A. Tahir and K.A. Long, KfK-INR)

For the HIBALL-I reactor study we have designed a new target[1-3] shown in Fig. 2.1-1. It is a single shell, multilayered target with a hollow DT shell of 4 mg. This target has a number of attractive features which make it suitable for use in a working reactor system like HIBALL-II. For example, it is made from inexpensive materials and has a relatively simple structure. The fuel is protected against radiative preheat by using a high-Z, low-ρ lead radiation shield around the fuel shell. In order to avoid mixing of lead from the radiation shield into the fuel by hydrodynamic instabilities, a low-Z, high-ρ lithium cushion is placed between the radiation shield and the fuel. Furthermore, our calculations show that this target design is completely stable towards hydrodynamic instabilities which cause shell breakup during the implosion.

The target is imploded by 10 GeV Bi^+ ions which impinge on the target surface uniformly. These ions deposit about 60% of their energy in the outer lead tamper and they emerge into the lithium absorber with a lower energy of 3.74 GeV. The thickness of the lithium absorber is adjusted in such a manner that the ions stop in this region just at the absorber-radiation shield boundary. As the incoming ions deposit their energy in the absorption region, the temperature increases and a radiation Marshak type wave[4-7] is launched into the radiation shield. The material from the radiation shield is ablated which exerts an ablation pressure on the payload (compressed part of radiation shield + lithium stabilizer). This ablation pressure together with the thermal pressure in the absorption region drives the target to void closure.

We have used an extensively updated version of the one-dimensional lagrangian ion-beam fusion code MEDUSA-KA[8] to simulate ablation, compression, ignition and burn of the HIBALL-II target. The MEDUSA-KA code has been developed from the well known laser-fusion code MEDUSA.[9] It considers a separate temperature for ions and the electrons, T_i and T_e, respectively. We have extended MEDUSA-KA to include radiation transport effects using a two-temperature (T_i, T_e) plus a radiation heat conduction approximation. In this model it is considered that the radiation field is in thermodynamic equilibrium with the electrons. One can thus define a specific internal energy for the radiation field characterized by T_e. Other thermodynamic variables including

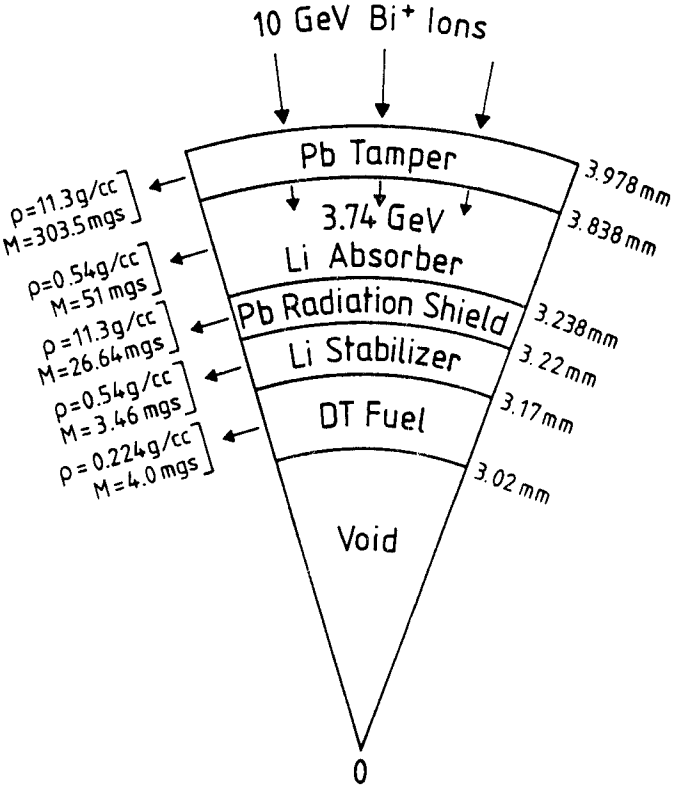

Fig. 2.1-1. HIBALL-II target.

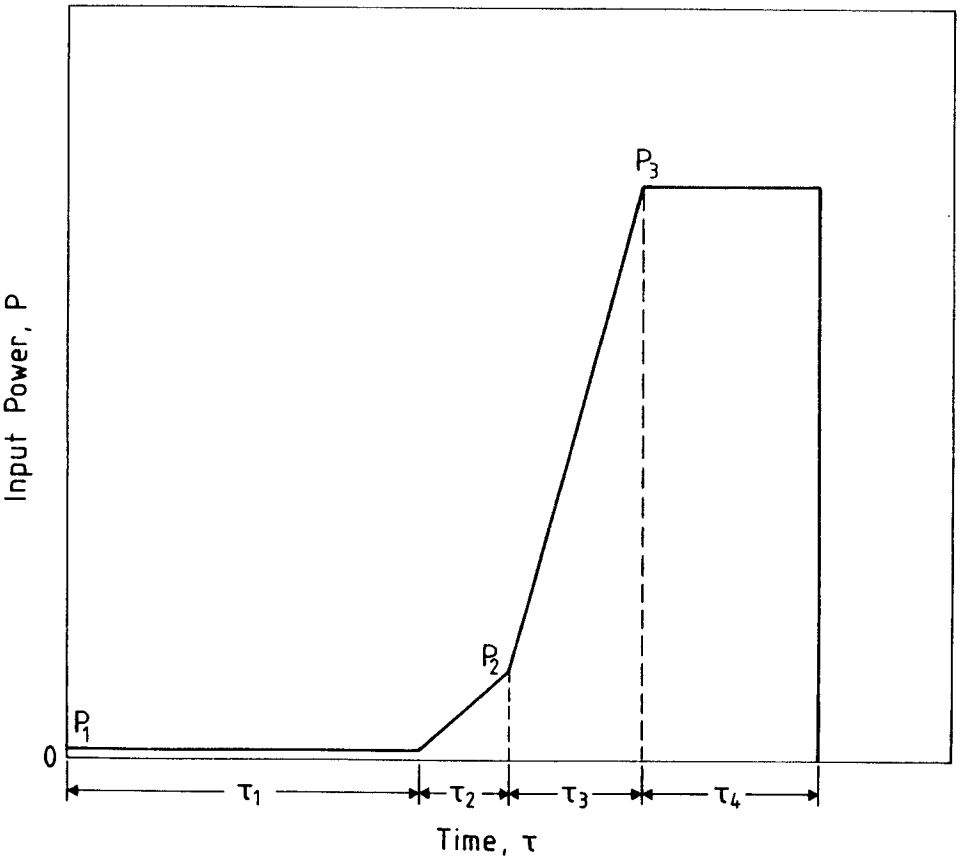

Fig. 2.1-2. Input pulse.

radiation specific heat, radiation pressure and compressibility can also be calculated from this specific internal energy and these quantities are added to the corresponding quantities for the electrons. Also, radiation conductivity is added to the electron thermal conductivity. One therefore solves a modified electron energy equation which also includes radiation. For further details see Refs. 1-3, 5, 10 and 11.

The deposition of the incident ion energy is calculated using analytic fits[12] to an average deposition profile produced by an energy deposition code GORGON.[13,14] The ranges and profiles of the bismuth ions in lead and lithium were calculated using the GORGON code.[13-15] The plasma parameters are calculated using the Thomas-Fermi model, and this yields the number of free and bound electrons. The stopping power due to the free electrons is calculated using a linear response theory within the Born approximation and is written in terms of the imaginary part of the inverse of the dielectric function.

The stopping power due to the bound electrons is calculated within the Thomas-Fermi model. Shell effects are taken into account by neglecting those electrons which are moving faster than the ion. The results obtained using this code are given in Refs. 13-15. The calculations do not include the plasma effects on the effective charge or of the time needed for the ion to reach its equilibrium effective charge in the plasma. In pellet calculations the nonlinear feedback of plasma heating on the energy deposition[16] is also not included in these calculations. A discussion of the problems involved in the calculation of energy deposition in hot plasmas and its incorporation in pellet calculations was given in Refs. 17-19.

The equation of state variables are calculated using analytic fits to the Los Alamos equation of state data.[20] Also, local α-particle energy deposition is considered and the neutrons are allowed to escape freely without interacting with the target materials.

A shaped input pulse shown in Fig. 2.1-2 is used to implode this target. The prepulse hits the target with a power $P_1 \sim 6$ TW and drives a shock through the lead radiation shield. The shock is then transmitted into the lithium stabilizer and subsequently into the fuel. The fuel is compressed to a density of 0.7 g/cc and is heated to a temperature of 6×10^3 K. When this shock breaks through the inner fuel boundary, the inner boundary expands and a density gradient is generated in the fuel region. After the prepulse delivers

its energy, the input power linearly rises to a maximum value of 500 TW. This linear rise in the power generates a second shock which is much stronger than the first shock. Moreover, as it travels down a density gradient in the fuel, it deposits much more entropy in the fuel center compared to the outer part of the fuel. Due to this selective shock heating a small fraction in the fuel center is placed on a very high adiabat which forms the "hot spot" after the void closure. As the main pulse with 500 TW power starts to deliver energy, the temperature in the absorption region increases to a few hundred eV which generates a radiation heat conduction wave through the radiation shield. The material is ablated from the radiation shield and the target is driven to the void closure. The void closes at t = 45.99 ns and a small amount of the radiation shield is left around the fuel and the lithium stabilizer in the form of a high-ρ tamper shell, which is advantageous as it improves fractional burn.[12,21-24] A small fraction of the fuel in the center is heated to a temperature of 1 keV which forms the hot spot where nuclear reactions start.

It is to be noted that the thermonuclear burn will propagate from the central hot spot into the surrounding cold fuel provided the following conditions are fulfilled. The rate at which α-particles redeposit their energy in the hot spot should exceed the radiation loss rate. This requires that the temperature in the hot burning zone be $\gtrsim$ 5 keV. Moreover, the ρR of the hot spot should be equal to the α-particle range. According to our calculations the range of the α-particles[25] is 0.36 g/cm^2 in the hot spot. In the present simulations we switch on nuclear reactions provided that the ρR of the hot spot is $\gtrsim$ 0.4 g/cm^2 and the hot spot temperature, $T_h \gtrsim 1$ keV. At 1 keV, although the radiation loss rate is greater than the α-particle energy deposition rate in the hot spot, this extra energy loss is compensated for by the compressional energy produced due to the compression of the hot spot by the surrounding fuel and the payload material imploding with large kinetic energy. This process goes on until the temperature becomes on the order of ~ 5-8 keV and the burn then rapidly spreads through the entire fuel. The total energy in the input pulse is 4.56 MJ and the target yields an output energy of 690 MJ such that the overall energy gain is 152. A summary of the implosion results together with input parameters is given in Table 2.1-1.

In our simulations we find that at the end of the compression phase the density in the lithium stabilizer becomes comparable to the fuel density. This avoids development of the hydrodynamic instabilities across this inter-

Table 2.1-1. A Summary of Simulation Results

Input Energy (MJ)	4.56
Output Energy (MJ)	690
Gain	151.6
Peak Power (TW)	500
Fractional Burn, ϕ (%)	~ 50
Fuel ρR at Ignition (g/cm^2)	2.87
Li Stabilizer ρR at Ignition (g/cm^2)	1.10
Pb Tamper (Compressed Part of the Radiation Shield) ρR at Ignition (g/cm^2)	1.63
Total ρR of the Compressed Part at Ignition (g/cm^2)	5.8
Void Closure Time (ns)	44.99
Ignition Starts at (ns)	45.96
Burn Starts to Propagate at (ns)	47.26
Burn Propagation Time (ps)	110
Total Burn Time (ps)	300

face which cause pusher-fuel mixing. The stability problem in the radiation shield (pusher) during the compression phase has been analyzed using a theory by Takabe.[26] In this theory the growth rate is calculated including the important physical effects taking place at the ablation surface, for example, ablative flow, heat conduction, compressibility and formation of highly structural density profiles. Use of this theory shows that the perturbations with wavelength on the order of minimum shell thickness (4 μ) are completely damped out and the target is completely stable. This is a very important result. For a detailed analysis see Ref. 1.

References for Section 2.1.1

1. N.A. Tahir and K.A. Long, "Theoretical Analysis and Numerical Simulations of Compression, Ignition, Burn and Hydrodynamic Stability of a High-Gain, Reactor-Size, Heavy Ion Beam Driven Inertial Fusion Target Calculation," (1985), submitted to Nuclear Fusion.

2. N.A. Tahir and K.A. Long, "Theory and Numerical Simulations of HIBALL-II Target," GSI Darmstadt Annual Report (1985), to be published.

3. N.A. Tahir and K.A. Long, "Influence of Radiation on Ignition and Burn Propagation in ICF Targets," GSI Annual Report (1985), to be published.

4. R.E. Marshak, Phys. Fluids 1, 24 (1958).

5. N.A. Tahir and K.A. Long, Laser & Particle Beams 2, 371 (1984).

6. N.A. Tahir and K.A. Long, GSI Darmstadt Annual Rep. GSI-84-5 (1984), p. 52.

7. K.A. Long and N.A. Tahir, GSI Darmstadt Annual Rep. GSI-84-5 (1984), p. 51.

8. N.A. Tahir and K.A. Long, Kernforschungszentrum Karlsruhe Report KfK-3454 (1983).

9. J.P. Christiansen, D.E.T.F. Ashby and K.V. Roberts, Comp. Phys. Comm. 7, 271 (1974).

11. N.A. Tahir and K.A. Long, GSI Darmstadt Annual Rep. GSI-83-2 (1983), p. 38.

12. N.A. Tahir and K.A. Long, Atomkernenergie/Kerntechnik 40, 157 (1982).

13. K.A. Long and N.A. Tahir, Kernforschungszentrum Karlsruhe Report KfK-3232 (1981).

14. K.A. Long, N. Moritz and N.A. Tahir, Kernforschungszentrum Karlsruhe Report KfK-3608 (1983).

15. K.A. Long, N. Moritz and N.A. Tahir, GSI Annual Rep. GSI-82-6 (1982), p. 54.

16. K.A. Long and N.A. Tahir, GSI Darmstadt Annual Rep. GSI-84-5 (1984), p. 73.

17. K.A. Long and N.A. Tahir, Presented at the meeting on "Atomic Physics for Ion Beam Fusion," Rutherford Laboratory, England, September 1984.

18. K.A. Long and N.A. Tahir, "HIBALL-I Target Calculations with Range Shortening and Its Compensation by Two Methods," GSI Darmstadt Annual Report (1985), to be published.

19. K.A. Long and N.A. Tahir, "Range Shortening Effects in HIBALL-II Type Target," GSI Darmstadt Annual Rep. (1985), to be published.

20. B. Bennett et al., Los Alamos Lab. Report LA-7130 (1978).

21. N.A. Tahir and K.A. Long, Nucl. Fusion 23, 887 (1983).

22. N.A. Tahir and K.A. Long, Phys. Lett. 90A, 242 (1982).

23. K.A. Long and N.A. Tahir, Phys. Lett. 91A, 451 (1982).

24. R.J. Mason, R.L. Morse, Los Alamos Report LA-5789-MS (1974).

25. K.A. Long, N. Moritz and N.A. Tahir, GSI Darmstadt Annual Rep. GSI-82-6 (1982), p. 56.

26. H. Takabe, ILE Progress Report on Inertial Fusion Program ILE-QPR-83-6 (1983), p. 28.

2.1.2 Remarks on the Target Design

The previous section presents a target which, according to the one-dimensional design calculation, has a gain of 151 and thus transforms the input energy of 4.56 MJ into an output of 690 MJ. There are some phenomena that have not been modeled in the calculation, such as transport effects of the different particles. Moreover, a real implosion will not be of ideal spherical symmetry because of[1]

- imperfection in target manufacture,
- spatial nonuniformity of ion irradiation,
- hydrodynamic instabilities in the compression process.

For estimating the reduction in compression and gain resulting from all of these, we rely on the literature, notably on the curves of gain versus input energy that have been published by LLNL at different times.[1,2] The conclusion is that, for the HIBALL case, the originally postulated values[1] of 2 g/cm^2 for the fuel ρR at ignition and about 80 for the gain are very reasonable. Therefore, the output energy of 400 MJ, its distribution into the four fractions of neutrons, gamma rays, x-rays and charged particle debris, and the spectra of each of these can be used from HIBALL-I. These are shown in Figs. 2.1-3 to 2.1-6 and in Table 2.1-2.

Table 2.1-2. Ion Average Energies

Normalized energy	0.85 keV/amu
D	1.70 keV
T	2.55 keV
He-4	3.40 keV
Li-natural	5.90 keV
Pb-natural	176.0 keV

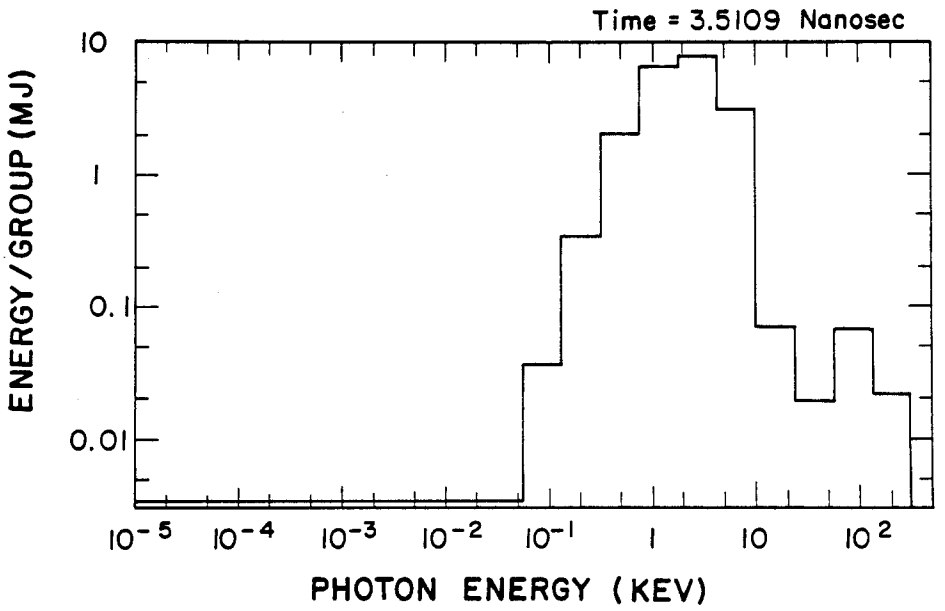

Fig. 2.1-3. Integrated radiation spectrum.

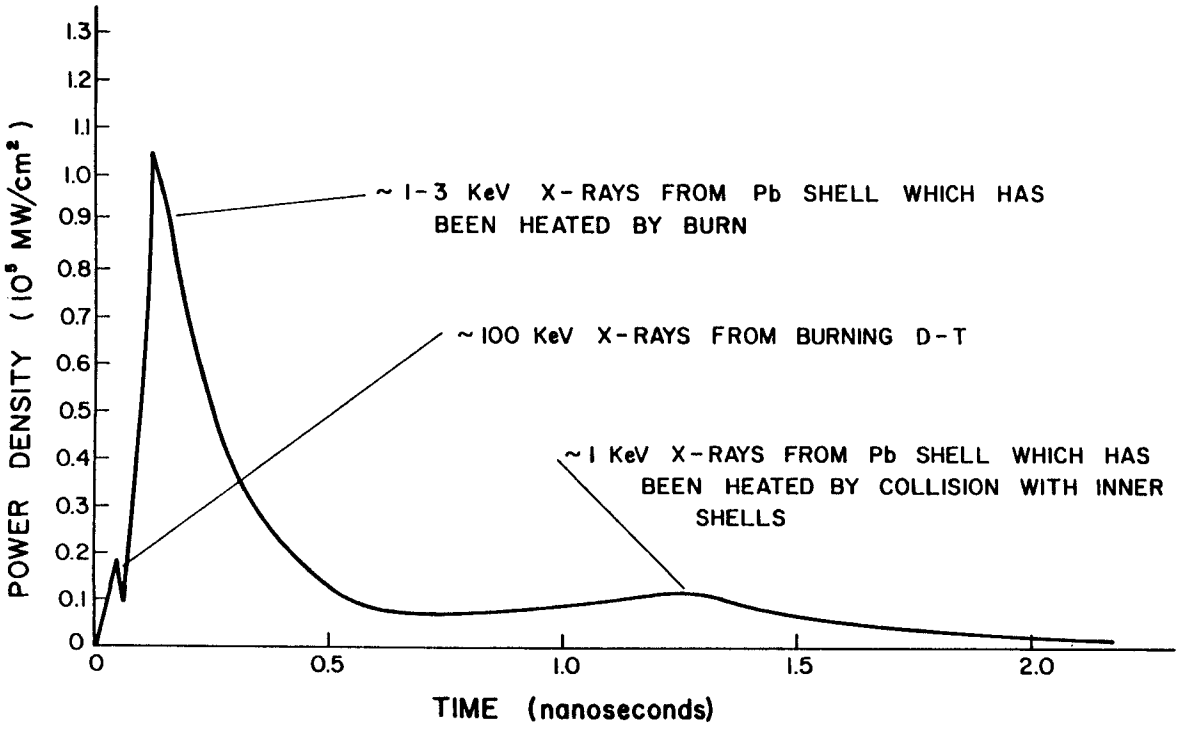

Fig. 2.1-4. X-ray power density from 400 MJ pellet at 5 meters.

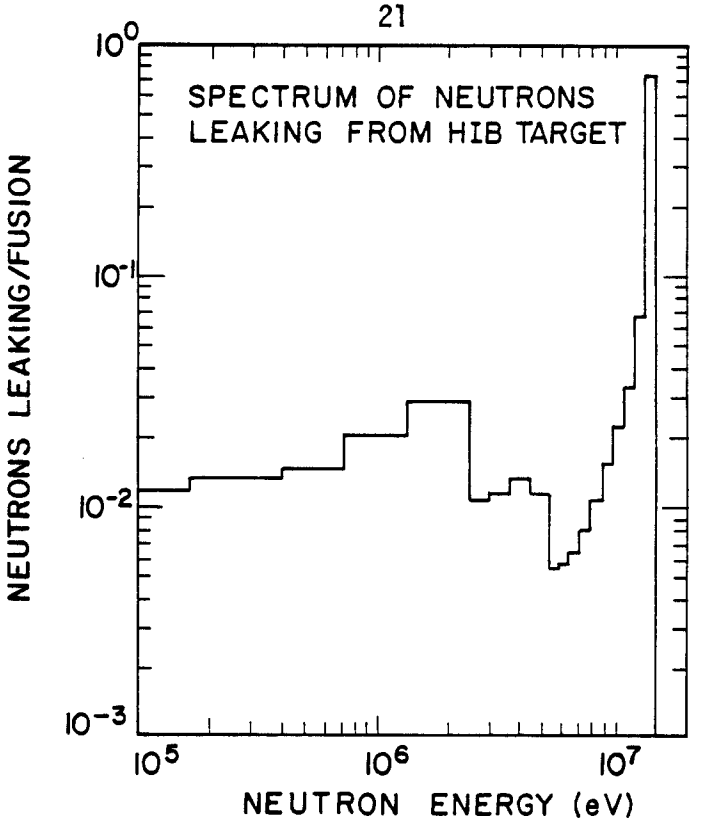

Fig. 2.1-5. Spectrum of neutrons leaking from HIB target.

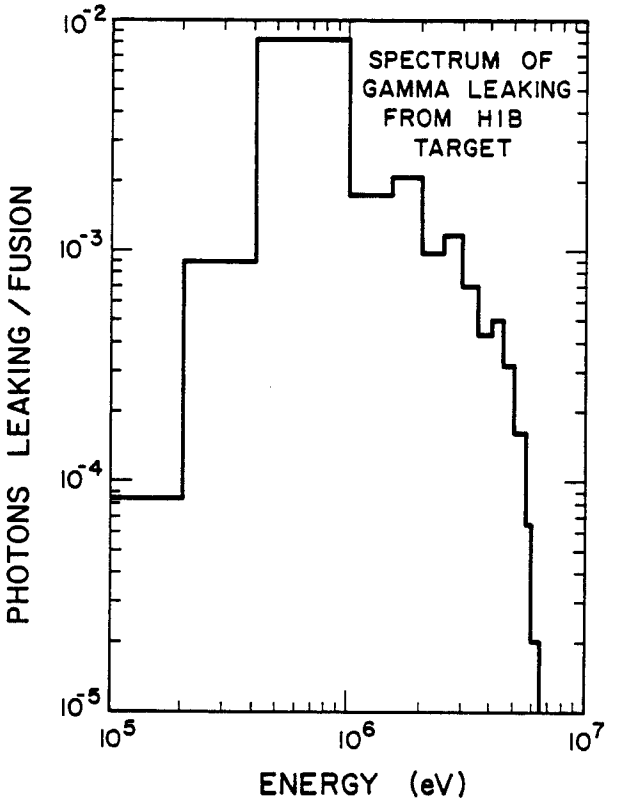

Fig. 2.1-6. Spectrum of gamma leaking from HIB target.

The input energy of 4.56 MJ allows for some percentage of the 5.0 MJ driver pulse to miss the target (see Sections 2.3.1 on target positioning tolerance and 4.2 on ion beam final focusing).

The target requires the bulk of the input energy to be delivered at a power of 500 TW, i.e. in about 10 ns, while the driver design of Chapter 3 is for 250 TW. A potential way to reduce the target power requirement to 250 TW is discussed in the following section.

References for Section 2.1.2

1. B. Badger et al., "HIBALL - A Conceptual Heavy Ion Beam Driven Fusion Reactor Study," KfK-3202/UWFDM-450, 1981.

2. J.D. Lindl and J.W.-K. Mark, in: Proc. 1984 Intern. Symp. on Heavy Ion Accelerators and their Application to Inertial Fusion, Institute for Nuclear Study, University of Tokyo (1984).

2.2 Spin Polarized Fuel for the HIBALL-II Target

The HIBALL-II driver provides a maximum power of 250 TW, whereas target simulation calculations show that the HIBALL target needs a power of 500 TW in the main pulse. This power requirement may undergo modification as more realistic physical assumptions are introduced in the simulation calculations and as the target design is optimized. On the other hand, it has been shown[1] that the power requirement for the HIBALL-I target can be halved if spin polarized fuel is used. Other estimates[2,3] give even higher reduction in driver power requirement. The exact demand on driver power can be determined only if a target is optimized for the use of polarized fuel, but it is safe to assume a power reduction by a factor of two. The idea of using polarized fuel in an ICF target is quite recent and poses two questions: (1) how to polarize the fuel, and (2) whether the fuel polarization will withstand the high temperature and densities encountered during the implosion and burn phase?

A prerequisite to the polarization of DT-fuel is the production of pure DT-molecules. Recently at Lawrence Livermore National Laboratory 95% pure DT-molecules have been produced.[4] They expect to reach the 99% mark by 1985. With pure DT-molecules they expect to be able to achieve 90% polarization of DT-fuel.

The fuel will be polarized while in the target factory. Ducts with a polarization retaining field of about 1 tesla will connect the target factory to the reactors. The target is injected into the reactor at a speed of 200 m/s and takes 80 ms to travel through the gun barrel to the cavity center, the point of beam intersection. During the injection, the outside edge of the fuel becomes heated to about 14 K. At this temperature and solid density the polarization relaxation time is of the order of a second. Thus, the polarization is not relaxed at the time that the beams begin to heat the target.

A more serious concern is that the high temperature reached in the fuel during the final stages of the implosion may quickly cause depolarization. However, since the implosion and burn of the fuel only require a total of a few tens of nanoseconds, the depolarization would have to occur very quickly to degrade the target performance. As a preliminary look, one can calculate the density and temperature of the fuel as functions of time to find the spin relaxation time at different times during the implosion. This has been attempted in Fig. 2.2-1 where one can see that the relaxation time is usually much longer than the characteristic time for the implosion. Even when the fuel begins to burn the relaxation time is an order of magnitude above the time scale for the burn (~ 100 ps). From this preliminary calculation, one can say that the use of polarized fuel in the target may reduce the requirements on the driver while keeping the yield per unit mass of fuel constant.

References for Section 2.2

1. W. Seifritz and B. Goel, Atomkernenergie 43, 198 (1983).

2. B. Goel, GSI-84-5, p. 64, Darmstadt (1984).

3. L. Cicchitelli, Atomkernenergie 44, 89 (1984).

4. E. Storm, 10th International Conference on Plasma Physics and Controlled Thermonuclear Fusion, London, Sept. 12-19, 1984.

2.3 Target Delivery

2.3.1 Introduction

By target delivery we denote the tasks of injecting the cryogenic target into the reactor chamber and of synchronizing the target motion and the ion pulse so that they both reach the focus location at the same time. The gene-

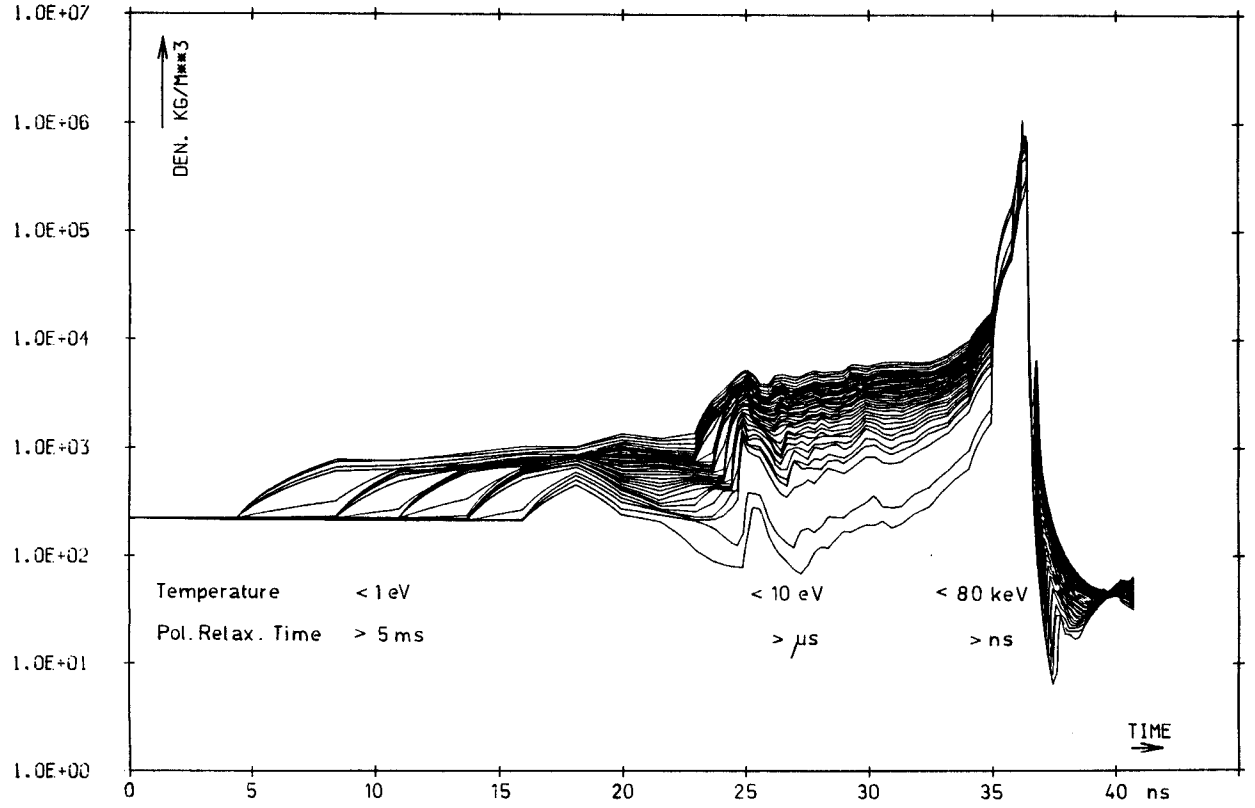

Fig. 2.2-1. Fuel density during compression and burn phase. Temperatures and polarization relaxation times in different phases are also indicated.

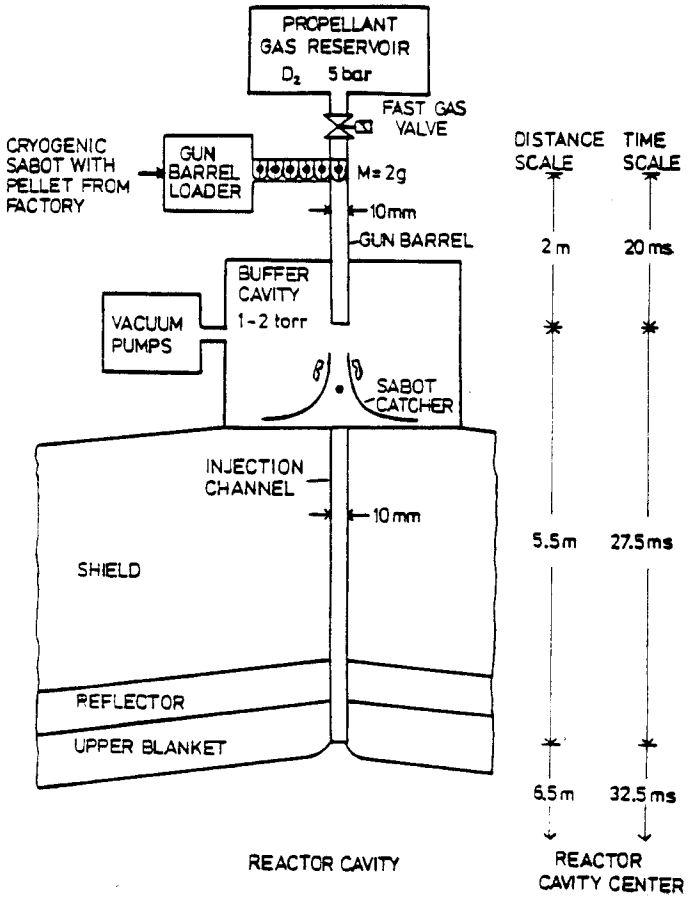

Fig. 2.3-1. Scheme of HIBALL-I pneumatic injection and design parameter values. Target velocity = 200 m/s.

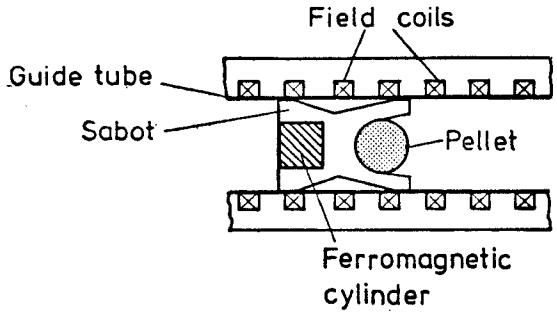

Fig. 2.3-2 Scheme of a magnetic linear accelerator for target injection.

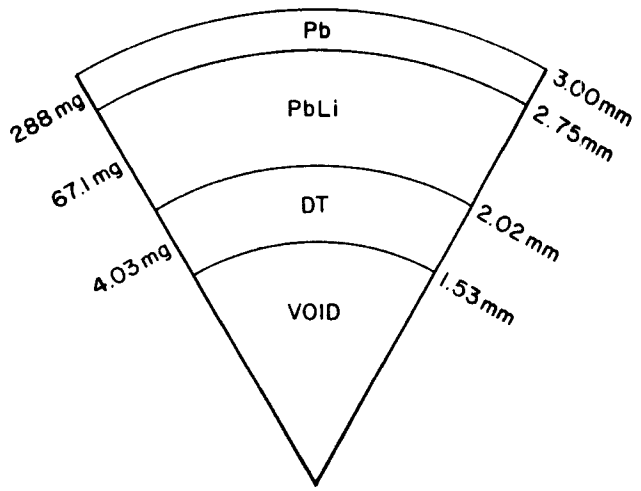

Fig. 2.3-3. HIBALL cryogenic target.

ral requirements on the injection process are that the target must not be altered to such a large degree that it will not properly implode. This includes limiting the heating during delivery so as to not cause the DT fuel to sublimate or melt. Section 2.3.3 deals with this question of target heating.

The basic parameter governing the injection and synchronization problems is the tolerance (admissible inaccuracy) of the target position at the time when it is hit by the ion pulse. This tolerance depends on the target size, on the geometry and intensity distribution of the ion focus and on the degree of irradiation uniformity required on the target surface. The tolerances adopted in HIBALL-I,[1] 0.5 mm in the vertical and 0.7 mm in the horizontal direction, were found assuming beams with a Gaussian radial intensity profile and 80% of the ions within a radius equaling the target radius of 3 mm.

Since the details of target illumination[2] as well as the beam size and profile obtainable from the final focusing system are not yet sufficiently known we feel it is reasonable to stay with the above tolerances. However, it is clear that missing the target with 20% of the ions is not very economical, and that with a beam size closer to that of the target, the positioning tolerances may be narrower. This might require injection and synchronization techniques different from the ones discussed subsequently.

Another key parameter is the target injection velocity. A low velocity obviously makes it easier to meet the positioning tolerance in the direction along the target trajectory, i.e. vertical, and it reduces the force to be applied to the target. On the other hand, it increases the time spent by the cryogenic target in the hot environment of the chamber before explosion. As shown in Section 2.3.3, a velocity of 200 m/s is sufficient to prevent detrimental heating of the target.

2.3.2 Target Injection

Two injection techniques appear to be feasible: a pneumatic injector gun as described in HIBALL-I[1] and an electromagnetic accelerator.[3] In any case, the target has to be mechanically and thermally protected during acceleration by a target carrier or sabot which must, however, be separated from the target after acceleration. This removal is easier with the electromagnetic technique.[3,4]

An aiming accuracy corresponding to the lateral positioning tolerance of 0.7 mm at a distance of about 10-12 m appears attainable with either method.

Table 2.3-1. HIBALL Target Delivery Parameters

Longitudinal positioning tolerance	0.5 mm
Lateral positioning tolerance	0.7 mm
Target velocity	200 m/s
Injection:	
Type	gas gun
Projectile (sabot + target) mass	2 g
Propellant gas	D_2
Prop. gas entering reactor cavity	1.6 mg/shot
Pressure of prop. gas reservoir	5 bar
Acceleration distance	2 m
Acceleration	10^4 m/s^2
Acceleration time	20 ms
Total target travel time	80 ms
Distance muzzle to focus	12 m
Tracking:	
Lateral tracking	none
Longitudinal tracking, type	light-beam interception
Last tracking position, distance from focus	3.0 m
Precision of arrival time prediction	±1 μs
Duration of processing tracking result	1 ms

Thus, no target trajectory corrections or corresponding ion beam steering measures are needed.

Table 2.3-1 gives the target delivery parameters for the pneumatic injector design which is shown schematically in Fig. 2.3-1. The principle of electromagnetic injection is depicted in Fig. 2.3-2.

2.3.3 Heating of Target and Sabot During Injection

The cryogenic fusion target must be injected into the target chamber in such a way that the cryogenic D-T fuel in the target remains solid. The inside boundary of the target fuel is required to remain colder than the sublimation temperature of 11.3 K and no part of the fuel is to become hotter than

the melting temperature of 19.7 K.[1] This section describes the calculations of the heating of the target during its injection through the target chamber and during its transit in a sabot down the injector tube.

The target that we consider in our discussions of target heating is shown in Fig. 2.3-3. This is a cryogenic target which has a layer of D-T fuel frozen onto the inside surface of a solid hollow spherical shell. This fuel must remain solid until the pressure caused by the absorption of the ion beam in the outer layers implodes it to ignition.

The baseline scheme for injection of the target is shown schematically in Fig. 2.3-1. This method uses a pneumatic gun to accelerate the target while it is encased in a sabot assembly. The sabot protects the target from frictional heat due to contact with the gun barrel and separates from the target after the assembly leaves the gun barrel but before it reaches the reactor chamber.

There are two periods of time during which we have considered heating of the target fuel: while the target and sabot assembly are in the gun barrel and while the target is in the reactor chamber. The latter was calculated and temperature profiles in the target were obtained for various periods of time in the chamber. These are shown in Fig. 2.3-4 and were obtained from the temperature diffusion computer code PELLET, which simulates the time dependent heating of a material with temperature-dependent thermal properties under the influence of a time-dependent surface heat load. A surface heat load, due to 500°C blackbody radiation in the target chamber, of 2.02 W/cm^2 has been assumed for the target in Fig. 2.3-3. It is seen in Fig. 2.3-4 that the maximum temperature in the fuel at 32.5 ms after the target enters the target chamber, the time at which a target moving at 200 m/s would intersect the ion beams, is slightly less than 14 K. This occurs at the DT-LiPb interface and is still below the melting temperature of DT so that a slight lowering of the injection velocity will not lead to melting of the fuel. Furthermore, the temperature at the inside boundary of the fuel is below the sublimation temperature. This calculation was based on an assumption that the target enters the cavity with a uniform temperature of 4 K. Since the fuel is only slightly below the melting and sublimation conditions, if the injection velocity is to be kept at 200 m/s the target must not be heated to any significant degree while it is in the gun barrel.

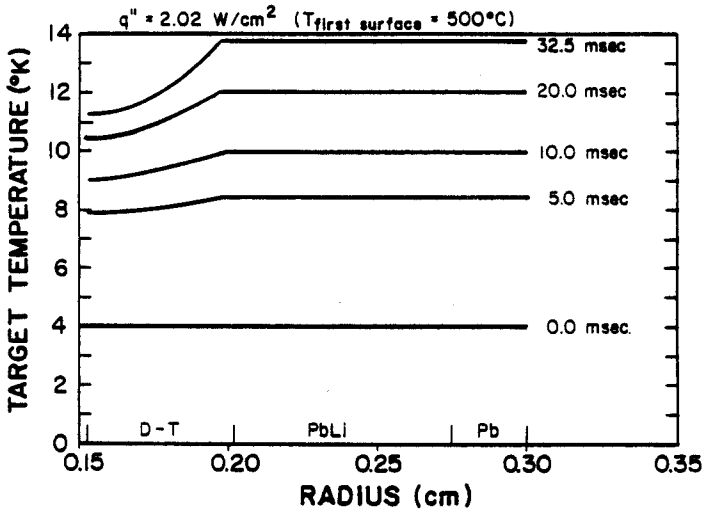

Fig. 2.3-4. Target temperature profiles due to heat in target chamber.

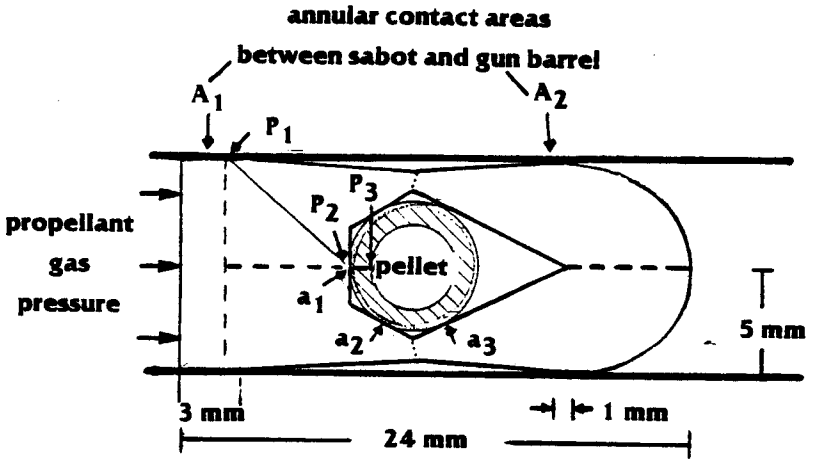

Fig. 2.3-5. HIBALL target and sabot.

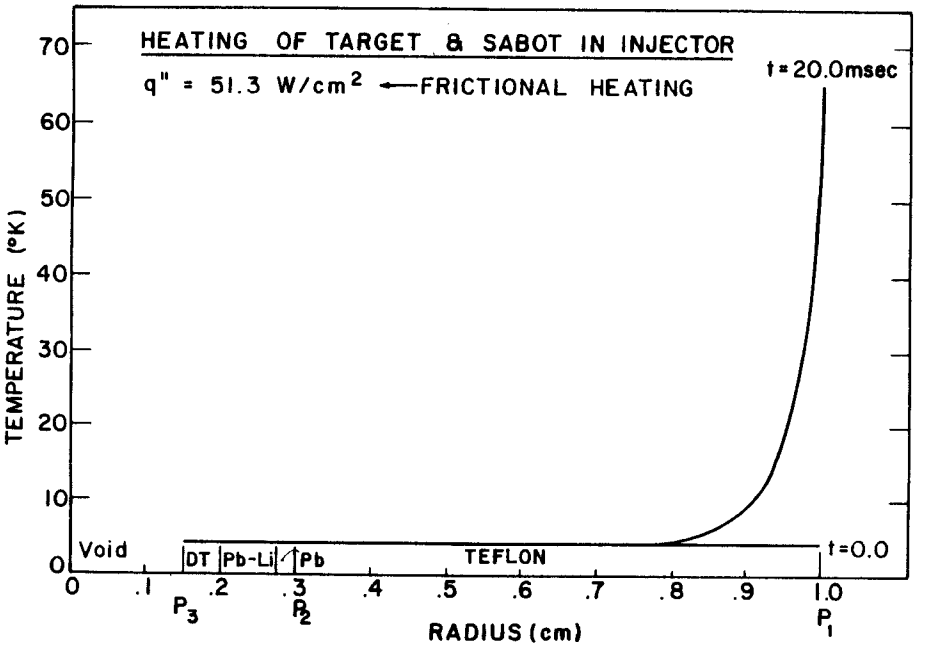

Fig. 2.3-6. Target and sabot temperature profiles due to heating in gun barrel.

A sabot which is shown in Fig. 2.3-5 with a pellet inside has been designed at Interatom[3]. The sabot is heated by friction with the gun barrel at annular contact areas A_1 and A_2. Heat is conducted to the target through contact areas a_1, a_2 and a_3. The sabot material is taken to be Teflon and the gun barrel material is steel, giving a coefficient of friction of 0.0513. The frictional heat load on the surface of the sabot is

$$\dot{q}_f = f\ A\ P\ \bar{V}$$

where f is the coefficient of friction, A is the contact area, P is the force per unit area exerted on the sabot by the gun barrel and $\bar{V}$ is the average velocity of the sabot in the gun barrel. With $\bar{V}$ = 100 m/s and P = 10^5 N/m^2, the frictional heat load is 51.3 W/cm^2.

The greatest conduction of heat from the contact between the sabot and gun barrel and the target fuel will occur along the path shown as $P_1P_2P_3$ in Fig. 2.3-5. Point P_1 is at the forward-most edge of contact area A_1, which is the largest contact area at 0.78 cm^2. Point P_2 is at contact area a_1 between the target and the sabot which is 0.03 cm^2 and is both much larger and closer to A_1 than either a_2 or a_3. Point P_3 is at the inside edge of the solid D-T fuel, at the point closest to P_2.

We have used the PELLET code to calculate the heating of the target by frictional heat from contact area A_1. PELLET is a one-dimensional computer code which we have applied to heat transfer along the line $P_1P_2P_3$. Heat transfer is actually a three-dimensional problem in the sabot assembly so that this one-dimensional analysis will overestimate the heat transferred to the target. Because the one-dimensional heat transfer is an overestimate and because we are considering the path of greatest heat transfer, the method is felt to be conservative.

The temperature profiles predicted by PELLET are shown in Fig. 2.3-6. Profiles are shown at the time that the acceleration starts and 20 ms later, when the target leaves the gun barrel. Notice that the target is not heated at all and that most of the sabot is not heated either. Thus the target enters the cavity at a uniform temperature of 4 K. We have still neglected heating during storage due to tritium decay and heating while the target is moving from the gun barrel to the target chamber.

Thus we have shown that the heating due to friction during acceleration and due to blackbody radiation in the target chamber of HIBALL do not damage the target.

2.3.4 Synchronization

The simplest way to ensure synchronicity of the target and the ion pulse would be to use an injection technique in which the total travel time of the target (e.g., 80 ms for v = 200 m/s) is reproducible to within ±1 μs and to trigger both the ion pulse and the target injector by fixed signals derived from a common time base. However, it appears difficult to attain that precision in a mechanical process. A more realistic method consists in tracking the target during its ballistic flight within the reactor chamber by photoelectric gates, calculating its time of arrival and triggering the ion pulse accordingly. The complete pulse buildup and transport procedure in the HIBALL-II driver takes only about four milliseconds. The driver is, therefore, triggered at a time when the target is only about 1 m from the focus location. By this time its arrival can be predicted to within ±1 μs, as shown in HIBALL-I.[1] (See also Section 3.2.3.)

References for Section 2.3

1. B. Badger et al., "HIBALL - A Conceptual Heavy Ion Beam Driven Fusion Reactor Study," University of Wisconsin Fusion Technology Institute Report UWFDM-450, Kernforschungszentrum Karlsruhe Report KfK-3202 (1981).

2. J.W.-K. Mark, Proc. Intern. Symp. on Accelerator Aspects of Heavy Ion Fusion, Report GSI 82-8 (1982), p. 454; W.A. Barletta, W.M. Fawley, D.L. Judd, J.W.-K. Mark and S.S. Yu, Proc. Internat. Symp. on Heavy Ion Accelerators and Their Applications to Inertial Fusion, Institute for Nuclear Study, University of Tokyo (1984), p. 99; T.D. Beynon and E.H. Smith, ibid, p. 537.

3. R. Kreutz, Reports KfK-3465 and 3466 (1983), and Fusion Technology (to appear).

4. E.W. Sucov (ed.), Report WFPS-TME-81-001 and DOE/DP/40086-1 (1981); E.W. Sucov, paper IAEA-TC-392/30 in "Fusion Reactor Design and Technology," Proc. 3rd Technical Committee Meeting and Workshop, Tokyo 1981 (Vienna 1983).

3. DRIVER

3.1 Considerations Leading to the Modified Driver of HIBALL-II

Since the completion of the first report on HIBALL we have reconsidered the ion charge state, as well as linac performance and the scheme of current multiplication. The main issue had been control of space charge effects, which strongly urged the use of Bi^{2+}. In 1982, following a detailed analysis of space charge problems presented at the GSI Symposium on Accelerator Aspects of Heavy Ion Fusion[1] and pursued thereafter, we chose single-charged Bi as a more convenient candidate. Here we benefit from the fact that accelerator space charge limits generally scale with q^2/A, with q the charge state; hence single-charged ions offer considerable relaxation. This is at the expense of a doubled linac length and higher demand on guiding magnetic fields due to the doubled magnetic rigidity. The final focusing, on the other hand, has strongly benefited from the allowance of a smaller emittance ε, due to the fact that q^2/ε is a quantity that should be kept about constant in the storage rings.

The next important issues is the filling time of the storage rings, which is inversely proportional to the linac current. At the 1982 GSI Workshop it was emphasized that the microwave instability should be the major mechanism to limit the filling time, and that the first HIBALL driver was operating in an unstable regime.[2] As an intermediate step, a scenario was studied which promised a very short filling time of the storage rings (1 ms) so that less than three e-foldings of the microwave instability, following the linearized theory, should occur.[3] The linac current had to be raised to the large value of 660 mA, which is still in accordance with space-charge transport theory, but demands excessive cost for RF installation, because more than 7.5 GW of RF power in short pulses is needed. The cost for the RF generators would amount to about half of the total driver cost.

Recent progress in simulation of the microwave instability suggests that, due to favorable nonlinear effects, the acceptable storage time can be made much longer than anticipated from the linearized theory.[4,5] On this basis we have proposed a revised scenario with 4 ms storage ring filling time; the linac current is reduced to the comfortable value of 165 mA. This promises a better balance between the load on the linac and storage rings from the design and cost point of view.

A further significant change has been the replacement of the linear induction bunchers in the final beam lines by a stack of RF buncher rings.

The fact that 20 such beam lines exist would have required a total induction voltage of about 10 GV, which is practically prohibitive in our scenario for cost reasons. The large space charge time shift during pulse compression in the buncher rings is presently being investigated by simulation, yet unpublished results have not indicated any problem for the parameters considered.

Results of computer simulations of the debunching process of the linac beam of the transfer ring have suggested that it is preferable to replace the large transfer rings of earlier designs by a multiplicity of smaller transfer rings. This considerably reduces longitudinal and also transverse emittance growth. The latter is due to the fact that the transverse space charge effect decreases with the radius of the ring, as long as the beam current is unchanged. Multiturn stacking in the earlier large transfer rings has been replaced by a system where two beams are repeatedly combined transversely by a combiner septum outside of the rings.

3.2 Driver Description

3.2.1 Accelerator Scheme

3.2.1.1 Linear Accelerator

The linac is to provide all the kinetic energy of the Bi^+ ions to drive the target, whereas the transfer and storage rings are to multiply the beam current in a first step, and the buncher rings to perform a second compression step. In order to keep the compression factors low, and to avoid deterioration of the beam quality by instabilities during storage, the linac should deliver as high a beam current as possible. The limit is set by economy, rather than by beam stability in the linac, at 100 to 200 mA. For much higher currents, the beam power, and hence the RF power, become so large that a prohibitive fraction of the total investment cost must be spent for tetrodes, klystrons and RF circuitry. We have chosen 165 mA, hence the beam power is 1.65 GW, requiring 2.5 GW of RF power, or roughly 0.5 MW/m of structure (assuming 5 km structure length), which gives a reasonable ratio of RF equipment to structure cost.

The beam is produced in 8 ion sources of the HORDIS type.[6] Each of these beams is statically preaccelerated by about 300 kV, and captured by a 10 MHz low-velocity linac of the RFQ type.[7] Near the ion sources 1.6 μs pulses separated by 0.4 μs gaps have to be shaped; these gaps are necessary to facilitate switching of the beam into separate transfer rings (Section 3.2.2).

Stepwise "funneling" of pairs of beams[8] brings the microbunch frequency up to 80 MHz in the main linac, which, however, may have a higher (harmonic) RF frequency for reasons of economy, depending on the ion velocity (which determines the most economic type of linac structure) and on bunch length. The debuncher at the end of the linac, however, operates at the bunch frequency again, in order to produce the smallest possible momentum width in long microbunches. The distance from the debuncher to the transfer rings, where the beam is no longer under control of RF buckets, should be as short as possible.

3.2.1.2 Transfer Rings and Transverse Stacking Procedure

The usual way to step up the beam currents by "transverse phase-space stacking" has been multiturn injection. n-folding the beam currents by n-turn injection requires either n-fold circumferences of the preceding transfer ring, or n preceding rings containing beams simultaneously and delivering their beams in a close sequence.

Since we are concerned about momentum blowup during debunching in the transfer rings, we would prefer small rings, i.e. either the second of the aforementioned alternatives, or a more economic version which is possible for n = 2, i.e. doubling the beam current in each step. Storage for only the first of the two beams is needed (except for the first combination step); the second beam is taken at "free flight" when it emerges from the foregoing combination step. No beam rotators are needed because this "free-flight" combination works as well vertically as horizontally.

Naturally, the number of such steps must be large. Therefore, the dilution factor in each step must be small, 1.2 or less. In order to have such a small dilution factor, combination of pairs of beams is proposed, in transverse phase space outside of the rings, by means of combiner septa. This element is the inversion of a beam splitter routinely used, e.g. at UNILAC of GSI. To make the beams fit optimally into a combined ellipse, some distortion is proposed by means of sextupole magnets. Injection into the subsequent ring is then by single-turn techniques.

We propose 3-turn injection from the linac into a first and a second transfer ring, a total of 4 doubling steps using these and 3 further rings in the manner just described, and 2-turn injection into the storage rings. This results in a stacking factor of $3 \cdot 2^5 = 96$. The five transfer rings each have twice the circumference of a storage ring and can be arranged on top of each

other, similar to the CERN booster rings. Multiturn injection from the linac into the first two rings is necessary in order to destroy the microbunch structure of the beams which, if conserved, would lead to momentum-spread blowup. The number of 3 has been chosen for the sake of a low dilution factor; a higher number of turns would be a possible different choice.

Figure 3.2-1 shows the complete scenario and Fig. 3.2-2 is a possible ground plan.

3.2.1.3 Storage Rings

The storage rings must be as small as possible, and therefore equipped with superconducting magnets, for the same reason as in HIBALL-I. To allow the transfer rings to be made with normal iron magnets, two-turn injection into the SR's gives a circumference ratio of 2 for the transfer rings to the storage rings.

There is one essential difference from the HIBALL-I storage rings. The RF system creates 0.25 MHz buckets only in order to conserve the 1.6 μs bunches, not to compress them adiabatically, because this would take too much time. To match the situation of non-parabolic charge-density distribution within the 1.6 μs bunches, the buckets must have a flat bottom, which requires at least two more RF harmonics.[9]

The residence time of the beam in the last transfer ring (waiting ring WR 3) is 192 μs or 12 turns. This time is marginal and may require a similar RF system as for the storage rings. In Fig. 3.2-1 such an RF system has been assumed.

3.2.1.4 Buncher Rings

Final bunch compression to the final length of 20 ns (effective) or 30 ns (basic width) is done in the buncher rings. The concept of linear bunchers, used in HIBALL-I, has been abandoned because of excessive cost. In contrast to the low-voltage RF cavities of the SR's, the high-voltage RF cavities of the BR's probably cannot contain ferrite loadings to reduce the size of the 0.25 MHz cavities. The vacuum reentrant, high-Q cavities of the BR's present a major mechanical design problem; nevertheless, it is believed that they can be constructed, and that they are less expensive than a large number of small ferrite-loaded cavities (which would also present a space problem). Some harmonic RF components of somewhat lower amplitude have to be added.[9]

The residence time of the beams in the BR's is 160 μs, or 20 turns. In this small number of turns the beam has to tolerate a space-charge betatron

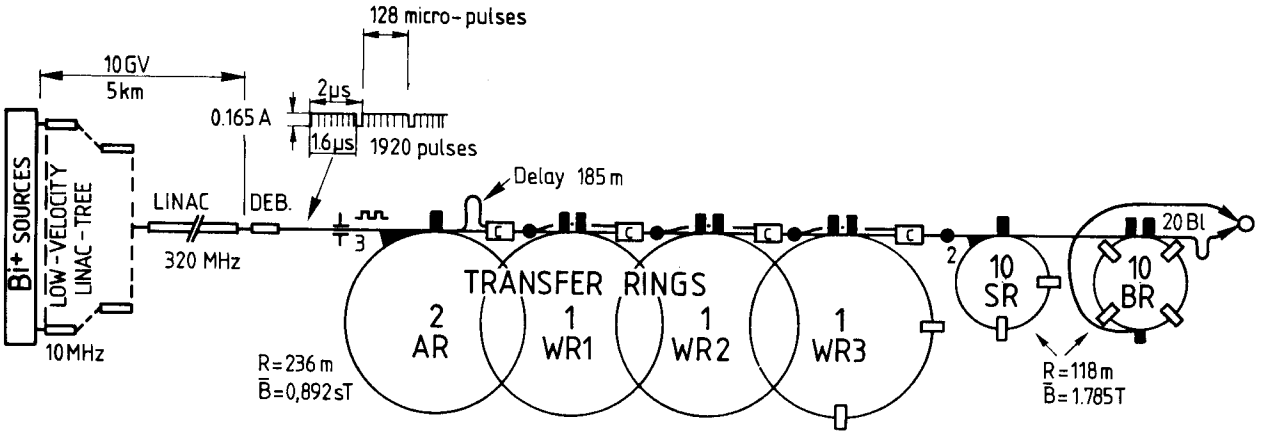

		H	V	V	V	V	H	
S=		3	2	2	2	2	2	$\prod_1^6 s_i = 96$
D=		2.7	1.2	1.2	1.2	1.2	2	
$\varepsilon_H = 1$	0.9	7.5	7.5	7.5	7.5		30	mm·mrad
$\varepsilon_V = 1$	0.9	0.9	2.2	5.2	12.5		30	mm·mrad
$\Delta Q =$ H		0.09	0.15	0.26	0.41		0.24	
$\Delta Q =$ V		0.26	0.29	0.31	0.32		0.24	

$\frac{\Delta p}{p} = \pm 5 \cdot 10^{-4}$ — $\pm 1 \cdot 10^{-4}$ — $\pm 1.3 \cdot 10^{-2}$

pulse length = 1.6 | 1.6 | 2 | 2 | 2 | 2 | 2 | 0.2 | 0.03 μs

$\hat{I}$ = 0.165 | 0.5 | 0.8 | 1.6 | 3.2 | 12.5 | 12.5 | 165 (BR exit) | 1250 A (Target)

Legend:

No of turns 5 — Multiturn Injection
Fast Kicker
RF Cavity
Switch
Combiner
Septum array (static)
Square wave deflector (vert.)
Delay (beam line of specified length)

S = Stacking factors (=current multiplier)
D = Dilution factors
ε = transverse emittance
H = horizontal
V = vertical
ΔQ = incoherent tune shift in rings
Δp/p = relative momentum deviation
$\hat{I}$ = peak beam current

Storage times
(open input gate ⟶ open output gate)

		turns	μs
AR	1+2	3	48
WR	1	3	48
WR	2	6	96
WR	3	12	192
SR	1	434	3472
⋮		⋮	⋮
SR	9	50	400
SR	10	2	16
BR	1....10	~20	~160

HIF DRIVER
4 ms Storagetime

Sept. 84

Fig. 3.2-1. HIF driver, 4 ms storage time.

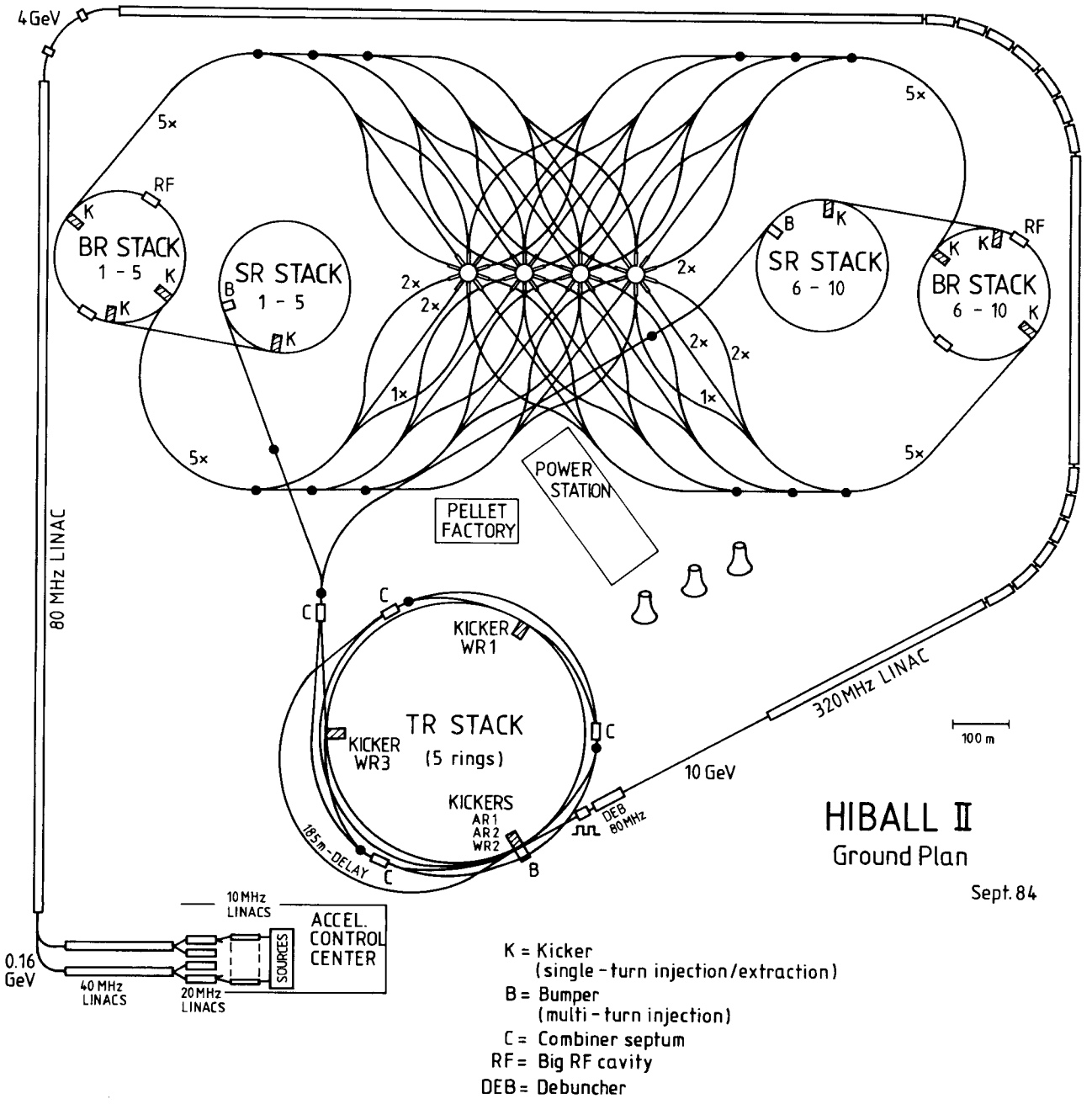

Fig. 3.2-2. HIBALL-II ground plan.

time spread of up to more than 50% of the original time, which, however, takes place over quite a few turns out of the 20. The question of integer resonance crossing under these conditions is presently being studied, but so far no serious effect has been found.

3.2.2 Timing

Figure 3.2-3 shows the beam pulse structure in the linac, in the first transfer ring, the storage rings and at the target.

As pointed out in Section 2.3.4, the synchronization of the driver to the pellet motion is straightforward with the present driver design, i.e. when the relatively low frequency voltages for the storage and buncher rings are switched off after each shot and switched on again so as to be in phase with the new target. The variable (0-100 μs) buffer time indicated in Fig. 3.2-3 is, therefore, an option which is not needed in the present design.

The situation would be more complex if the bunching RF power supplies had to be running continuously. In that case, the discrete instants 4 μs apart at which the ions can be switched out of the buncher rings would be predetermined and could not easily be shifted according to the measured target motion. The maximum longitudinal target positioning error thus introduced would be ±2 μs • 200 m/s = ±0.4 mm, still within our assumed tolerance. If a finer adjustment were needed, shot-to-shot beam steering would be a remedy (see discussion in HIBALL-I).

3.3 Components

3.3.1 Ion Sources

The multipole magnet, cusped field or reflex ion sources have undergone some development progress in recent years. An improved design for gaseous elements, CORDIS,[6] delivers a more stable beam over longer discharge pulses, and consumes less power than the older ELSIRE design. A version with an evaporation oven for low-melting metals, HORDIS II,[6] delivered a Bi^{+} beam of 37 mA into a normalized emittance of 0.16×10^{-6} m, giving a brilliance nearly four times greater than needed for the present driver design. No further attempts have been undertaken to raise the Bi^{+2} output level beyond the level reported in HIBALL-I.

Space charge compensation is needed in the transfer line from the source to the RFQ input. Successful measures have been developed in the course of work on static beam transport to keep compensating electrons inside the ion beam. The typical buildup time for the electron cloud is on the order of 10-

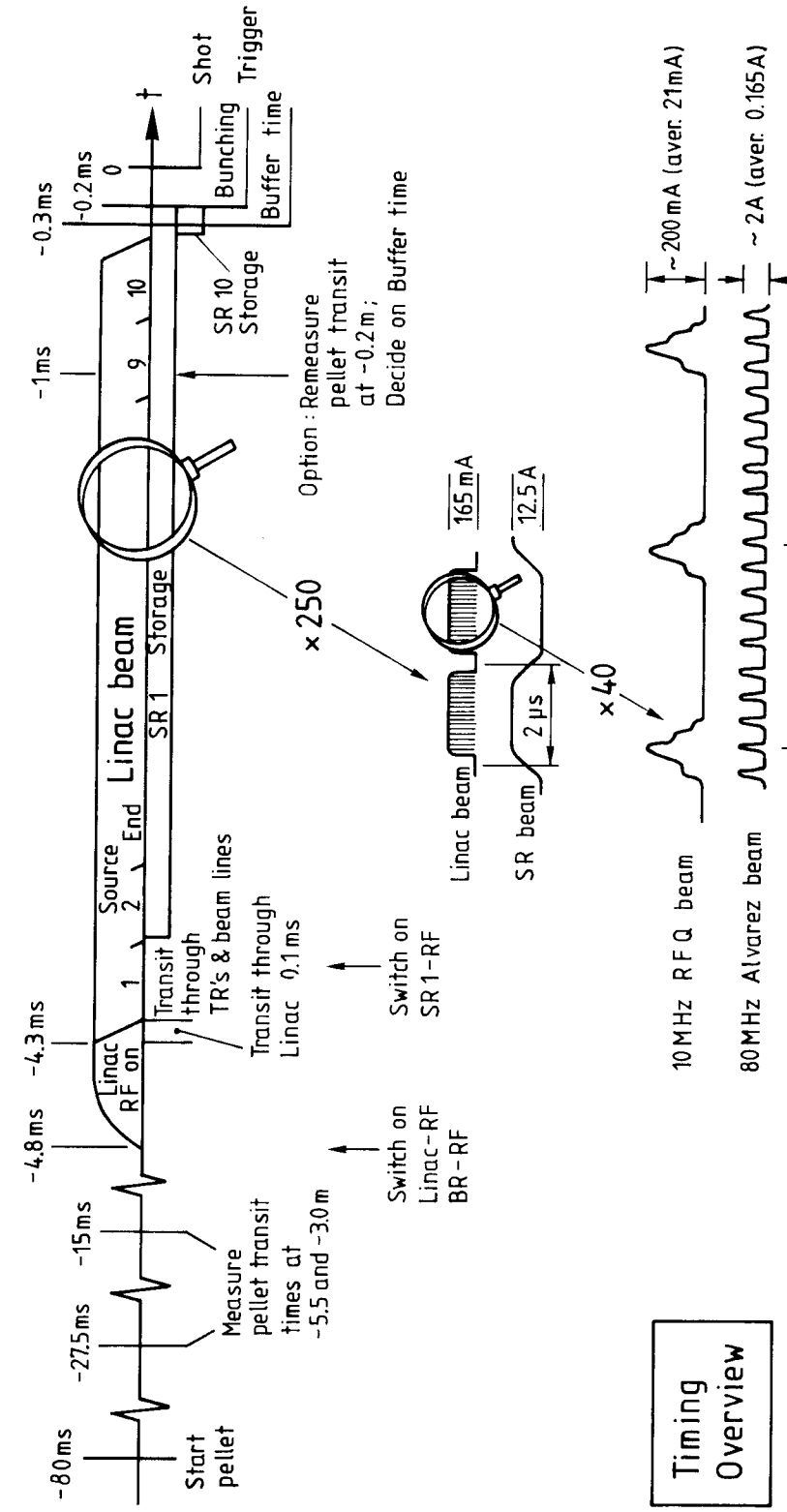

Fig. 3.2-3. Timing overview.

50 μs; shorter times can be attained but not analyzed at present because the buildup time of the discharge in the source is of the same order. Subtle techniques for analyzing the space charge potential in beams have been developed.[10] Development of intensity modulation techniques directly after the source, not using the source discharge itself, is urgently needed.

3.3.2 RFQ Type Low Velocity Accelerators

In the last two years RFQ accelerating structures have found very widespread acceptance.[11] Many labs are developing light-ion RFQ structures of the four-vane type, the frequency range of which is from 440 MHz down to 80 MHz, and the maximum mass-to-charge ratio A/q is 7.

There is, however, limited activity in developing structures suitable for heavier masses, or lower charge states. For given normalized acceptance and surface field strength, the frequency is roughly proportional to $(A/a)^{1/2}$. For Bi^+ ions, and beams of 20 mA, the frequency must be at 10 to 15 MHz. Four-vane structures then can no longer be applied.

Two types are under consideration: spiral-supported Q rods (Los Alamos, Frankfurt) and split-coaxial cavities (GSI, Frankfurt, INS). The latter have been briefly described in HIBALL-I, and in some GSI reports.[7] At GSI, one module is being successfully operated with Ar^+ and Kr^+ ions, at beam (output) intensities of up to 22 mA (Kr^+). Four more modules have been manufactured in 1984 and were being copper-plated and assembled at the end of 1984. This prototype ("MAXILAC") can be used for $A/q \leq 130$; the frequency is 13.5 MHz. This choice facilitates a latter injection of the beam into UNILAC. For Bi^+ ions, 10 MHz is a very safe extrapolation.

Because of the stable design and easy adjustment, the split-coaxial type has proven to be a good choice. Even the tank diameter of 1.2 m need not be changed for a new design because it allows direct access of inspection personnel to the inner system. (A tank diameter of, e.g., 0.6 m, would mean only a slightly lower shunt impedance.) Practical aspects like these are extremely important in accelerator development

3.3.3 Funneling

The funneling principle is quite simple: RF deflector fields kick two bunched beams into a common path. Studies have been done at KfK[8] answering essentially two questions:

a. Can the tendency of overcrowding the funnel line with deflectors, septum magnets and/or electrostatic septa, transverse quadrupole lenses,

rebuncher cavities (longitudinal lenses), pumps and diagnostic devices, be managed?

b. What is the loss of beam brilliance induced by fringing fields and by the curvature of the sine deflector voltage?

Typical situations at 1.7 MeV/u (54 MHz deflector), and 19 MeV/u (160 MHz deflector) have been analyzed. For both cases, and for Bi^{+2} and Bi^{+} ions the answer is yes for question (a), and the brilliance loss is negligible. The deflector field strength has been (conservatively) limited to 5 MV/m.

3.3.4 Beam Load of Linac Cavities and Its Compensation

Losses at the septum of a storage ring (or a synchrotron) must be minimized, and therefore the beam quality, especially the beam energy, must be precisely constant over a pulse. (Losses in a proton facility generally may radioactivate machine parts, but not immediately destroy them, because of the longer stopping range of protons.)

The key parameters which must remain constant are the RF voltage in the linac cavities, its distribution along the gaps of multigap-cavities, and its phase. As soon as beam bunches pass through the cavity gaps, their mirror currents flow around the inductive volume of the cavity and change the voltage in the gaps. These currents are in competition with the currents fed into the coupling loop from the driving amplifier. Also, the bunches draw energy out of the stored cavity field. This leads to a new voltage level. The transition from the unloaded to the loaded voltage level takes about the same time (i.e., has a time constant on the same order) as the loading process of the cavity at the RF pulse onset, namely, about Q RF periods, where Q is the figure of merit of the loaded RF cavity.

Feedback stabilization by amplitude and phase control loops usually must be slow to remain stable. Thus they cannot prevent an initial drop of voltage, but can only raise the voltage to the old level after Q RF periods, or optimistically a fraction of them. Nevertheless, most proton linacs, including the new CERN II linac, rely upon it. There are two alternative methods.

The older CERN I linac had additional beam-load amplifiers whose anode voltage pulse was triggered when the beam came on. Though what this system did was unsatisfactory for technical reasons and was later shut down, it was what is called a "feed-forward." More precisely, a feed-forward should feed additional power proportional to the beam currents, whose pulse shape is not always a simple rectangle. This has been successfully tried with the GSI RFQ

linac: the control signal is taken from a beam transformer at the RFQ entrance, amplified and simultaneously fed to an amplitude and a phase controller.

Some imperfections remain: the transformer signal is a little (~ 10 RF periods) ahead of the average beam load; amplifiers and controllers have a finite time constant; the anode current has to step up, and may cause anode voltage transients; and finally, changes of voltage distribution in multigap cavities cannot be corrected. A second method uses the fact that during buildup of the RF field in the cavity the amplifier has to deliver more power than corresponds to the RF voltage at that time. If the beam pulse sets on at a time when the RF voltage is still rising, the voltage continues with a more-or-less flat envelope. The method consists of individually timing the onset of the RF pulse for every cavity. Since a learning process is required, its result may come too late for the protection of machine elements against damage.

The best method is then a combination of both individual methods, and in fact this is what is done experimentally.

However, this problem needs continuous study and refinement, keeping in mind the need for fast beam intensity modulation.

3.3.5 Ring Components

In fusion driver storage rings, care must be taken in the proper design, or development, of the following items:

a. Any component, e.g., resonator cavities, kickers, diagnostic elements, vacuum joints, must present a low ohmic resistance to longitudinal current RF Fourier components within the instability excitation bands.

b. Injection and extraction kickers are excited at an unusually high repetition rate. Many of them can be replaced by square-wave RF deflectors fed resonantly. For the rest, e.g., the extraction kickers of the storage rings operated at a rep rate of 20 s^{-1}, technical development has to be directed into enhanced cooling, power supplies for high repetition rates, etc. On the other hand, the rise time of any kicker may be relatively long, up to 2 μs; the state of the art is at a few ns.

c. In the buncher rings, the combination of low frequency (0.25 MHz and harmonics thereof) and high voltage requires high-Q vacuum reentrant cavities of a huge size; ferrite or dielectric loading of the cavities, which would decrease the size, is prohibited.

d. In case of beam losses any machine element hit by the beam will be destroyed. The danger of damage is especially great for injection and extraction elements, and for beam diagnostic devices. All these elements must, among other features, be prepared for quick change, even in spite of some radioactivity levels. This is an engineering challenge.

A comment on item (a) should be given; this is probably the most important issue. High-intensity machines for relativistic protons can contribute some experience, but in some respect they behave in a different way: transverse collective instabilities used to be more critical than longitudinal instabilities. In a subrelativistic machine, in contrast to the aforementioned relativistic machines, longitudinal collective instabilities become more probable, and hence more critical, at $\beta < 0.5$. The classes of disturbing construction elements become different, e.g., vacuum bellows will play a minor role, whereas ferrite cavities, ferrite kickers, etc., become more and more disturbing. The character of the onset of instabilities is also expected to be different; in subrelativistic machines self-stabilizing mechanisms are expected to be effective.

Unfortunately, those few machines which could serve as subjects of investigation, e.g., the CERN booster rings, are extremely busy, and there is no access time for experiments. For years it was hoped that the SNS machine at Rutherford Lab, U.K., would be open for experiments of this kind. New hopes concentrate upon the LEAR ring at CERN, and on the GSI (W. Germany) machines SIS and ESR, of which the latter two do not yet exist.

3.4 Progress in Beam Simulation

Given the fact that presently existing accelerator facilities are not suitable to test most of the high-current beam dynamics problems of the driver accelerator, more emphasis had to be put on computer simulation. We have developed 2- and 2-1/2-dimensional many-particle simulation programs[12,13] and applied them to problems of emittance growth, beam stability and interface problems between different accelerator devices and between driver and target. Since completion of the first HIBALL study we have thus been able to analyze qualitatively and quantitatively several of the key problems in beam dynamics and to determine the new driver scenario on a more consistent theoretical basis.

In the following we list the issues that have entered particularly into the new design, as well as those relevant to the driver-target interface.

Detailed results will be found in Subsections 3.4.1-3.4.5.

(i) Debunching of Linac Beam -- The undesired momentum width blowup due to space charge during stacking and debunching of the linac beam in the first transfer ring could be reduced by choosing a substantially smaller ring radius.

(ii) Longitudinal Microwave Instabilities -- A newly found mechanism suppressing destructive growth of the instability has been used to keep the holding time in storage rings (thus also the linac current) as a "free" parameter for design.

(iii) Final Bunch Compression -- It was found that longitudinal pulse compression dynamics behave in the desired way if two RF harmonics are switched on in the buncher rings.

(iv) Prepulse Formation -- We have found a method of producing an extended prepulse by applying an RF voltage to the beam.

(v) Final Transport -- "Perfectly" matched beam distributions have been found for very high space charge conditions, which considerably raises the confidence that no beam degradation occurs during the long final transport lines.

3.4.1 Debunching of Linac Beams

The problem is the increase in $\Delta p/p$ due to space charge after the microbunches have left the holding RF buckets of the linac, i.e. on their flight to the transfer ring and during the first revolutions. The critical current above which the effect can be noticeable depends on the momentum spread and bunch length. The electrostatic energy of the bunch is transferred into longitudinal "thermal" energy (i.e., momentum width) during free flight (see Fig. 3.4-1).

The amount of momentum width blowup depends on the critical ratio of electrostatic to "thermal" energy. In the limit where this ratio is large, the final momentum width after debunching of an initially parabolic bunch has been found as given by[14]

$$\left(\frac{\Delta p}{p}\right)^2_{deb} \gtrsim \frac{q\,\frac{I}{A}\,B_f^{-1}}{(\pi mc^2/e\eta\gamma\beta^2)}\,\frac{Z_o g}{2\beta\gamma^2} \qquad (3.4\text{-}1)$$

with: q -- charge state

I -- electric current

B_f -- bunching factor

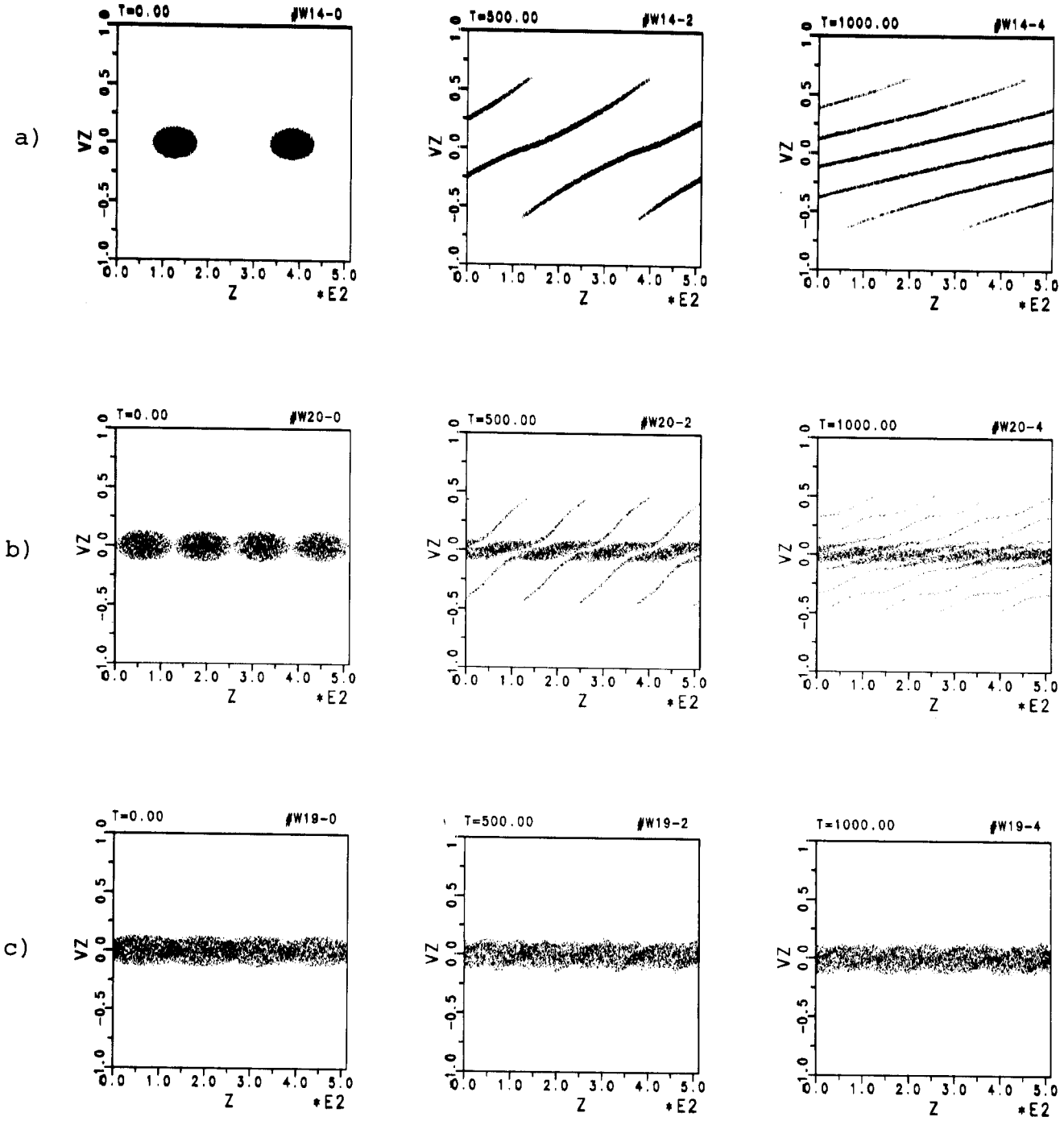

Fig. 3.4-1. Computer simulation of debunching of a periodic chain of intense microbunches injected into the transfer ring. Shown are projections into the longitudinal phase space at different times of the debunching process.
(a) separated microbunches
(b) no gaps between microbunches of subsequently injected turns
(c) 30% overlap of microbunches

$\eta \simeq 1/\gamma^2$

Z_o -- impedance of vacuum (377 Ω)

$g = 1 + 2 \ln R_{pipe}/R_{beam}$.

Hence, it is given by the current, however small the initial Δp/p is. As an example, we find for 10 GeV Bi^+ and a bunching factor of $B_f = 1/4$:

$$\left(\frac{\Delta p}{p}\right)_{deb} = \pm 1.8 \times 10^{-4} \quad . \tag{3.4-2}$$

This corresponds to a $(\Delta p/p)_{fwhm} = \pm 3.5 \times 10^{-4}$, which is a factor 3.5 larger than demanded. A larger current or charge state makes the effect worse.

To cure the effect we suggest the following: choose the radius of the debuncher ring small enough to avoid debunching during the first revolution; by properly tuning the revolution frequency it can be realized that the second turn is injected such that its microbunches are adjacent to those of the previous turn, and so on. If no gaps are left between the microbunches, or even a slight overlap is achieved, there is practically no momentum blowup (Fig. 3.4-1b,c), hence Eq. (3.4-1) is invalidated.

3.4.2 Longitudinal Microwave Instability

In storage rings with high currents of nonrelativistic heavy ions, as considered for drivers in inertial fusion, control of the resistive microwave instability has been recognized as a key issue during the last HIF Workshop held at GSI in 1982. By means of computer simulation with the particle-in-cell code SCOP-RZ[13] we have shown that the predictions from the linearized theory of instability are overly pessimistic. This is due to an early nonlinear saturation of the instability, which prevents a harmful broadening of the momentum distribution. The main effect of the initially unstable behavior is the development of a thin stabilizing tail in the momentum distribution towards lower momenta, which produces enough Landau damping to suppress any further microwave activity.

The main concern has been the effect of a broadband (Q = 1) resonator centered at about the lowest magnetic cutoff frequency $\omega_c = \gamma\omega_o R/b$, with R the machine radius and b the vacuum chamber radius. This resonator is supposed to describe the effect of many cross section variations. The resistive impedance of this resonator (~ 10 Ω) is supplemented by the large (purely capacitative) impedance due to space charge ($\gtrsim$ 1 kΩ). The large ratio ImZ/ReZ of about 100

is the reason why nonlinear coupling effects dominate over the growth of a single mode for HIF parameters. In Fig. 3.4-2a,b we show the momentum distributions for two distinct cases. Case (a) refers to a nearly relativistic beam with ImZ/ReZ = 2 and a momentum width which is a factor 2.2 below the Keil-Schnell stability limit. The distribution becomes rapidly unstable and shows the expected overall broadening. In case (b) we have assumed ImZ/ReZ = 16 and a momentum width that is even a factor 4 below the Keil-Schnell limit. The instability is substantially weaker and stops after having developed a stabilizing tail.

The main part of the distribution remains narrow, hence the initially high phase space density is not diluted. The fraction of total intensity within the stabilizing tail decreases with increasing ratio ImZ/ReZ. For the heavy ion fusion case, where this ratio is about 100, we thus expect only a few percent of tail population. This simulation result is consistent with the prediction of stability obtained from solution of the dispersion integral for a narrow Gaussian momentum distribution with a broad stabilizing tail (of Gaussian shape, but containing only a few percent of the total intensity), as an approximation to the saturated distribution obtained from simulation.

Future experimental verification of this stabilizing mechanism is highly desirable. Such experiments will have to check whether the predicted rapid coupling to higher harmonics above the cutoff frequency takes place in a real machine to the same degree as in the simulation, where the deviations (in impedance) from a circular conduction pipe have been incorporated in the simplified model of a Q = 1 resonator near cutoff.

3.4.3 Final Bunch Compression

The final longitudinal compression of intense beams to the desired 20 ns pulse length at the target takes place in the buncher rings and in the final transfer lines to the target chamber. In longitudinal phase space such a compression is essentially a 90° rotation of the phase space ellipse, if space charge forces are absent. During the final part of compression outside of the ring, the bunch is not exposed to an applied RF force; hence particles move at constant velocity (in the absence of space charge) until the ellipse is upright at the target position. Including space charge at the current levels considered here, we find that compression is practically just as effective, provided that the bunching RF amplitude is about doubled to counteract the repulsive space charge force.[4] Results for the final stage of such a self-

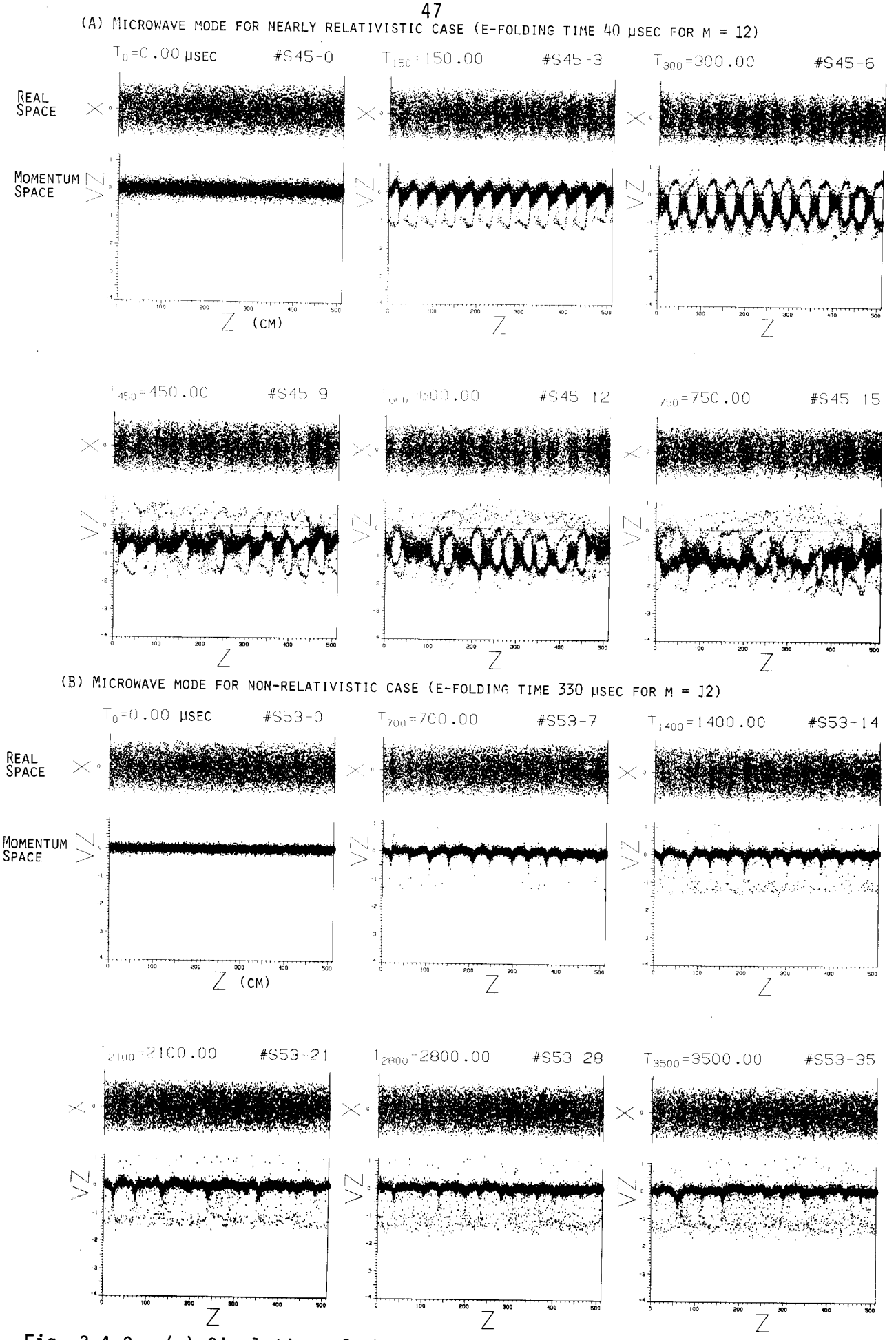

Fig. 3.4-2. (a) Simulation of the resistive microwave instability for a nearly relativistic beam, showing destructive effect on the moment distribution.
(b) Same, but nonrelativistic energy (heavy ion fusion case) showing the self-stabilizing effect of a tail in momentum space.

consistent computer simulation are shown in Fig. 3.4-3. The initial bunch (prior to applying the RF) had nearly constant line density in real space and a Gaussian velocity distribution. Due to the rotation in phase space these profiles appear interchanged in the final compression stage, with only a slight modification by space charge, hence the final line density is approximately Gaussian. The longitudinal emittance increases by only about 5%.

3.4.4 Prepulse Formation

An important question has been to provide a prepulse, which contains several percent of the total intensity over a time longer than the duration of the main pulse (see Section 2.1.1). It was felt that the prepulse should use the same beam lines as the main pulse, since no space is available in the reactor chamber for additional entrance ports, aside from the extra cost of additional beam lines.

Here we suggest a method that requires no extra hardware except for an additional RF cavity in each storage ring. The idea is to generate a tail in the momentum distribution towards larger momenta; the subsequent bunch compression is a rotation in phase space, hence the momentum tail transforms into a prepulse (Fig. 3.4-4).

The RF voltage required for this shaping of the momentum distribution depends on the desired length of the prepulse and is of the order of 100 kV for a frequency of typically 50 MHz. We observe that the intensity and length of the prepulse can be varied by proper tuning of the frequency and amplitude of the RF voltage. The use of several RF cavities also allows shaping of the momentum distribution and thus the prepulse profile in order to match the target requirements.

3.4.5 Final Transport

Transport of high-current beams over long distances is necessary for two different reasons: first, in order to transfer the beam from the buncher rings to the reactor chamber; and secondly to provide a sufficiently long drift distance for the final longitudinal bunch compression, which necessarily has to take place outside of the buncher rings.

The question of whether such transport can be expected to occur without degradation of beam emittance and no loss of beam intensity has been pursued intensively during the past years. An important step towards defining an optimum channel has been the discovery by simulation[15] of stable and emittance conserving transport for currents close to the space charge limit, pro-

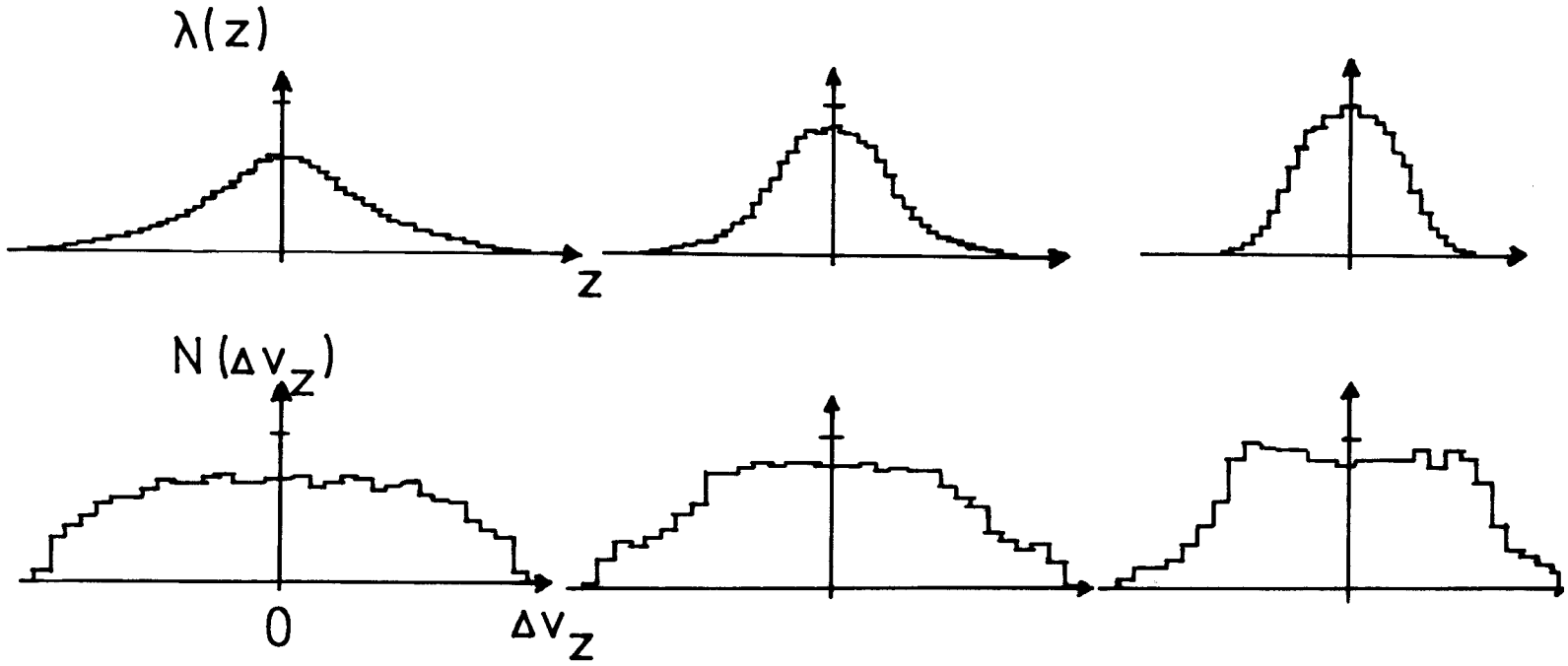

Fig. 3.4-3. Final stage of simulation of bunch compression by RF field. Shown are the line density [$\lambda(z)$] and the velocity distribution [$N(\Delta v_z)$] at different times close to the maximum compression point.

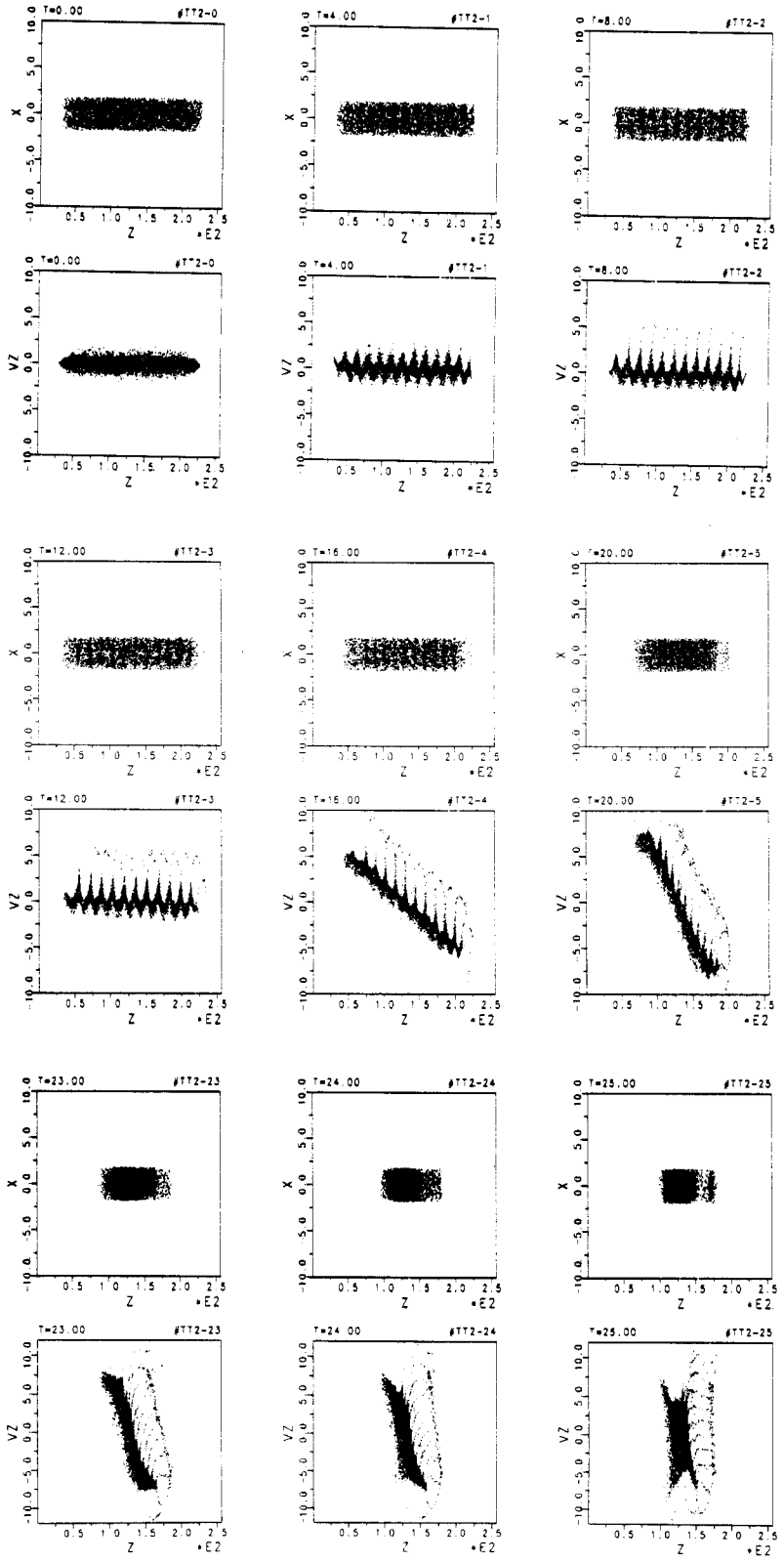

Fig. 3.4-4. Simulation of prepulse formation by RF voltage. Shown are projections into the longitudinal-transverse real space (z - x) and longitudinal phase space (z - v_z) at different times. Shaping RF voltage is on between T = 0-12. At T = 12 the bunch compression voltage is turned on. The prepulse has a peak at its very front for T = 25, which is smeared out shortly sooner or later.

vided that σ_0, the betatron phase advance per focusing period (in the absence of space charge), was chosen to be 60°. The effect of space charge is to reduce the phase advance to a value σ, which one attempts to make as small as possible for optimum current transmission. This becomes evident from the relationship for current[16]

$$I \sim a^2 \sim \varepsilon/\sigma$$

where a is the channel aperture and ε the beam emittance.

In Fig. 3.4-5 is shown the result of a simulation,[17] where the beam has been transported over 50 cells of a periodic channel very close to the space charge limit (σ_0 = 60°, σ = 5°). The initial distribution is a "water-bag" (i.e., uniform) in phase space; the final distribution to high accuracy is the same. In particular, no particles have been scattered out in phase space. We have also examined the effect of fringe fields and found it was negligible. More detailed results are found in a recent survey article.[18] In view of recent experimental results[19] that very closely confirm the theoretical predictions, it can be concluded that long periodic transport for heavy ion fusion is now a reliable concept.

References for Chapter 3

1. L. Teng, Proc. of the Symposium on Accelerator Aspects of HIF, 1982, GSI Darmstadt, GSI-82-8, (1982) p. 356.

2. J. Laclare, Proc. of the Symposium on Accelerator Aspects of HIF, 1982, GSI Darmstadt, GSI-82-8, (1982) p. 278.

3. I. Hofmann, A. Jahnke, K. Beckert, D. Böhne, R.W. Müller, IEEE Trans. Nucl. Sci. NS-30, 3070 (1983).

4. I. Hofmann, I. Bozsik and A. Jahnke, IEEE Trans. Nucl. Sci. NS-30, 2546 (1983).

5. I. Hofmann, "Suppression of Microwave Instabilities," in: Proc. INS Intern. Symp. on Heavy Ion Accelerators and Their Application to Inertial Fusion, Institute for Nuclear Study, University of Tokyo (1984).

6. R. Keller et al., "High-Current Ion Sources Development," GSI-83-2, p. 3; or GSI-83-1, p. 288.

7. R.W. Müller et al., "Experimental Results with a Very-Heavy-Ion RFQ Accelerating Structure," GSI-84-11, p. 77 (LINAC 84, Seeheim, FRG).

8. K. Bongardt, D. Sanitz, "Funneling of Heavy Ion Beams," GSI-82-8, p. 224 (Proc. Symp. on Accel. Aspects of HIF, Darmstadt 1982).

9. I. Hofmann, I. Bozsik, A. Jahnke, "High-Current Beam Transport Experiments in a Magnetic Quadrupole Channel at GSI," GSI-84-11, p. 315 (LINAC 84, Seeheim).

10. P. Kreisler, "Untersuchungen des Raumladungspotentials von Ionenstrahlen," GSI-84-10 (Thesis, Univ. Frankfurt).

11. H. Klein, "Development of the Different RFQ Accelerating Structures and Operating Experiences," IEEE Trans. NS-30, 4 (1983), 3313 (Part. Acc. Conf., Santa Fe, NM, 1983).

12. I. Bozsik and I. Hofmann, Nucl. Instr. Meth. 187, 305 (1981).

13. I. Hofmann and I. Bozsik, Proc. of the Symposium on Accelerator Aspects of HIF, 1982, GSI Darmstadt, GSI-82-8, p. 181 (1982).

14. I. Hofmann, "Storage Ring Physics Issues for GSI Program," in: Proc. INS Intern. Symp. on Heavy Ion Accelerators and Their Application to Inertial Fusion, Institute for Nuclear Study, University of Tokyo (1984).

15. I. Hofmann, Nucl. Instr. Meth. 187, 281 (1981).

16. M. Reiser, Part. Acc. 8, 167 (1978).

17. J. Struckmeier, J. Klabunde and M. Reiser, Proc. Linear Accelerator Conference, 1984, GSI Darmstadt.

18. I. Hofmann, Proc. Linear Accelerator Conference, 1984, GSI Darmstadt.

19. C. Kim, Proc. Linear Accelerator Conference, 1984, GSI Darmstadt.

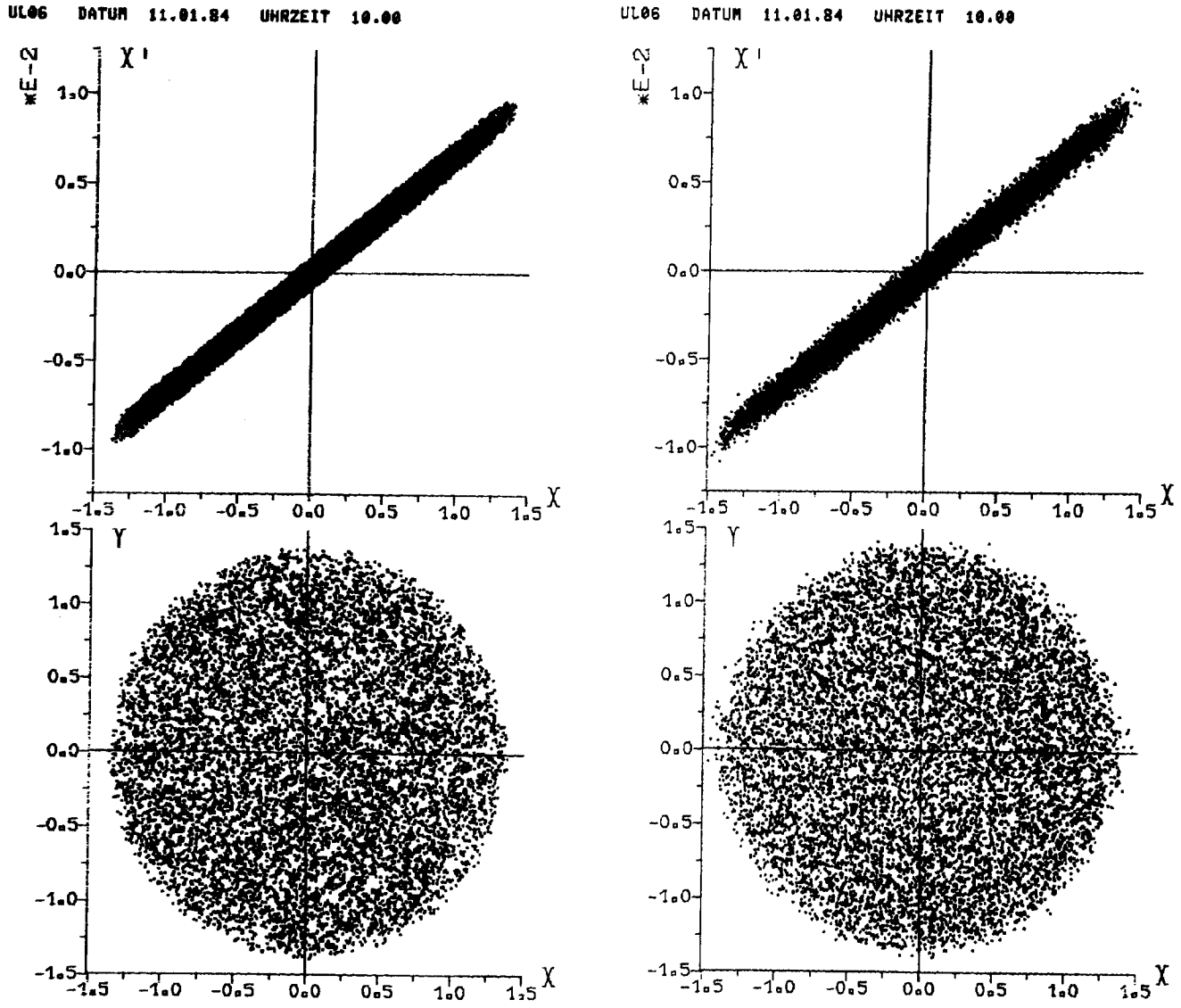

Fig. 3.4-5. Simulation of matched "water-bag" distribution for high-current transport in periodic channel. Projections into vertical phase space (x - x') and real space (x - y) at start and after 50 cells.

4. BEAM TRANSPORT

4.1 Beam Stripping During Transmission

The maximum allowable gas density at the time of beam propagation is determined by the stripping of the beam ions while they are moving through the reactor cavity. In HIBALL-I where Bi^{+2} was the driver ion species, a Born approximation calculation of the stripping cross section for 10 GeV Bi^{+2} on Pb was performed.(1) In HIBALL-II, the driver ion species is 10 GeV Bi^{+}. In the years since the completion of the HIBALL-I report, there has been some experimental work to test the accuracy of the Born approximation. The stripping cross section has been reevaluated to include both changes.

The change in ionization state of the beam ions will undoubtedly have some effect on the stripping cross section but this is not easily quantified. The outer atomic electronic structure changes from a single 6p electron to two 6p electrons where the electrons are in different p shells. For both Bi^{+2} and Bi^{+} stripping involves the removal of an electron from a half filled p shell. It is assumed that the difference in ionization potential for the $6p^1$ and $6p^2$ electrons does not play a major role in the stripping. Thus, to a first approximation, it will be assumed that the stripping cross section is the same for both ions.

There have been measurements completed at Lawrence Berkeley Laboratory(2) of the charge-changing collision cross sections for heavy ions moving at the same speed as Bi^{+} in HIBALL-II. Measured cross sections for the loss and capture of electrons by Xe and Pb ions encountering N_2 molecules are shown in Fig. 4.1-1 for highly ionized beam ions and for a few values of $\beta = v/c$. A comparison has been given here for the measured electron loss cross sections with the major theoretical methods. The Born Approximation Sum Rule (BASR) is the method used in HIBALL-I. One can see that the BASR values are high by at least a factor of four.

Therefore, the stripping cross section of 7×10^{-16} cm^2 which was used in HIBALL-I is probably a conservative value which can be used for HIBALL-II as well. If there were a great advantage to choosing a value a few times smaller than this, one could do so with a small loss in conservatism. The present gas condensation calculations predict that a 5 Hz rep rate is possible with this cross section.

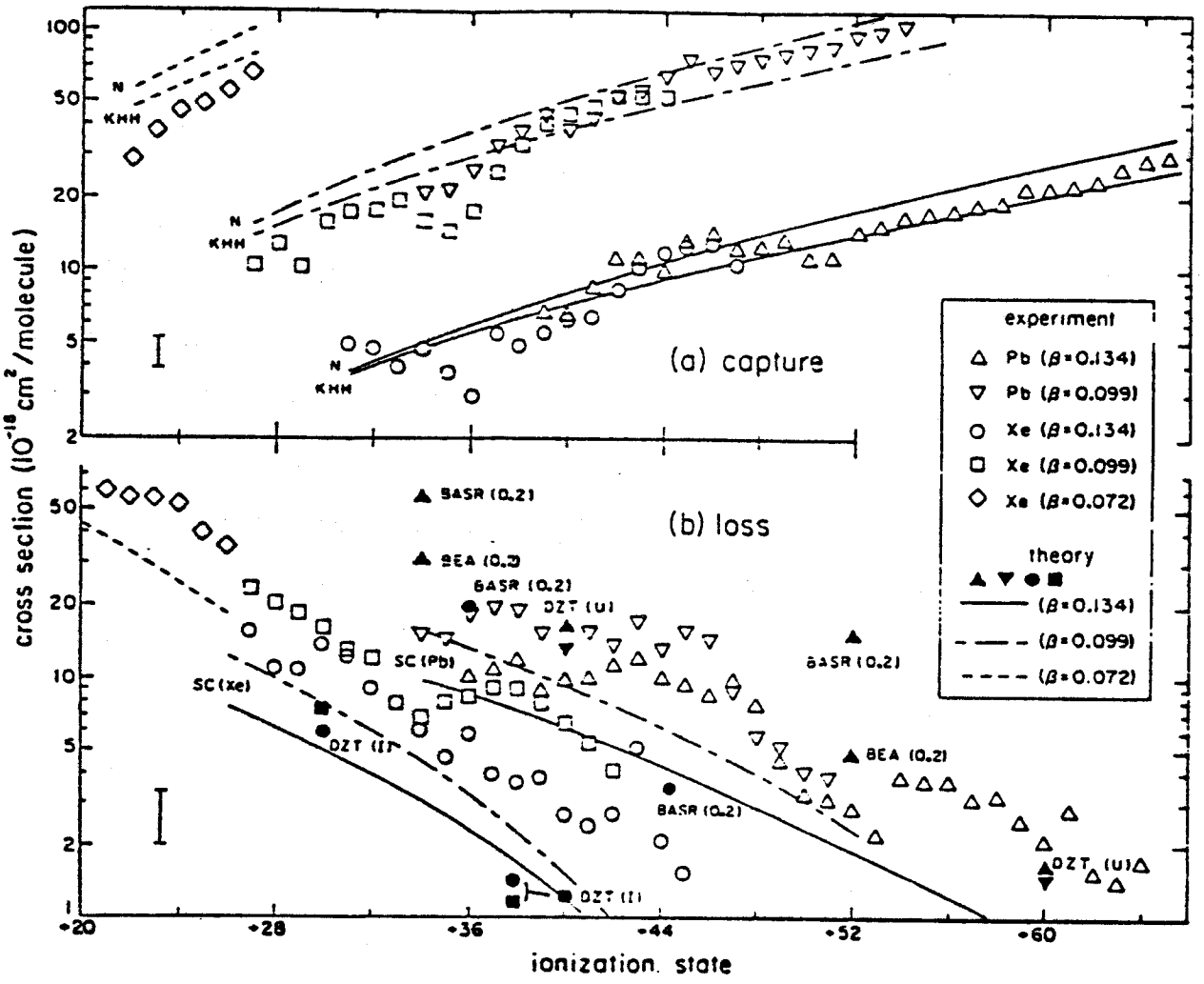

Fig. 4.1-1. (a) Capture and (b) single-electron-loss cross sections in N_2 as a function of the ionization state for Pb and Xe ions. Experiment is shown as open symbols, theory with the corresponding closed symbols and with broken and solid lines.

At a Pb density of 8×10^{10} atoms/cm^3 the mean free path between Bi^+-Pb charge changing collisions is 150 m. The fraction of beam stripped is thus,

$$1 - \exp(-7 \text{ m}/150 \text{ m}) \text{ or about } 5\%.$$

References for Section 4.1

1. G.H. Gillespie, Y.K. Kim and K.T. Cheng, "Born Cross Sections for Ion-Atom Collisions, Phys. Rev. A 17, No. 4, 1284-1295 (April, 1978).

2. J.A. Alonso and H. Gould, "Charge Changing Cross Sections for Pb and Xe Ions at Velocities Up To 4×10^9 cm/s," Phys. Rev. A 26, 1134 (1982).

4.2 Design of the Final Focusing System

4.2.1 Introduction

The final focusing system is the last stage of the ion beam guidance line and performs the task of directing the ions onto the fusion pellet. The following conditions determine the design of the focusing ion optics:

1. it must concentrate the accelerated ion beam onto the target of 4 mm radius with minimal loss of intensity which means weak effects of chromatic or geometric lens aberrations;
2. the constructional arrangement of the reactor vessel restricts the mechanical construction of the ion optical lenses used; and
3. the geometry of the final focusing system prevents the contamination of wide regions of the beam guidance lines by neutron radiation emitted from the fusion target.

4.2.2 Choice of the Ion Optical Lens

For the inertial confinement fusion study HIBALL-II the use of 10 GeV Bi^+ ions is assumed. Hence the momentum of these ions leads to a magnetic rigidity of 208 T-m. At present, magnetic quadrupole lenses seem capable of focusing such stiff ion beams.[1,2]

The phase space area of the proposed ion beam amounts to $x_0 \cdot x_0' = y_0 \cdot y_0' =$ 30 πmm mrad, so that the ions impinge upon a spot of 3.5 mm radius with maximal angles of about ±9 mrad (leaving 0.5 mm for image aberrations). Under the simplified assumption that the ions travel straight trajectories inside the reactor chamber, the beam diameter at the reactor wall reaches 160 mm. However, the influence of space charge due to the strong beam current demands even larger apertures.

The comparatively short focal lengths for the high rigidity of the ion beam require strong magnetic flux gradients in the quadrupole lenses up to the

maximal 9 T/m. To reduce electric power consumption, the quadrupole lenses could be driven by superconducting coils. However, such conductors are sensitive to neutron radiation thus requiring heavy shielding between the coils and the particle beam. Consequently, the distance between the coils and the optical axis becomes even larger.

Our goal was to reduce the magnetic flux gradients and thus the necessary flux density at the beam envelope to below 2 T. In this case, the magnetic flux can be guided by iron structures and the magnetic flux density at the conductor coils remains near 2 T, even if the coils are removed from the beam tube because of the required shielding.

In Fig. 4.2-1, the shape of an "iron-dominated" quadrupole lens is shown, designed with conventional techniques. The outer diameter of 2.4 m lets the lens fit in the vertical distance of the beam lines at the reactor wall. The aperture diameter of 0.4 m is sufficiently larger than the expected beam envelope of ±0.18 m maximal. The current coils are mounted to the iron yokes at a large distance of about 0.4 m from the optic axis to ensure enough space for radiation shielding. Nevertheless, the magnetic quadrupole field in the beam region is quite accurate and the influence of higher multipole terms is less than 1 percent. For this calculation we have chosen iron with material properties of STABOLEC 520-50 A. The flux density gradient of 9 T/m is achieved with a driving current of about 200 kA per coil (current density 10 A/mm^2). The electric power needed amounts to approximately 2 MW for one quadrupole lens and normal conducting coils.

4.2.3 The Proposed Final Focusing System

The design of the final focusing system is shown in Fig. 4.2-2. The essential optical elements are the magnetic quadrupole lenses arranged in two triplets. As mentioned above, the beam envelope near the last focusing lens should be about 18 cm in diameter. On the contrary, the coasting beam has an envelope of only 2 to 3 cm. To enlarge the beam, a crossover is not recommended because of the strong space charge of the beam. Therefore, first a long drift distance ensures the widening of the beam. Because of the high rigidity of the ion beam the task of focusing the beam is assigned to two lens triplets, with a laminar beam in between. In this region the beam line is bent for the purpose of separating the neutron radiation line from the upstream part of the beam guidance system. As Fig. 4.2-3 shows, the backstreaming neutrons from the fusion process cannot pass beyond the bending magnet.

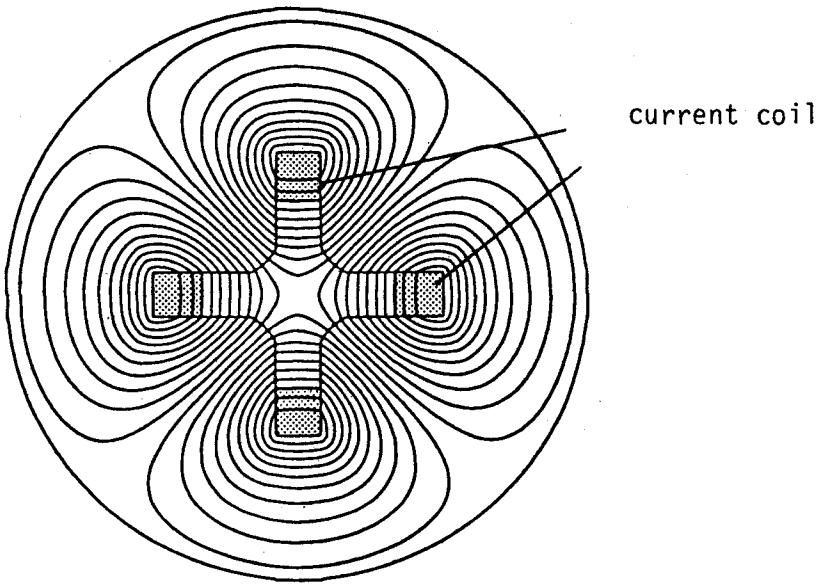

Fig. 4.2-1. Shape of the last quadrupole of the final focusing system. The distance between the current coils and the beam tube is large to allow sufficient shielding against neutron radiation.

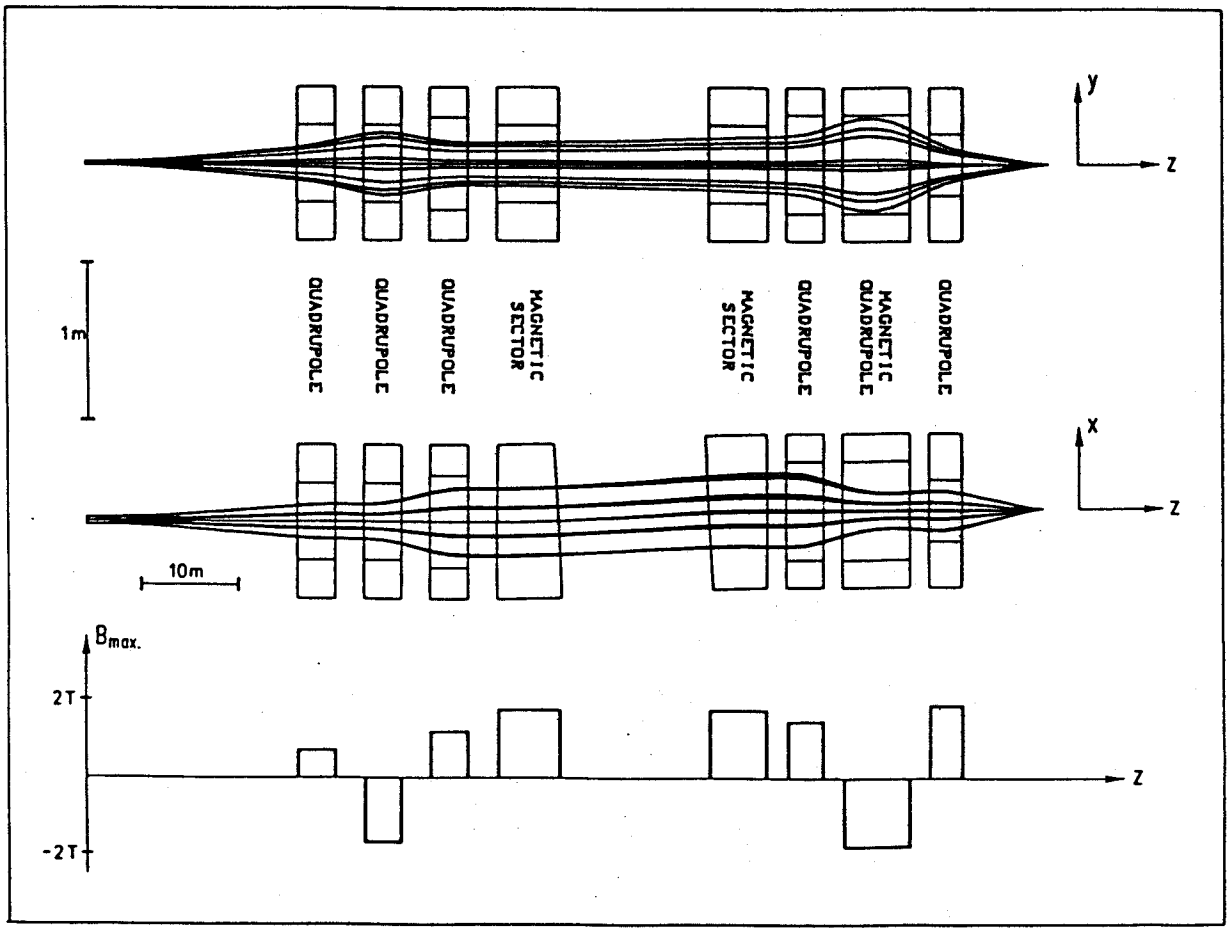

Fig. 4.2-2. The final focusing system for the HIBALL-II reactor design in projections on the horizontal (upper part) and vertical (lower part) planes. The transversal directions are 8 times enlarged compared to the longitudinal direction. The system uses iron-dominated lenses with pole tip flux densities below 2 T.

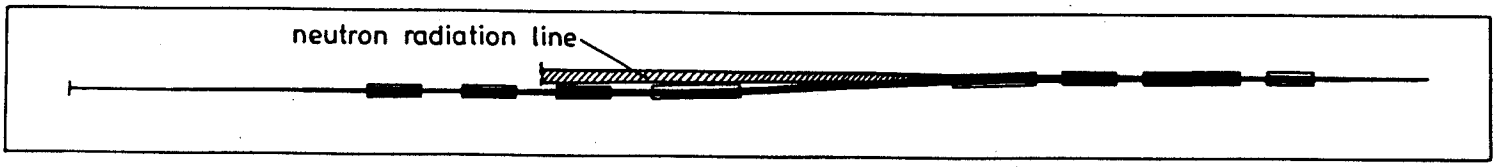

Fig. 4.2-3. The lower part of Fig. 4.2-2, i.e. the projection of the final focusing system on the vertical plane is shown again, but with equal scales in the transversal and the longitudinal direction. Note that backstreaming neutrons cannot pass beyond the bending magnet.

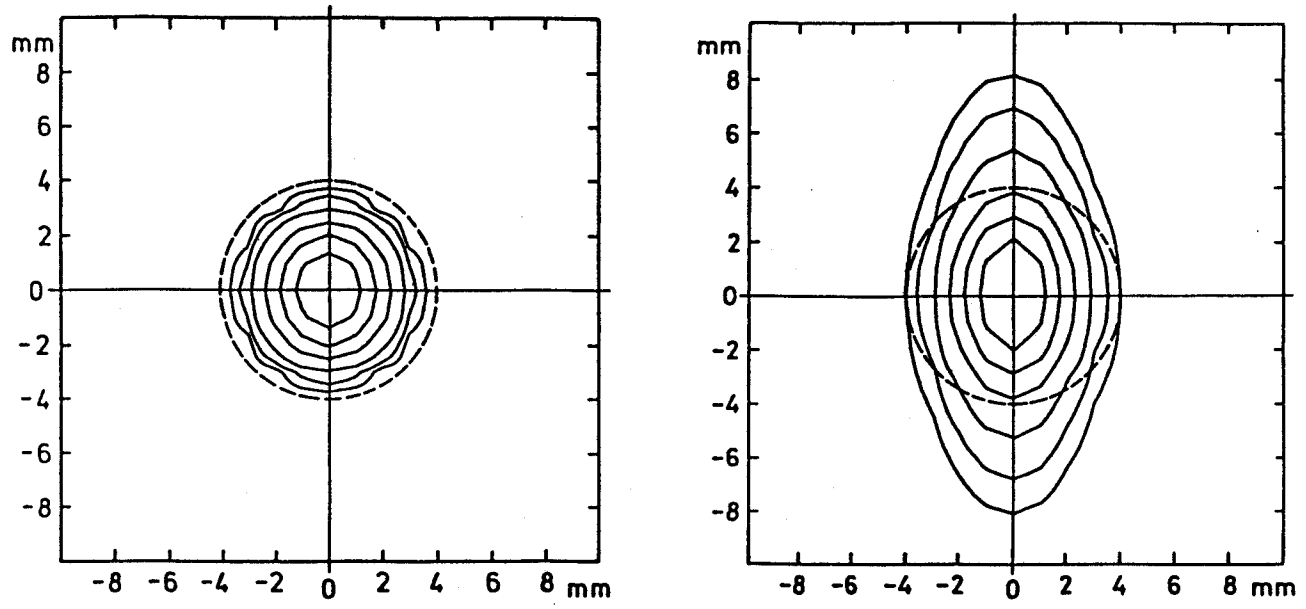

Fig. 4.2-4. Ion beam intensity distribution at the pellet as obtained by the final focusing system of Fig. 4.2-2 for an ion beam with negligible momentum spread (left diagram) and one with a momentum spread of ±1% (right diagram). The shape of the fusion target is indicated by dashed lines.

Note that another bending magnet is inserted to compensate the dispersion and to achieve an achromatic spot on the target.

4.2.4 Optical Aberrations of the Focusing Lens System

The optical properties of the final focusing system are determined by the use of our computer code "GIOS"[3] which can perform third order calculations including the effects of fringing fields and of space charge influences.

The proposed final focusing system is optimized to be essentially free of geometric aberrations of second and higher order, and hence needs no correction by multipole elements. However, since the focal length of the quadrupole lenses depends on the momentum deviation, the focusing system has a second order chromatic aberration. The intensity distribution at the target is shown in Fig. 4.2-4 for a monochromatic beam and for a beam with a momentum spread of ±1%. The shape of the spot shows that part of the beam misses the target if the momentum spread does not vanish. The result of quantitative calculations on the efficiency is presented in Fig. 4.2-5. It should be mentioned that the field strength of the last two quadrupole lenses is adjusted according to the selected momentum spread to achieve maximal efficiency.

The momentum spread of the beam arises mainly from the beam bunching. The resulting momentum distribution along the beam bunch is sketched in Fig. 4.2-6a. If one folds it with Fig. 4.2-6b which shows the efficiency of intensity on the target versus the momentum deviation for a monochromatic beam, it gives an idea on the time dependence of the intensity on the target.

4.2.5 Uncertainty of the Technical Realization

One of the unknowns in the HIBALL-I study is the degree of the space charge neutralization of the ion beam with the existing rest gas pressure. In case any such effect occurs, the rate of neutralization may be different for the head and the tail of the beam bunch or it may fluctuate with time. Calculations on the sensitivity of the optical system versus variations of the effective ion current lead to the following results:

- Assuming space charge compensation is uniform along the optical system, the calculated efficiency varies only slightly with the effective beam current, i.e. a one percent change in current results in about 0.16 percent change in efficiency. Similar consequences follow from variations of space charge compensation in the reactor chamber only (see Fig. 4.2-7).
- On the other hand, the efficiency is very sensitive to the variation of effective beam current (see Fig. 4.2-8) in the first region of the focus-

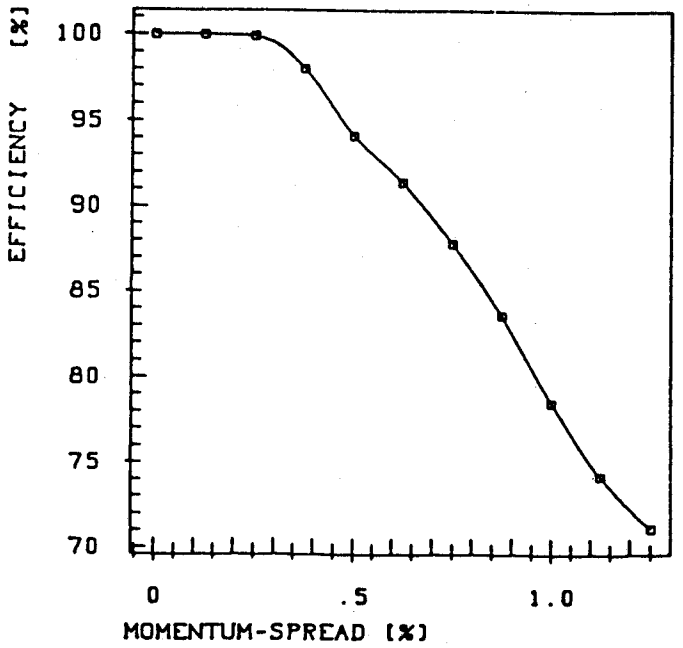

Fig. 4.2-5. The percentage of the ion current which reaches the fusion target is plotted as a function of the momentum spread of the beam.

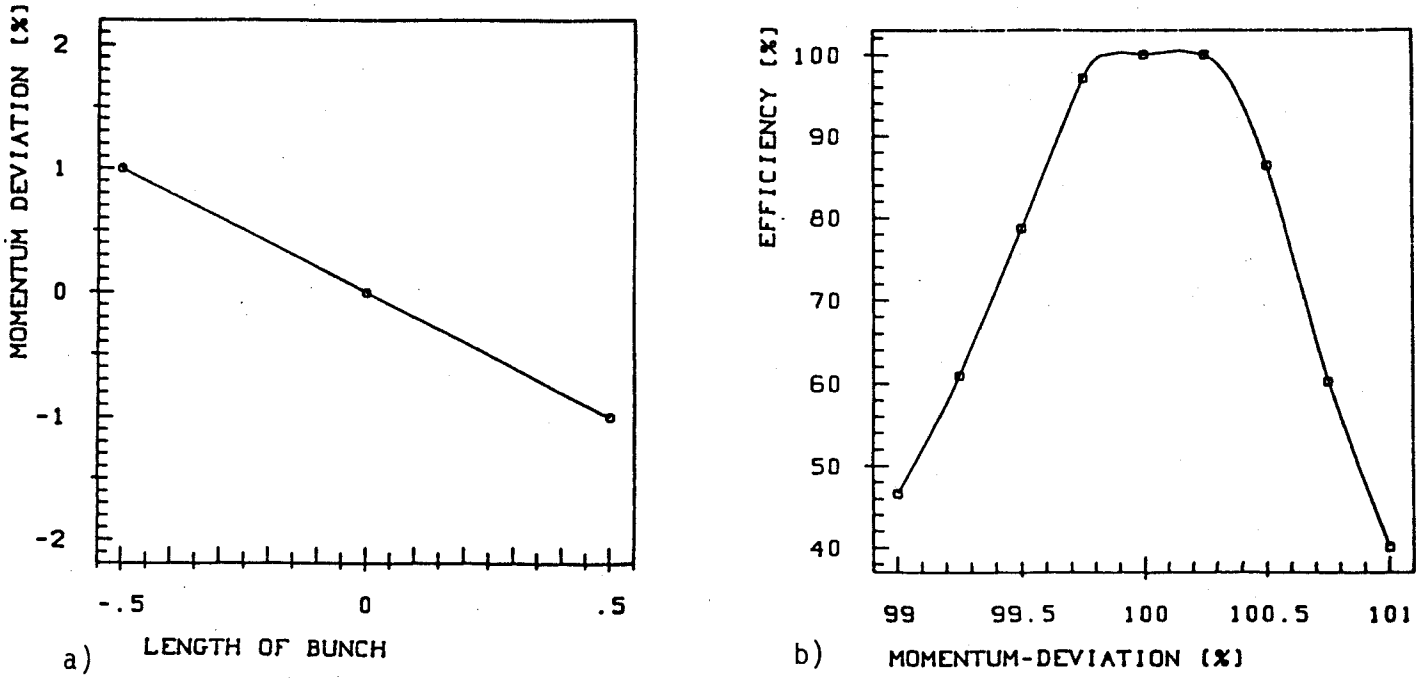

Fig. 4.2-6a. Schematic of the momentum distribution in a bunched beam.

b. The percentage of ion current which reaches the fusion target as a function of the momentum deviation. Fig. 4.2-6a folded with Fig. 4.2-6b gives an indication of the time dependence of the intensity on the pellet.

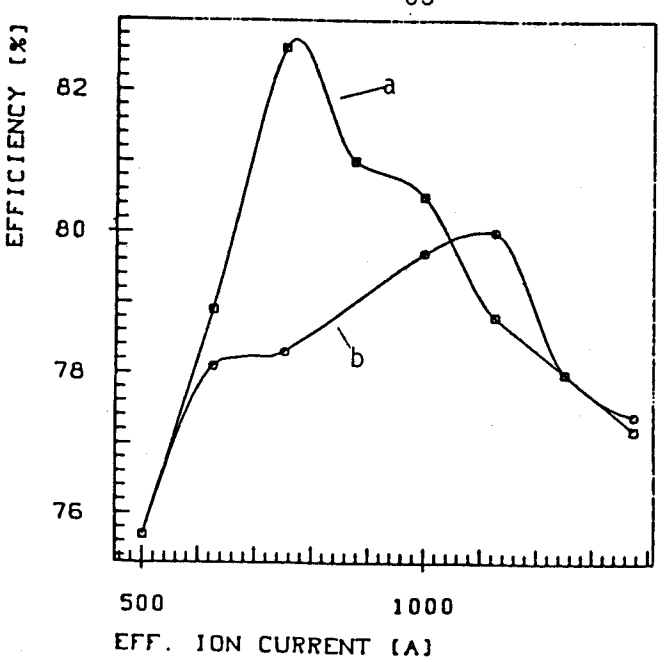

Fig. 4.2-7. The percentage of ions which reach the fusion target as a function of the space charge compensation:
a) uniform throughout the entire system;
b) compensation in reactor vessel region only.

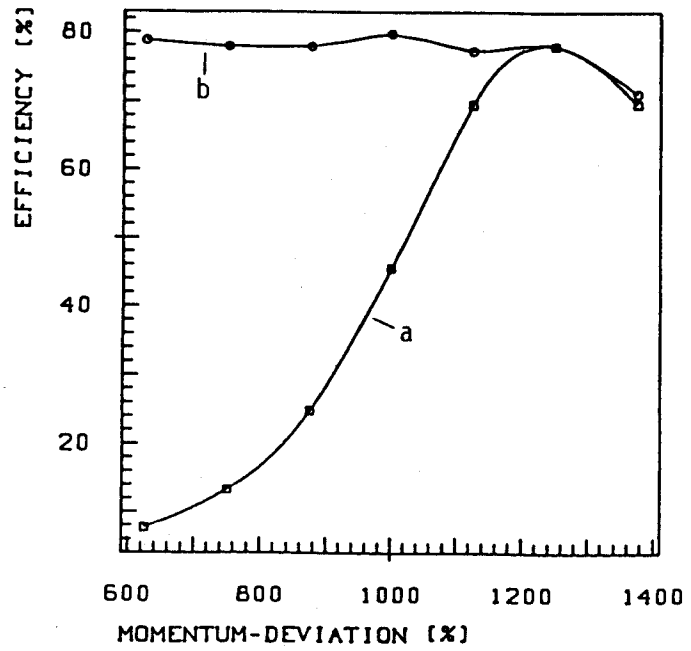

Fig. 4.2-8. The percentage of ion current which reaches the fusion pellet plotted as a function of the space charge compensation in the first drift region only:
a) all other system parameters fixed;
b) the last two quadrupoles adjusted in flux density to achieve maximal efficiency.

ing system exclusively (the first drift distance up to the first quadrupole lens). In detail, one gets a change in efficiency of about 20% due to a change of 1% in effective beam current, for all other systems parameters fixed. With adjusted flux densities for the last two quadrupole lenses, according to various effective beam currents, the efficiency stays constant. However, for low effective current the required flux density at the pole tips reaches 2.2 T.

4.2.6 Uncertainties in the Calculations

The ion optical design program "GIOS" calculates space charge effects assuming an equal density distribution within the beam cross section. The so called KV distribution is assumed as invariable and effects resulting from varying the form of the density distribution thus cannot be calculated by this code. Not affected by this restriction are all terms of first and second order because of negligible external hexapole influence. However, a radial dependence of the space charge density is expected leading to an octupole moment. The comparison with ray tracing methods verifies this suspicion. Fig. 4.2-9 shows the ion density distribution along the final focusing system as calculated by computer code "BEAMTRACE."[4]

4.2.7 Conclusion

Even for large image distances a small spot is feasible. The optical system can be realized for the assumed high rigidity ion beam by classical iron-dominated magnetic quadrupole lenses with a field strength at the pole tips of less than 1.8 T. The layout of the system presented corresponds with presently existing technical expertise. A more exact prediction of the efficiency can be given with a better knowledge of the intensity distribution in the four-dimensional phase space ellipsoid of the coasting beam and its variation by external and self-fields.

References for Section 4.2

1. J. Brezina and H. Wollnik, GSI Report 83-2 (1982), p. 24.

2. H. Wollnik and J. Brezina, Proc. Symp. on Acc. Aspects of Heavy Ion Fusion, GSI Report 82-8 (1982), p. 387.

3. H. Wollnik, J. Brezina, M. Berz and W. Wendel, Proc. 7th Int. Conf. on Atomic Masses, (1984), in print.

4. M. Berz, Diploma Thesis, Giessen University (1983).

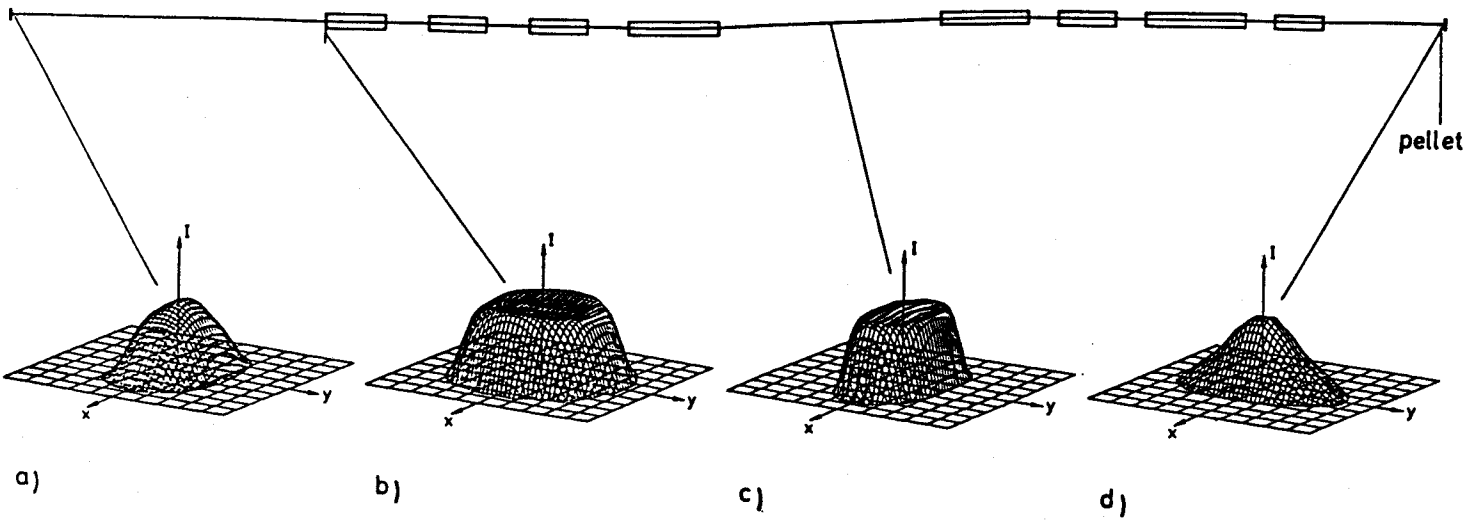

Fig. 4.2-9. The ion density distribution is shown at four positions along the final focusing system, the distribution in x-y space changes between uniform and parabolic, leading to different octupole momments of the self-field of the beam.

4.3 Shielding of Final Focusing Magnets

4.3.1 Introduction

Fusion reactors are required to accommodate a variety of penetrations. The purpose and size of these penetrations vary depending on the reactor type.[1-3] However, in all cases proper shielding is required to protect vital components in the penetration from excessive radiation damage caused by the streaming radiation. A major penetration in a heavy ion beam fusion reactor is the ion beam line penetration and a large number of these penetrations (~ 20) is required to provide uniform illumination of the target.

The HIBALL-II reactor utilizes twenty 10 GeV Bi^+ ion beams to bring the target to ignition. Each beam port is rectangular in shape with a height of 0.216 m and a width of 0.166 m at the reactor cavity wall of radius 7 m. The twenty beam ports occupy 0.12% of the 4π solid angle at the target. A number of magnets are arranged along the beam line to focus the ion beam to a spot about 7 mm in diameter at the target. Adequate shielding is required to reduce the radiation effects in the magnets below the design limits. In a previous study[4] it was shown that radiation effects in the magnets can be reduced significantly by tapering the inner surface of shield along the direct line-of-sight of source neutrons in both the quadrupole and drift sections leading to a number of neutron dumps along the beam penetration. A similar shield configuration is used to protect the final focusing magnets of HIBALL-II.

The final focusing system in HIBALL-II utilizes two deflection sector magnets resulting in two vertical bends in the beam line penetration. These bends significantly reduce the amount of radiation streaming to the periodic transport system as compared to HIBALL-I where a straight beam line was used.

In this section the neutronic analysis for the beam line penetration is presented. Radiation effects in the magnets are determined and neutron streaming along the penetration is assessed. Neutron spectra in different shield zones along the beam line are determined. These are useful in calculating the dose outside the final focusing system.

4.3.2 Magnet and Shield Configuration

The final focusing system in HIBALL-II focuses the Bi^+ ion beam from the periodic transport line onto the target. The system consists of six quadrupole lenses and two deflection magnetic sectors. Two deflecting sector fields are required to obtain achromatic focusing. Figure 4.3-1 shows the variation

of the vertical and horizontal width of the beam along the optic axis as it is transported from the periodic transport line to the target. The position of the six quadrupole lenses and two magnetic sectors is also shown. The square line represents the relative focusing strength (field gradient) of the quadrupoles. The deflection radii and angles for the two deflecting sectors are also indicated. A description of the overall geometry is given in Table 4.3-1. The lengths of the different magnetic elements as well as the field free drift sections are given. The aperture radii as well as the pole tip field strengths and field gradients are also included. Only quadrupoles with magnetic flux densities below 2 tesla are used such that iron dominated quadrupole lenses can be used. Quadrupole Q6 is driven with normal coils while all other quadrupoles are driven with superconducting coils.

The inner dimensions of the magnet shield along the beam lines were determined using the beam envelopes shown in Fig. 4.3-1. A minimum clearance of 1 cm is maintained between the shield and the ion beam. In order to minimize the radiation effects in the magnets the inner surface of the shield is tapered along the direct line-of-sight of source neutrons generated at the target such that no direct source neutrons will impinge on the shield in the magnet sections. The shield is tapered also in the drift sections between magnets leading to vertical neutron dumps in these sections. Since scattering is forward peaked for high energy neutrons, the position of the neutron dump in the drift section is chosen to be closer to the target. This shield configuration was found to increase the shielding effectiveness considerably.[4] Figures 4.3-2, 4.3-3, 4.3-4 and 4.3-5 show vertical and horizontal cross sections of the final focusing system. These cross sections are given for four axial zones covering the 100 m long system. The shield configuration and the locations of the neutron dumps are illustrated. Since no direct source neutrons will stream past the neutron dump between S1 and S2, tapering the inner surface of shield beyond this point is not required and no neutron dumps are needed. The coils used to drive the iron dominated magnets are also shown. The shield in front of the coils was required to have a minimum thickness of 0.3 m.

The final focusing system in HIBALL-II has several attractive features. Table 4.3-2 gives a comparison between some of the general features that impact the neutronics characteristics of the final focusing systems in HIBALL-I and HIBALL-II. The phase space volume for the ion beams in HIBALL-II is re-

Table 4.3-1. Description of the Final Focusing System

Element	Length (m)	Field Strength (T)	Aperture Radius (m)	Field Gradient (T/m)
Q1	22	0	0	0
	4	0.65	0.20	2.6
	3	0	0	0
Q2	4	-1.55	0.25	-6.2
	3	0	0	0
Q3	4	1.15	0.25	3.833
	3	0	0	0
S1	6.469	1.757	0.20	[R=120m, θ=3.840°]
	16	0	0	0
S2	6.283	1.757	0.25	[R=120m, θ=3°]
	2	0	0	0
Q4	4	1.45	0.32	4.531
	2	0	0	0
Q5	7.173	-1.7	0.32	-5.313
	2	0	0	0
Q6	3.508	1.8	0.20	9.0
	8.5	0	0	0

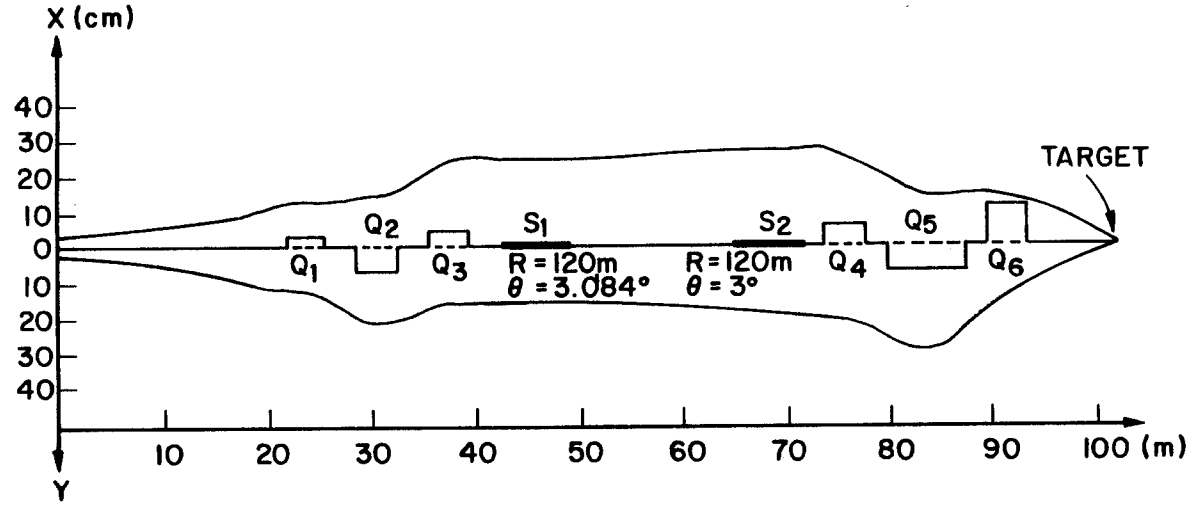

Fig. 4.3-1. Vertical and horizontal envelopes of the ion beam.

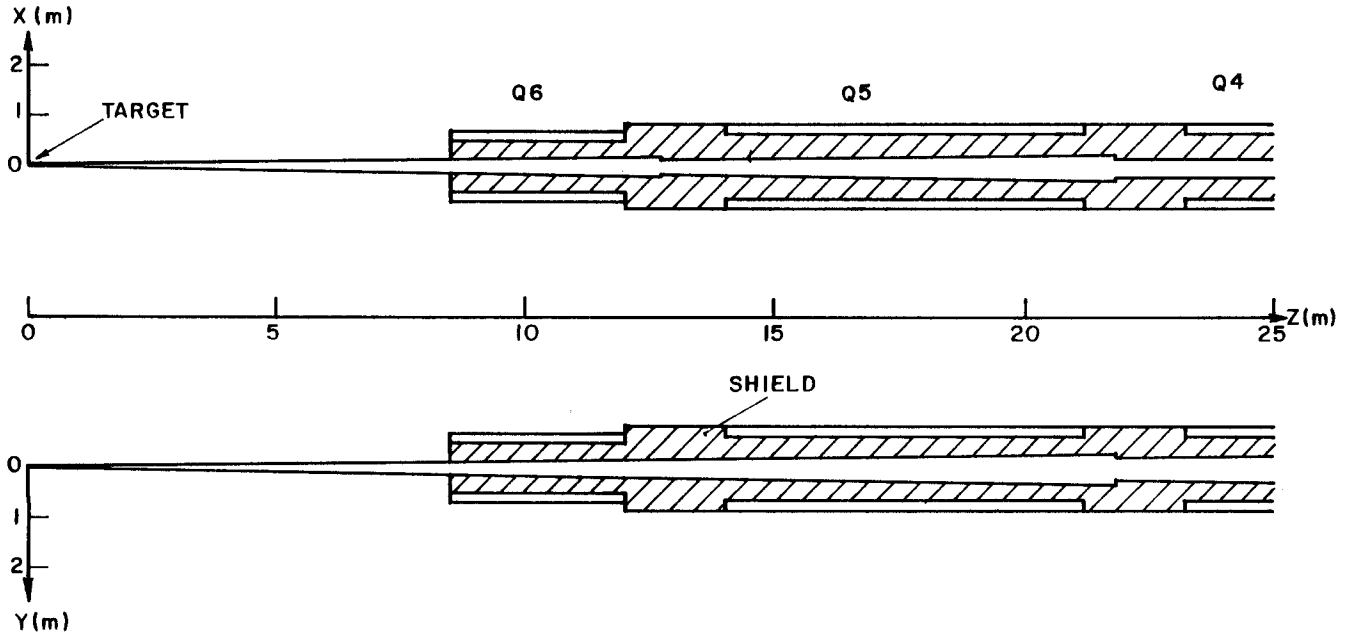

Fig. 4.3-2. Vertical and horizontal cross sections of the final focusing system in the zone $0 \leq z \leq 25$ m from the target.

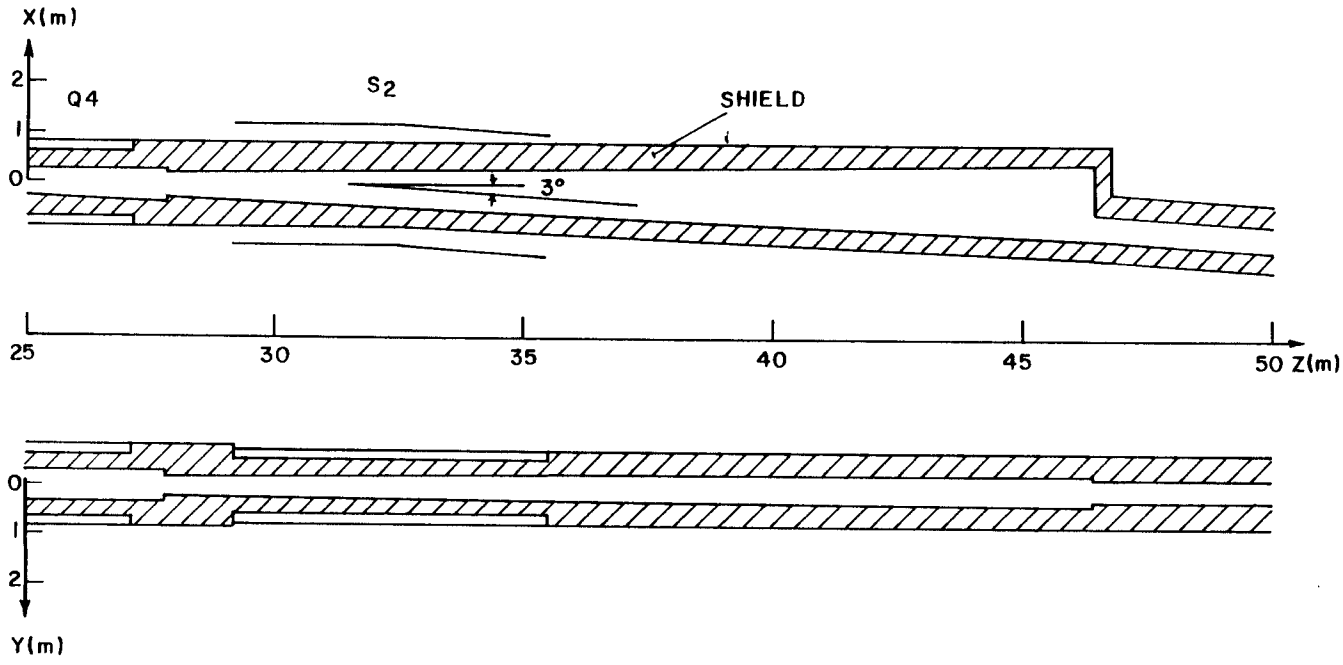

Fig. 4.3-3. Vertical and horizontal cross sections of the final focusing system in the zone $25 \leq z \leq 50$ m from the target.

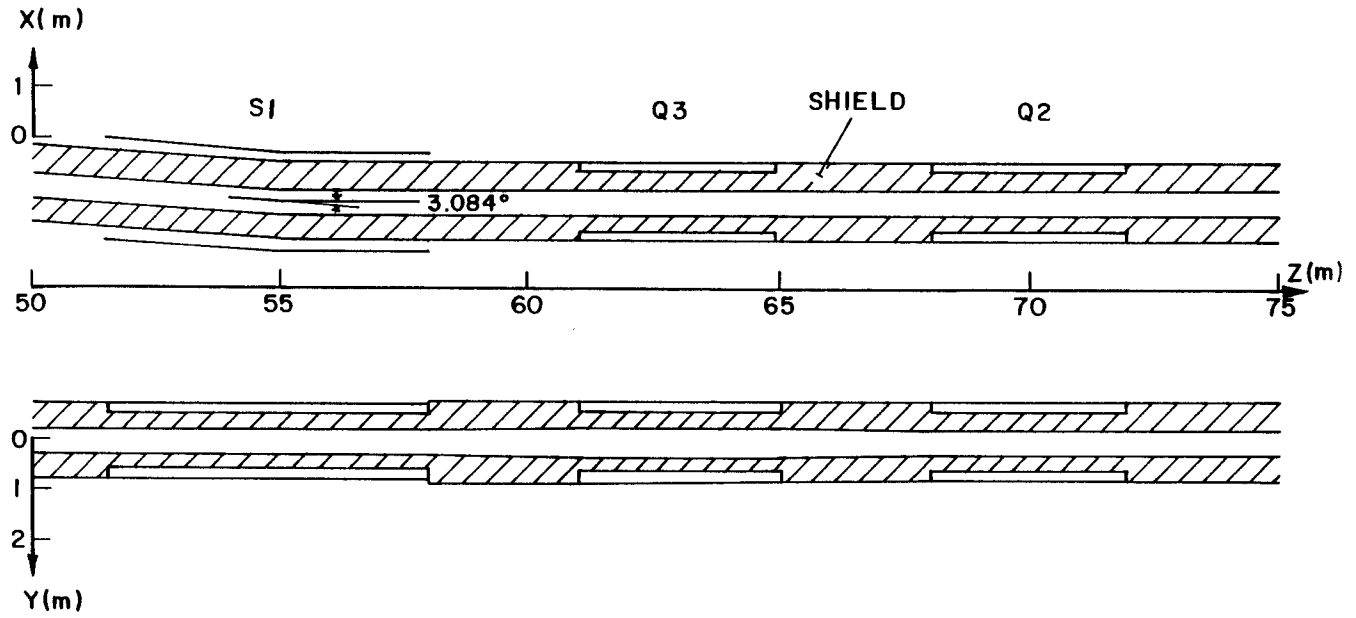

Fig. 4.3-4. Vertical and horizontal cross sections of the final focusing system in the zone $50 \leq z \leq 75$ m from the target.

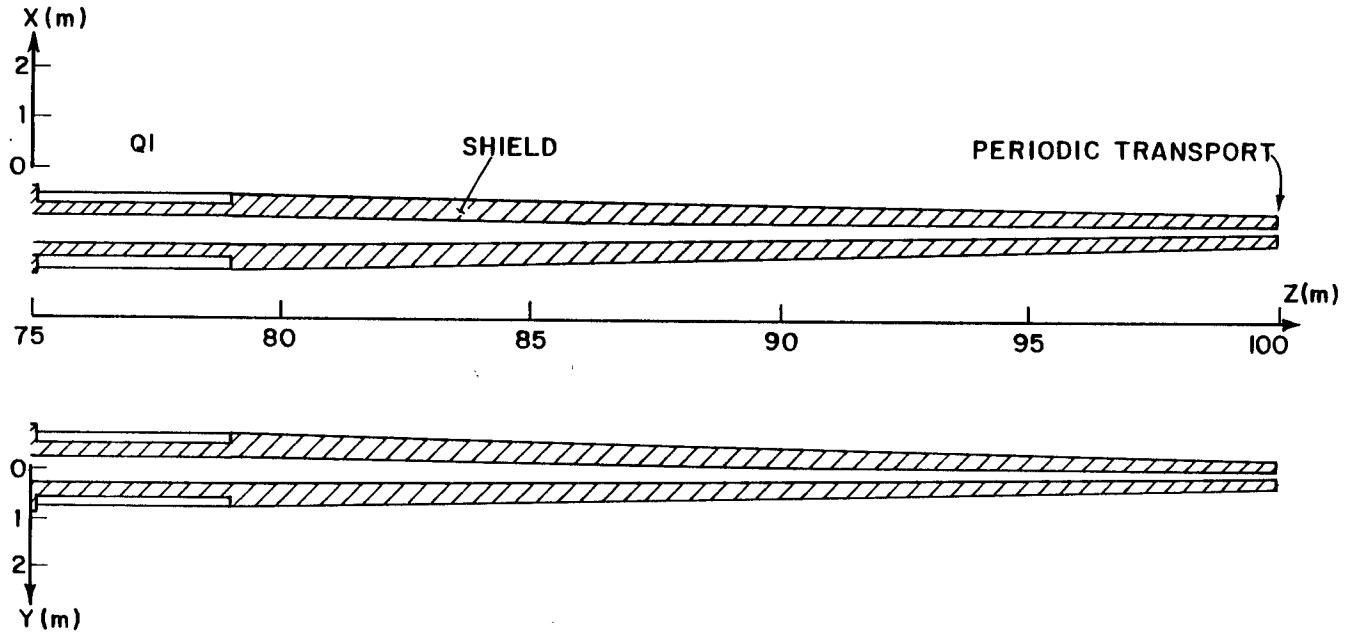

Fig. 4.3-5. Vertical and horizontal cross sections of the final focusing system in the zone $z \geq 75$ m from the target.

Table 4.3-2. General Features of the Final Focusing Systems in HIBALL-I and HIBALL-II

	HIBALL-I	HIBALL-II
Number of quadrupole lenses	8	6
Number of deflection sectors	0	2
Total system length (m)	60	100
Beam port size at vacuum wall (cm x cm)	102.8 x 34.3	21.6 x 16.6
Vertical angle between beams (degrees)	32	16
Largest beam elevation above reactor midplane (m)	16.6	13.0
Number of neutron dumps in the system per line	8	4

duced as compared to HIBALL-I. This results in reduced quadrupole apertures. Consequently, the beam port area at the vacuum wall of radius 7 m is reduced by a factor of ~ 10. This leads to significant reduction in radiation streaming into the final focusing system. Furthermore, the reduced aperture allows for use of smaller magnets. A normal coil driven final focusing magnet (Q6) with 1.6 m outside diameter yoke is used.*) This allows for reduction of the vertical angle between beams to 16°. The beam bending by two sets of sector magnets also allows for dumping all direct streaming source neutrons ($\bar{E}_n$ ~ 12 MeV) in the system with the periodic transport system being completely concealed from the direct line-of-sight of source neutrons. Four neutron dumps are used along the beam line with most of the source neutrons being dumped in the large final dump 46.5 m from the target. Only slowed down neutrons with a much softer spectrum will stream past this final dump. This results in significant reduction in the amount of radiation streaming into the periodic transport as compared to HIBALL-I which utilizes straight beam lines.

*)The final magnet considered here is not the one described in Section 4.2.2 but a similar design described elsewhere.[5]

4.3.3 Calculational Model

HIBALL-II utilizes a 2 m thick blanket consisting of SiC tubes through which the $Li_{17}Pb_{83}$ liquid metal eutectic flows. The tubes occupy 33% of the blanket region. A cylindrical vacuum wall 7 m in radius is used. The first wall is made of HT-9 and is 1 cm thick. A 0.4 m thick reflector composed of 90 v/o HT-9 structure and 10 v/o $Li_{17}Pb_{83}$ coolant is used and followed by a 2.9 m thick reinforced concrete biological shield. The results presented here are based on a DT yield of 400 MJ and a repetition rate of 5 Hz yielding 7.1 x 10^{20} fusion neutrons per second. Neutron multiplication, spectrum softening and gamma production in the target have been taken into account by performing one-dimensional neutronics and photonics calculations[6] in the spherical target using the discrete ordinates code ANISN.[7]

The twenty beam ports are arranged in two rows which are symmetric about the reactor midplane (Z = 0). The beam ports are 2 m apart vertically at the vacuum wall. Because of symmetry only half a penetration is modeled in the present analysis with reflecting albedo boundaries at the planes of symmetry. Hence, only 1/40 of the reactor is modeled. This corresponds to a "pie slice" of the upper half of the reactor with an azimuthal angle of 18°. The angle between the centerline of the beam line penetration and the reactor midplane is 8°. The axes are rotated by 8° around the y axis for the penetration centerline to coincide with the x axis of the calculational model. The magnet shield is considered to consist of 63 v/o type 316 stainless steel, 15 v/o lead, 17 v/o B_4C and 5 v/o H_2O.

The neutronics and photonics calculations were performed using the three-dimensional Monte Carlo code MORSE.[8] A coupled 25 neutron-21 gamma group cross section library was used. The spectra of neutrons and gammas emitted from the target are used to represent the source which is considered to be a point isotropic source at the origin. To get statistically adequate estimates for the flux along the beam line penetration with a reasonable number of histories, an angular source biasing technique was used. The biasing technique is similar to that used previously for the analysis of the beam line penetration in HIBALL-I.[9]

This neutronic analysis has several goals. The first goal is to assess the shielding requirements for the superconducting and normal coils. The radiation effects are to be calculated in these coils and compared to the design limits. Because of the $1/R^2$ geometrical attenuation, the largest radi-

ation effects occur in the magnets closer to the source. For this reason and to reduce the computing time, only the final two quadrupoles Q5 and Q6 are modeled. Vertical and horizontal cross sections of the geometry used in the computational model are given in Figs. 4.3-6 and 4.3-7. Zone 1 represents the biological shield and zones 2 and 3 represent the reflector and blanket, respectively. The inner vacuum region (zone 14) is extended to the region outside the biological shield and focusing magnets. This allows the neutrons leaking out of the biological shield to have additional collisions in the focusing magnets instead of being discarded as they would be if an outer vacuum region is used. The peak radiation effects are expected to occur in zones 5 and 7 for Q6 and Q5, respectively. Forty thousand histories were used in the Monte Carlo calculation leading to statistical uncertainties of less than 40% in the coil regions.

Another goal of this analysis is to quantify radiation streaming along the beam line penetration and determine the neutron flux in the neutron dumps and different shield sections for activity and dose calculations. For this purpose, the geometrical model was extended to model the beam line up to the final neutron dump 46.5 m away from the target. Since no direct source neutrons will stream past this dump, only negligible activation will occur in the remainder of the beam line. To quantify the streaming past this dump, a trapping surface was used at the duct opening at this final dump. Twenty thousand histories were used in this calculation.

4.3.4 Radiation Effects in the Coils

The limits on the radiation effects in superconducting and normal coils are design dependent. The most conservative limits were picked. The design criteria are also different for superconducting and normal coils.

For superconducting coils, the dpa limit in the copper stabilizer is determined by the field at the coil and the total resistivity limit allowed by the magnet designer. The dpa limit decreases as the resistivity limit decreases because of the decreased allowable radiation induced resistivity. The magnetic field at the coils is less than 1 tesla. For oxygen free high conductivity (OFHC) copper with a residual resistivity ratio of 107, the atomic displacements should not exceed 2×10^{-4} dpa for the resistivity not to exceed 5×10^{-8} Ωcm in a 1 tesla field.[10] However, 80% of the radiation induced defects can be removed by room temperature annealing. Several magnet anneals can be performed during the reactor life. A minimum period of 5 full

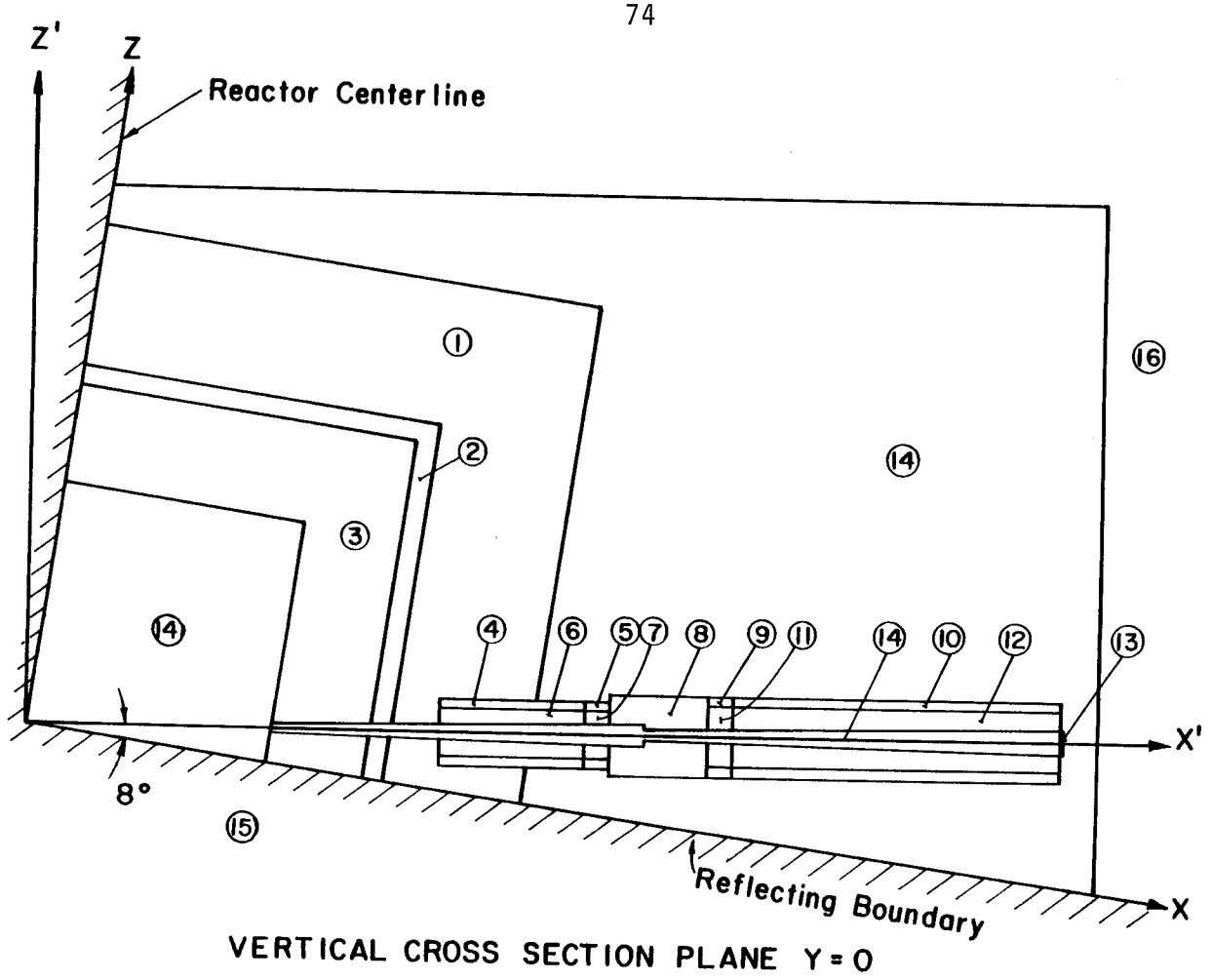

Fig. 4.3-6. Vertical cross section of computational model.

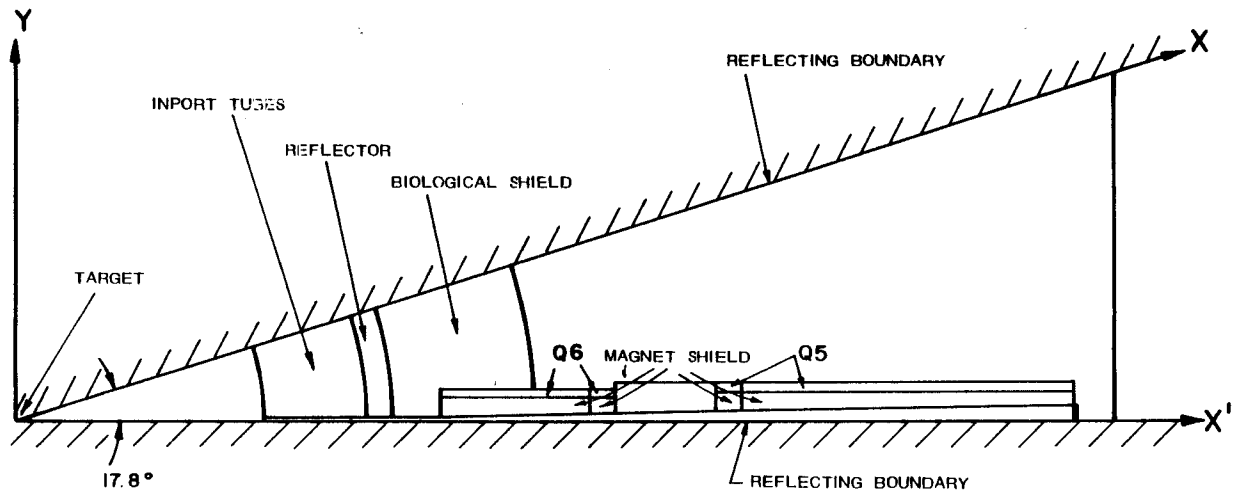

Fig. 4.3-7. Cross section at plane z' = 0 for the computational model.

power years (FPY) is required before the first magnet anneal which results in a period of 1 FPY between the final two anneals for an estimated reactor life of 21 FPY. Therefore, the limit on the dpa rate is 4. x 10^{-5} dpa/FPY.

The dose limit for the electrical insulator depends on the insulator type. For epoxies the dose should not exceed 4 x 10^{8} rad after 21 FPY of reactor life while the limit for polyimides is 5 x 10^{9} rad for the same period.[11] This implies that the dose rates should not exceed 1.9 x 10^{7} and 2.4 x 10^{8} rad/FPY for epoxies and polyimides, respectively. Irradiation of the superconducting material (NbTi) results in degradation of the critical current density. In this work, we require that the peak neutron fluence (E > 0.1 MeV) not exceed 3 x 10^{22} n/m^2 which corresponds to a 10% decrease in the critical current density.[12] The limit on the peak magnet heat load is considered to be 0.1 mW/cm^3.

For normal coils a fluence limit of 1.1 x 10^{26} n/m^2 (E > 0.1 MeV), which corresponds to 3% swelling of polycrystalline solid MgO insulators, is considered.[13] The fluence limit will be about an order of magnitude higher if compacted MgO powder is used. Ceramic resistivity degradation due to instantaneous dose rates were determined to be significant only for very high dose rates (> 10^{4} rad/s) in conjunction with the high voltage gradients across the insulator (> 10^{4} V/cm).[14] In this work, the limit on the instantaneous dose rate in the MgO insulator is taken to be 10^{4} rad/s.

Although the final focusing magnets Q6 and Q5 are to be driven by normal and superconducting coils, respectively, the radiation effects in zones 4, 5, 9 and 10 were calculated for both normal and superconducting coils to investigate the possibility of replacing one coil type by the other. Table 4.3-3 gives the radiation effects in the coils of Q5 and Q6 if they are designed to be superconducting. It is clear that the peak heat load and the peak neutron fluence are well below the design limits for both magnets. After an estimated reactor life of 21 FPY peak dpa values of 3.78 x 10^{-4} and 6.5 x 10^{-5} are obtained in the coils of Q6 and Q5, respectively. This implies that no magnet annealing is required for Q5, while if Q6 is driven by superconducting coils it will require two anneals. The total dose in the insulator after 21 FPY is 6.3 x 10^{8} rad in Q6 and 1.3 x 10^{8} rad in Q5. This suggests that epoxies can be used as electrical insulators in the coils of Q5 while if Q6 is driven by superconducting coils the more radiation resistant polyimides have to be used.

Table 4.3-3. Radiation Effects in Superconducting Coils

Quadrupole Lens	Zone Number	DPA Rate in Cu (dpa/FPY)	Dose Rate in Insulator (rad/FPY)	Power Density in Coil (mW/cm^3)	Neutron Fluence (E > 0.1 MeV) (n/m^2/FPY)
Q6	4	9.8×10^{-7}	2.4×10^{7}	0.0023	1.6×10^{19}
	5	1.8×10^{-5}	3.0×10^{7}	0.0076	3.2×10^{20}
Q5	9	3.1×10^{-6}	6.3×10^{6}	0.0018	5.0×10^{19}
	10	3.2×10^{-7}	5.6×10^{5}	0.0002	6.2×10^{18}

The radiation effects in the coils of Q5 and Q6 are given in Table 4.3-4 if they are designed to be normal. It is clear that these values are much lower than the specified design limits. This suggests that a reduced shield thickness can be used with normal coils. The fluence in zone 7 after 21 FPY is 7.9×10^{24} n/m^2 (E > 0.1 MeV) which is still well below the design limit of 1.1×10^{26} n/m^2. The instantaneous dose rate in MgO if it were used in this zone is 250 rad/s (i.e., if the coil was not shielded) which is also well below the design limit of 10^4 rad/s. This implies that if normal conductors are used to drive the quadrupole lenses, no shielding is required provided that the inner surfaces of the coils are tapered along the direct line-of-sight of source neutrons. This results in further reduction of magnet size.

4.3.5 Radiation Streaming Along the Beam Line

To quantify radiation streaming along the beam line penetration, a computational model for the penetration up to the final neutron dump was used. Particles crossing the trapping surface at the 65 cm x 42 cm duct opening 46.5 m from the target were counted according to energy bins to determine the amount and spectrum of streaming radiation. The neutron and gamma streaming currents are 6.68×10^{11} n/cm^2s and 1.13×10^{11} γ/cm^2s, respectively. It is interesting to note that the neutron and gamma streaming currents at the periodic transport (end of final focusing system) in HIBALL-I were 4.4×10^{12}

Table 4.3-4. Radiation Effects in Normal Coils

Quadrupole Lens	Zone Number	Neutron Fluence (E > 0.1 MeV) after 21 FPY (n/m^2)	Instantaneous Dose Rate in MgO (rad/s)
Q6	4	3.36×10^{20}	0.50
	5	6.72×10^{21}	1.00
Q5	9	1.05×10^{21}	0.16
	10	1.30×10^{20}	0.02

n/cm^2s and 1.7×10^{11} γ/cm^2s, respectively. A smaller streaming current is obtained in HIBALL-II as a result of the beam line penetration bending at S2. The reduction in gamma streaming is less pronounced than that in neutron streaming because most of the gamma photons are produced along the beam line duct. Figure 4.3-8 shows the spectra of neutrons and gammas streaming past the final dump in HIBALL-II. The average energies of streaming neutrons and gammas are 0.77 and 1.52 MeV, respectively. The corresponding values for neutrons and gammas streaming into the periodic transport in HIBALL-I were 11.7 and 1.5 MeV, respectively. Since only slowed down neutrons will stream past the final dump in HIBALL-II, the neutron spectrum is much softer than that in HIBALL-I.

Further reduction in both streaming current and average energy will result as the neutrons travel further up the beam line penetration to the periodic transport 100 m from the target. The neutron streaming current through the duct opening at the vacuum wall of radius 7 m is 8.26×10^{14} n/cm^2s with an average energy of 12 MeV. This implies that the neutron streaming current is reduced by about three orders of magnitude and the average energy is reduced by about an order of magnitude as the neutrons travel a distance of ~ 40 m in the duct with its 3° bend. The gamma streaming current is reduced by about an order of magnitude in this part of the duct. Since the neutrons

Table 4.3-5. Volumetric Averaged Neutron and Gamma Fluxes in Different Shield Zones Along the Beam Duct

Distance from Target (m)	Neutron Flux (n/cm^2s)	Gamma Flux (γ/cm^2s)
8.5-12	8.34×10^{10} (0.12)*	1.81×10^{10} (0.13)
12-14	5.26×10^{11} (0.13)	1.34×10^{11} (0.18)
14-21.2	1.11×10^{10} (0.16)	1.32×10^{9} (0.27)
21.2-23.2	2.16×10^{11} (0.22)	5.06×10^{10} (0.26)
23.2-27.2	1.67×10^{10} (0.54)	5.66×10^{9} (0.56)
27.2-29.2	6.23×10^{11} (0.16)	1.81×10^{11} (0.18)
29.2-35.5	1.44×10^{10} (0.40)	1.59×10^{9} (0.58)
35.5-46.5	3.32×10^{10} (0.10)	5.15×10^{9} (0.09)
46.5-47	1.77×10^{12} (0.10)	5.32×10^{11} (0.11)

* Fractional standard deviation

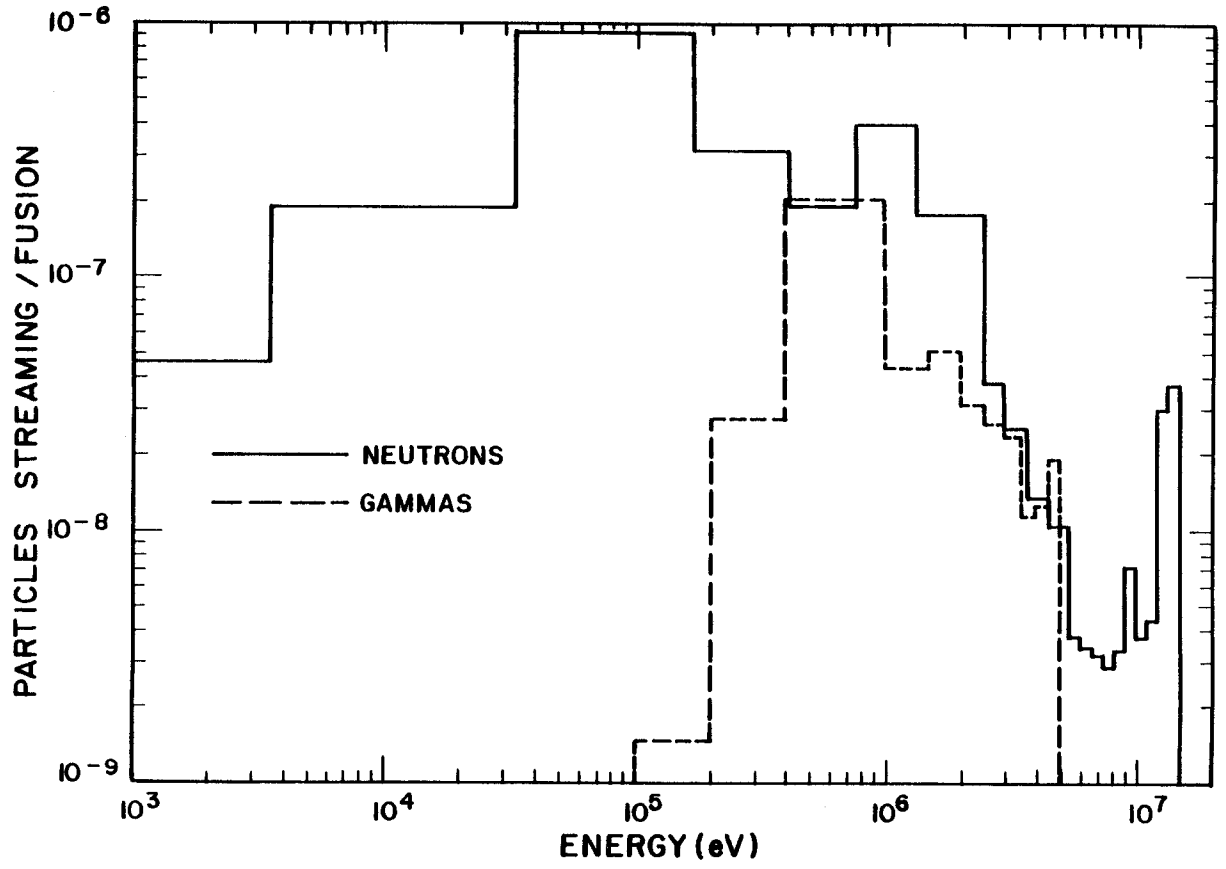

Fig. 4.3-8. Spectrum of radiation streaming past the final dump.

streaming past the final neutron dump will travel ~ 54 m in a duct with a 3.084° bend before reaching the periodic transport system, it is expected that the neutron streaming current will be reduced by at least another three orders of magnitude with further spectrum softening. Even more reduction is expected because scattering becomes more isotropic as the neutron energy goes down. Therefore, the final focusing system designed for HIBALL-II results in much less radiation streaming into the periodic transport as compared with that in HIBALL-I.

The neutron spectra were calculated in different sections of the shield along the beam line duct for activation and dose calculations. The total (energy integrated) neutron and gamma fluxes averaged over zones with a 0.5 m thickness are given in Table 4.3-5. The last zone represents the final neutron dump. It is clear that the largest neutron activation will occur in this dump. If necessary extra shielding can be used behind this dump to reduce the dose after shutdown to permissible levels. While in general these neutron fluxes will not cause large mechanical damage, they are sufficiently large to induce considerable radioactivity in the beam line (see Chapter 9).

4.3.6 Beam Line Activity and Dose Levels

The shielding effects of the various components in the beam line imply that these components will become activated. The fluxes generated from the shielding calculations were combined with the DKR code to estimate the induced activity in the beam lines and the resultant dose rate outside the shield. The analysis had to be restricted to one dimension, consequently all magnet shields were taken to be 0.3 m thick and all shielding in drift regions was taken as 0.5 m thick. The shields were 316 SS. Calculations[15] were performed only for that part of the beam line out to the beam dump in the first deflection magnet. These calculations showed that the resulting activity is relatively modest, i.e. only 66 curies at shutdown following two years of operation. The largest contribution to this activity is ^{56}Mn with a 2.58 hr half life.

While these activities are low relative to those in the chamber, they are large enough to cause concern about radiation levels on the outer surfaces. In the calculations presented above the fluxes and thus the activities are only given on a volume average basis. The source distribution for shielding purposes is based on a redistribution of the activity according to an exponential with a 0.05 m relaxation length. An additional 1/r term was used for

calculations in the radial direction. Two cases were investigated, namely the outside drift region between the last two magnets (Q5 and Q6) and behind the beam stop in the last deflection magnet.

Outside the drift region between the last two magnets, the dose following shutdown after two years of operation was 1.1 mrem/hr. After one day of decay it had fallen to 0.02 mrem/hr due to the decay of ^{56}Mn. The activities behind the beam stop at the same times were 2.6 mrem/hr and 0.03 mrem/hr.

These quite conservative calculations indicate that the shielding presented for the beam line is adequate. In fact, it may be reduced in certain portions of the line such as the drift spaces between the magnets.

4.3.7 Summary

A shield configuration was developed for the final focusing system of HIBALL-II. The inner surface of the shield is tapered along the direct line-of-sight of source neutrons with a number of neutron dumps used in the drift sections between the magnetic elements. Using a minimum shield thickness of 0.3 m it was found that the superconducting coils will be well protected. The radiation effects in the normal coil which drives the final focusing magnet are several orders of magnitude lower than the design limits. No shielding is required in front of the normal coils. A superconducting coil can be used to drive the final quadrupole lens. However, polyimides should be used for electrical insulation and magnet annealing will be required twice during the reactor life. As a result of using two deflection sectors in the system, the periodic transport system is completely concealed from the direct line-of-sight source neutrons. Consequently, neutron streaming into the periodic transport is more than four orders of magnitude less than that in HIBALL-I where a straight beam line was used. Furthermore, the spectrum of streaming neutrons is much softer.

References for Section 4.3

1. J. Jung and M.A. Abdou, Nuclear Technology 41, 71 (1978).

2. M. Ragheb, A. Klein, and C.W. Maynard, Nuclear Technology/Fusion 1, 99 (1981).

3. L. El-Guebaly and C. Maynard, Trans. American Nuclear Society 43, 612 (1982).

4. M.E. Sawan, W.F. Vogelsang, and D.K. Sze, Trans. American Nuclear Society 39, 777 (1981).

5. F. Arendt, in: GSI-83-2 (1983), p. 68.

6. M.E. Sawan, W.F. Vogelsang, and G.A. Moses, Trans. American Nuclear Society 38, 575 (1981).

7. RSIC Code Package CCC-254, "ANISN-ORNL," Radiation Shielding Information Center, ORNL.

8. RSIC Code Package CCC-203, "MORSE-CG," Radiation Shielding Information Center, ORNL.

9. B. Badger et al., "HIBALL - A Conceptual Heavy Ion Beam Driven Fusion Reactor Study," KfK-3202/UWFDM-450, 1981.

10. M.E. Sawan, "Radiation Limits in Copper Stabilizer of Superconducting Magnets," MARS Project Memo WIS-MARS-82-029 (1982).

11. R. Coltman, Jr. and C. Klabunde, J. Nuclear Materials 103 & 104, 717 (1981).

12. M. Soll, J. Nuclear Materials 72, 168 (1978).

13. L.J. Perkins, "Recommendations for Fluence/Dose Limits for Ceramic Insulators in Normal Conducting Magnets," MARS Project Memo WIS-MARS-82-012 (1982).

14. L.J. Perkins, "Radiation Dose-Rate Resistivity Degradation in Ceramic Insulators and Assessment of the Consequences in Fusion Reactor Applications," University of Wisconsin Fusion Engineering Program Report UWFDM-469 (1982).

15. B. Badger et al., "Annual Report of Research Performed on the HIBALL Project Between January 1 and December 31, 1982," Fusion Power Associates Report FPA-82-6 (December 1982).

5. REACTOR CHAMBER DESIGN

5.1 General Requirements and Description

5.1.1 Requirements

The design requirements of the HIBALL chamber are determined by a number of seemingly conflicting considerations. The basic requirements are: (1) the chamber be capable of dissipating the energy from the target in a coolant operating at temperatures consistent with material requirements and the need to produce steam at suitable conditions, (2) the cavity atmosphere be suitable for propagating and focusing a heavy ion beam on the target, (3) the system be maintainable in a reasonable fashion, (4) the system be able to breed tritium at a ratio greater than or equal to unity, (5) the tritium be recoverable without excessive accumulation in the breeding material, and (6) the dose rate outside the shielding be at an acceptable level.

The two requirements which have the greatest impact are the need to dissipate the target energy and propagate the beam through the chamber to the target. The fusion yield of the HIBALL target is 400 MJ and the repetition rate is 5 Hz, yielding a fusion power of 2000 MW per chamber. Three-dimensional neutronics studies reported in Section 5.3.4 indicate that because of endothermic reactions in the target the actual energy available is only 396 MJ/shot, of which 285 MJ is from 12 MeV (average energy) neutrons, 90 MJ is from x-rays and 21 MJ from target debris, i.e. He, unburned D and T, Pb, and Li. A very small amount appears as high energy gamma radiation. This means that although the greatest part of the energy is carried by neutrons and therefore is volumetrically deposited in the blanket materials, a significant amount, namely 109 MJ, is in a form that would be deposited on or very near the surface of any first wall material.

5.1.2 The INPORT Concept

A persistent technical problem in inertial confinement fusion (ICF) has been the protection of the first load bearing walls from target debris, x-rays and neutrons. Various schemes have been proposed in the past: swirling liquid metal pools[1], wetted walls[2,3,4,5], magnetic protection[6], gaseous protection[7], dry wall ablative shields[8-11], and free falling sheets of liquid metals[12-15]. None of these schemes have been completely satisfactory, but the free falling liquid metal column protection scheme, used in HYLIFE,[15] seems to be the best developed thus far.

One disadvantage of the HYLIFE scheme is the disassembly of the liquid metal columns following each shot and the need to reestablish them before the subsequent shot. The low repetition rate results in a small ΔT, a high recirculation rate, and a large pumping power. This is especially true for PbLi alloys. Ideally, this scheme can be vastly improved if it were possible to slow the flow of liquid metal such that it can absorb the energy of several shots before exiting the reactor.

Such a scheme was developed in late 1979 for the HIBALL project.[16] The basis of this new design is the use of braided SiC tubes which are flexible, sufficiently strong, compatible with the LiPb alloy used in HIBALL, and porous enough to allow a liquid layer to cover the outside surface while the bulk of the fluid flows down the center of the tube (Fig. 5.1-1). This idea is called the INPORT concept, standing for the Inhibited Flow - Porous Tube Concept. The film thickness of roughly 1 mm is sufficient to absorb the energy from x-rays and target debris while several banks of tubes provide adequate LiPb alloy to moderate the neutron flux and reduce the total damage and damage rate in the first structural wall (Fig. 5.1-2). Figure 5.1-3 shows the radial blanket in the HIBALL chamber and the overall chamber design is shown in Fig. 5.1-4.

It is clear that the INPORT concept enhances ICF reactors by remedying two of the major drawbacks of the HYLIFE concept: the recirculation rate and disassembly after each shot. The rest of this section will discuss other aspects of the INPORT concept in more detail.

5.1.3 Mechanical Description of Chamber

The chamber is an upright cylinder with internal dimensions of 11.5 m height on axis and 10 m in diameter, Fig. 5.1-4. From the center and outward in all directions, the chamber is characterized by three distinct zones; the blanket, reflector and shield. Along the vertical sides of the cavity, the blanket consists of a 2 m thick zone of SiC tubes through which $Li_{17}Pb_{83}$ is circulated, Fig. 5.1-3. It is followed by a reflector zone made of mainly HT-9 which is 40 cm thick and finally by the shield, which is primarily concrete and is 2.9 m thick. The top of the chamber has wedge shaped blanket modules, 50 cm thick, which are also filled with $Li_{17}Pb_{83}$. They too are followed by 40 cm of HT-9 reflector and a 2.9 m concrete shield. The bottom of the cavity has a pool of $Li_{17}Pb_{83}$ one meter thick, followed by a 40 cm thick reflector which has holes in it to allow the coolant to drain out. A

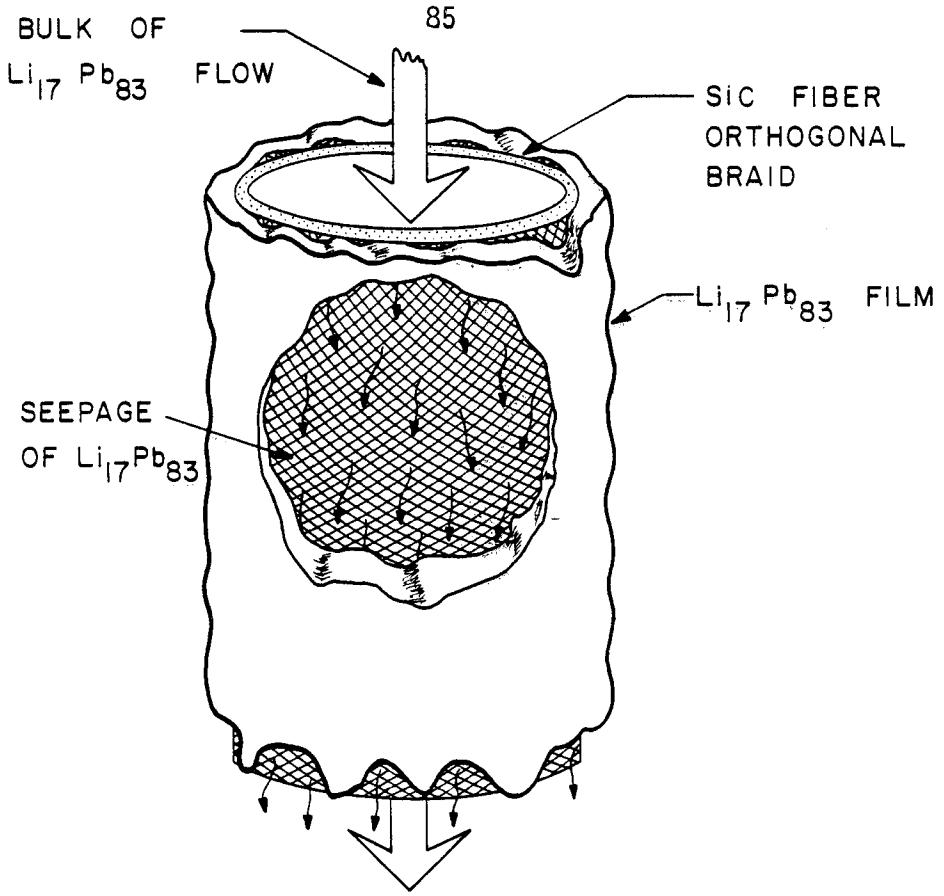

Fig. 5.1-1 Schematic of INPORT unit concept.

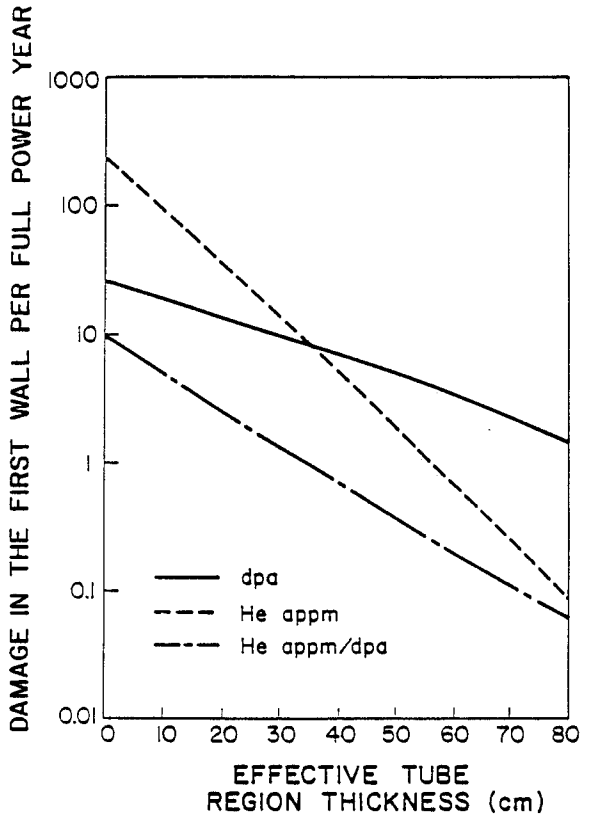

Fig. 5.1-2 Effect of INPORT tubes on damage in HT-9 first wall.

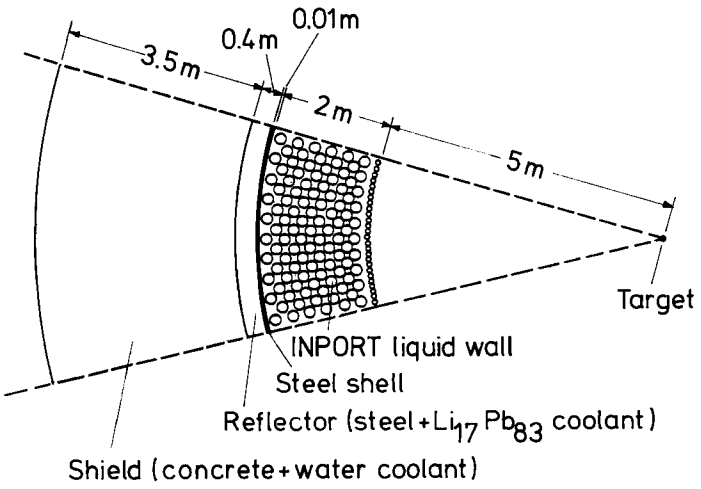

Fig. 5.1-3. Section through the HIBALL chamber wall.

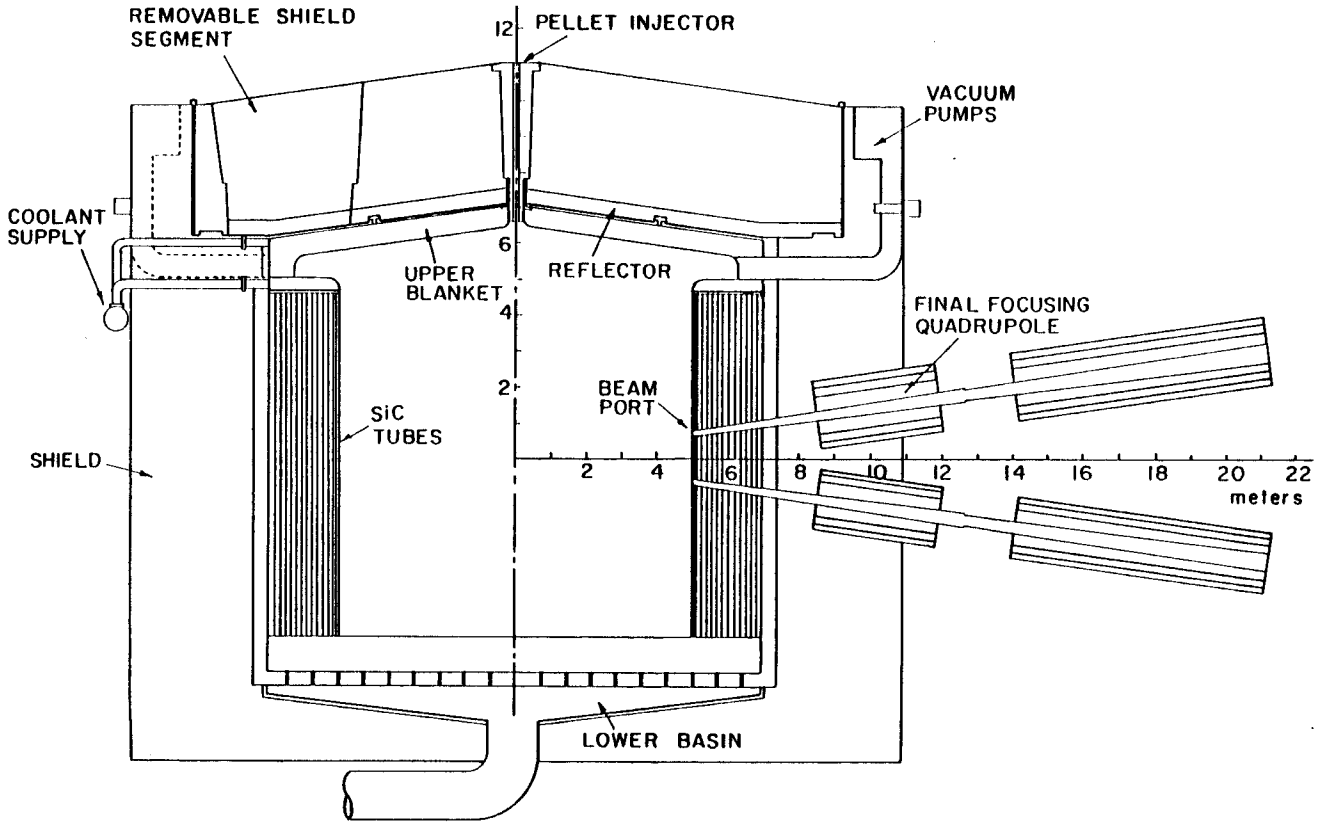

Fig. 5.1-4. Cross section of HIBALL chamber.

catch basin then directs the flow to an outlet tube through which it is pumped to the steam generator.

The top of the chamber has a unique design. Although the blanket modules are designed to stay stationary, the reflector and shield are capable of being rotated about the central axis. This is needed to provide access to the blanket modules for replacement. The upper blanket modules are locked to the reflector by means of studs which fit in milled slots. During reactor operation when the modules are filled with $Li_{17}Pb_{83}$, the stud latches are actuated and the modules are locked to the reflector. However, during servicing, when the modules are drained of all the breeding material, the stud latches are deactivated. At this time the blanket modules are only supported on the outer periphery and in the center, where they are attached to a central hub. This makes it possible to rotate the reflector and shield while the blanket modules remain stationary.

The cavity is sealed to the outside by a liner which is welded to the reflector at the upper end of the cavity. A circumferential weld (or seal) between the liner on the stationary part of the top shield and the rotatable part maintains the cavity atmosphere during operation.

At the junction between the top blanket modules and the SiC tubes, there are 20 apertures, 65 cm high and 1.2 m wide. These are the vacuum system ports. The vacuum ducts are concealed from direct line of sight of neutrons and lead to pumping stations located in the upper corner of the reactor chamber. These pumps are used to evacuate the cavity prior to operation and to pump the noncondensable gases, such as the hydrogen species and the helium during operation. The pumping system is discussed further in Section 5.5.

There are 20 beam ports in each chamber. Each pair of beams comes in at ±8° to the horizontal, spaced at 36° circumferentially. The blanket is divided in such a way that every third module has two beam ports built in. At the first surface (5 m radius) the beam ports are 12 cm wide and 15.4 cm high. Distribution manifolds surround the beam tubes such that the SiC tubes are attached to them on the top and bottom. Each beam transport line is attached to the chamber at the point of entry and constitutes the vacuum interface between the cavity and the beam handling system.

5.1.4 Chamber Parameters

Table 5.1-1 presents reference parameters which have been used as a basis for the calculations in the following sections of this chapter. These values

Table 5.1-1

Cavity and INPORT Region	
Neutron energy/shot (MJ)	285
X-ray energy/shot (MJ)	90
Debris energy/shot (MJ)	21
Gamma energy/shot (MJ)	< 1
Cavity shape	cylindrical
Cavity diameter to vacuum wall (m)	14
Cavity height at center (m)	11.5
Coolant and breeding material	$Li_{17}Pb_{83}$ (natural)
INPORT tube structural material	SiC
INPORT region support structure	HT-9
First surface radius (m)	5
INPORT tube region packing fraction	0.33
INPORT tube length (m)	10
INPORT tube diameter (cm)	
First two rows	3
Remainder	10
Number of first row tubes	1230
Number of remaining tubes	3060
Number of beam penetrations	20
Total area of beam penetrations at the first surface (m^2)	3.6
Pb atom density (x 10^{-10} atom/cm^3) just before shot	4
Noncondensable atom density at 500°C (x 10^{-10} atoms/cm^3)	0.13
Chamber top thickness (m)	0.5
Coolant volume fraction	0.97
Bottom region thickness (m)	1
Coolant volume fraction	1
Vacuum Wall (first material wall)	
Structural material	HT-9
Inside diameter (m)	14
Thickness (m)	0.01

Table 5.1-1 (continued)

Reflector	
Structural material	HT-9
Coolant	$Li_{17}Pb_{83}$
Coolant volume fraction	0.9
Inside diameter (m)	14.02
Thickness (m)	0.4
Shield	
Structural Material	Concrete (unreinforced)
Coolant	H_2O
Coolant volume fraction	0.05
Inside diameter (m)	14.82
Thickness (m)	3.5
$Li_{17}Pb_{83}$ Coolant	
Inlet temperature (°C)	330
Outlet temperature (°C)	500
Pressure (MPa)	0.2

were chosen on the basis of: (1) defining the nature and role of the system, (2) consistency with known materials characteristics of various parts of the system, or (3) as a result of previous calculations. A more detailed parameter set is given in Appendix A.

References for Section 5.1

1. A.P. Fraas, "The BLASCON - An Exploding Pellet Fusion Reactor," Oak Ridge National Laboratory, Oak Ridge, TN, TM-3231 (July 1971).

2. L.A. Booth, "Central Station Power Generation by Laser-Driven Fusion," Nucl. Eng. and Design 24, 263, North-Holland Publishing Co. (1973).

3. J. Hovingh, J.A. Maniscalco, M. Peterson, R.W. Werner, "The Preliminary Design of a Suppressed-Ablation-Laser-Induced Fusion Reactor," Proc. 1st Top. Mtg. on the Tech. of Controlled Nucl. Fusion, I, 96, San Diego, CA (1974).

4. J.K. Baird and V.E. Anderson, "Combination First Wall and Parabolic Lithium Mirror for a Laser-Driven Pellet Fusion Reactor," Proc. 6th Symp. on Eng. Prob. of Fusion Research, 1015, San Diego, CA (1976).

5. R.R. Holman and W.P. Kovacik, "Conceptual Approach to Laser Fusion Hybrid Reactor," Trans. ANS 1977 Summer Mtg., 56, New York, NY (1977).

6. T. Frank, D. Freiwald, T. Merson, J. Devaney, "A Laser Fusion Reactor Concept Utilizing Magnetic Fields for Cavity Protection," Proc. 1st Top. Mtg. Tech. of Controlled Nucl. Fusion, I, 83, San Diego, CA (1974).

7. B. Badger et al., "SOLASE, A Laser Fusion Reactor Study," University of Wisconsin Fusion Technology Institute Report UWFDM-220, (Dec. 1977).

8. F.H. Bohn, H. Conrads, J. Darvas, and S. Forster, "Some Design Aspects of Inertially Confined Fusion Reactors," Proc. 5th Symp. of Eng. Prob. of Fusion Research, 107, Princeton, NJ (1973).

9. J.M. Williams, F.T. Finch, T.G. Frank, and J.S. Gilbert, "Engineering Design Considerations for Laser Controlled Thermonuclear Reactors," Proc. 5th Symp. of Eng. Prob. of Fusion Research, 102, Princeton, NJ (1973).

10. S.G. Varnado and G.A. Carlson, "Considerations in the Design of Electron-Beam-Induced Fusion Reactor Systems," Nucl. Tech. 29, 415 (June 1976).

11. J. Hovingh, "First Wall Studies of a Laser Fusion Hybrid Reactor Design," Proc. 2nd Top. Mtg. on the Tech. of Controlled Nucl. Fusion, II, 765, Richland, WA (1976).

12. R.J. Burke, "Outline for a Large-Pulse Electron-Beam-Ignited Fusion Reactor," Argonne National Laboratory, Argonne, IL, CTR/TM-31 (1974).

13. W. Seifritz and H. Naegel, "Uranium and Thorium Shells Serving as Tampers of DT-Fuel Pellets for the Electron-Beam-Induced Fusion Approach," Trans. ANS 21, 18 (1975).

14. J.R. Powell, O. Lazareth and J. Fillo, "A Liquid Wall Boiler and Moderator (BAM) for Heavy Ion-Pellet Fusion Reactors," Brookhaven National Laboratory, Long Island, NY, BNL-50744 (Nov. 1977).

15. W.R. Meier and J.A. Maniscalco, "Reactor Concepts for Laser Fusion," Lawrence Livermore National Laboratory, Livermore, CA, UCRL-79694 (1977).

16. G.L. Kulcinski, G.A. Moses, J. Sapp, M. Sawan, I.N. Sviatoslavsky, D.K. Sze, and W.F. Vogelsang, "The INPORT Concept - An Improved Method to Protect ICF Reactor First Walls," J. Nucl. Materials 103 & 104, 103 (1982).

5.2 Mechanical Response of INPORT Units

5.2.1 Introduction

Target generated x-rays partially vaporize the PbLi film of the first two rows of the cavity tube bank. This generates an impulsive reaction, producing a dynamic radial loading on the INPORTs. In this section numerical results are presented for the mechanical response of INPORTs to such sequential impulsive pressure distributions.

The initial cavity design used INPORTs constructed of pliable braided silicon carbide fiber. (The yarns are typically composed of 500 fibers, each approximately 10 μm in diameter.) Support was provided at the top with the lower end free to move. For this case, the theoretical results of the mechanical analysis showed that the cyclic displacements would be excessive, producing contact and interference between the tubes.

In the second design considered, INPORTs had flexural rigidity, the result of the soft braid being stiffened by chemical vapor deposition of additional silicon carbide. From the response calculations, the bending stresses were found to substantially exceed the strength of the silicon carbide. The large unsupported span of the INPORT in a beam mode is the primary reason for this result. Providing intermediate support to reduce the effective span did not appear to be a practical solution. Details of the analysis and mechanical response for these two cases are presented in the original HIBALL report.

The general design which was adopted consists of INPORTs with braided pliable walls, supported at both top and bottom. The ends incorporate mechanisms to provide for pretension loads. One possible design of this type is shown conceptually in Fig. 5.2-1.

5.2.2 Quantitative Characterization of the Impulse

One can conservatively estimate the bulk kinetic energy of the vaporized fluid to be equal to the thermal energy of the gas.

$$\left(\frac{3}{2}\right)\left(\frac{M_{gas}}{m_{ion}}\right) k_B T_{gas} \doteq \left(\frac{1}{2}\right) M_{gas} V^2 \qquad (5.2\text{-}1)$$

Here the left side represents the thermal energy of the gas which is equal to the deposited x-ray energy less the energies of ionization and vaporization. The bulk velocity of the gas is denoted by V while m_{ion} represents the average mass of ions in the gas. For the case of 87.6 MJ of x-ray energy and 13.3 kg of vaporized PbLi, T_{gas} = 1.26 eV. The reactive impulse equals $M_{gas}V$.

$$\Delta I = M_{gas} \left(\frac{3k_B T_{gas}}{m_{ion}}\right)^{1/2} = 1.89 \times 10^9 \text{ dyne-s} . \quad (5.2\text{-}2)$$

This can also be expressed as an impulsive pressure per unit surface area.

$$\Delta P = 600 \text{ dyne-s/cm}^2 \quad (5.2\text{-}3)$$

The result is conservative since it is assumed that all vaporized atoms are initially moving towards the center of the cavity with their thermal velocity. This will clearly overestimate the reactive impulse.

5.2.3 INPORT Displacement Histories

The displacement analysis is based upon modal superposition. For this purpose it is necessary to determine the natural vibration frequencies for each mode. From numerical values shown in Fig. 5.2-2 it can be seen that tension increases have a modest influence on frequencies for lower modes but a stronger effect on higher modes. For a uniformly distributed impulse, the largest contribution to the total motion is from the lowest mode which has a natural frequency less than 1 Hz for the tension range considered. With the cavity operating at a repetition rate of 5 Hz, mechanical resonance is not a problem for this frequency spectrum.

A typical startup and shutdown result is shown in Fig. 5.2-3. Radial motion progresses with a small overshoot followed by a steady state displacement. After 3 seconds (15 impulses), the load sequence stops and the INPORT response consists of damped free vibration about the original straight position. Parametric comparisons are made from the next four figures. In Fig. 5.2-4 it can be seen that modest increases in tension substantially reduce displacements but larger increases are not relatively as effective. A decrease in length (e.g., by intermediate supports) would substantially reduce the midpoint displacement as shown in Fig. 5.2-5. In contrast, the results of Fig. 5.2-6 indicate that variations in the damping level do not produce dramatic changes in the response, particularly for the steady state amplitude. This is also shown in Fig. 5.2-7 which includes the academic case of 99% critical damping.

From these results, it appears that the INPORT concept can lead to a viable design for a range of physical parameters. The best estimates for a practical design correspond to the data for Fig. 5.2-3, resulting in steady state motion which is just slightly more than 1% of the INPORT's length.

Fig. 5.2-1

SUPPORT MECHANISMS FOR INPORTS

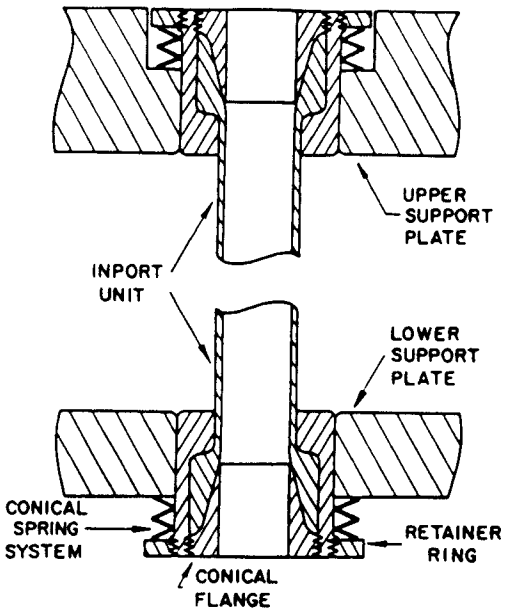

Fig. 5.2-2

INPORT VIBRATION FREQUENCY vs. TENSION

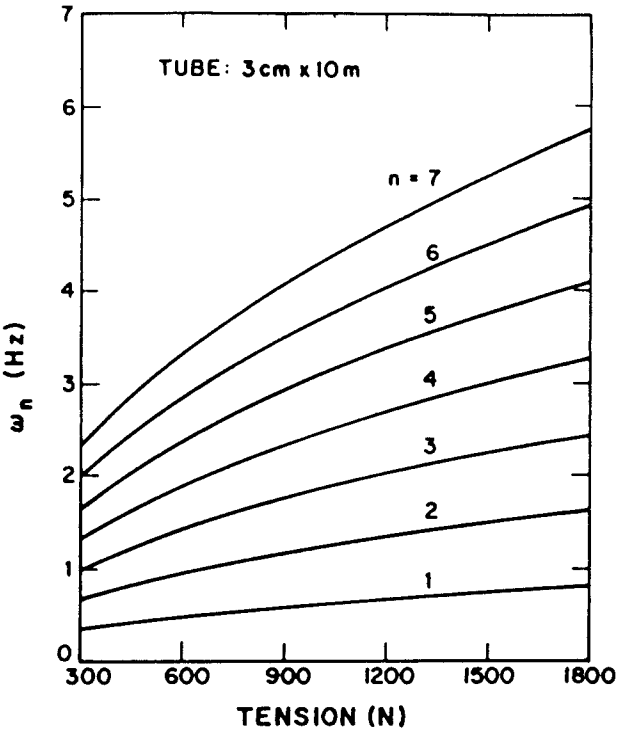

Fig. 5.2-3

INPORT MECHANICAL RESPONSE - STARTUP AND SHUTDOWN

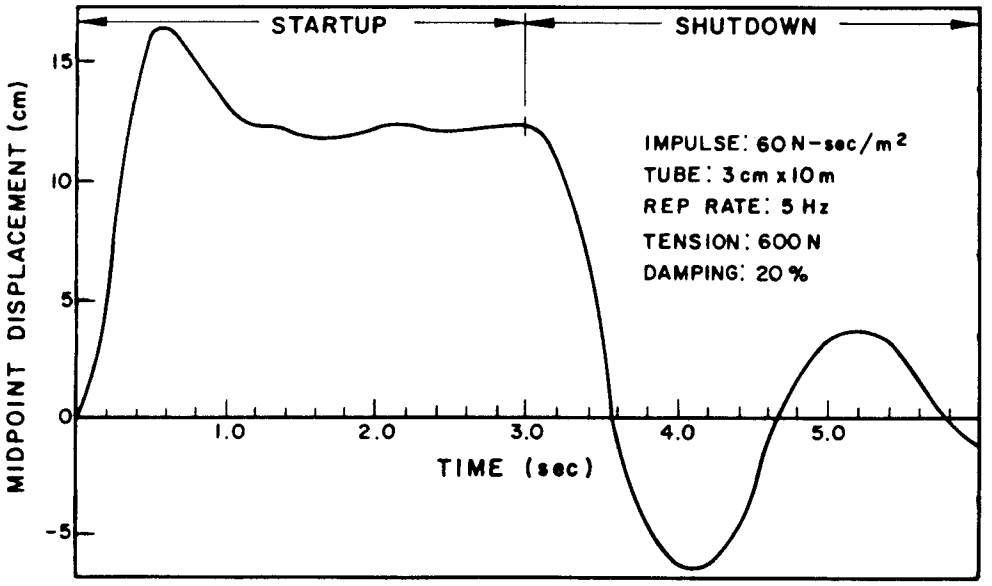

Fig. 5.2-4

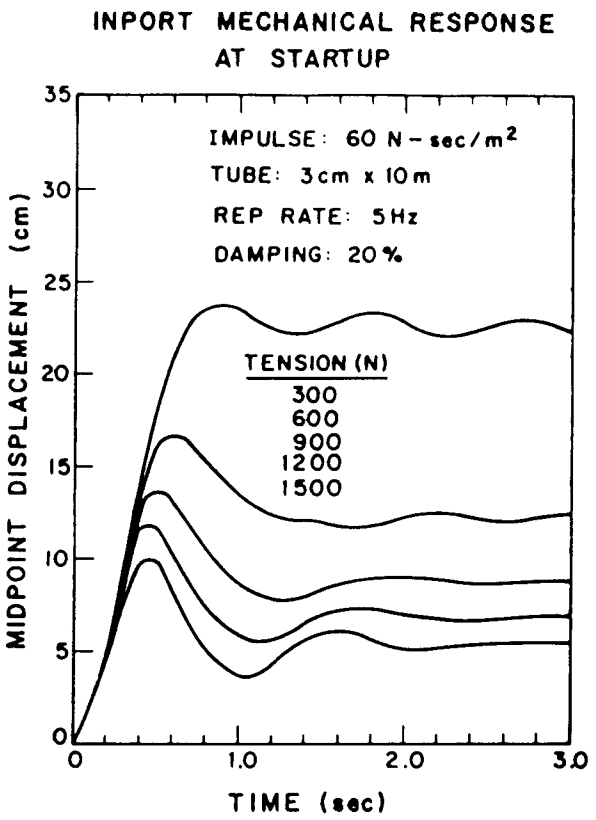

Fig. 5.2-5

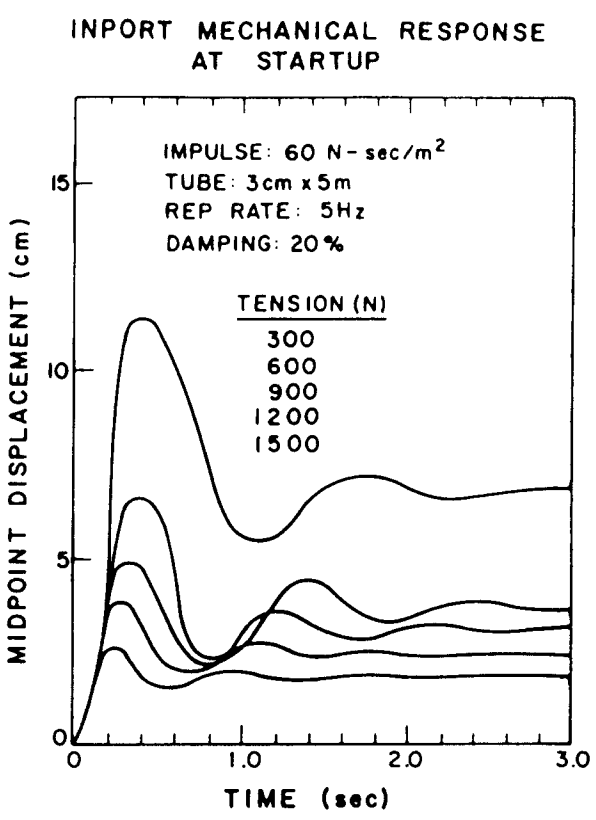

Fig. 5.2-6

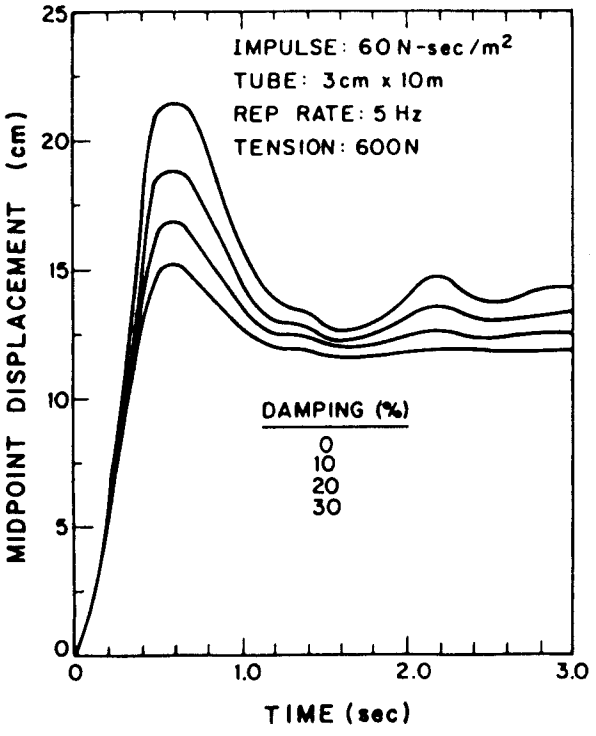

Fig. 5.2-7

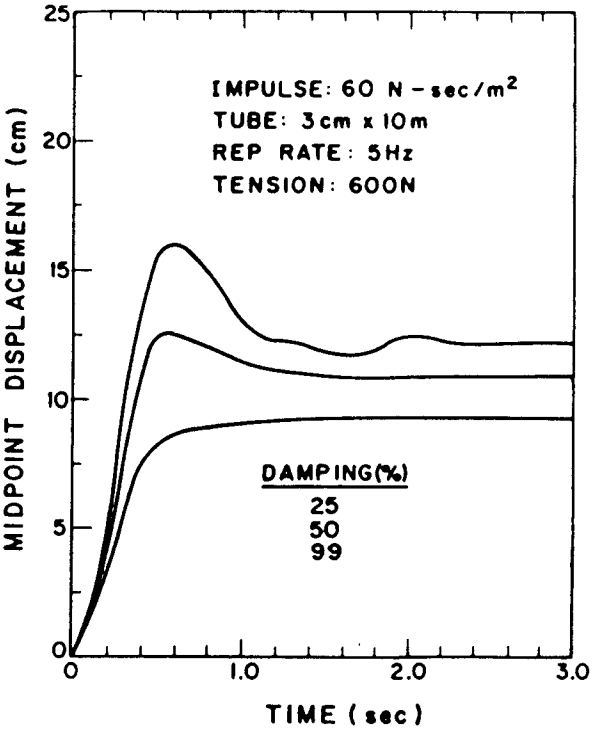

5.3 Neutronics and Photonics

5.3.1 Introduction

The neutronics and photonics analysis for HIBALL is presented in this section. The biological shield is also designed. The actual cylindrical cavity is modeled in a detailed three-dimensional neutronics and photonics analysis with all cavity geometrical details included. A time-dependent neutronics analysis is also presented to properly account for the pulsed nature of the neutron source.

5.3.2 One-Dimensional Time Integrated Studies

5.3.2.1 Introduction

In this section, a consistent coupled target-blanket neutronics and photonics study of HIBALL is given. The neutron and gamma source for blanket calculations was obtained from the target neutronics and photonics results.

The HIBALL blanket is required to breed tritium and convert the kinetic energy of the fusion reaction into heat. Furthermore, the INPORT tubes are required to protect the vacuum wall and HT-9 structure in the reflector from radiation damage. One-dimensional steady state calculations are performed to determine the optimum blanket thickness which yields the largest possible energy multiplication with adequate tritium breeding ratio and first wall protection. The thickness of biological shield required to reduce the biological dose to permissible levels is also determined.

5.3.2.2 Blanket and Shield Model

HIBALL incorporates four cylindrical cavities; each is 7 m in radius and 10 m high. The INPORT tubes occupy 33% of the 2 m thick blanket region yielding an effective blanket thickness of 66 cm. The LiPb coolant occupies 98% of the tube volume with the SiC occupying the remaining 2%. The first wall is made of ferritic steel (HT-9). The first wall has a thickness of 1 cm. A 0.4 m thick reflector composed of 90 v/o HT-9 and 10 v/o $Li_{17}Pb_{83}$ coolant (7.42% Li-6) is used. The reactor utilizes a 2.9 m thick concrete shield. A schematic of the blanket, first wall, reflector, and shield configuration is given in Fig. 5.1-3.

5.3.2.3 Calculational Method and Nuclear Data

The one-dimensional discrete ordinates code ANISN[1] was used with a P3-S4 approximation. Spherical geometry was used in the calculations and the results represent the conditions at the central plane of the reactor. This yields conservatively high damage rates and low tritium breeding ratios. The

neutron and gamma spectra obtained from the target calculations are used to represent the source for the blanket calculations. An isotropic point source is used at the center of the cavity. The calculations account for neutron spectrum softening, neutron multiplication, and gamma production in the target. A coupled 25 neutron-21 gamma group cross section library based on ENDF/B-IV was used. The library consists of the RSIC DLC-41B/VITAMIN-C data library[2] and the DLC-60/MACKLIB-IV response data library.[3] The results are based on a DT yield of 400 MJ and a repetition rate of 5 Hz.

5.3.2.4 Tritium Breeding and Nuclear Heating

Table 5.3-1 gives the tritium breeding in the different zones. The contributions from $^{7}Li(n,n'\alpha)t$ and $^{6}Li(n,\alpha)t$ are also shown. Table 5.3-2 gives the neutron, gamma, and total energy deposition in the different zones. Notice that more than 50% of energy deposited comes from gamma-ray heating because of neutron reactions in the HT-9 structure. The energy multiplication defined as the total energy deposited in the system, including the energy deposited by X-rays and target debris at the first surface of the blanket, divided by the fusion reaction yield of 17.6 MeV is also included.

5.3.2.5 Radiation Damage to Structural Materials

Using INPORT tubes with an effective thickness of 66 cm results in a peak dpa rate of 2.7 dpa/FPY in the HT-9 first wall. The helium and hydrogen production rates are 0.36 and 1.4 appm/FPY, respectively. It is clear from the results that the INPORT tubes reduce displacement damage and gas production in the HT-9 first wall considerably, allowing it to last for the whole reactor lifetime.

5.3.2.6 Biological Shield Design

The reactor cavity shield is designed such that the biological dose rates outside the shield do not exceed approximately 5 mrem/hr during reactor operation. This design criterion has been set in order to allow hands-on maintenance of auxiliary components outside the reactor during operation. The shield consists of 87 v/o ordinary concrete (Type 3 concrete from reference 4), 8 v/o carbon steel (C1020) reinforcement, and 5 v/o water coolant. The concrete used has a density of 2.3 g/cm^3. The carbon steel used has a density of 7.93 g/cm^3 and consists of 99.4 w/o iron, 0.2 w/o carbon, and 0.4 w/o manganese.

Table 5.3-1 Results for Tritium Production

Region	Element	Tritium Production (Tritons/Fusion)
Blanket	^{6}Li	1.1500
	^{7}Li	0.0270
	Total	1.1770
First Wall	Total	0.0
Reflector	^{6}Li	0.0180
	^{7}Li	0.0
	Total	0.0180
Tritium Breeding Ratio		1.1950

Table 5.3-2 Nuclear Energy Deposition (MeV/Fusion)

Blanket	Neutrons	7.467
	Gamma	6.687
	Total	14.154
First Wall	Neutrons	0.016
	Gamma	0.180
	Total	0.196
Reflector	Neutrons	0.232
	Gamma	3.367
	Total	3.599
System Total		17.949
Overall Energy Multiplication		1.281

Table 5.3-3 Dose Rates (mrem/hr)
Outside a 3.5 m Thick Shield During Operation

	With Reinforcement	Without Reinforcement
Neutron Dose	4.9×10^{-7}	1.4×10^{-5}
Gamma Dose	2.1×10^{-2}	2.64
Total Dose	2.1×10^{-2}	2.64

A series of one-dimensional calculations has been performed. The neutron and gamma fluxes at the outer surface of the shield were used to determine the corresponding biological dose values for different shield thicknesses.

Table 5.3-3 gives a comparison between the dose levels obtained at the outer surface of a 3.5 m thick shield with and without steel reinforcement. It is clear from the results that including 8 v/o steel reinforcement reduces the biological dose rate by nearly two orders of magnitude. The reduction in the gamma dose is more pronounced than the reduction in the neutron dose. Still almost all of the contribution to the dose comes from gamma radiation. These results suggest that reinforced concrete shield thickness smaller than that used in HIBALL-I[5] can be used. The variation of the anticipated dose rate with shield thickness is shown in Fig. 5.3-1. These results show that a shield thickness of 2.9 m can be used, yielding an acceptable dose rate of 2.2 mrem/hr.

The results given in the HIBALL-I report[5] indicated that the dose outside the shield from activation of the reflector and shield after shutdown is quite low. This very low value indicates that the main concern in designing the biological shield for HIBALL is in reducing the dose during operation to acceptable levels. We conclude from the present study that a shield thickness of 2.9 m will be adequate for all hands-on maintenance during operation.

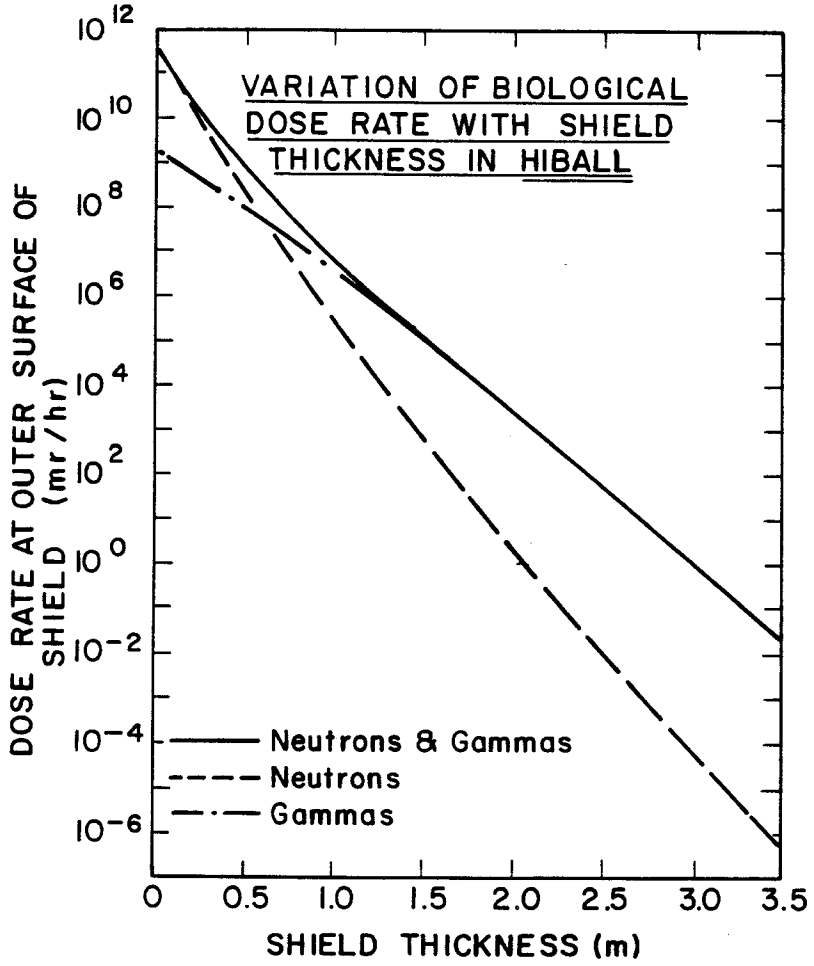

Fig. 5.3-1. Variation of biological dose rate with shield thickness in HIBALL.

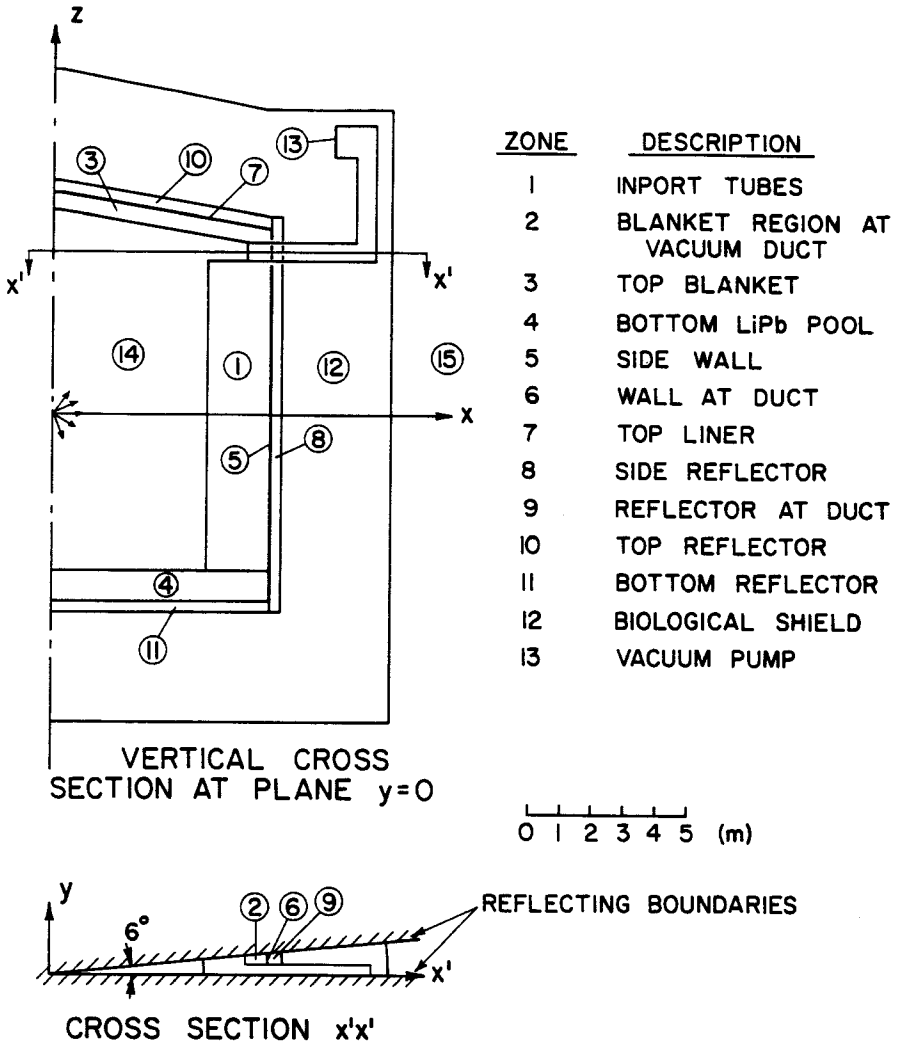

ZONE	DESCRIPTION
1	INPORT TUBES
2	BLANKET REGION AT VACUUM DUCT
3	TOP BLANKET
4	BOTTOM LiPb POOL
5	SIDE WALL
6	WALL AT DUCT
7	TOP LINER
8	SIDE REFLECTOR
9	REFLECTOR AT DUCT
10	TOP REFLECTOR
11	BOTTOM REFLECTOR
12	BIOLOGICAL SHIELD
13	VACUUM PUMP

Fig. 5.3-2. HIBALL geometry for Monte Carlo calculations.

5.3.2.7 Summary

A one-dimensional spherical geometry neutronics and photonics analysis was performed to design the blanket and shield for HIBALL. An effective tube region thickness of 66 cm results in an overall energy multiplication of 1.28 and a breeding ratio of 1.195. The INPORT tubes reduce radiation damage in the HT-9 first wall considerably, allowing it to last for the whole reactor lifetime. A 2.9 m thick reinforced concrete shield was chosen, resulting in a dose rate of 2.2 mrem/hr outside the shield during reactor operation.

5.3.3 Three-Dimensional Time Integrated Studies

5.3.3.1 Introduction

The one-dimensional calculations are not capable of adequately modeling the cylindrical HIBALL reactor with the large penetrations for vacuum pumping. In this section, a three-dimensional neutronics and photonics analysis is presented which adequately models the HIBALL reactor cavity.

5.3.3.2 Reactor Geometrical Model and Method of Calculation

The INPORT tube region has a thickness of 2 m and a height of 10 m. The INPORT tubes have a packing fraction of 0.33 with $Li_{17}Pb_{83}$ occupying 98 v/o of the tubes and the remaining 2 v/o occupied by SiC. The tube support structure is made of HT-9 and occupies 0.7 v/o of the tube region. A one meter deep $Li_{17}Pb_{83}$ pool exists at the bottom of the reactor cavity. The upper blanket consists of 30 segments that consist of 97 v/o $Li_{17}Pb_{83}$, 1 v/o HT-9, and 2 v/o SiC and are 50 cm thick. The $Li_{17}Pb_{83}$ in the region connecting the top blanket with the INPORT tubes helps protecting the HT-9 structure between the vacuum ducts. Thirty vacuum pumps are used to maintain the cavity pressure at 10^{-4} torr. Each vacuum duct is 1 m wide and 0.6 m high. The first wall is 1 cm thick and is made of HT-9. The side wall is 12 m high. The top liner is 7 and 6 m above the midplane at reactor centerline and side wall, respectively. A 40 cm thick reflector consisting of 90 v/o HT-9 and 10 v/o $Li_{17}Pb_{83}$ is used. A 40 cm thick splash plate is used at the bottom of the reactor and is referred to as the bottom reflector in the following analysis. A 2.9 m thick biological shield surrounds the reactor.

The neutronics and photonics calculations were performed using the multigroup three-dimensional Monte Carlo code MORSE.[6] A coupled 25 neutron-21 gamma group cross section library was used. The combinatorial geometry capability of the MORSE code was used to model the problem geometry. A point isotropic source was used at the center of the reactor cavity with neutron and

gamma spectra obtained from the target neutronics and photonics calculations. 4000 histories were used yielding less than 2% statistical uncertainty in the estimates for the tritium breeding ratio and the energy multiplication.

Because of symmetry, only 1/60 of the reactor was modeled with reflecting albedo boundaries used at the planes of symmetry. The geometry for the computational model used is given in Fig. 5.3-2. To quantify nuclear heating in the vacuum pump, a 2 cm thick region consisting of 50 v/o 316 SS and 50 v/o Cu is designated as zone 13 to simulate the cryopanels.

5.3.3.3 Tritium Production

Table 5.3-4 shows the results for tritium production per DT fusion reaction in the different reactor zones. The contributions from $^{6}Li(n,\alpha)$ and $^{7}Li(n,n'\alpha)$ reactions are shown separately. The contribution from ^{7}Li represents ~ 2% of the total tritium production.

We notice that as much tritium production occurs in the top blanket as in the bottom $Li_{17}Pb_{83}$ pool, even though the top blanket is only half as thick as the bottom pool and includes 1 v/o HT-9 structure. The reason is that the 2 v/o SiC present in the top blanket enhances neutron slowing down and hence increases the tritium breeding effectiveness.

The overall tritium breeding ratio is 1.25 ± 0.025. The overall tritium breeding ratio obtained here with the actual reactor cavity cylindrical geometry is larger than that obtained from the one-dimensional spherical geometry calculations (1.195). This results from the neutron source being surrounded by a larger volume of breeding material in the actual cylindrical case as compared with the case of an equivalent spherical blanket.

5.3.3.4 Nuclear Heating

Table 5.3-5 shows the nuclear energy deposition for neutrons and gammas in the different zones. The average power density is also included. It is clear that the contributions from neutron and gamma heating are nearly the same in the breeding blanket while the gamma contribution in the first wall and reflector is about an order of magnitude higher than the neutron contribution. About 60% of the total reactor thermal power comes from gamma heating. The energy deposited in the biological shield represents only 0.27% of the total reactor thermal power. The total recoverable neutron and gamma energy in the reactor per DT fusion is 17.553 ± .292 MeV which is slightly less than that obtained for an equivalent spherical reactor (17.95 MeV).

Table 5.3-4 Tritium Production (Tritons/Fusion)

Region	Zone Number	$^{6}Li(n,\alpha)T$	$^{7}Li(n,n'\alpha)T$
Breeding Blanket	1	0.729	0.018
	2	0.014	0.00001
	3	0.212	0.004
	4	0.235	0.004
	Region Total	1.190	0.026
Reflector	8	0.022	0.000002
	9	0.001	0.0000001
	10	0.009	0.000002
	11	0.002	0.0000001
	Region Total	0.034	0.000004
System Total		1.224	0.026

Table 5.3-5 Nuclear Heating

Region	Zone Number	Energy Deposition (MeV/fusion)		Average Power Density (W/cm^3)
		Neutrons	Gammas	
Breeding Blanket	1	4.806	4.839	4.409
	2	0.074	0.017	3.911
	3	1.339	1.147	3.515
	4	1.430	1.007	1.800
	Region Total	7.649	7.010	4.409
First Wall	5	0.004	0.050	1.222
	6	0.0001	0.0004	2.010
	7	0.003	0.039	3.068
	Region Total	0.007	0.089	1.653
Reflector	8	0.155	1.628	0.939
	9	0.007	0.066	1.020
	10	0.070	0.733	1.465
	11	0.013	0.126	0.257
	Region Total	0.245	2.553	0.941
System Total		7.901	9.652	3.345

A volumetric nuclear heating rate of 6×10^{-11} W/cm^3 was obtained in the vacuum pump (zone 13). The fractional standard deviation was 0.25. Because the vacuum ducts do not see direct line-of-sight source neutrons and they are bent twice, neutron streaming through the ducts was found to not cause any serious problem to the vacuum pump.

The energy flow for the HIBALL fusion reactor design is illustrated in Fig. 5.3-3. The values given for the power correspond to one reactor cavity. Therefore, these values need to be multiplied by 4 to calculate the power from the whole power plant. This corresponds to a total power plant thermal power of 10,193 MW(th). The overall energy multiplication of the blanket, wall and reflector is 1.274.

5.3.3.5 Summary

A three-dimensional Monte Carlo analysis was performed for the reactor chamber. An overall tritium breeding ratio of 1.25 and an overall energy multiplication of 1.274 were obtained. The tritium breeding ratio is higher than that for the equivalent spherical reactor cavity. Nuclear heating in the vacuum pumps was found to be very small. The power in the biological concrete shield represents only 0.27% of the total reactor thermal power. The thermal power for the HIBALL power plant is 10,193 MW(th).

5.3.4 Time-Dependent Neutronics and Photonics

5.3.4.1 Introduction

In an inertial confinement fusion reactor the neutron source has a pulsed nature because of the very short burn time over which the fusion reactions occur (10-100 ps). Furthermore, the neutron pulse does not reach the first surface of the blanket until ~ 100 ns after the burn and the neutron slowing down time in the blanket is much greater than the duration of the neutron source. Neutron interaction with the dense (~ 10^{25}/cm^3) target material leads to a considerable time of flight spread as neutrons reach the first surface. Therefore, time dependent neutronics studies are essential for the proper analysis of inertial confinement fusion reactors.

As a result of the pulsed nature of the neutron source, high instantaneous damage rates are present in an inertial confinement fusion reactor wall and structure. This can lead to significant changes in the microstructure[7] of the first wall material. Accurate instantaneous damage rates can be calculated by performing time-dependent neutronics studies.

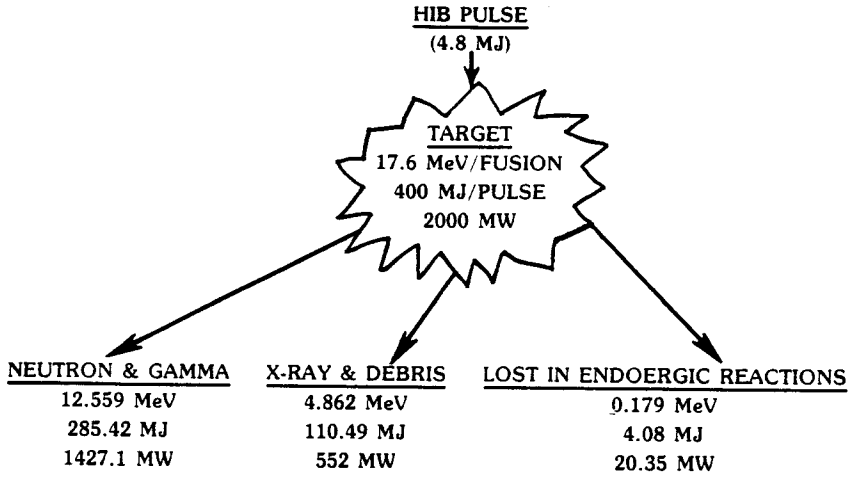

	NEUTRON & GAMMA	X-RAY & DEBRIS	TOTAL	
BREEDING BLANKET	14.659 MeV 333.16 MJ 1667.5 MW	4.862 MeV 110.49 MJ 552 MW	19.521 MeV 443.65 MJ 2219.5 MW (87.05%)	
WALL	0.096 MeV 2.24 MJ 10.8 MW		0.096 MeV 2.24 MJ 10.8 MW (0.42%)	22.415 MeV 509.39 MJ 2548.3 MW
REFLECTOR	2.798 MeV 63.5 MJ 318.0 MW		2.798 MeV 63.5 MJ 318.0 MW (12.53%)	

OVERALL ENERGY MULTIPLICATION = 1.274

Fig. 5.3-3. **Energy flow in HIBALL for a 4.8 MJ heavy ion beam pulse.**

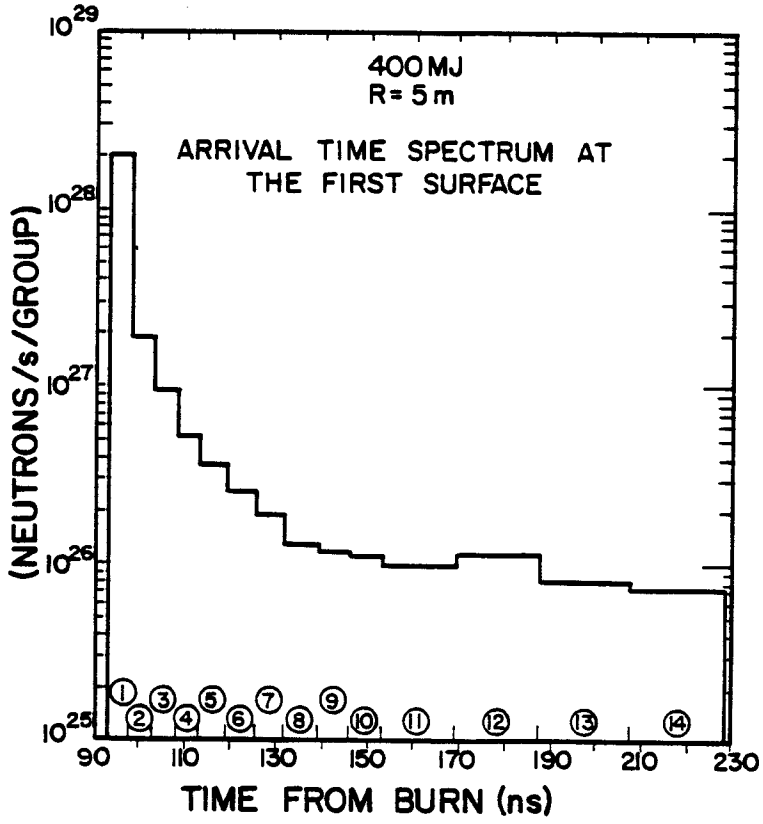

Fig. 5.3-4 Arrival time spectrum at the first surface of the blanket. Encircled numbers indicate the energy groups associated with the various times.

A modified version of the time dependent discrete ordinates code TDA[8] has been used to perform time-dependent neutronics analysis. The effects of the INPORT first wall protection concept on the peak instantaneous and average dpa and gas production rates in the HT-9 first wall have been investigated. Also, the instantaneous energy deposition rates at different positions in the blanket and first wall have been calculated.

5.3.4.2 Computational Model

A schematic of the blanket, first wall, reflector, and shield configuration is given in Fig. 5.1-3.

The spectrum of neutrons generated in the target was used as a source for the time dependent blanket neutronics analysis. Spherical geometry was used in the calculations. A P3-S8 approximation was used with a coupled 25 neutron-21 gamma group cross section library.

As neutrons travel from the target to the first surface of the blanket considerable time of flight spreading occurs because of the broad energy distribution of these neutrons. The arrival time spectrum at the first surface located 5 m from the neutron source is shown in Fig. 5.3-4. The numbers at the bottom of the graph indicate the energy groups associated with the various times.

5.3.4.3 Atomic Displacement Rate

The instantaneous damage rates in the first wall have been calculated. The instantaneous dpa rate in the protected ferritic steel first wall is given in Fig. 5.3-5. It is clear that the damage occurs over a relatively long time resulting in a peak instantaneous dpa rate of 0.009 dpa/s at 140 ns after burn. This peak corresponds to the 14 MeV source neutrons arriving without collision. A broad peak at ~ 270 ns corresponds to neutrons emitted in (n,2n) reactions with lead in the INPORT tubes. This considerable time spread results from the relatively long slowing down time in the blanket allowing neutrons of energies greater than the dpa threshold energy of iron (~ 1 keV) to exist in the first wall over a long period of time. The wall protection is found to decrease the total cumulative dpa and the peak instantaneous dpa rate by factors of 9.4 and 1190, respectively.

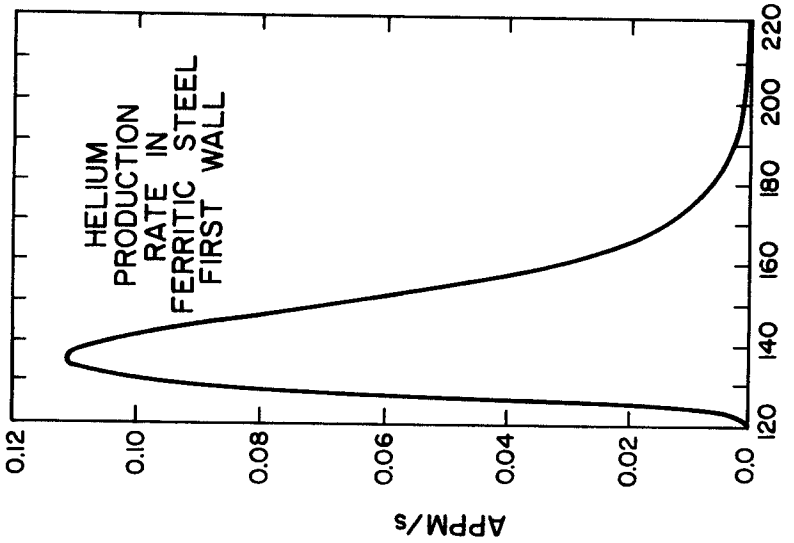

Fig. 5.3-6. Helium production rate in the protected first wall.

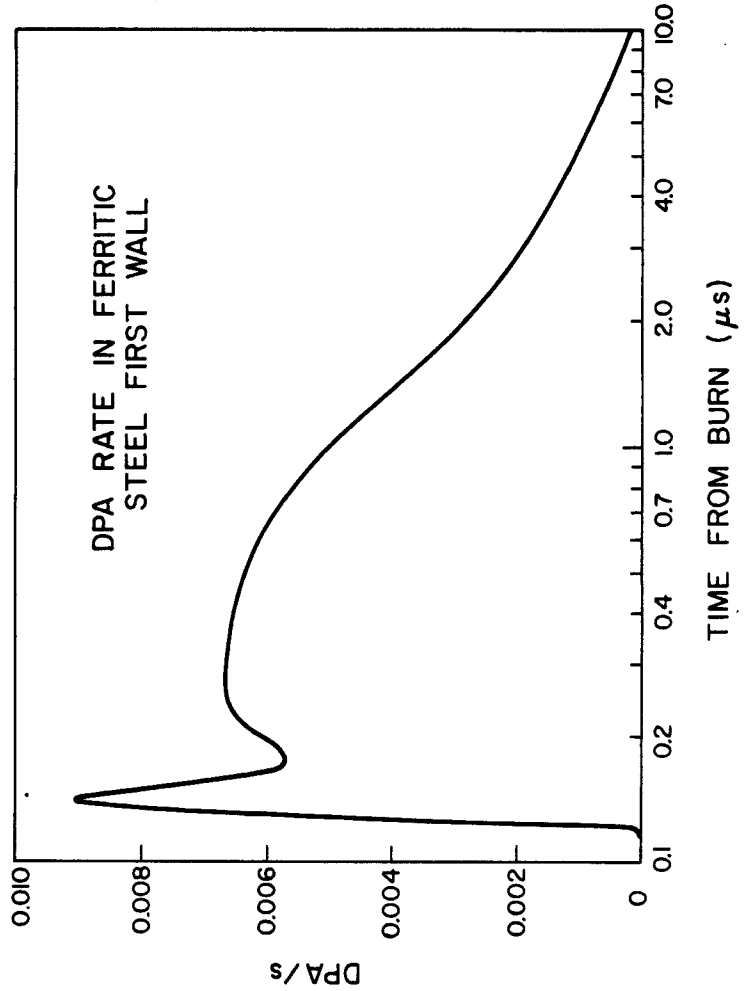

Fig. 5.3-5. DPA rate in the protected first wall.

5.3.4.4 Helium Production Rate

The instantaneous helium production rate in the protected ferritic steel first wall is given in Fig. 5.3-6. A peak instantaneous helium production rate of 0.11 appm/s occurs about 15 ns after the leading edge of the pulse arrives at the wall. It is clear that the time spread here is much smaller than that for the dpa. Only one peak occurs because the (n,2n) neutrons do not contribute to helium production. The total helium production in a full power year is found to decrease by a factor of 630 while the peak instantaneous helium production rate is found to decrease by a larger factor of 1627 when the INPORT tubes are used.

5.3.4.5 Energy Deposition Rate

The time-dependent neutron and gamma fluxes are used together with the appropriate kerma factors for neutron and gamma energy deposition to calculate the energy deposition rate in the blanket and first wall. The results are given in Fig. 5.3-7 at the blanket first surface, the center of the blanket, and the first wall. The time distribution is very narrow at the first surface and broadens as one moves towards the first wall. While the time spread at the first surface is determined by the time of flight spread, the spread at the first wall is determined by the slowing down time in the inner blanket. For a 400 MJ fusion yield the peak instantaneous power densities in the blanket and the first wall are found to be 1.82×10^8 and 2.73×10^5 W/cm^3, respectively. This corresponds to peak to average temporal power density ratios of 8.48×10^6 and 1.65×10^5, respectively. The INPORT concept is found to decrease the peak instantaneous power density in the wall by a factor of ~ 1210 and the total nuclear heating in the wall by a factor of ~ 18. These results are useful for stress analysis studies.

5.3.4.6 Summary

Time dependent neutronics analysis for the HT-9 first wall has been performed. The time dependence of the neutron source is modified in such a way that the multigroup treatment adopted in the time dependent transport code predicts the correct time of flight spread of neutrons in each group as they travel from the source to the first surface of the blanket. A modified version of the time dependent discrete ordinates code TDA has been used.

Neutron slowing down in the INPORT first wall protection system is found to have a significant effect on the time dependent spectrum and damage in the first wall. The time over which the damage occurs is found to be determined

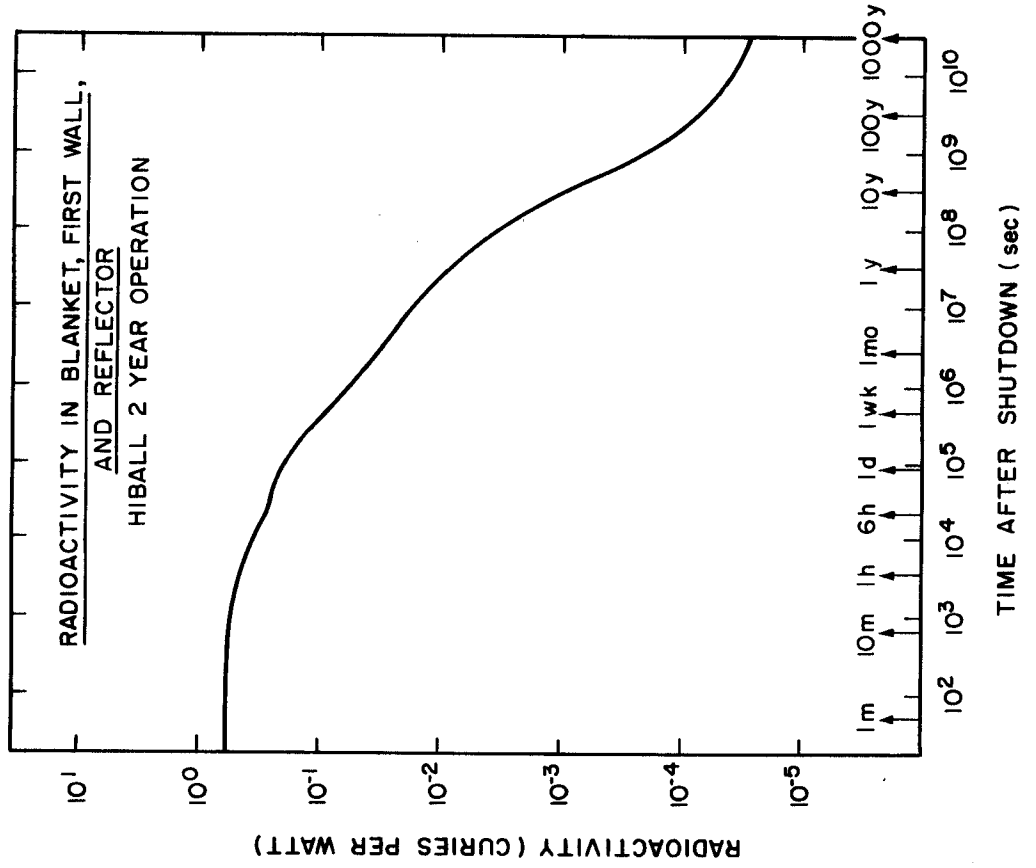

Fig. 5.3-8 Radioactivity in HIBALL blanket, first wall, and reflector after 2 years operation.

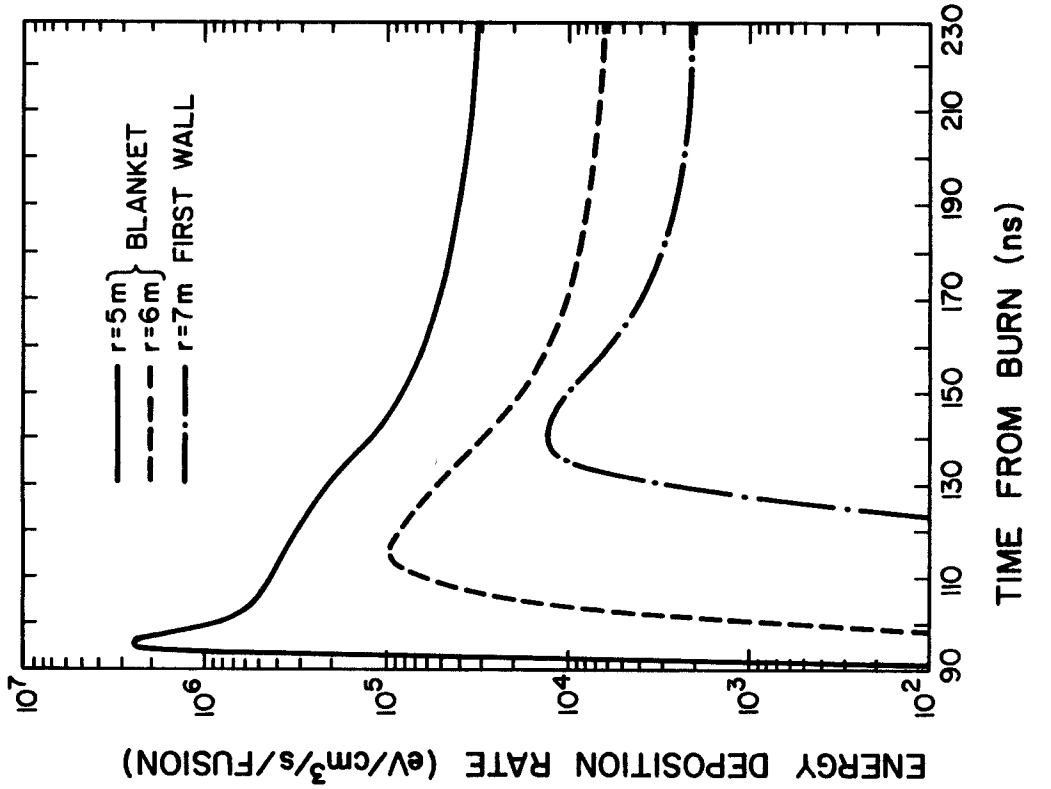

Fig. 5.3-7 Energy deposition in HIBALL blanket and shield.

primarily by the slowing down time in the blanket. In the case of an unprotected wall, where no slowing down occurs in front of the wall, the spread is determined primarily by the time of flight spread.

Using the INPORT first wall protection concept results in significant reductions in peak instantaneous and total dpa and helium production rates allowing the first wall to last for the reactor lifetime (~ 20 FPY). Our results also show that the peak power density in the first wall resulting from nuclear heating decreases considerably when the INPORT tube concept is used to protect the wall.

5.3.5 Radioactivity and Afterheat

Radioactivity will be induced in the coolant and structure of the reactor through activation by the fusion neutrons. The reactor was modeled in spherical geometry with materials and dimensions consistent with a cut through the midplane of the reactor. No impurities or corrosion products in the coolant were considered, with the exception of bismuth (see Chapter 9). The multigroup neutron flux used in the activation calculations was taken from the one-dimensional ANISN calculations. For the purpose of the calculation the reactor was broken up into 37 intervals and the average flux in each interval was used. The DKR code[9] was used to calculate the radioactivity parameters -- activity, afterheat, and biological hazard potential (BHP).

The activities were calculated for an operating time of two years. The activity at times after shutdown of much less than two years is relatively independent of operating time while the activity at times very much longer than two years after shutdown is approximately proportional to operating time.

The total activity per unit of thermal power is shown in Fig. 5.3-8. The level at shutdown is 0.62 Ci/W_{th}. The activity falls off rather slowly with time after shutdown requiring approximately three weeks to be reduced by a factor of 10 and two years to be reduced by a factor of 100. The initial activity is dominated by the contributions of ^{56}Mn and ^{203}Pb. ^{56}Mn ($T_{1/2}$ = 2.58 hr) decays away first followed by ^{203}Pb ($T_{1/2}$ = 52 hr). Note that unless flow were maintained, the ^{203}Pb activity would not be present in the reactor itself but would be associated with the coolant storage facility. The next major decrease in activity is due to the decay of ^{51}Cr ($T_{1/2}$ = 27.7 days). It is followed by the decay of ^{55}Fe ($T_{1/2}$ = 2.7 yr) which produces the large activity drop between 1 and 100 years. The long term activity is due to ^{93}Mo and ^{93}Nb originating in the small amount of Mo in the steel (HT-9).

The afterheat is shown in Fig. 5.3-9. The value at shutdown is 0.66% of the operating power. Since the decay energies of the various isotopes are different the afterheat curve has a shape which differs from that of the activity. It falls off much more rapidly, by a factor of 10 in about two days and a factor of 100 in two weeks. At shutdown ^{56}Mn is the dominating isotope. The decay of this isotope plus the relatively rapid decay of ^{203}Pb account for the order of magnitude drop in two days. ^{51}Cr, which contributes significantly to the activity in the one week to one month period, contributes very little to the afterheat. Thus, the afterheat in this period is governed primarily by the decay of ^{203}Pb. The decay energy of ^{55}Fe is also low as is the decay energy of the remaining isotopes which leads to the rather low residual afterheat subsequent to about 100 years.

The Biological Hazard Potential (BHP) is shown in Fig. 5.3-10. BHP is defined as the ratio of the activity present in the system per unit of power to the level of activity allowed per unit volume of air in the U.S. Nuclear Regulatory Commission Regulations (10 CFR 20). Thus it is a measure of the potential hazard of a radioactive material. The shape of the curve is similar to the shape of the activity curve being 26.0 at shutdown and requiring almost one month to be down by a factor of ten and with a long term reduction of only three orders of magnitude.

The activity in the shield is 6.3×10^{-3} Ci/W_{th} after shutdown which is significantly lower than the activity in the reflector. The time behavior of the activity is dominated after the first day by the activity of ^{55}Fe which continues to be the major contributor until times greater than 100 years. The afterheat at shutdown is 7.7×10^{-2}% of the operating power which while relatively small, will still require some residual heat removal capacity. The afterheat drops off faster with time than does the activity primarily because of the low decay energy of ^{55}Fe. The BHP is also relatively low and falls off slowly, again because of the hazard characteristics of nuclei involved. To get a somewhat different appreciation of the magnitude of the activities in the shield the above values at shutdown correspond to an average activity of 3.4×10^{-3} Ci/cm^3, an afterheat of 4.1×10^{-5} W/cm^3, and a BHP of 6.7×10^{-11} km^3/cm^3.

The dose due to activation products was calculated using the activities calculated above along with a one-dimensional gamma transport program. The results of this calculation indicated that the dose outside the shield from

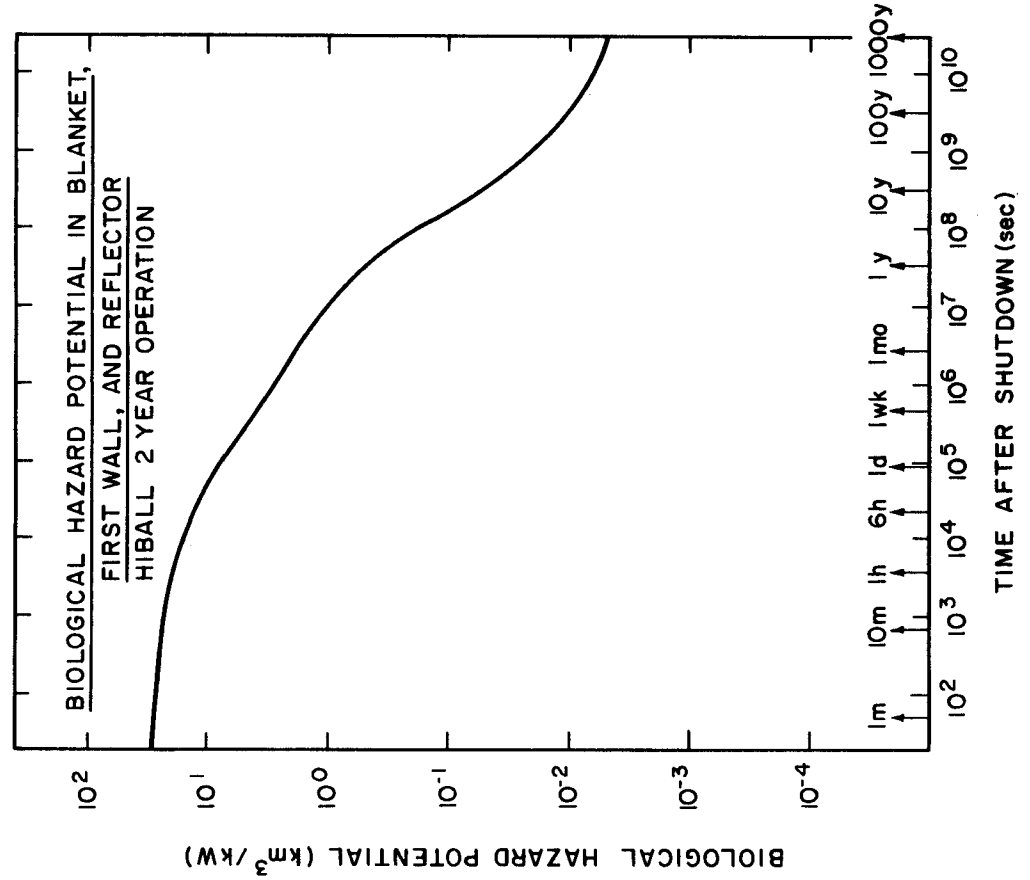

Fig. 5.3-10 Biological hazard potential in HIBALL blanket, first wall, and reflector after 2 years operation.

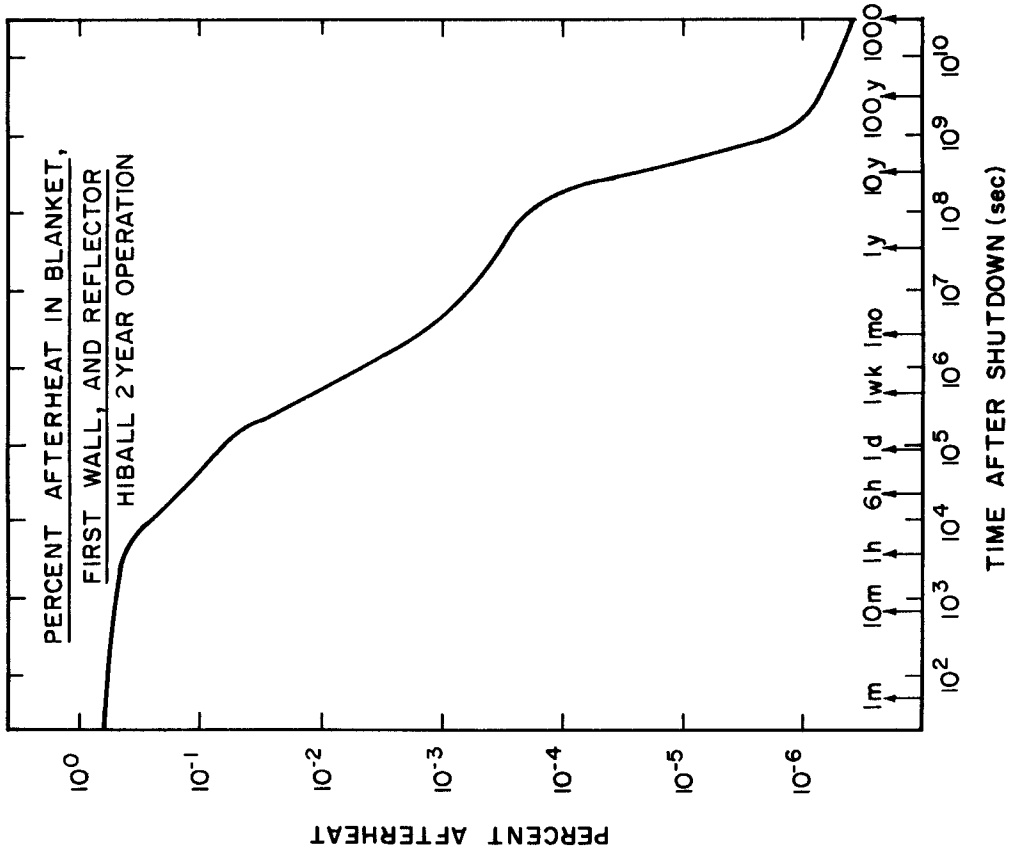

Fig. 5.3-9 Percent afterheat in HIBALL blanket, first wall, and reflector after 2 years operation.

activation of the reflector and materials in the shield is quite low, ~ 10^{-4} mrem/hr at shutdown.

References for Section 5.3

1. RSIC Code Package CCC-254, "ANISN-ORNL," Radiation Shielding Information Center, ORNL.

2. RSIC Data Library Collection, "VITAMIN-C, 171 Neutron, 36 Gamma-Ray Group Cross Sections Library in AMPX Interface Format for Fusion Neutronics Studies," DLC-41, ORNL.

3. RSIC Data Library Collection, "MACKLIB-IV, 171 Neutron, 36 Gamma-Ray Group Kerma Factor Library," DLC-60, ORNL.

4. D.K. Trubey and M.B. Emmett, "Some Calculations of the Fast-Neutron Distribution in Ordinary Concrete from Point and Plane Isotropic Fission Sources," ORNL-RSIC-4, Oak Ridge National Laboratory (1965).

5. B. Badger et al., "HIBALL, A Conceptual Heavy Ion Beam Driven Fusion Reactor Study," University of Wisconsin Fusion Technology Institute Report UWFDM-450 (Sept. 1981); also KfK-3202.

6. RSIC Code Package CCC-203, "MORSE-CG," Radiation Shielding Information Center, ORNL.

7. N. Packen et al., J. Nucl. Mater., 78, 143 (1978).

8. RSIC Code Package CCC-180, "TDA," Radiation Shielding Information Center, ORNL.

9. T.Y. Sung and W.F. Vogelsang, "DKR: A Radioactivity Calculation Code for Fusion Reactors," University of Wisconsin Fusion Technology Institute Report UWFDM-170, (Sept. 1976).

5.4 Behavior of LiPb Vapor

A unique engineering problem for ICF reactors is the design of a first surface which can carry away the steady state average surface heat and at the same time survive the transient temperature increase generated by x-ray and ion debris from the target explosion. In HIBALL, the INPORT tubes serve this function. The INPORT tubes, filled with flowing $Li_{17}Pb_{83}$ coolant, protect the first structural wall from excessive neutron damage. The SiC tubes themselves are protected from the short range x-ray and ion debris by a thin layer of LiPb that flows down the outside of the porous tube.

After a target explosion, the x-ray energy is deposited within 10^{-3} cm of the first surface. The temperature of a thin layer of $Li_{17}Pb_{83}$ is raised above its boiling temperature, and is vaporized. This ablated material flows toward the center of the cavity and intercepts the ions generated by the explosion. The energy associated with the ions is absorbed by the $Li_{17}Pb_{83}$ vapor and does not directly impinge on the first surface. The vapor is superheated to a high temperature and starts to release its energy by thermal radiation toward the cool first surface. The liquid surface temperature increases upon receiving energy from this thermal radiation and condensation of the vapor. The higher surface temperature increases the vapor pressure and consequently increases the vaporization rate. The cavity pressure is very high after the initial x-ray deposition, and varies from the combined effects of evaporation and condensation. It is of critical importance to beam transport and, to a lesser degree, vacuum pumping to calculate the pressure history after an explosion.

There are a number of factors that determine the time required for the LiPb vapor to clear from the cavity. The density required for ballistic ion propagation has an obvious effect and it is not a particularly well known quantity. No experimental measurements are known of the relevant ion-ion collision cross sections so the value used is based on theoretical calculations. Others have argued[1] that the rate of heat transfer across the condensing surface limits the rate of condensation and this has been found to be true in HIBALL. A final point is that the choice of the liquid metal undergoing the vaporization and condensation has an effect on the condensation rate due to the thermal speed of the condensing material. This is most important late in the condensation phase when the condensation heat flux is low, meaning that the heat conduction across the condensing surface is less important.

In this section, the behavior of the LiPb vapor is discussed. In Section 5.4.1 the deposition of target generated x-rays and the subsequent vaporization of the LiPb is described. Section 5.4.2 deals with the stopping of target generated ions in the vapor, the flow of LiPb into the reactor chamber and the radiation of photon energy from the vapor back onto the tubes. Section 5.4.3 contains a description of the vaporization and condensation of the LiPb vapor. The pressure history of the cavity is thus established. Work that is in progress and conclusions are discussed in 5.4.4.

5.4.1 X-Ray Energy Deposition and the Resulting Evaporation

The deposition of target x-rays in the film, the heat transfer in the film and the vaporization of LiPb have been calculated. The x-ray energy spectrum obtained from the target calculations[2] discussed in Section 2.1.2 is peaked around 3 keV and extends up to 300 keV. Since most of the photons have energies well below 100 keV, we have used the Biggs data.[3,4] Figure 5.4-1 shows the volumetric energy deposition in Pb using the spectrum given in Fig. 2.1-5. The A*THERMAL[5] code was used in this calculation. Note that 88 MJ or 22% of the target yield is in the form of x-rays. The amount of mass vaporized due to the x-ray energy deposition is computed using a simple adiabatic model. It is assumed that all mass with a deposited energy greater than the vaporization energy, 8.7×10^5 J/cm^3, will be vaporized. This adiabatic model becomes more accurate for very short x-ray deposition times, i.e. instantaneous. From the x-ray energy deposition curve (Fig. 5.4-1) this corresponds to a thickness of approximately 2.5 microns. To account for the mass that has been raised to saturated liquid conditions, we have assumed that there is some additional vaporization. This additional vaporization accounts for the energy content above $C_p(T_b - T_o)$ as is shown schematically in Fig. 5.4-2. This gives an additional thickness of the vaporized layer of about 1.8 microns. Therefore, the total thickness of material vaporized $\simeq$ 4.3 microns. This is equivalent to 13 kg of vaporized material per shot.

5.4.2 LiPb Gas Dynamics and Radiation

As discussed in the preceding section, target generated x-rays vaporize several kilograms of LiPb from the INPORT tubes. The resulting vapor absorbs the target generated ions, reaches a temperature of about 1.4 eV and becomes partially ionized. As this gas spreads from the tubes into the center of the reactor cavities, it radiates a heat flux back onto the tubes. Eventually, the gas uniformly fills the cavity and cools enough that the heat flux on the

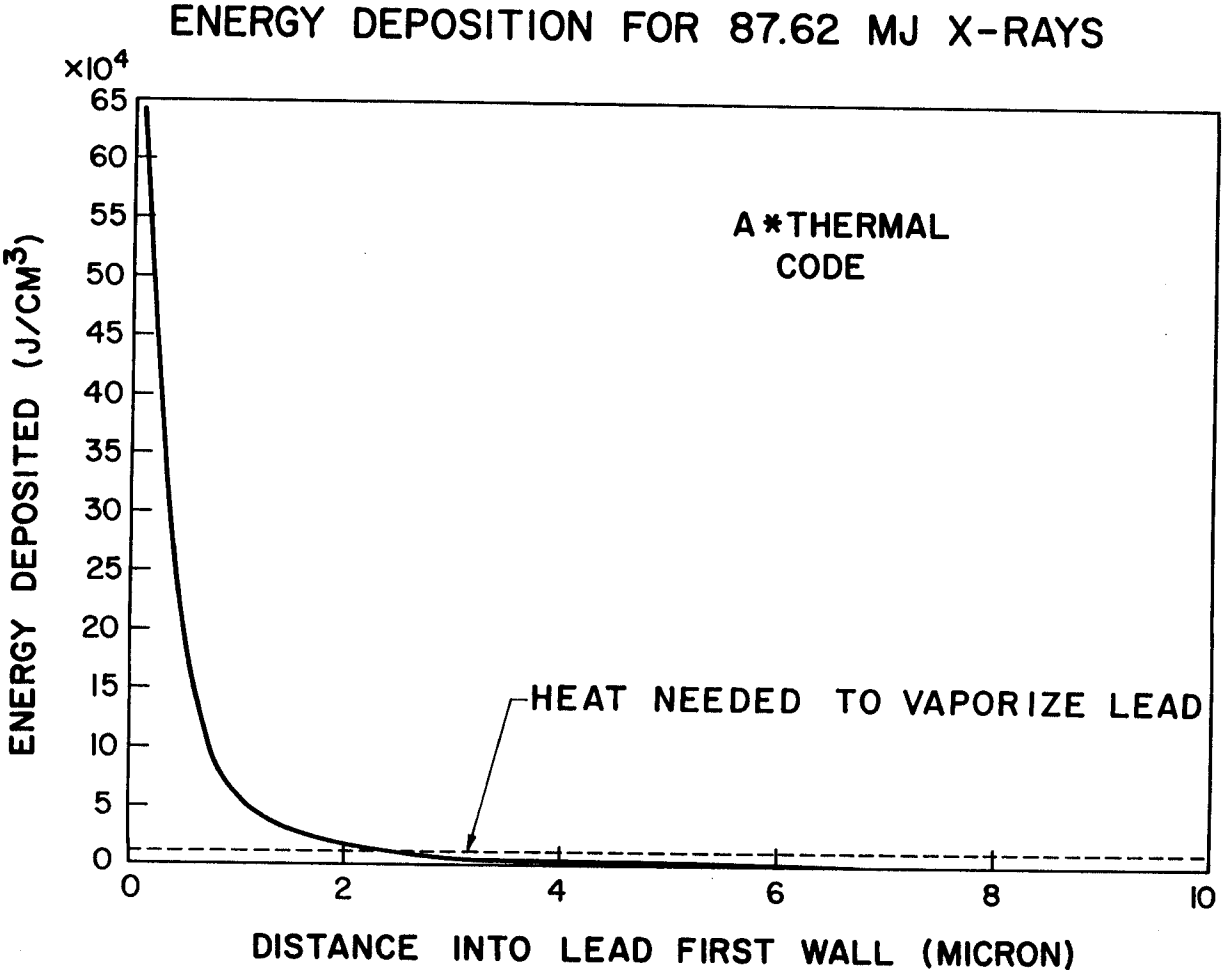

Fig. 5.4-1. X-ray volumetric energy deposition in liquid lead.

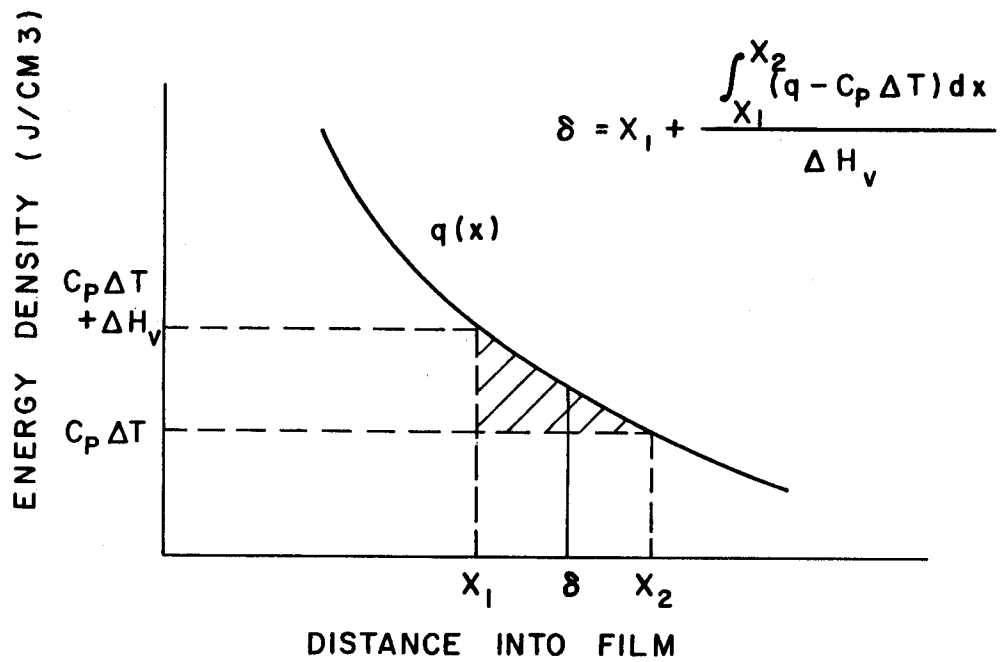

Fig. 5.4-2. Conceptual representation of LiPb vaporization.

tubes is insignificant. Before this happens, though, there may be some additional vaporization of LiPb due to the heat flux. As the gas radiates, it also cools, affecting the rate of recondensation. For these reasons, it is important to consider the behavior of this gas between the time of vaporization and recondensation.

We have modeled the behavior of the LiPb gas with the 1-D Lagrangian radiation-hydrodynamics computer code, FIRE.[6] This code has explicit hydrodynamics and implicit energy transport where heat is conducted through two fluids -- the gas at a local temperature of T_{gas} and the radiation fluid at a temperature of $T_{radiation}$. In these calculations, conduction through the radiation field dominates the thermal transport. Transport coefficients and equation of state information is obtained from a table of data provided by a calculation with MIXER.[7]

FIRE cannot accurately model the behavior of a fluid which is as dense as a liquid. Thus, analytical calculations of the dynamics must be performed from the time when the LiPb is at liquid density until the time that the density is low enough for FIRE calculations to be appropriate. It is assumed that the gas obeys an isothermal blowoff formalism where the temperature of the gas is that due to the deposited target generated x-ray energy minus the energy of vaporization and the energy of ionization. It is arbitrarily assumed that the energy from target generated ions is uniformly deposited in the gas at 1.5×10^{-4} seconds after vaporization and that FIRE can be used any time after this. Thus, at this time the computer calculations are started with the gas density profile being the Gaussian shape predicted by the blowoff model and the total energy in the gas being the target generated x-ray and ion energy minus the vaporization and ionization energy.

The FIRE calculation simulates the gas dynamics until the time the gas reaches the center of the cavities. Figure 5.4-3 shows the positions of the Lagrangian zone boundaries for a typical calculation during this period. Upon reaching the center, the gas begins to convert its bulk kinetic energy into heat, but FIRE, being a one-dimensional code, predicts that the gas will reflect off the center and propagate back toward the tubes. This is not physically realistic because the system does not have the symmetry needed for such reflections. For this reason this first simulation calculation is stopped at the time when the gas reaches the center, typically about 1 millisecond after vaporization.

To simulate the behavior past this time it is assumed that the gas has a uniform temperature and density and has no bulk kinetic energy immediately after the gas collapses in the center. It is found that the temperature that will lead to the proper amount of energy in the gas,

$$E_{gas} = E_{x\text{-}ray} + E_{ion} - E_{vaporization} - E_{ionization} - E_{radiation},$$

where $E_{radiation}$ is the energy radiated back into the tubes by this time. We then use FIRE again with this new initial condition and with the gas constrained not to move. By combining both uses of FIRE, the heat flux on the tubes due to radiation and the average temperature of the gas versus time are calculated.

The results consist of the heat flux on the first row of tubes and the average gas temperature as a function of time, which are shown in Figs. 5.4-4 and 5.4-5. Notice that there is in each case a large pulse of heat reaching the surface immediately after the gas collapses in the center. This is an effect of the conversion of bulk kinetic energy into heat. There is also a pulse in the average temperature of the gas which is due to this conversion of kinetic energy into heat and which causes the increase in heat flux. The same process has been seen in imploding wire experiments.

5.4.3 Evaporation and Condensation Calculation

The rates that LiPb evaporate and condense are governed by the density and temperature of vapor and the temperature of the surface of the film. For HIBALL, the surface temperature of the film is calculated using a simple temperature diffusion method where the heat flux on the surface is due to radiation and mass flow between the reactor cavity gas and the film. The mass flow rates due to condensation and evaporization are

$$\dot{m}_{cond} = 3.64\ P_g (M/RT_g)^{1/2} \qquad (5.4\text{-}1)$$

and

$$\dot{m}_{vap} = P_s \left(\frac{M}{RT_s}\right)^{1/2} \qquad (5.4\text{-}2)$$

respectively. In these equations, $\dot{m}_{cond}$ and $\dot{m}_{vap}$ are mass flow rates in units of g/s-cm^2, P_g is the pressure of the vapor in torr and M is the molecular weight of the vapor. T_g and T_s are vapor and film surface temperatures in K,

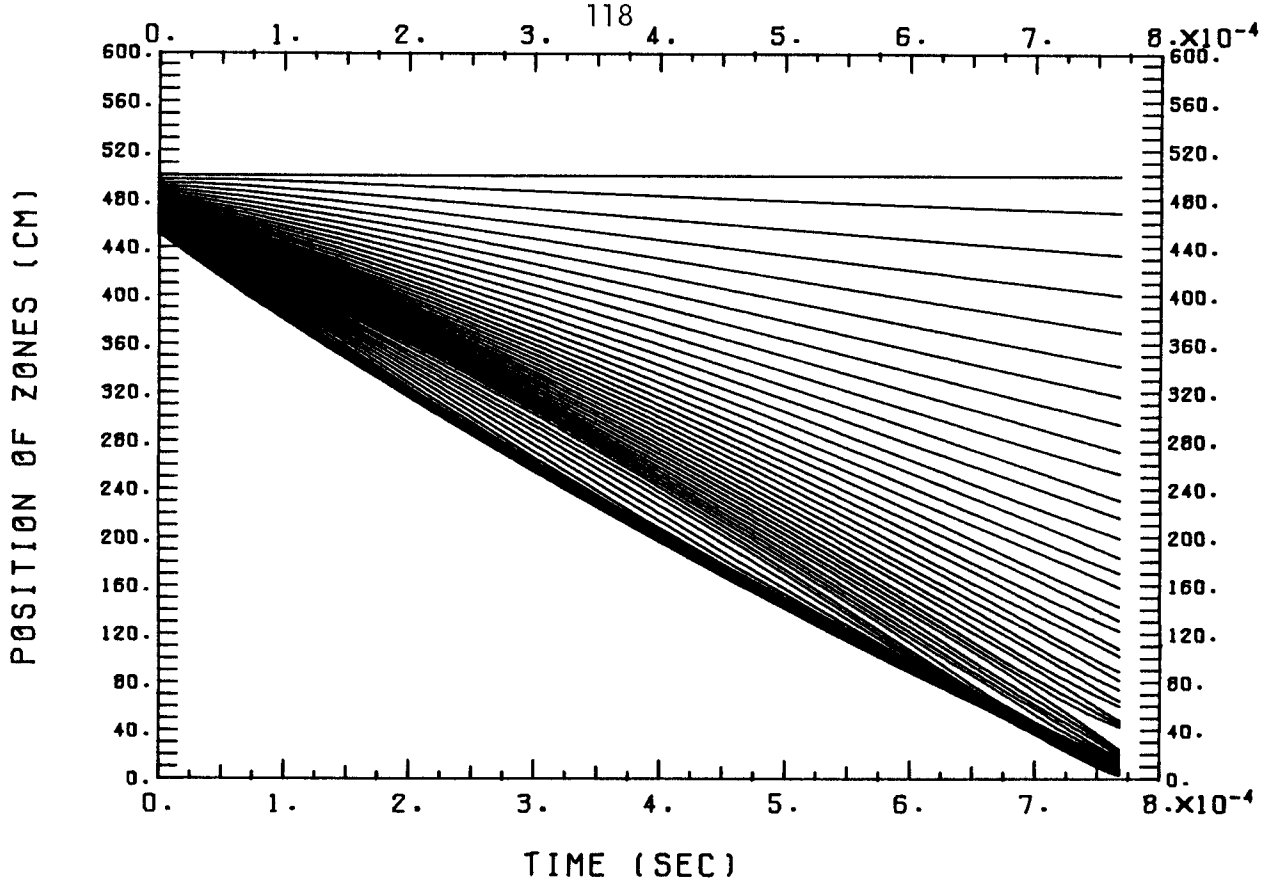

Fig. 5.4-3. Positions of Lagrangian zones during blowin of vapor.

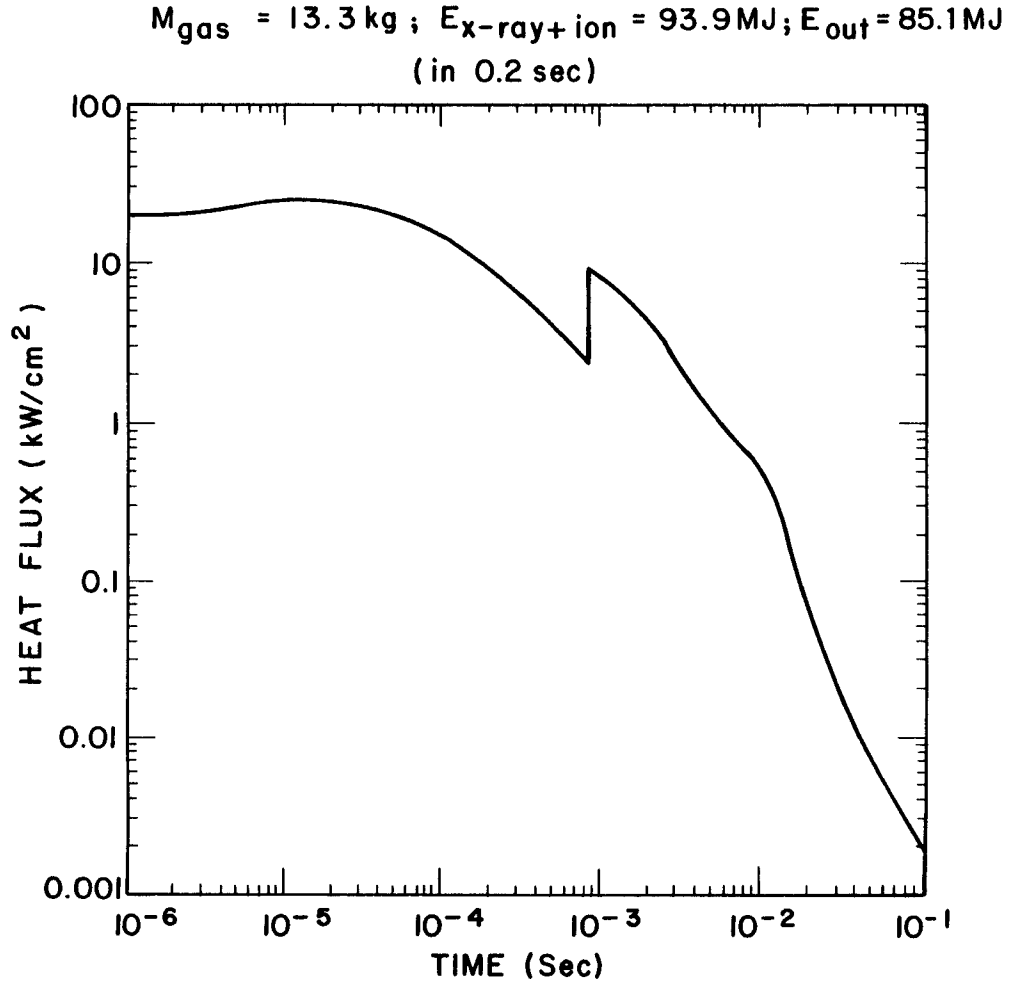

Fig. 5.4-4. Radiation heat flux on the first row of INPORT tubes versus time after the target microexplosion.

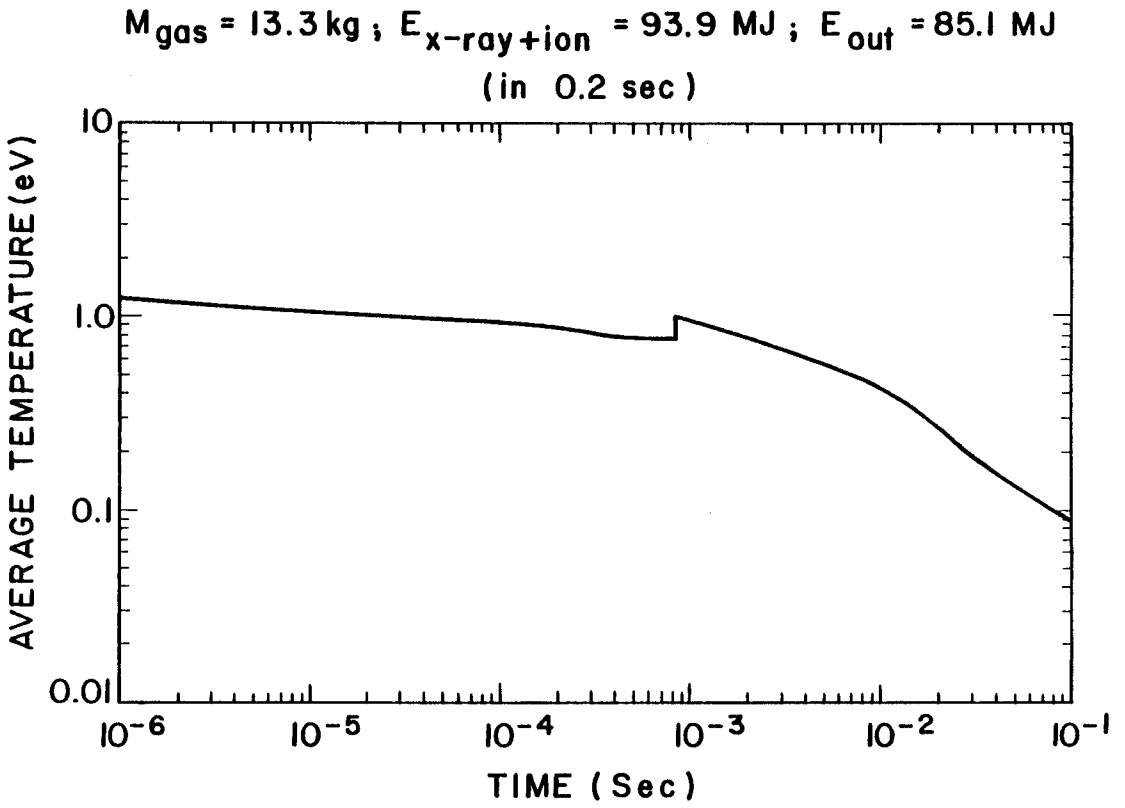

Fig. 5.4-5. Average gas temperature of the LiPb vapor in the reactor cavity versus time after the target microexplosion.

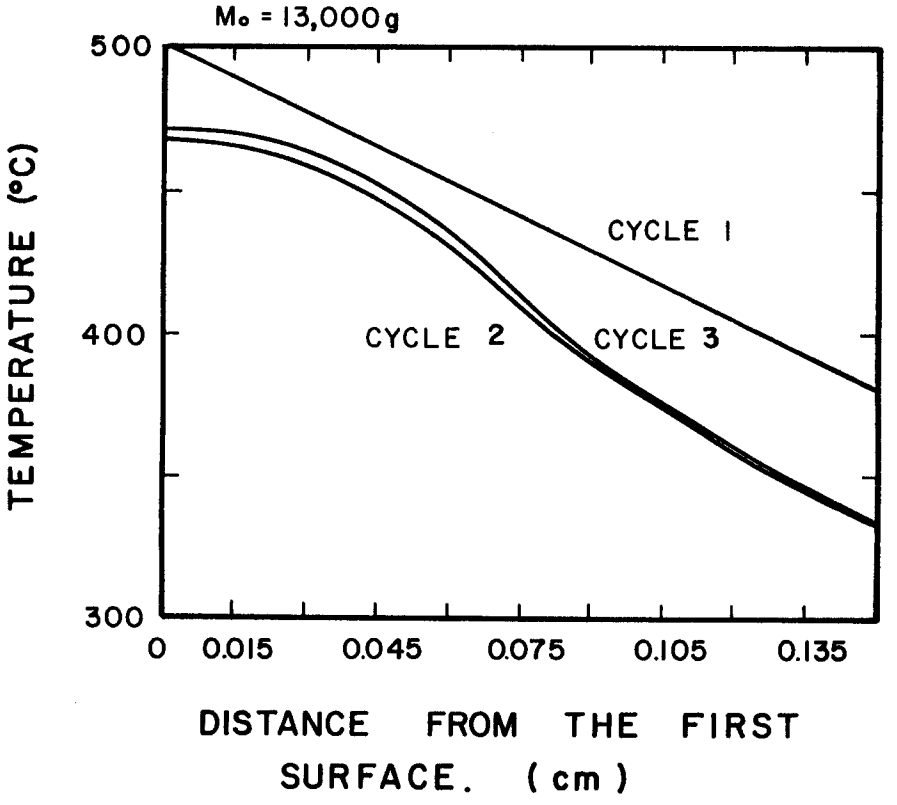

Fig. 5.4-6. Temperature of the LiPb at the start of the first three cycles. Mass of vaporized gas = 13,000 g.

P_s is the saturation pressure at the film surface temperature and R is the gas constant.

This model is the basis of a finite difference computer code that was written to calculate the time-dependent film temperature profile and the mass flow. Using this code, one can show how the temperature profile just before the next target microexplosion approaches a cyclic steady state. This is shown for HIBALL in Fig. 5.4-6. It is seen that the temperature almost converges after 3 cycles. The surface heat loads are shown in Fig. 5.4-7 as functions of time after a microexplosion for the case when the film has reached cyclic steady state. One should note that the radiation heat flux is dominant over the early part of the cycle but that when most of the condensation is occurring the condensation heat flux dominates. The average number density of the reactor cavity gas is shown in Fig. 5.4-8. The gas reaches 4×10^{10} atoms/cm^3 in about 0.2 s, allowing a 5 Hz repetition rate.

5.4.4 Work in Progress and Conclusions

The model described above predicts that HIBALL-II may operate at a 5 Hz repetition rate. In this model, the radiation heat flux on the first row of INPORT tubes is assumed to be unaffected by the condensation process -- a significant assumption since the radiation heat flux dominates the total surface heat flux shortly after the target microexplosion. Among other things, it is also known that calculations of the mass flow rates are possible which include the effects of non-Maxwellian velocity distributions and the presence of noncondensable gases.

A considerable amount of work has taken place since the HIBALL-I report was published on improving the models and calculational tools for studying condensation and evaporation phenomena in ICF reactor cavities. A major part of this is the development of the CONRAD computer code. This code simultaneously simulates the dynamics of the reactor cavity gas, the radiation spectrum and surface heat load, heat transfer in the film and mass transfer between the gas and the film. A separate effort has been ongoing to study the effect of noncondensable gases on the condensation with a kinetic theory formalism[8] that has shown the condensation rate to be lowered by such noncondensables. A third independent effort has uncovered better expressions for the mass transfer rates as functions of gas density and temperature and surface temperature.[9] In the near future, these will be all combined to allow more accurate calculation of the repetition rate.

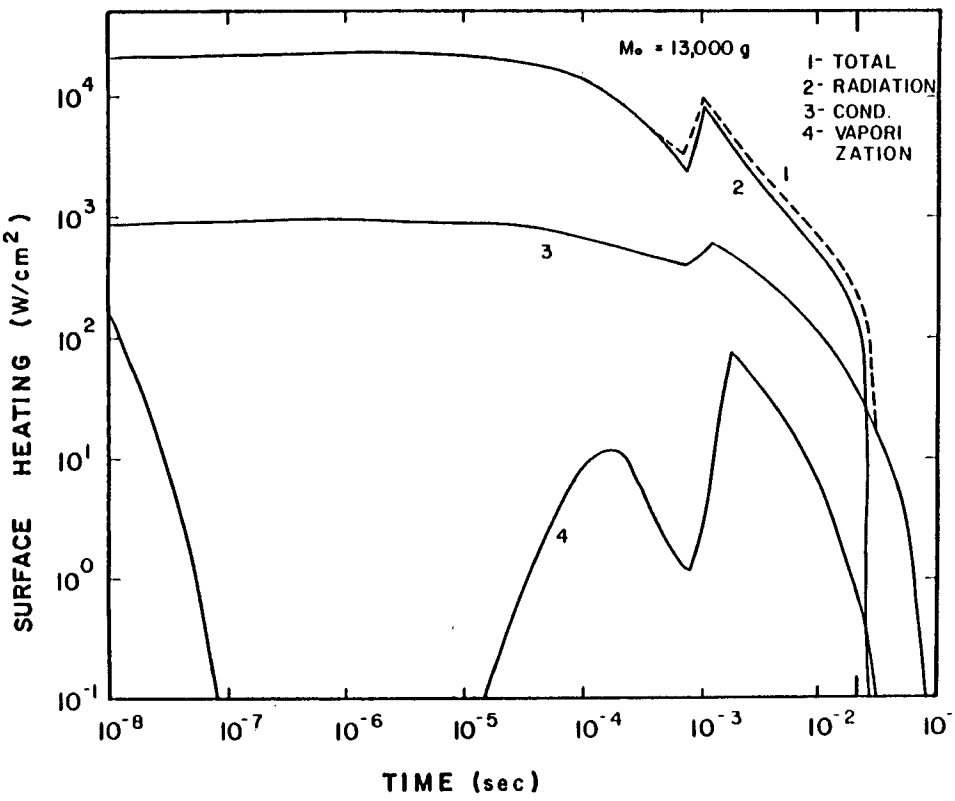

Fig. 5.4-7. First surface heat flux. Mass of vaporized gas = 13,000 g.

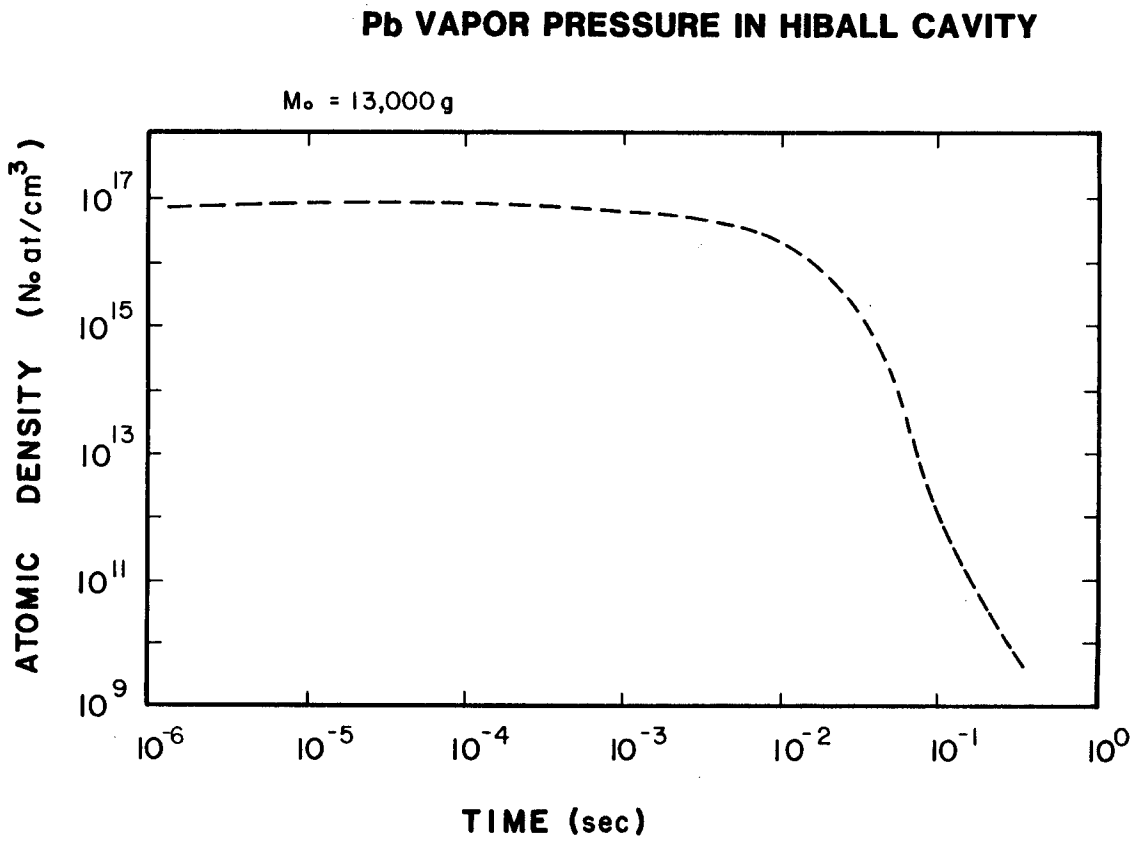

Fig. 5.4-8. Atomic density in cavity versus time. Mass of vaporized gas = 13,000 g.

Since these new tools are in a developmental stage, they have not been applied directly to the HIBALL-II case. The present best estimate of the repetition rate remains at 5 Hz.

References for Section 5.4

1. J. Martinez-Sanchez, private communication.

2. G. Moses et al., "High Gain Target Spectra and Energy Partitioning for Ion Beam Reactor Design Studies," University of Wisconsin Fusion Technology Institute Report UWFDM-396 (November 1980).

3. F. Biggs and R. Lighthill, "Analytical Approximation for X-Ray Cross Sections II," SC-PR-71-0507, Sandia Laboratory, Albuquerque, NM, December 1971.

4. T.O. Hunter and G.L. Kulcinski, "Description of the Response of Reactor First Walls to Pulsed Thermonuclear Radiation (Part I)," University of Wisconsin Fusion Technology Institute Report UWFDM-196 (March 1977).

5. A.M. Hassanein, Ph.D. Thesis, University of Wisconsin (1982).

6. T.J. McCarville, R.R. Peterson and G.A. Moses, "Improvements in the FIRE Code for Simulating the Response of a Cavity Gas to Inertial Confinement Target Explosions," Computer Physics Communications 28, 367 (1983).

7. R.R. Peterson and G.A. Moses, "MIXERG - An Equation of State and Opacity Computer Code," Computer Physics Communications 28, 405 (1983).

8. L. Pong and G.A. Moses, "Vapor Condensation in the Presence of a Noncondensable Gas," University of Wisconsin Fusion Technology Institute Report UWFDM-565 (July 1984).

9. D.A. Labuntsov and A.P. Kryukov, "Analysis of Intensive Evaporization and Condensation," J. Heat Mass Transfer 22, No. 7, 989-1002 (1979).

5.5 Vacuum System

5.5.1 General Description

The previous section described the behavior of the LiPb vapor in the cavity after each shot. The present section will deal with the noncondensable fraction of the gas load within the cavity, namely D_2, T_2 and He. An attempt to assess the effect of the LiPb vapor on the vacuum systems for the cavity and the beam lines will be made.

The equilibrium pressure of the noncondensable fraction has to be maintained reasonably low, although its effect on beam propagation is not as great as LiPb at the same number density. Furthermore, the noncondensable partial pressure has to be kept low because it provides a continuous source of molecules migrating into the beam lines where the pressure must be kept at $\sim 10^{-7}$ torr.

Most of the recent fusion reactor design studies have utilized compound cryopumps for pumping hydrogen and helium. In these pumps, hydrogen species are condensed on chevrons cooled to ~ 15 K while the helium is cryotrapped on molecular sieves attached to panels which are at 4.2 K. Typically these pumps have speeds of ~ 5 ℓ/s cm^2 for D_2, T_2 and ~ 2 ℓ/s cm^2 for He. A major disadvantage of any cryopump is the need for periodic regeneration. This is done by valving the pump off and warming up the cryosurfaces. Although regeneration may only take ~ 20-30 min, during this time the pump is not available for operation. Some designs have resorted to providing twice as many pumps as needed, such that only half are online at any one time. This is not space efficient, particularly where there are space limitations. In several past designs the University of Wisconsin group has proposed the use of back to back cryopumps where two sets of cryopanels, with integral baffles and chevron shields are provided. While the front panel is in use, the rear panel is being regenerated and the pump body itself constitutes the shutoff valve. Although some development work will be needed to perfect the seals for such a pump, we feel that it holds the promise for substantially increasing the pumping capacity in systems which are space limited. Such pumps are proposed for the present study.

In the HIBALL design, vacuum ports have been provided at the junction between the upper blanket modules and the top of the INPORT tubes. There are 30 ports 65 cm high and 120 cm wide, connected to rectangular ducts of the same dimensions, leading to cryopumps located in the upper corners of the

cavity as shown in Fig. 5.1-4. These pumps are well out of the radiation field and Monte Carlo analysis has shown that the effect of neutron streaming on them is negligible.

5.5.2 Pumping of Noncondensable Species

Table 5.5-1 gives the source and species of the noncondensable gas load. The vacuum ducts are assumed to be about 400°C in order to condense any LiPb vapor that they admit. At this temperature the throughput is:

$$D_2 = 108 \text{ torr} \cdot \ell/s$$
$$T_2 = 89 \text{ torr} \cdot \ell/s$$
$$He = 110 \text{ torr} \cdot \ell/s$$

The conductance of a short duct ($L < 25$ r) for molecular flow is given by the relationship:[3]

$$\frac{1}{C_{duct}} = \left(\frac{3}{16}\frac{LU}{A^2} + \frac{1}{A}\right)\sqrt{\frac{2\pi M}{RT}}\frac{s}{cm^3}$$

where C_{duct} is the conductance of the duct in cm^3/s, L the length in cm, A the cross-sectional area in cm^2, U the perimeter in cm, M the molecular weight in g, R the gas constant (8.3×10^7 ergs/mole) and T the temperature in degrees Kelvin.

For the given duct area of 65×120 cm^2, L = 450 cm, M = 5 for D_2T_2 and taking T = 673 K we get for the 30 ducts:

$$C_{D_2T_2} = 2 \times 10^6 \ \ell/s$$
$$C_{He} = 2.2 \times 10^6 \ \ell/s \ .$$

The area available for locating the cryopumps is ~ 85 m^2 and the utilization factor for back to back pumps is ~ 85%. The total pumping speeds (using 5 ℓ/s cm^2 for D_2, T_2 and 2 ℓ/s cm^2 for He) are then:

$$S_{D_2T_2} = 3.6 \times 10^6 \ \ell/s$$
$$S_{He} = 1.44 \times 10^6 \ \ell/s \ .$$

Table 5.5-1. Gas Load on Cryopumps

Source	Species	Atoms/Shot	Total (atoms/shot)
Target Injector	D	2.83×10^{20}	
Unburned Fuel	D	3.4×10^{20}	6.23×10^{20}
Unburned Fuel	T	3.4×10^{20}	
Newly Bred	T	1.76×10^{20}	5.16×10^{20}
DT Reaction	He	1.4×10^{20}	
T_2 Breeding	He	1.76×10^{20}	
T_2 Decay	He	1.9×10^{11}	3.16×10^{20}

The effective pumping speed is obtained from:

$$\frac{1}{S_{eff}} = \frac{1}{S_p} + \frac{1}{C_{duct}}$$

where S_p is the pump speed and C_{duct} the conductance of the ducts. The effective pumping speed is then:

$$S_{eff}\ D_2\ T_2 = 1.3 \times 10^6\ \ell/s$$

$$S_{eff}\ He = 8.7 \times 10^5\ \ell/s\ .$$

Using the throughputs obtained earlier, the equilibrium pressures of the noncondensable species in the cavity at 400°C are:

$$P_{D_2T_2} = \frac{(108+89)\ \text{torr}\ \ell/s}{1.3 \times 10^6\ \ell/s} = 1.5 \times 10^{-4}\ \text{torr}$$

$$P_{He} = \frac{110\ \text{torr}\ \ell/s}{8.7 \times 10^5\ \ell/s} = 1.3 \times 10^{-4}\ \text{torr}\ .$$

The equivalent pressure rise/shot at 400°C consistent with a cavity volume of 900 m^3 is 4.4×10^{-5} torr for D_2T_2 and 2.5×10^{-5} torr for He. The time needed to evacuate the chamber to the equilibrium pressure is given by:

$$t = \frac{V}{S_{eff}} \text{Ln} \frac{P_1}{P_2}$$

where t is the time, V the cavity volume, S_{eff} the effective pumping speed, P_1 the pressure in the cavity after a shot and P_2 the equilibrium pressure. For both D_2, T_2 and He, it is found that the time needed to reach equilibrium pressure is less than 200 ms. Thus, from the standpoint of reconditioning the chamber with respect to the noncondensable species, a repetition rate of 5 Hz is reasonable.

5.5.3 Effect of LiPb Vapor on the Vacuum Ducts

It was mentioned earlier that the walls of the vacuum ducts will be maintained at 400°C. At this temperature, the surfaces are essentially black to LiPb vapor, and will condense it immediately upon contact. There will not be a boundary layer developed and the vapor will obey molecular flow conditions. For this reason all the LiPb vapor which enters the vacuum ducts will be condensed before it reaches the cryopumps. Since it will be maintained molten, the LiPb will be returned to the cavity and will rejoin the bulk of the breeding material. The chevrons in front of the cryopumps are cooled to ~ 70 K with liquid N_2 and will certainly cryotrap any itinerant LiPb molecules before they can contaminate the hydrogen and helium pumping surfaces.

5.5.4 Effect of Cavity Atmosphere on the Beam Lines

The beam lines' interface with the reactor cavity presents some unique problems to the beam line vacuum system. Because the pressure in the cavity during operation never gets below 10^{-4} torr, it represents a continuous gas load which is admitted into the beam lines. Beam stripping and charge exchange problems require that the beam line pressure be on the order of 10^{-7} torr. The storage rings themselves operate at vacuum on the order of 10^{-10} torr.

In the early stages of the study rotating shutters in the beam ports were proposed in order to minimize the influx of LiPb vapor into the beam lines. The chief concerns were the accumulation of LiPb on the beam ducts amounting to ~ 3 tonnes/day for the 20 beams, and the migration of the vapor deep into the beam line system due to viscous effects. A reassessment of this problem has lead to the conclusion that shutters may not be needed. There are two complementary developments which have led to this conclusion; they are:

1. If the beam duct wall temperature can be carefully controlled such that the condensed vapor runs off in liquid form and is returned to the cavity, then accumulation ceases to be a problem.
2. With a sticking coefficient of unity on the beam duct walls, the vapor does not develop a boundary layer and there are no viscous effects from the walls. Using molecular flow theory, it is evident that the expanding vapor which enters the beam port is immediately condensed on the walls. It can be shown that the pressure can fall two orders of magnitude per meter of beam line if the narrow dimension of the line is < 40 cm.

Although the problem of LiPb vapor in the beam line needs a more rigorous analysis before it can be put to rest, for the present it is assumed that the rotating shutters will not be needed.

The noncondensable species, however, will not condense on the beam line walls but will proceed further into the beam lines. The conductance of a beam line for D_2, T_2 and He at 673 K is estimated at ~ 125 ℓ/s which gives rise to a throughput of ~ 1.25×10^{-2} torr ℓ/s. For this gas load to be pumped at 10^{-6} torr requires a cryopump system with a capacity of 1.25×10^{4} ℓ/s, namely ~ 0.25 m^2 of cryosurface for each beam line. Differential pumping downstream from the main beam line pumping station will quickly reduce the pressure to the prescribed value of 10^{-7} torr and lower.

References for Section 5.5

1. B. Badger et al., "NUWMAK - A Tokamak Reactor Design Study," University of Wisconsin Fusion Technology Institute Report UWFDM-330, March 1979.

2. B. Badger et al., "WITAMIR-I, A University of Wisconsin Tandem Mirror Reactor Design," University of Wisconsin Fusion Technology Institute Report UWFDM-400, Sept. 1980.

3. H.A. Steinherz, "Handbook of High Vacuum Engineering," Reinhold Publishing Corporation, New York, 1963.

5.6 Steady-State Thermal-Hydraulic Analysis

The original design of HIBALL (designated HIBALL-I) was reviewed in this design study. The purpose of our work was to optimize the original design for HIBALL-II so that the repetition rate could be more easily achieved while minimizing the thermal hot spots on the INPORT tubes. For this work we used the original neutronic analysis in HIBALL-I and the same governing equations for mass and energy balances. The initial and boundary conditions used in the original analysis are presented in Table 5.6-1, with a conceptual picture of the cavity and INPORT tubes given in Fig. 5.6-1.

The first thing to notice is that there are actually two hot spot locations, one at the midplane of the front row of INPORT tubes and one at the outlet of the back row of INPORT tubes. This occurs because the lithium-lead breeder/coolant flow is split at the entrance to provide extra cooling of the front INPORT tubes. This extra cooling is needed to offset the high surface energy deposited on these tubes. To minimize this hot spot we have performed a simple optimization study where the flow split to the front tubes is reduced until the outlet temperature, T_3, at the back tube is reduced to a value below

Table 5.6-1. Initial Results for Steady State HIBALL Design

Repetition rate (N_p - Hz)	5
Total energy deposited per pulse (Q_{tot} - MJ)	509.5 MJ
Volumetric energy deposited per pulse (Q_v - MJ)	399.0 MJ
Surface energy deposited per pulse (Q_s - MJ)	110.5 MJ
Mass flowrate of LiPb ($\dot{m}_{tot}$ - kg/hr)	3.38 (10^8)
Original flowrate to front INPORT tubes ($\dot{m}_{FO}$ - kg/hr)	2.21 (10^8)
Inlet temperature of LiPb to cavity (T_{in} - K)	330°
Inlet temperature for back tubes (T_2 - K)	398.6°
Outlet temperature for back tubes (T_3 - K)	579.3°
Inlet temperature for front tubes (T_{in} - K)	330°
Outlet temperature for front tubes (T_5 - K)	410°
Mean inlet for LiPb pool (T_{mean} - K)	468.3°
Outlet temperature of LiPb from cavity (T_{out} - K)	486.2°
Bulk LiPb temperature at hot spot location (T_4 - K)	370°
Average hot spot temperature for front tubes ($T_{hot\ spot}$ - K)	522.1°

Table 5.6-2. Summary of Optimization Study

m_F/m_{FO}	100%	85%	83%	80%
T_{in} (°C)	330	330	330	330
T_2	398.64	383.82	382.27	380.11
T_3	579.27	525.5	519.8	512.1
T_4	370.05	376.36	377.5	379.26
T_5	410.1	422.72	424.96	428.52
T_{mean}	468.27	468.27	468.77	468.27
$T_{hot\ spot}$	522.1	529.86	530.98	532.76
T_{out}	486.22	486.22	486.22	486.22
$T_{hot\ spot} - T_3$	-57.17	4.36	11.14	20.75

that of the front tube midplane hot spot value, $T_{hot\ spot}$. In HIBALL-II, to satisfy this requirement (Table 5.6-2), the front tube flow rate is altered to about 83% of the original value. This causes the hot spot at the front tube to rise only 8 degrees above its original value and assures that the back tube outlet temperature remains below it. The back tube outlet temperature T_3 is kept below $T_{hot\ spot}$ in the HIBALL-II design because vapor condensation is assumed to occur only in the front tubes. This assumption is conservative because it actually increases the hot spot temperature. In reality some vapor condensation will occur on the back tubes, which will raise T_3 and lower $T_{hot\ spot}$. This will tend to even out the small temperature differences between the two locations.

Figure 5.6.1

CONCEPTUAL PICTURE OF HIBALL CAVITY

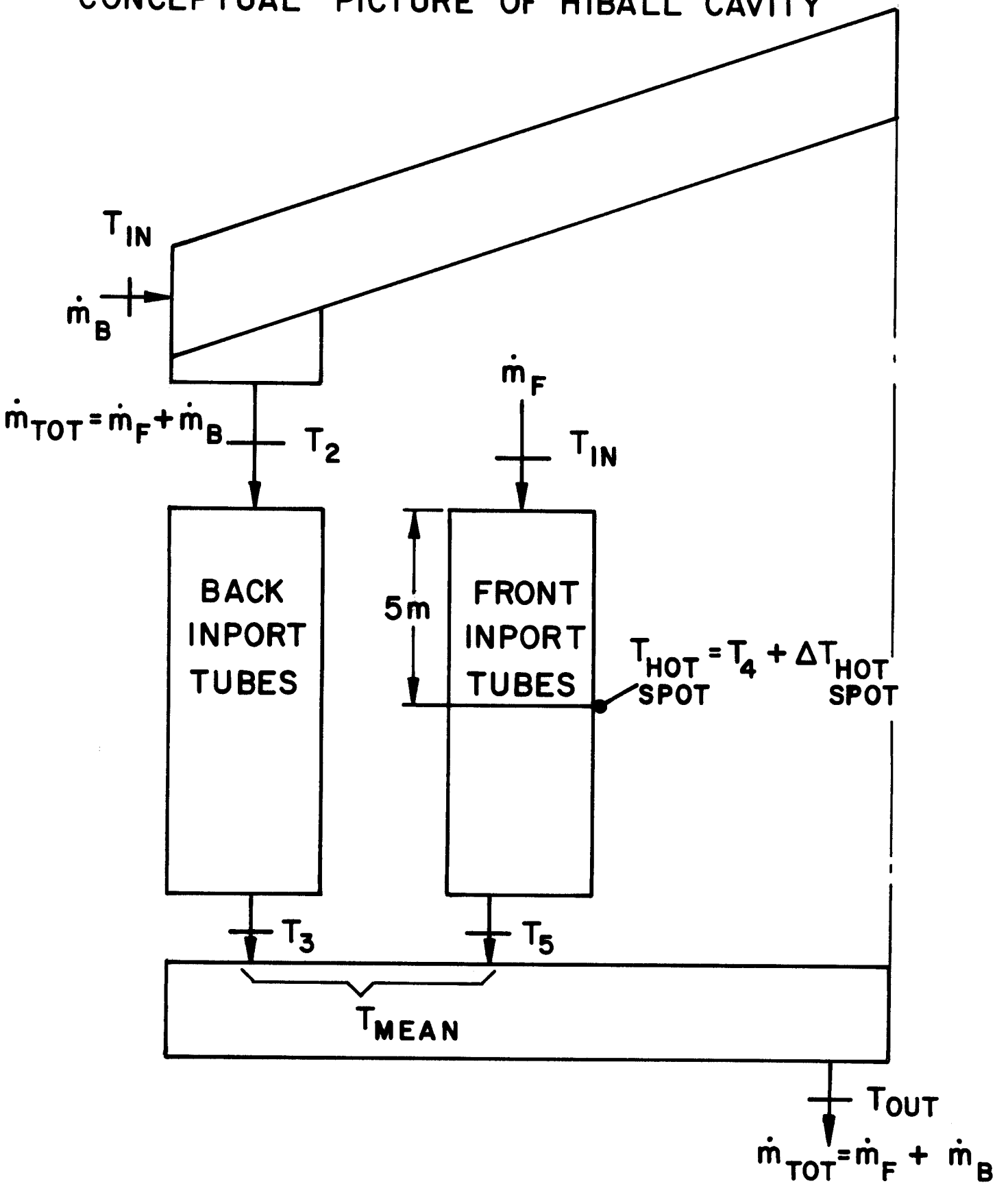

5.7 Support Mechanism and Static Stress Considerations

5.7.1 General Description

The SiC tubes are designed to be suspended from the top on a support plate which also is the coolant distribution manifold. Restraint against lateral motion is provided by a support plate on the bottom which also contains the flow control nozzles. Several schemes for attaching the INPORTs to the support structure were considered. One is shown in Fig. 5.2-1.

The cylindrical blanket zone is divided into 30 modules, each subtending 12° of cavity circumference. Each module consists of the upper distribution manifold and tube support plate, the tubes themselves and the bottom support plate.

The first two rows of tubes are 4 cm apart and consist of 3 cm diameter tubes spaced at ~ 5.1 cm center to center. The remaining tubes are 10 cm in diameter, follow behind and are arranged on a 12.5 cm triangular pitch in between support struts.

The upper tube support plate is welded to struts which are anchored into the 40 cm thick reflector wall. The sections at the end of each strut slide into milled slots in the reflector. Pulling up on the upper manifold, which is part of the tube support plate, disengages the module from the reflector. Figure 5.7-1 shows a top and side view of a single module support structure (holes in the plate have been omitted for clarity).

5.7.2 Tube Support

The tube distribution between two struts is shown in Fig. 5.7-2(a) and the loading on the plate in Fig. 5.7-2(b). The upper support plate was modeled as a statically indeterminate beam of varying cross sections and concentrated loads. Using a maximum design stress of 70 MPa (10 ksi) for HT-9, a plate thickness of 3 cm was calculated.

Similarly, the struts were analyzed as cantilevered beams of varying cross section and a distributed loading as shown in Fig. 5.7-3. The weight of the tubes is reacted by a moment on the tee sections and an upward force exerted by the reflector. For a design stress of 70 MPa and a strut thickness of 3 cm, we calculate h equal to 70 cm.

5.7.3 INPORT Tube Static Stresses

The static stresses in the SiC tubes can be divided into two parts, longitudinal and circumferential. Circumferential stresses are from the pressure of the coolant and vary linearly from the top to the bottom. The

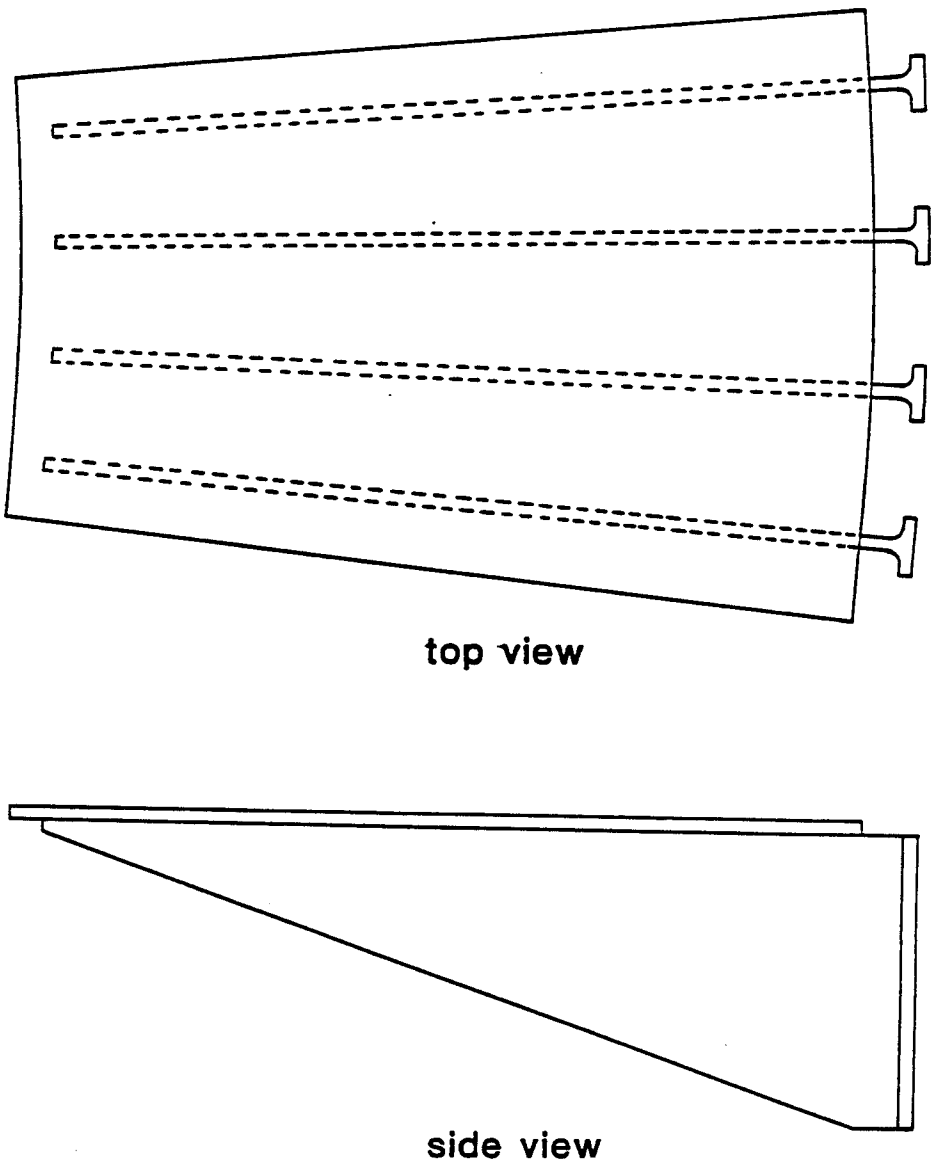

Fig. 5.7-1. Top and side views of upper support plate and strut.

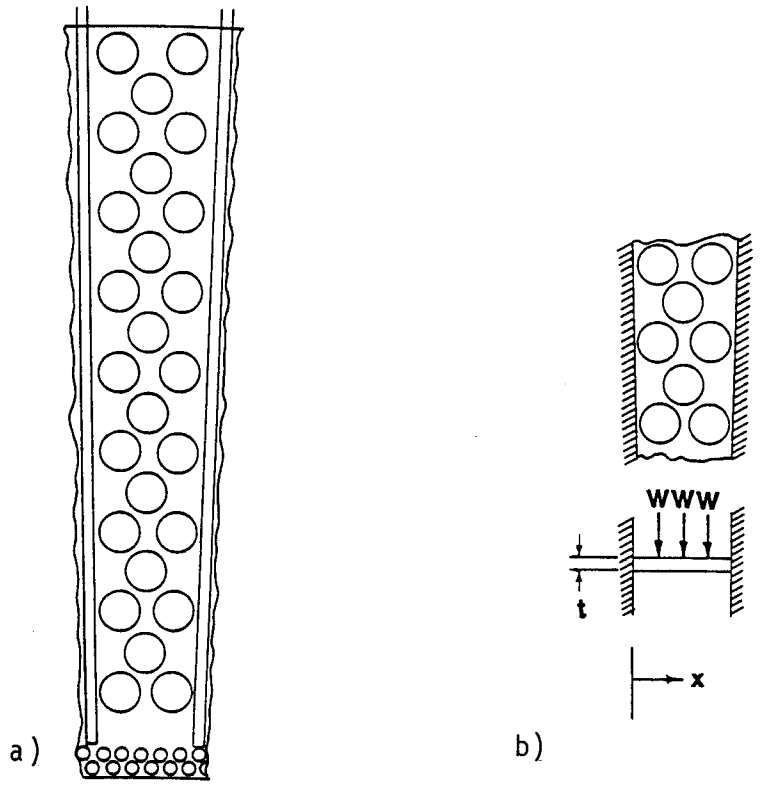

Fig. 5.7-2. a) Tube distribution between support struts.
b) Loads on upper support plate.

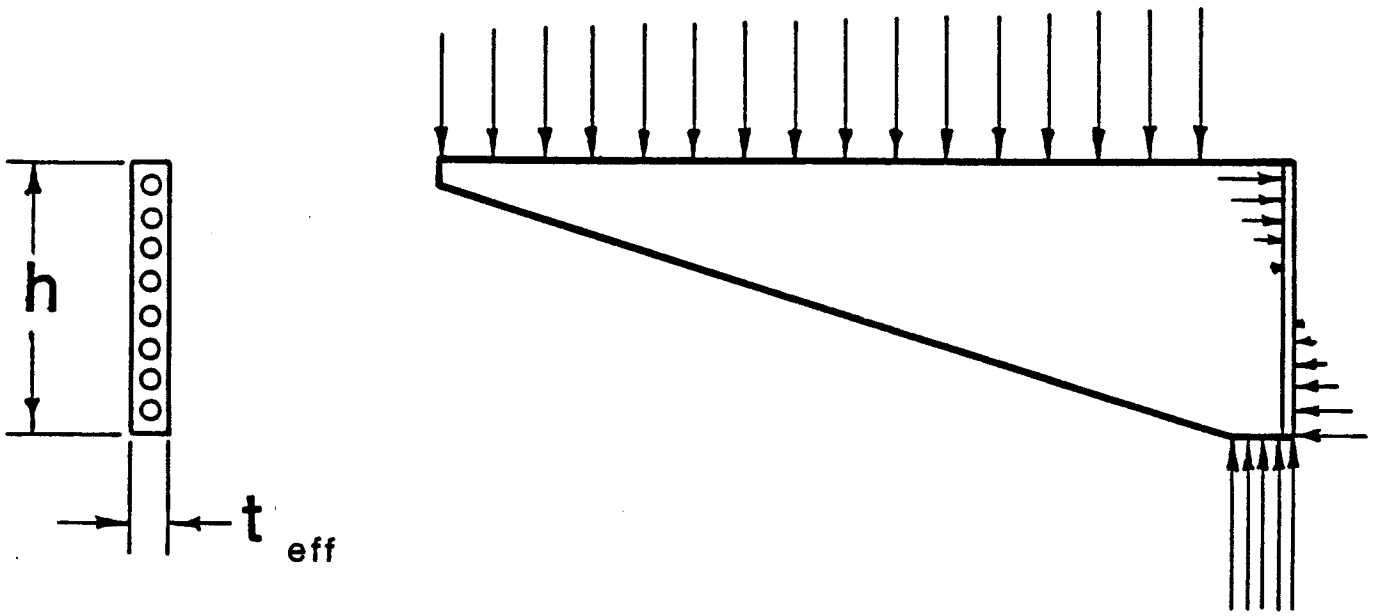

Fig. 5.7-3. Loading and reactions on support strut.

longitudinal stresses are due to the dead weight (weight of the coolant) and are maximum at the top, falling off linearly to zero at the bottom.

A reliable value for allowable stress is not known for braided SiC tube construction; however, estimates can be made based on experience with other composite materials. Various sources give SiC fiber strength of 2450-3720 MPa (355-540 ksi). Experience with graphite material systems indicates that the strength for orthogonal layup could be ~ 276 MPa (40 ksi) considering each principal stress individually. Ceramic materials have a wide variation in strength due to their extreme sensitivity to minute flaws, consequently a safety factor of two was taken giving an allowable stress of 139 MPa (20 ksi).

In this design the wall thickness is 2.25 mm for the 10 cm diameter tubes and 0.9 mm for the 3 cm diameter tubes. This means that there will be 5 plies and 2 plies in the 10 cm and 3 cm diameter tubes respectively (the thickness per ply is 0.45 mm). The fibers in the orthogonal layup are at 45° and cover 50% of the surface area. The fibers themselves have a density factor of 75%.

In calculating the stresses, it was assumed that the incoming coolant had an initial pressure of 0.1 MPa (~ 15 psi). At the bottom of the tubes the added head produces a pressure of 1.04 MPa (150 psi). The masses supported by the tubes are 700 kg and 61 kg for the 10 cm and 3 cm diameter tubes, respectively. Stress distribution as a function of tube distance from the top is shown in Fig. 5.7-4 and Fig. 5.7-5.

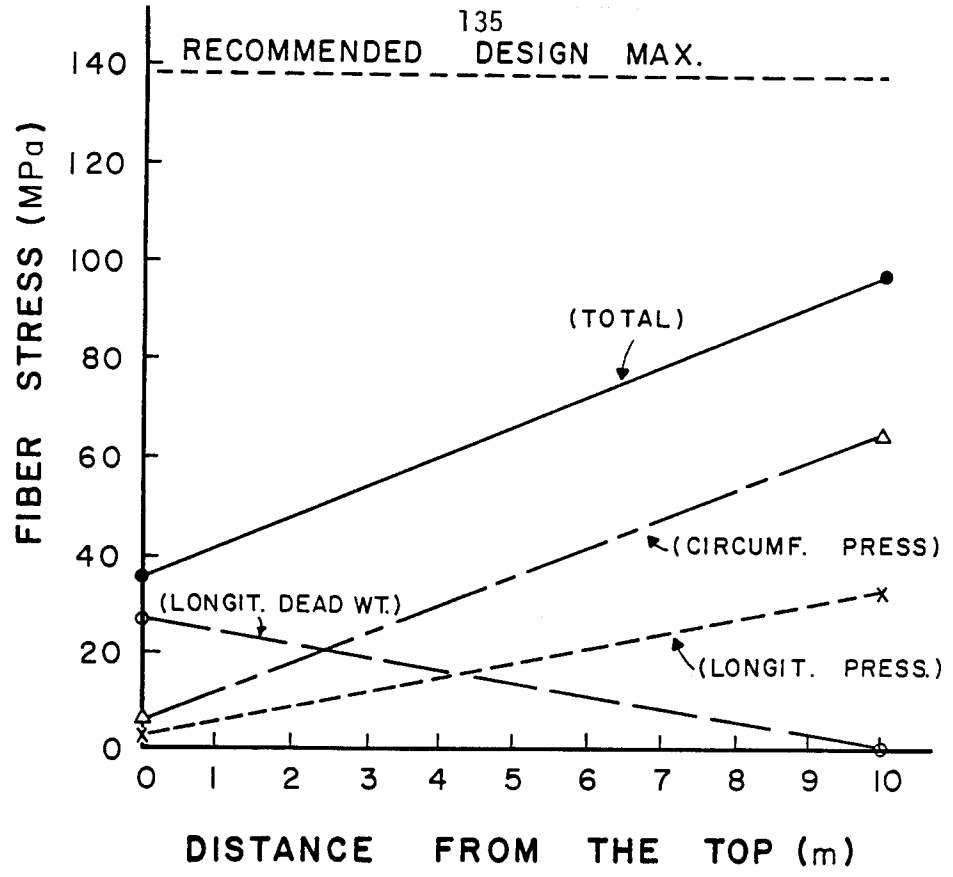

Fig. 5.7-4. Stresses in 10 cm diameter INPORT tubes.

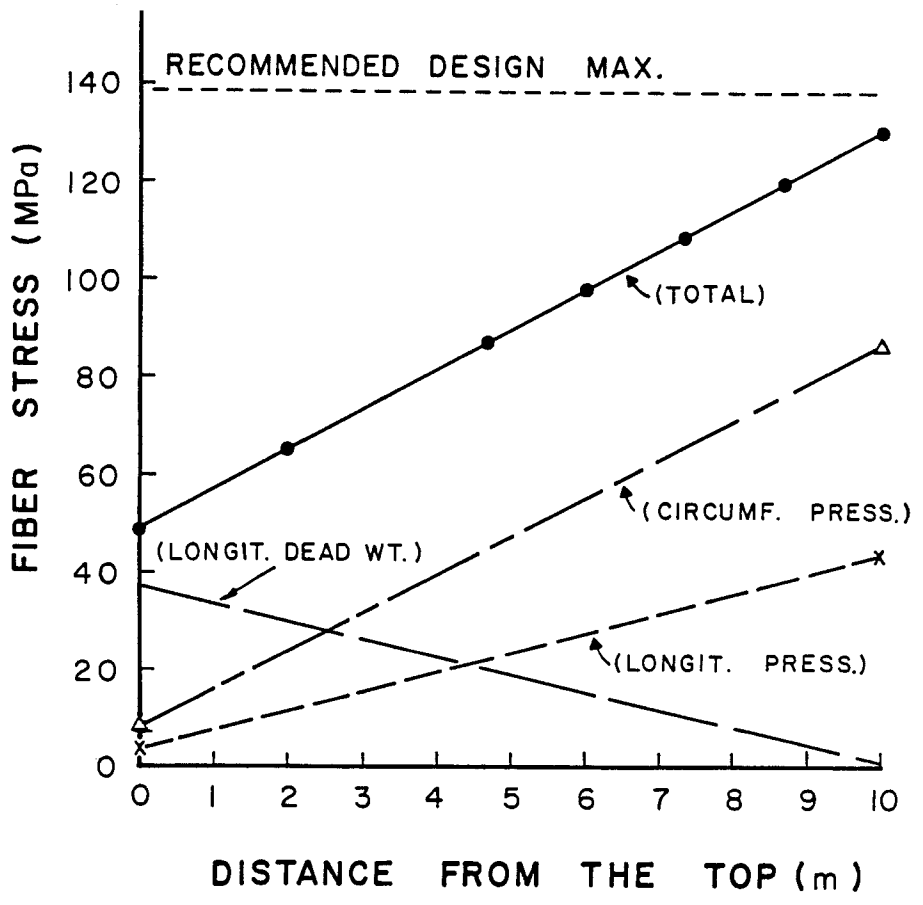

Fig. 5.7-5. Stresses in 3 cm diameter INPORT tubes.

5.8 Upper Blanket

5.8.1 Overall Design Description

The design of the upper part of the cylindrical chamber has to conform to several basic requirements which are:

1. The provision of a wetted surface similar to the INPORT units.
2. A design which gives easy access to the inside of the chamber.
3. Incorporation of removable modules for maintenance.

To this end, the upper part of the blanket is divided into 30 identical modules which is equal to the number of modules in the radial blanket. The modules are wedge shaped as shown in Fig. 5.8-1, 680 cm long and 140 cm wide at the rear. The radial and the upper modules coincide vertically, such that when an upper module is removed, the radial module immediately below it can be taken out through the empty space thus provided.

In this design, the upper module consists of several frames of rigidized SiC covered by porous SiC cloth and bolted together. The coolant enters in at the back of the module, flows radially toward the center of the cavity through the upper channels shown in Fig. 5.8-1, then passes through holes into the lower part of the module and flows radially outward. Some of the coolant permeates the porous SiC cloth and provided the needed wetted surface. The bulk of the coolant, however, remains within the module finally exiting it at the back and merging with coolant flowing through the rear tubes of the radial modules.

Section 5.8.2 describes the procedure for selecting four lobes of SiC cloth for each upper module. The maximum radius of curvature of each lobe at the rear is 16.3 cm. Each segment is connected to a single support plate which in turn is used to attach the module to the roof structure. The module frames have thin perforated semicircular lower membranes which prevent the SiC fabric from excessive deflection and also provide damping of shock waves transmitted through the coolant. The four segments terminate in a single rear exit which funnels the coolant into the back tubes of the radial module.

Support of the upper modules is difficult for several reasons. The 50 cm column of LiPb in the modules is quite heavy; furthermore, the maintenance scheme assumes that the upper reflector/shield can be rotated during routine replacement of cavity components. In this design, the inner end of the support plate to which the blanket modules are attached rests on a hub which can be rotated with respect to the reflector/shield assembly. Thus, when the

Fig. 5.8-1

DESIGN OF AN UPPER BLANKET SEGMENT

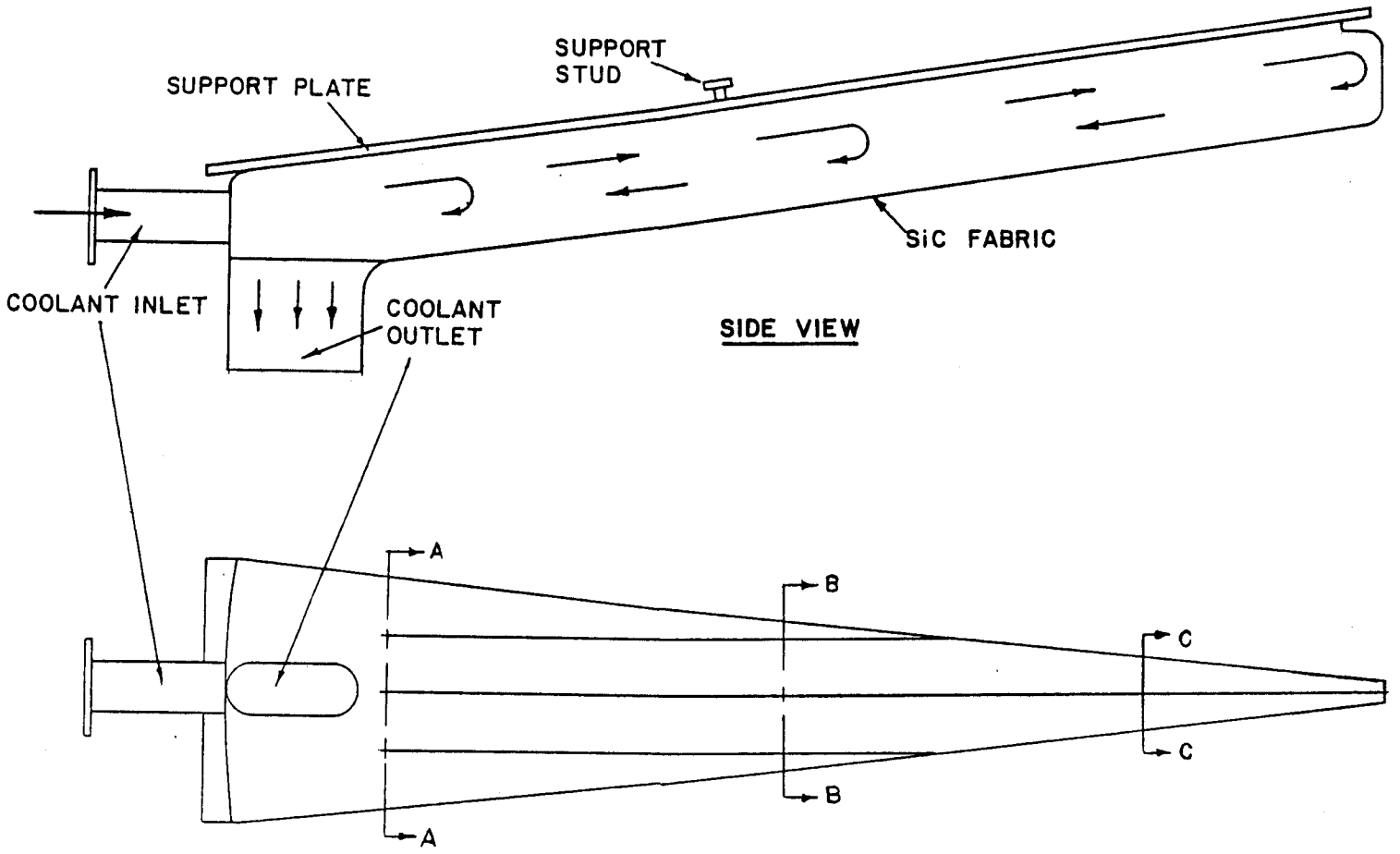

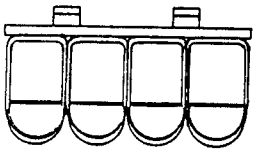

SECTION A-A

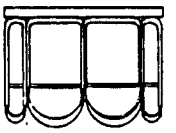

SECTION B-B

SECTION C-C

reflector/shield assembly is rotated for maintenance, the hub remains stationary. The rear end of the support plate rests on a ledge which is an extension of the cylindrical reflector. Along the length of the module, the support plate is attached to the upper reflector at several appropriate radial locations. These support studs are mechanically latched to the upper reflector during reactor operation. During reactor maintenance, when the coolant is drained out of the whole cavity, the mechanical latches are decoupled, such that the upper reflector/shield assembly can be rotated, while the upper blanket modules remain stationary. Table 5.8-1 gives the parameters of the upper blanket modules.

5.8.2 Stress Analysis of Upper Blanket Covering

The original shape of the upper blanket fabric covering was a partial conical shell with an internal pressure which varied linearly from 2 psi (0.0138 MPa) at the vertex to 20.18 psi (0.139 MPa) at the base as indicated in Fig. 5.8-2. The inclined length along the frame is 610 cm and the horizontal base width (chord) is 130 cm.

The most highly stressed area is at the bottom center (base) of the conical shell. The circumferential and axial stresses are denoted by σ_ϕ and σ_x, the former being the larger of these two principal values. The magnitude of σ_ϕ is strongly influenced by the local radius of curvature at the point under examination. For example a relatively shallow conical section with a

Table 5.8-1 Upper Blanket Design Parameters

Module Structural Material	SiC
Number of Modules	30
Length of Module (cm)	680
Length of Porous Cloth (cm)	610
Maximum Width of Module (cm)	140
Width of Porous Cloth Termination (cm)	130
Maximum Radius of Lobe (cm)	16.3
Number of Lobes/Module	4
Effective Thickness of Porous Fabric (cm)	0.1
Maximum Pressure on Fabric (MPa)	0.139
Maximum Hoop Stress on Fabric (MPa)	22.7

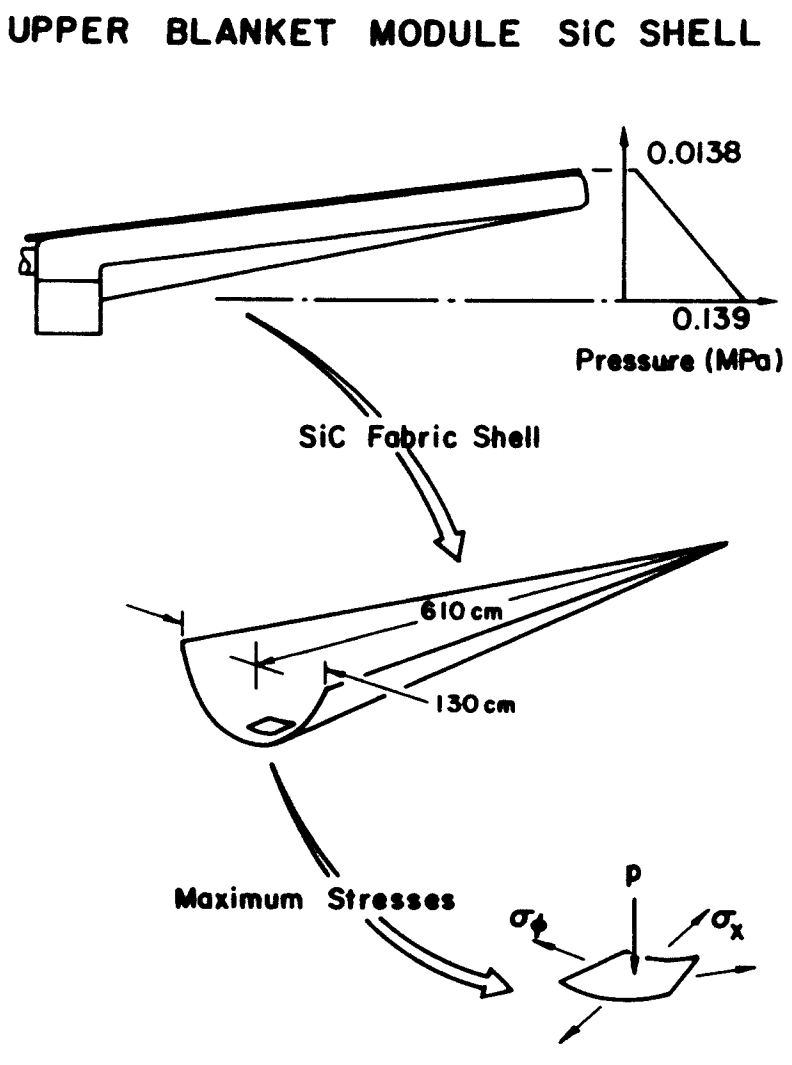

Fig. 5.8-2

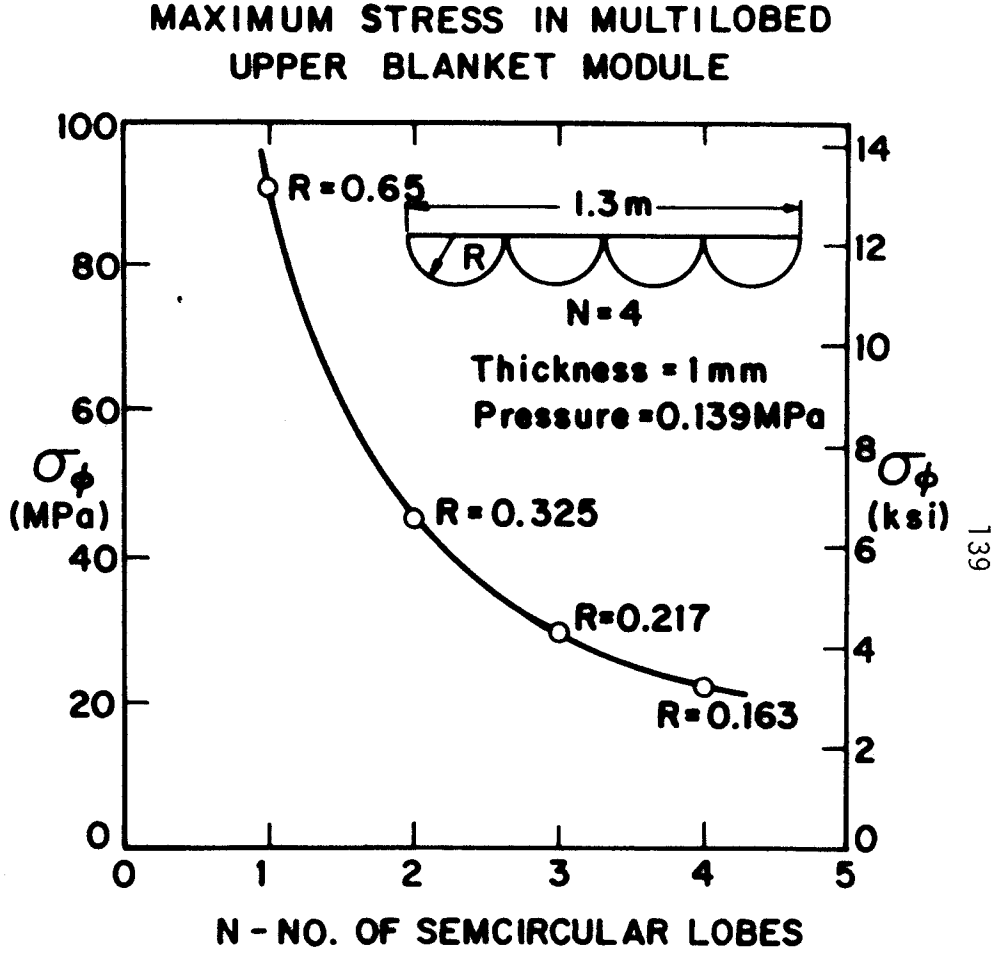

Fig. 5.8-3

drop of 25 cm has a radius of curvature of 97.1 cm and corresponding stress of 135.1 MPa. While the geometry is acceptable, the stress is too high for this application. The stress can be lowered by reducing the radius of curvature with the best configuration being semicircular. However, since the drop equals the radius of curvature for semicircular lobes (65 cm), this does not produce a practical design. A compromise to limit both stresses and the drop distance is a multilobe design. Results are shown in Fig. 5.8-3 for a fixed chord (130 cm), pressure (0.139 MPa) and material thickness (1 mm). From this data the four lobe configuration was selected and the mechanical design is based upon this geometric configuration.

6. TRITIUM

6.1 Introduction and Overview

This section describes the tritium systems of HIBALL -- the tritium pathways are summarized in Fig. 6.1-1 and the inventories in the various reactor components are given in Table 6.1-1. The four reactor chambers are fueled with multilayer targets containing 4.0 mg DT, which are fired at a rate of 5 s^{-1} per chamber. A one day fuel supply consists of 2.76 kg D and 4.15 kg T. The fraction of fuel burned is 0.29; thus, the unburned fuel, 1.97 kg/d of deuterium and 2.95 kg/d of tritium, must be handled by the exhaust system. In addition, 2.8 kg/d of D_2, the target injector propellant gas leaking into the cavity, and 1.5 kg/d of tritium bred by the $Li_{17}Pb_{83}$ will enter the exhaust processing system. The details of the target fabrication are unspecified. Some recommendations on possible techniques and the need to minimize the tritium inventory during target manufacture are discussed in Section 6.2.6.

The reactor chambers are evacuated by compound cryopumps with on-line times of 2 hours and a subsequent tritium inventory of 0.37 kg. The pumps are regenerated so that helium is released first, then the hydrogen isotopes are released and sent to the fuel cleanup unit. The purpose of the fuel cleanup unit (T_{INV} = 0.031 kg) is to remove impurities from the hydrogen isotopes before sending them to the cryogenic distillation unit. The distillation system consists of 4 columns (T_{INV} = 0.083 kg) which separate the isotopes into an H stream which is vented, a pure D_2 stream for the target injector, and a pure DT stream for the target factory and storage.

In the total blanket systems the low solubility of tritium in the $Li_{17}Pb_{83}$ alloy results in an inventory of 2.5 g T in the coolant (1.9×10^7 kg). Tritium is bred at a rate of 4.4×10^{-6} kg/s in each blanket and extracted from the reactor chamber by vacuum pumps operating with sufficient speed to maintain the vapor pressure of tritium above the eutectic at 10^{-4} torr. The tritium inventory in the silicon carbide tubes (1.6×10^4 kg) at 500°C is unknown, but has been estimated as 0.008 kg. The liquid metal protects the silicon carbide from interacting with the energetic hydrogen species in the debris from the imploded target; however, it is in intimate contact with tritium dissolved in the liquid metal which may result in chemical reactions.

The liquid metal coolant is circulated to the steam generator. Although the tritium pressure above the eutectic is only 10^{-4} torr, the permeation of

Table 6.1-1. HIBALL Tritium Inventory

Fuel cycle (kg):		
Cryopumps	0.37	
Fuel cleanup	0.031	
Isotopic separation	0.083	
Subtotal		0.484
Blanket (kg):		
$Li_{17}Pb_{83}$ (cavity and reflector)	0.003	
SiC tubes	0.008	
Subtotal		0.011
Target manufacture (kg):	4.1	4.1
Storage (kg):		
Targets	4.1	
Uranium beds	4.1	
Subtotal		8.2
TOTAL INVENTORY (kg)		12.795
TOTAL ACTIVE INVENTORY (kg)		4.595

Figure 6.1-1

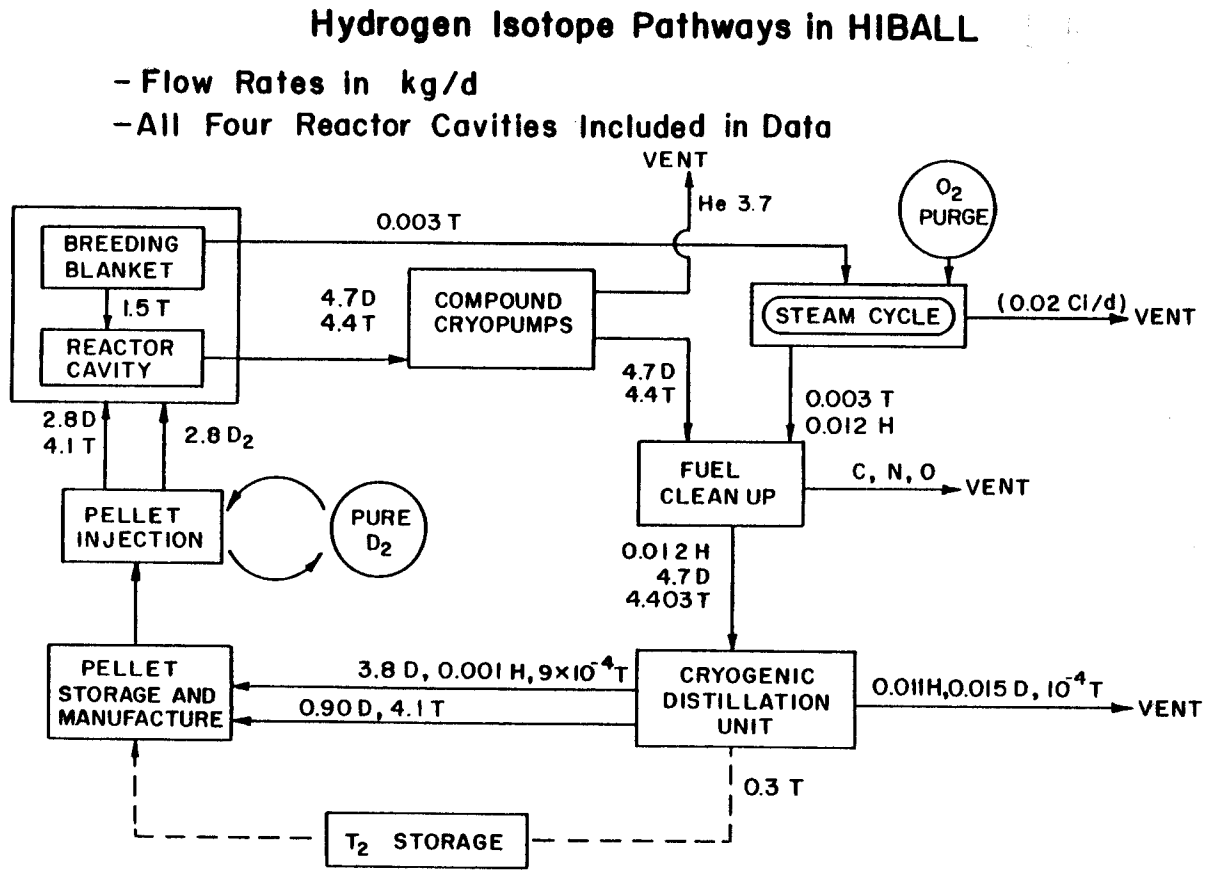

tritium through clean HT-9 could result in a loss of 33.3 g T_2/day to the steam cycle. Oxide coatings or other tritium barriers have been proposed to reduce the permeation by factors of 10 to 100. Additionally, a steam generator is proposed with double walled tubes in which the inner space is purged with an oxygen atmosphere. This could provide a very effective barrier limiting losses to less than 1 Ci/d. The tritiated water from the sweep gas is condensed and eventually merged with the reactor exhaust for reprocessing.

6.2 Fuel Cycle

Each reaction chamber is equipped with a target injection system and vacuum cryopumps. The exhaust streams from regeneration of the cryopumps of the four chambers are combined and sent into the fuel cleanup and processing system.

6.2.1 Fueling

The HIBALL reactor is fueled by injection of a cryogenic DT target. The target consists of three shells: the equimolar DT fuel, a Li-Pb ablator (Li:Pb mole ratio 18.1:1), and a lead outer shell as the high-Z component. The target composition is given in Fig. 6.2-1. The targets are injected at a velocity of 200 m/s with a target injection gun that also releases 1.6 mg of D_2 propulsion gas into the chamber per shot. The target is loaded into a plastic 2-piece carrier called a sabot. During injection, the sabot is shed into a buffer cavity and does not enter the reactor. Deuterium propulsion gas in the buffer cavity which does not reach the reaction chamber (139.4 mg/shot) will be recycled periodically with the hydrogen isotopes.

The choice of lithium and lead for target materials is favorable because they are compatible with the $Li_{17}Pb_{83}$ liquid wall. Debris from the target shells will dissolve in the liquid wall. In Table 6.2-1 the change in blanket composition with time is shown. Since the ratio of Li:Pb in the target is greater than in the eutectic (17:83 atom%), the ratio of Li:Pb in the blanket slowly increases with time. As a result of these additions, according to the phase diagram,[1] the melting point of the alloy increases ~ 14°C/yr; therefore, quantities of lead will have to be added and properly mixed to maintain the eutectic composition.

The fractional burnup (f_b) of the target is given by $f_b = T_b/(T_b + T_p)$, where T_b is the amount of tritium burned per day and T_p is the unburned tritium fuel that must be pumped out of the chamber per day. In the HIBALL reactor the fractional burnup is 29% which is comparable to other ICF reactor systems

Layer	Materials	Weight (mg)	Atoms x 10^{20}	Density g/cm^3	Thickness mm
3	Pb	288	8.34	11.3	0.245
2	Li Pb	26 41	22 1.2	1.26	0.739
1	D T	1.6 2.4	4.8 4.8	0.21	0.477

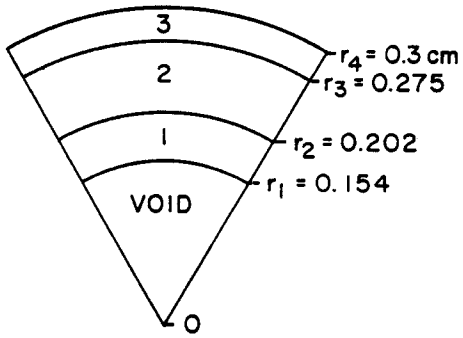

Fig. 6.2-1 HIBALL pellet composition.

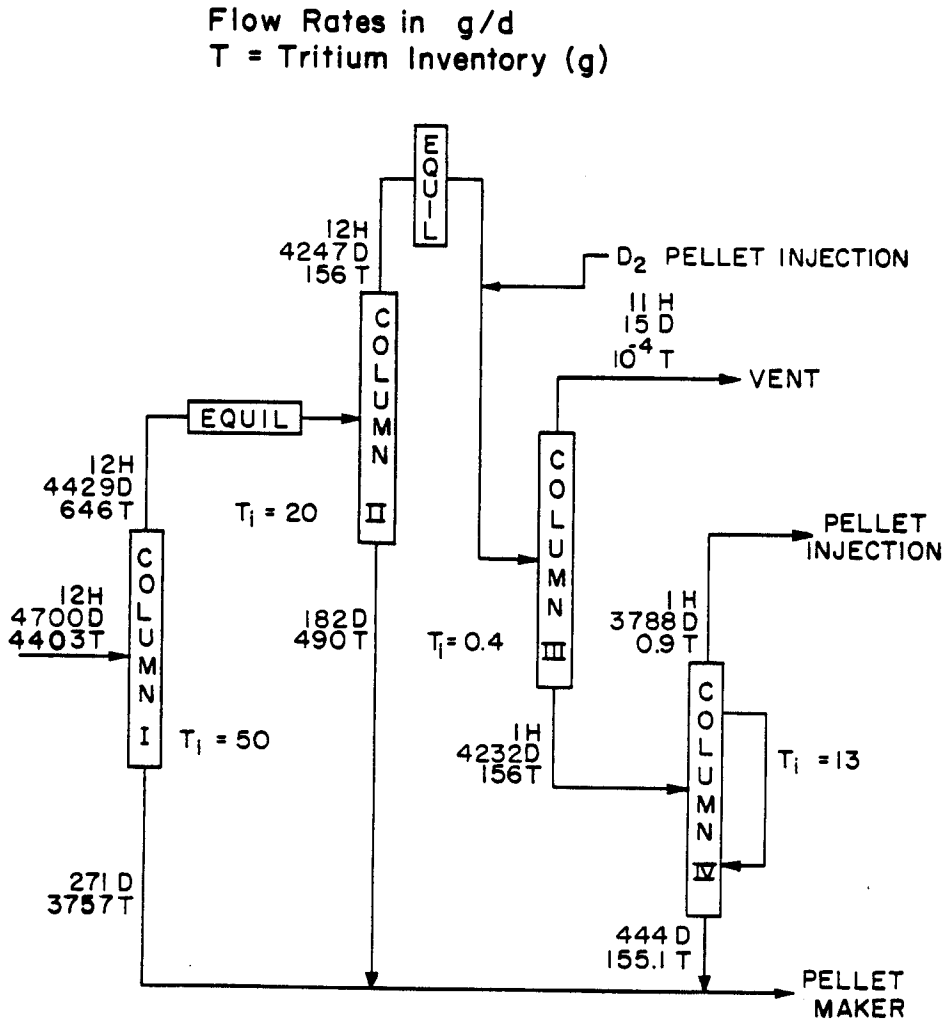

Fig. 6.2-2 HIBALL Isotope Separation Unit.

Table 6.2-1. Change in $Li_{17}Pb_{83}$ Composition with Time

Mass Changes

	TARGET		Reactions	Li
	Pb (kg)	Li (kg)	Li(n,α)T (kg)	(Net)* (kg)
1 shot	3.29×10^{-4}	2.65×10^{-5}	2.03×10^{-6}	2.45×10^{-5}
1 day	142	11.4	0.877	10.5
1 year	5.18×10^{4}	4.16×10^{3}	320	3.84×10^{3}

*Li (net) = Li (target) - Li (reactions)

	Composition Changes		
	Original blanket	1 year operation	% change
Mass Li (kg)	3.26×10^{4}	3.64×10^{4}	11.8
Mass Pb (kg)	4.74×10^{6}	4.79×10^{6}	1.09
Ratio Li:Pb	0.205	0.228	
Formula	$Li_{17}Pb_{83}$	$(Li_{18.6}Pb_{81.4})$	

(20-40%).[2] At this point there has been no consideration of the possibility of misfirings. The fusion power desired requires the consumption of 1.2 kg T/d and 0.8 kg D/d.

The target injection rate of 5 s^{-1} per chamber requires 1.73×10^{6} targets/day, which deliver 4.1 kg T/d and 2.8 kg D/d. In addition, 2.8 kg D_2/d enter the chamber if pneumatic pellet injection is used (Section 2.3.2). The details of the target fabrication have not been developed at this time; however, the effects of target manufacture on the tritium inventory are discussed in Section 6.2.6.

6.2.2 Exhaust

Each fusion event will cause a pressure rise in the chamber as Li-Pb is evaporated from the walls and gases from the D-T reaction and unburned fuel are released. The major components present in the exhaust are given in Table 6.2-2. Between fusion events, the chamber must be evacuated to at least 10^{-4} torr, as higher pressures will cause interference and scattering of the ion

Table 6.2-2. Exhaust Gas Composition

	mg/shot	kg/d[a]
Deuterium target (unburned)	1.13	1.95
Tritium target (unburned)	1.70	2.92
Helium (DT fusion)	0.93	1.61
Helium (breeder)	1.17	2.01
Tritium (breeder)	0.87	1.51
Li-Pb vapor[b]	0	0
D_2 target injection	1.6	2.8
TOTAL GASES	7.40	12.8
TOTAL TRITIUM	2.57	4.44

[a]All four cavities.

[b]Lithium and lead vapor will condense on cold surfaces before reaching cryopumps.

Table 6.2-3. Vapor Pressure of $Li_{17}Pb_{83}$ at 500°C

	Li	Pb
Activity	1.3×10^{-4}	0.81
Pressure (pure), torr	2.86×10^{-3}	1.69×10^{-5}
Pressure (above eutectic), torr	3.7×10^{-7}	1.4×10^{-5}

beams. The equilibrium vapor pressures of lithium and lead above $Li_{17}Pb_{83}$[3] are given in Table 6.2-3 and are less than the 10^{-4} torr pressure in the chambers; therefore, most of the vaporized liquid metal will recondense on the INPORT units. Any Li-Pb vapor that enters the vacuum or beam ports will condense on the cold duct surfaces and will not contaminate the cryopumps.

The bismuth from the ion beam is chemically similar to lead and will dissolve completely in the wetted wall with very little vaporization. After 20 years of operation the bismuth concentration in the liquid metal is still less than 1 wppm, much less than the typical natural Bi impurity in the lead used in the liquid alloy.

6.2.3 Cryopumps

The reactor chambers are evacuated with compound cryopumps, capable of pumping both the hydrogen isotopes and helium at the high volumetric flow rates required. For each chamber, this requires pump speeds of 2.7×10^6 ℓ/s for the hydrogen isotopes and 1.3×10^6 ℓ/s for He in order to maintain the cavity at 10^{-4} torr. The separation of hydrogen isotopes from helium on the cryosorption panels is extremely sharp.[4] By controlled heating, the helium panel is regenerated first, then the hydrogen isotopes are removed and sent to the fuel cleanup unit. The on-line time for the pumps is two hours and the tritium inventory in the pumps is 0.37 kg.

6.2.4 Fuel Cleanup

The exhaust from the cryopumps enters the fuel cleanup unit where hydrogen isotopes are separated from other gas impurities, chiefly hydrocarbons and silanes from reactions with the SiC. The fuel cleanup unit is patterned after the Tritium Systems Test Assembly (TSTA) designs.[5] Impurities are first adsorbed onto molecular sieve beds at 75°K while hydrogen isotopes flow into the distillation unit. These impurities are then recovered from the sieves and catalytically oxidized to form tritiated water and tritium free compounds. The tritiated water is condensed and electrolyzed to recover the tritium. For a flow rate of 360 mole/d of hydrogen isotopes TSTA has estimated an inventory in the fuel cleanup unit of 2.5 moles of hydrogen isotopes. In HIBALL the exhaust contains 734 moles T_2/d and 1175 moles D_2/d giving an inventory of 31 g of tritium.

6.2.5 Isotopic Separation Unit

Hydrogen isotopes from the fuel cleanup unit enter the cryogenic distillation system in the atomic ratio 12 H:2350 D:1467 T. The goals of the separation system are to separate and vent hydrogen, to form a purified D-T stream for the target manufacturing system and storage, and to form a pure D_2 stream for the target injection system. The separation scheme, patterned from the literature,[6,7] is shown in Fig. 6.2-2. The tritium inventory in the separation system is estimated as 83.4 g.

6.2.6 Tritium Considerations in Target Manufacture

The details of the target manufacturing system have not been addressed at this time; thus the tritium inventory in the target manufacturing process and the inventory that must be kept in storage as targets to insure production in case of a malfunction are unknown. This inventory will be dependent on:

(1) the number of targets produced per day;
(2) the time required to make a day's quantity of targets;
(3) the process used - batch or continuous; and
(4) the amount of tritium that must enter the recycling system due to rejection of targets that do not conform to specifications.

The fusion targets for HIBALL must be produced economically at a rate of 1.73×10^6/d. Three possible pathways for target production are outlined in Fig. 6.2-3. After selected steps in the manufacturing process, the product is examined to insure it meets certain specifications,[8] and at this point a number of targets may be rejected. If the rejected targets contain D-T, the fuel must be recovered and reprocessed. To minimize the tritium handling, the filling of the targets with DT fuel should come as late in the manufacturing process as possible or at least following steps with large rejection rates.

To minimize the tritium storage for the target manufacturing system, the time required to fill the targets with DT should be as short as possible. For instance, if the DT fuel is diffused into a hollow shell, the targets will be produced in a batch process and the fill-time will be dependent on the permeation rate of DT through the shell at temperatures below the shell melting point. In SOLASE[9] two target designs were examined. Plastic targets required a 1 day fill-time resulting in a one day fuel storage, while glass targets required a five day fill-time with a five day fuel inventory in storage. The technique of preforming the Li-Pb shell followed by diffusion of the D-T, as given in Path I and Path III in Fig. 6.2-3 is probably unreasonable because all of the Li in the shell would form a deuteride/tritide before any gas would penetrate the shell. The hydride formation from lithium[10] results in nearly a 30% volume decrease. Such a large volume change would most likely strain the shell so that it would crack and disintegrate.

While microdrilling of laser targets and parts has been achieved, [11] the filling and sealing process as proposed in Path I has not been demonstrated. Although the drill-and-fill process is continuous, requiring less tritium storage than batch processes, the high symmetry requirements of the target would probably result in a high rejection rate of improperly sealed shells and a significant amount of tritium recycle and recovery. Therefore, this option remains unproven.

Hollow hydrogen shells have been prepared by introducing a stream of gas bubbles into a controlled jet producing uniform hydrogen spheres.[12] Pre-

Figure 6.2-3

POSSIBLE PELLET MANUFACTURING SCHEMES

STEP	PROCESS	TRITIUM RECYCLE?	
1	FORMATION OF Li-Pb SHELL	NO	
2	DT FILL		
	(a) BATCH GAS DIFFUSION	YES	PATH I
	(b) CONTINUOUS DRILL, FILL & SEAL	YES	
3	Pb COATING	YES	
4	CRYOGENIC PROCESS		
1	FORMATION OF CRYO. DT SHELL	YES	
2	Li — Pb COATING	YES	PATH II
3	Pb COATING	YES	
1	FORMATION OF Li-Pb SHELL	NO	
2	Pb COATING	NO	
3	DT FILL		PATH III
	(a) BATCH GAS DIFFUSION	YES	
4	CRYOGENIC PROCESS		

sumably DT shells could be produced by the same technique, then coated with the Li-Pb shell followed by the lead overlayer. There are four major processes that have been developed for producing metallic coatings onto microspheres[13]: magnetic sputtering, electroplating, electroless plating, and chemical vapor pyrolysis. At present the sputtering technique seems to have the most general applicability. After the coatings are applied initial cooling of the target freezes the DT nonuniformly. By vaporizing the inner coating of fuel with a laser or heat pulse and quickly refreezing the DT, a uniform layer can be produced.[14,15]

Hendricks et al. proposed a process in which cryogenic spheres are transported past sputtering guns which apply consecutive layers onto the sphere.[8] A cold helium gas jet[16] could be used to keep the targets frozen and levitated as they pass the sputtering guns and quality control apparatus. This process is outlined in Path II. This method has the disadvantage of handling tritium throughout the process; however, there is no batch diffusion step requiring a large storage inventory. While the tritium reprocessing of imperfect D-T spheres would be minimal, the processing after the coatings are applied would require more sophistication. From a comparative standpoint, Path II is probably the superior method from tritium considerations, assuming the coatings can be applied to high standards requiring minimal tritium recycling.

Until the details of the target manufacturing system are known it will be assumed that one day's fueling supply (4.1 kg T) will be involved in the target manufacturing system.

6.2.7 Storage

The storage requirements for HIBALL include a one day supply of targets to fuel the reactor (4.1 kg T) and a one day supply kept on uranium beds to feed into the target manufacturing system. (This storage inventory will depend on the target manufacturing process as discussed in the preceding section.) The storage inventory of 8.2 kg T represents a large fraction of the total inventory.

References for Section 6.2

1. R. Hultgen, et al., "Selected Values of the Thermodynamic Properties of Binary Alloys, American Soc. for Metals, Metals Park, Ohio, 1973, pp. 1078-1079.

2. M.S. Ortman, E.M. Larsen, S.I. Abdel-Khalik, "A Study of the Tritium Handling Systems in Magnetic and Inertial Confinement Fusion Reactors With and Without Tritium Breeding," Nuclear Technology/Fusion 1, 255-274 (April 1981).

3. J.A. Blink, O.H. Krikorian and N.J. Hoffman, "The Use of Lithium in Fusion Reactors," Lawrence Livermore National Laboratory, Livermore, CA, UCRL-85145 (June 1981).

4. J.L. Anderson, "Design and Construction of the Tritium Systems Test Assembly," Proceedings Tritium Technology in Fission, Fusion and Isotropic Applications, Dayton, Ohio, April 29 - May 1, 1980, CONF-800427, American Nuclear Society (1980), 341-346.

5. E.C. Kerr, J.R. Bartlit and R.H. Sherman, "Fuel Cleanup System for the Tritium Systems Test Assembly: Design and Experiments," Proceedings Tritium Technology in Fission, Fusion and Isotropic Applications, Dayton, Ohio, April 29 - May 1, 1980, CONF-800427, American Nuclear Society (1980), 115-118.

6. J.L. Anderson and R.H. Sherman, "Tritium Systems Test Assembly Design for Major Device Fabrication Review," LA-6855-P, Los Alamos Sci. Lab (June 1977).

7. B. Badger et al., "WITAMIR-I - A Tandem Mirror Reactor Study," University of Wisconsin Fusion Technology Institute Report UWFDM-400, Chapter XI (Dec. 1979).

8. C.D. Hendricks, W.L. Johnson, "Power Production of Inertial Confinement Fusion Targets," Lawrence Livermore Laboratory, UCRL-52539, February 15, 1979.

9. R.W. Conn et al., "SOLASE, A Laser Fusion Reactor Study," University of Wisconsin Fusion Technology Institute Report UWFDM-220, Chapter IV (1977).

10. W.M. Mueller, J.P. Blackledge and G.G. Leborwitz, Metal Hydrides, Academic Press, New York, 1968, pp. 217-220.

11. B.W. Weinstein, C.D. Hendricks, J.T. Weir, "Laser Microdrilling in the Fabrication of Laser Fusion Targets," Lawrence Livermore Laboratory, UCRL-77406, October 15, 1975.

12. C.D. Hendricks, "Fabrication of Targets for Laser Fusion," Lawrence Livermore Laboratory, UCRL-76380, January 20, 1975.

13. S.F. Meyer, "Metallic Coating of Microspheres," Lawrence Livermore Laboratory, UCRL-84463, August 15, 1980.

14. R.L. Woerner and C.D. Hendricks, "Fabrication of Cryogenic Laser Fusion Targets," Lawrence Livermore Laboratory, UCRL-79442, September 27, 1977.

15. K. Kim and H. Rieger, "Fabrication and Characterization of Cryogenic Targets for Inertial Confinement Fusion," Dept. of Electrical Engineering, University of Illinois, Urbana, Report 1979, UCRL-15113 (1980).

16. W.L. Johnson, S.A. Letts, D.W. Myers, J.K. Crane, J.D. Illige, and C.W. Hatcher, "Plasma Processed Coating of Laser Fusion Targets," Lawrence Livermore Laboratory, UCRL-83000, September 19, 1979.

6.3 Blanket System

6.3.1 Solubility of Tritium in $Li_{17}Pb_{83}$

In order to determine the tritium inventory in the breeding material and the method of extraction, the solubility of tritium in $Li_{17}Pb_{83}$ at the reactor temperatures (300-500°C) must be known. Ihle et al.[1] has determined the deuterium solubility in Li-Pb alloys at 677 and 767°C, much higher temperatures than the reactor conditions.

Recent experiments conducted by Chan and Veleckis[2] at Argonne National Laboratory indicate hydrogen solubilities that are fairly temperature independent and lower than both the data found by Ihle et al. The Sievert's constant used in this study for tritium solubility in $Li_{17}Pb_{83}$ at 500°C (based on the Argonne results) is 3.8 appm $H/kPa^{1/2}$ or 1.4×10^{-2} wppm $T/torr^{1/2}$ which at 10^{-4} torr gives a tritium concentration of 1.4×10^{-4} wppm in $Li_{17}Pb_{83}$. The mass of $Li_{17}Pb_{83}$ in the four chambers and the reflectors is 1.78×10^{7} kg, resulting in a low tritium inventory of 0.0025 kg.

6.3.2 Tritium Breeding and Recovery

The breeding ratio of $Li_{17}Pb_{83}$ is 1.25 resulting in a breeding rate of 4.4×10^{-6} kg T/s in each chamber. The $Li_{17}Pb_{83}$ alloy (4.5×10^{6} kg/ chamber) serves both as breeder and coolant and is circulated through the power cycle at a rate of 3.38×10^{8} kg/hr, so that the average residence time of the coolant in the chamber is 48 s. At a T_2 partial pressure in the chamber of 10^{-4} torr, the concentration of tritium in the alloy is 1.4×10^{-4} wppm.

The pressure that must be maintained in the reactor to allow the tritium to be released from the liquid metal is less than or equal to 10^{-4} torr.[3] The quantity of bred tritium that must be extracted is 7.4×10^{-4} mole T_2/s. This is a volumetric flow rate of 3.7×10^{5} ℓ/s at 700°K and 10^{-4} torr. The high pumping rate necessary to remove the exhaust between shots (~ 4×10^{6} ℓ/s

Table 6.3-1. Breeder and Coolant Characteristics Per Chamber

Blanket temperature (°C)	
Inlet	330
Outlet	500
Tritium concentration (wppm)	1.4×10^{-4}
Inventory (kg)	
Tritium	6.24×10^{-4}
$Li_{17}Pb_{83}$	4.46×10^{6}
Tritium Breeding	
Ratio	1.25
Rate (kg/s)	4.4×10^{-6}
Flow Rate (kg/s)	
$Li_{17}Pb_{83}$	9.4×10^{4}

at 10^{-4} torr and 700°K), is sufficient to remove the tritium at the breeding rate and a separate extraction unit will not be needed. The breeder and coolant characteristics are summarized in Table 6.3-1. Although the diffusion of tritium in $Li_{17}Pb_{83}$ is unknown, the high surface area of the flowing liquid metal in the chamber should allow easy release of tritium from the eutectic into the chamber.

6.3.3 Silicon Carbide Interactions with Hydrogen Isotopes

The silicon carbide tubes are surrounded with the alloy containing 1.4×10^{-4} wppm tritium in equilibrium with 10^{-4} torr T_2 pressure in the gas phase and 500°C, resulting in some solution of the tritium in the silicon carbide. Experiments on deuterium solubility in SiC at 1000 to 1400°C[4] are shown in Fig. 6.3-1. The solubility is very temperature dependent, decreasing as the temperature increases. A 0.61 power pressure dependence on the solubility was determined, indicating that the hydrogen dissolves monatomically. It also can be observed that the temperature dependence differs substantially for vapor deposited β-SiC and powdered α-SiC. The solubility is apparently due to chemical bond formation between hydrogen atoms and the lattice atoms. The presence of Si-H and C-H bonds have been observed[5] in reactions of SiC with hydrogen ions.

Table 6.3-2. Thermodynamics for Hydrogen-Silicon Carbide Interactions

(kcal/mole)	Free Energy 600°K	700°K	800°K
H_2 Interactions			
α-SiC(s) + 2 H_2(g) → Si(s) + CH_4(g)	10.45	12.70	15.03
α-SiC(s) + 1/2 H_2(g) → Si(s) + 1/2 C_2H_2(g)	38.85	37.98	37.13
α-SiC(s) + 2 H_2(g) → SiH_4(g) + C(s)	35.41	37.51	39.65
H Interactions			
α-SiC(s) + 4H(g) → Si(s) + CH_4(g)	-168.9	-161.5	-153.9
α-SiC(s) + 1 H(g) → Si(s) + 1/2 C_2H_2(g)	- 6.00	- 5.58	- 5.11
α-SiC(s) + 4 H(g) → SiH_4(g) + C(s)	-144.0	-136.7	-129.3

Fig. 6.3-1. Hydrogen solubility in SiC compared to metals.

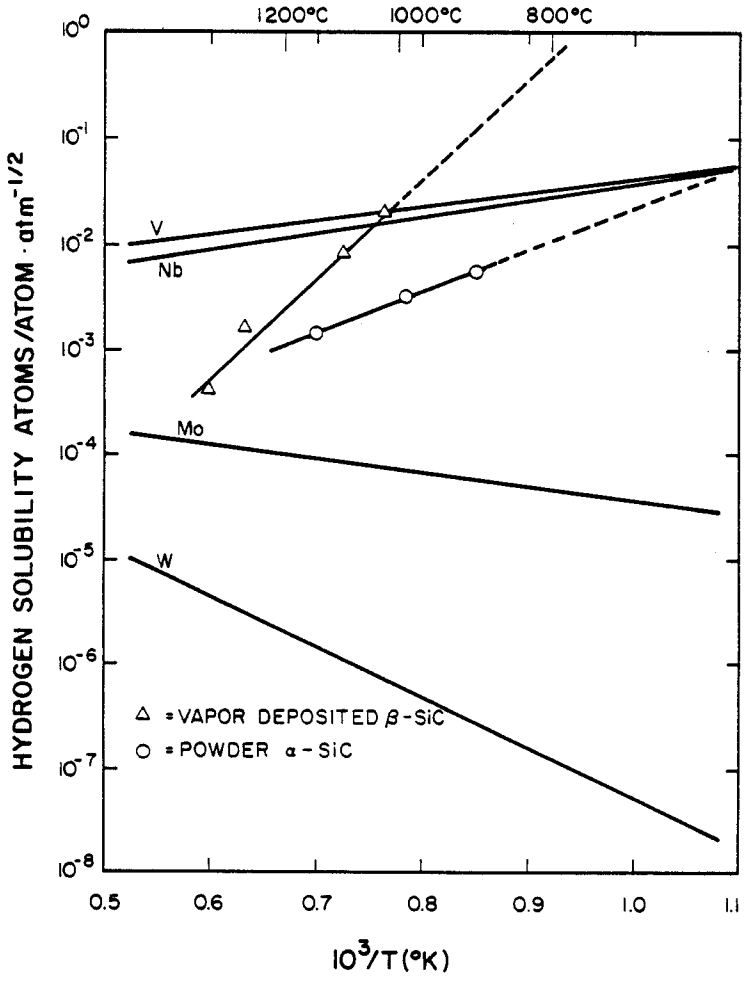

Due to the large exothermicity of the dissolving process, extrapolations to the lower temperatures of the INPORT tubes result in high tritium inventories. Because of the potential for chemical bond formation, such an extrapolation may not be valid, however, because other chemical equilibria may predominate at the lower temperatures. Also, it is impossible to predict that the fibrous β-SiC will behave similarly to the vapor deposited β-SiC. As an initial estimate, therefore, the hydrogen solubility at the lowest temperature measured, 1000°C in Fig. 6.3-1, was assumed to be representative of the solubility at the lower temperatures. At 1000°C and 10^{-4} torr T_2 pressure, the tritium solubility is calculated to be 0.5 wppm (T/SiC), resulting in an inventory of 0.008 kg in 1.6 x 10^4 kg of the SiC INPORT tubes.

Thermodynamic[6] calculations for silicon carbide reactions with hydrogen to produce hydrocarbons and silanes are given in Table 6.3-2. Hydrogen molecular reactions are unfavorable, while hydrogen atomic reactions have negative free energies. The SiC fibers are coated with a layer of liquid metal which should protect them from gaseous hydrogenic reactions; however, hydrogenic atoms dissolved in the liquid metal may lead to the formation of gaseous hydrocarbons and silanes. The magnitude of these potential reactions requires further experimental investigation.

References for Section 6.3

1. H.R. Ihle, A. Neubert and C.H. Wu, "The Activity of Lithium, and the Solubility of Deuterium, in Lithium-Lead Alloys," Proc. Tenth Symp. Fusion, Padova, Italy, September 4-9, 1978, Pergamon Press, New York, 639-644 (1979).

2. Y.C. Chan and E. Veleckis, "A Thermodynamic Investigation of Dilute Solutions of Hydrogen in Liquid Li-Pb Alloys," J. Nucl. Mater. 122 & 123, 935-940 (1984).

3. K. Ruttiger, "Vacuum Degassing in the Liquid State," Vacuum Metallurgy, O. Winkler and R. Bakish (eds.), Elsevier Publishing Company, New York (1971), 337-463.

4. R.A. Causey, J.D. Fowler, C. Ravanbakht, T.S. Elleman and K. Eghese, "Hydrogen Diffusion and Solubility in Silicon Carbide," J. Amer. Cer. Soc. 61, No. 5-6, 221-225 (1975).

5. R.B. Wright, R. Varma, D.M. Gruen, "Raman Scattering and SEM Studies of Graphite and Silicon Carbide Surfaces Bombarded with Energetic Protons, Deuterons and Helium Ions," J. Nucl. Mater. 63, 415-421 (1976).

6. JANAF Thermochemical Tables, D.R. Stull et al., The DOW Chemical Company, Midland, Michigan, 1964.

6.4 Tritium Containment Systems

The active tritium inventory in the HIBALL facility is 4.6 kg or 4.6 x 10^7 Ci, with an additional inventory of 8.2 kg or 8.2 x 10^7 Ci in storage and target manufacture. Tritium is being processed at a rate of 4.4 x 10^7 Ci/d in the fuel cycle and 4.1 x 10^7 Ci/d in the target fabrication facility. Losses of tritium to the environment must be limited to 10-100 Ci/d. By the use of containment schemes similar to those found in the TSTA[1] design and in a previous reactor design,[2] low tritium losses are predicted, as discussed in Chapter 9.

6.4.1 Permeability of Tritium into Steam Cycle

The complete power system has not been designed in the HIBALL-II study; however, it will be conceptually similar to the liquid metal/steam cycle system considered for MARS.[2] The most difficult tritium loss pathway to control is the permeation of tritium from the $Li_{17}Pb_{83}$ breeder/coolant through the walls of the steam generator. Once in the steam cycle the tritium is generally considered lost to the environment because the tritium exchanges with protium forming HTO. Separation of HTO from the bulk of the steam is technically difficult and expensive.[3]

Hydrogen permeation data for HT-9, the alloy in the steam generator tubing, and chromium ferritic steels has been reviewed.[4] The tritium permeation through clean HT-9 can be expressed by the relationship,

$$P = \frac{1.8 \times 10^3}{\sqrt{3}} \exp\left(\frac{-11100}{RT}\right) \frac{\text{mole } T_2 \quad \text{mm}}{\text{d} \quad \text{m}^2 \quad \text{atm}^{1/2}} \cdot$$

For HIBALL:

Tube thickness = 1 mm

Area = 5.2 x 10^4 m^2

Pressure above coolant = 10^{-4} torr

Temperature range = 315-490°C

In order to calculate the total tritium loss to the steam cycle, the area of the tubing is assumed to have a linear relationship with temperature, and the permeation in each temperature range is plotted against area (m^2), Fig. 6.4-1. The area under the curve represents the total loss of tritium, 33 g T_2/day. Losses of this magnitude are unacceptable and must be minimized.

6.4.2 Reduction of Tritium Permeation

One factor which reduces the permeation is an oxide layer on the steam side of the heat exchanger. *In situ* formed oxide coatings are effective in reducing tritium permeability[5]. For ferritic steels at 660°C, permeabilities are reduced by factors of 100 or more due to the oxide coating. At lower temperatures (315-490°C) the ability to maintain an effective oxide coating decreases.[6] For HIBALL the permeability through HT-9 is assumed to be decreased by about a factor of 10 due to the oxide layer on the steam generator side of the tubing.

Another method of achieving lower losses of tritium to the steam cycle includes formation of a permeation resistant nickel-aluminide layer[7] on the liquid metal side of the tubing. This is accomplished by addition of aluminum to the liquid-metal coolant, which forms an aluminum layer on nickel alloy surfaces, reducing the permeation by a factor greater than 100 for 304 SS at 550°C. The HT-9 alloy, however, is low in nickel and thus would not be adaptable to this scheme. The use of a metal in the steam generator different from that in the reactor may cause enhanced corrosion through mass transfer mechanisms.

Work has been done on the development of multilayered metal composites and impurity coated refractory metals as tritium barriers.[8] Reductions of a factor of 50 have been demonstrated for stainless steel structures containing an intermediate layer of Cu-Al-Fe alloy at 600°C. Metallic coatings with low hydrogen permeability coefficients would also present a barrier to the tritium.

An assumed a factor of 10 reduction in permeation due to the oxide coating results in 3.3 g T_2/day lost to the steam cycle. In order to further reduce this quantity, the tubes in the steam generator will have a double-walled construction, with a purge gas containing a low partial pressure of O_2 sweeping the tubing gap[9] as discussed in Chapter 8. Although double-walled tubing is expensive and difficult to produce,[3] this concept provides an effective tritium containment scheme. The oxygen in the purge gas maintains an oxide layer which converts tritium to HTO by combining it with the hydrogen that diffuses through the steam side. The permeating tritium appears to combine with the oxide on the metal and does not depend upon a gas phase reaction.[10] This significantly reduces the free tritium partial pressure, and

Table 6.4-1. Parameters in Steam System

Tritium diffusion from the LiPb side	3.3 g/d
Steam generator surface area	5.2×10^4 m^2
Tritium diffusion rate	1.5×10^{10} atoms T/$cm^2 \cdot s$
O_2 pressure in purge gas	1 torr
Maximum HTO pressure	0.1 torr
Temperature range	315-490°C
Required purge gas flow rate	5.3 ℓ/s
HT partial pressure in gap	1×10^{-16} torr
Total tritium loss to water	0.02 Ci/d

Fig. 6.4-1

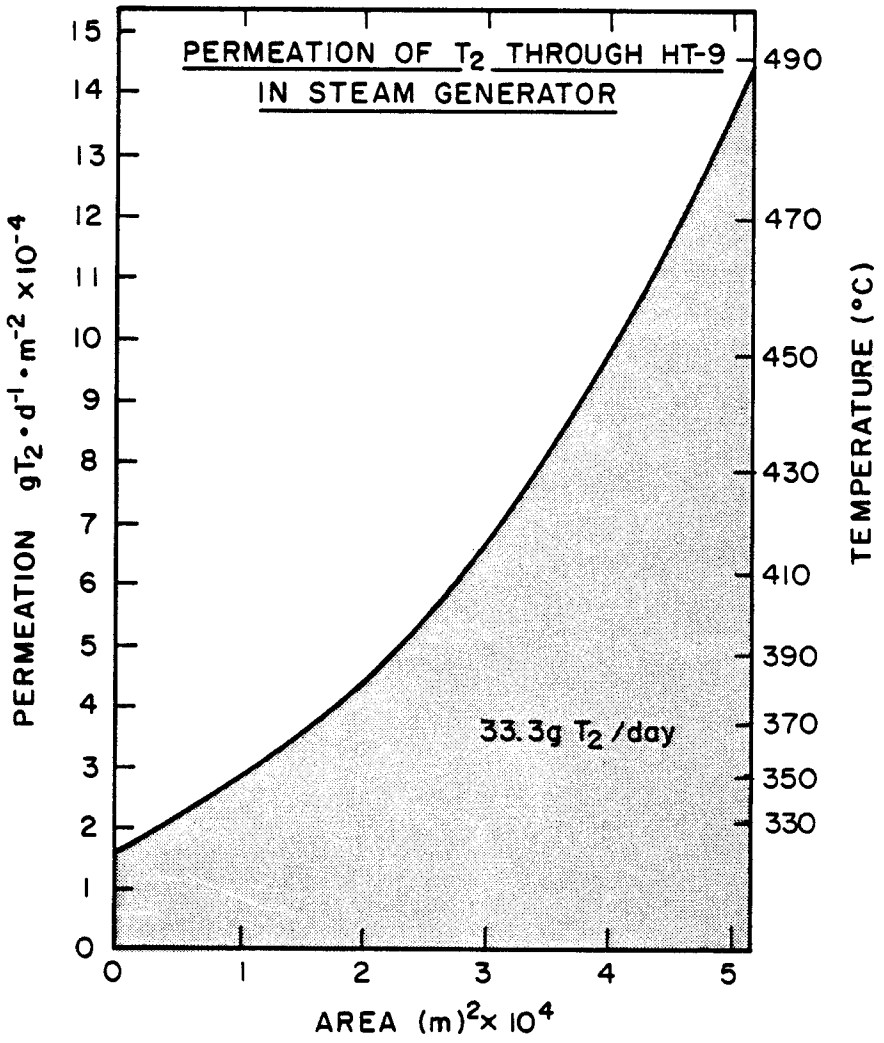

thus reduces the diffusion driving force to the steam side, as discussed in Section 8.3.

If the oxygen partial pressure in the purge gas is assumed to be 1 torr and the maximum HTO pressure allowed in the gap is 0.1 torr, then the volumetric flow rate of the purge gas is 5.3 ℓ/s. The HT pressure in the gap is about 10^{-16} torr, resulting in ~ 10^{-2} Ci/d loss to the steam generator. The parameters for the steam cycle are given in Table 6.4-1. If the steel forming the gap oxidizes too rapidly, the oxygen pressure can be reduced to 10^{-2} torr, which increases the tritium permeation to only 10^{-1} Ci/d.

The HTO that is formed in the purge flow is condensed and sent to a fuel cleanup unit where tritiated water is electrolyzed and hydrogen isotopes are then sent to the cryogenic distillation system for separation.

Secondary and tertiary containment schemes have not been addressed in detail. However, the designs for containment in the TSTA facility[1] will be tested in the near future, providing essential information to the fusion community on the aspects of tritium handling and containment.

References for Section 6.4

1. R.V. Carlson and R.A. Jalbert, "Preliminary Analysis of the Safety and Environmental Impact of the Tritium System Test Assembly," Proceedings Tritium Technology in Fission, Fusion and Isotopic Applications, Dayton, Ohio, April 29 - May 1, 1980, CONF-800427, American Nuclear Society (1980), 347-352.

2. B.G. Logan et al., "Mirror Advanced Reactor Study," Lawrence Livermore National Laboratory, UCRL-53480 (July 1984), Section 16.

3. A.B. Johnson, Jr. and T.J. Kabele, "Tritium Containment in Fusion Reactors," Topical Meeting on Technology of Controlled Nuclear Fusion, Richland, Washington, Sept. 21, 1976, 1319-1328, CONF-760935.

4. B. Badger et al., "WITAMIR-I - A Tandem Mirror Reactor Study," University of Wisconsin Fusion Technology Institute Report UWFDM-400, Chapter XI (Dec. 1979).

5. J.T. Bell, J.D. Redman and H.F. Bittner, "Tritium Permeability of Structural Materials and Surface Effects on Permeation Rates," Proceedings Tritium Technology in Fission, Fusion and Isotopic Applications, Dayton, Ohio, April 29 - May 1, 1980, CONF-800427, American Nuclear Society (1980), 48-53.

6. T.A. Renner and D.J. Rave, "Tritium Permeation Through Fe-2-1/4 Cr-1 Mo Steam Generator Material," Nucl. Technol. 47, 312-319 (1979).

7. J.C. McGuire, "Hydrogen Permeation Resistant Layers for Liquid Metal Reactors," Proceedings Tritium Technology in Fission, Fusion and Isotopic Applications, Dayton, Ohio, April 29 - May 1, 1980, CONF-800427, American Nuclear Society (1980), 64-68.

8. V.A. Maroni, E.H. Van Deventer, T.A. Renner, R.H. Pelto, and C.J. Wierdak, "Experimental Studies of Tritium Barrier Concepts for Fusion Reactors," Proceedings Radiation Effects and Tritium Technology for Fusion Reactors, Gatlinburg, Tennessee, October 1-3, 1975, CONF-750989 Vol. IV, 329-361.

9. D.C. Schluderberg, J.H. Huang, L. Pong and D.K. Sze, "Thermal and Mechanical Design of a Double-Walled Steam Generator," Nuclear Tech./Fusion, 4, 1509-1513 (1983).

10. D.F. Holland, Idaho Nuclear Engineering Laboratory, private communication, 1984.

7. MATERIALS

7.1 Introduction

The materials problems in HIBALL-II can be categorized according to where the materials are located, for example:

A. Inside Reactor Cavity
   i) SiC tubes
   ii) HT-9 support structure

B. Reflector Region
   i) HT-9 structure

C. Reactor Vessel Shield
   i) HT-9 structure
   ii) Pb gamma shield
   iii) B_4C neutron absorber

Since the most severe problems are associated with those components inside the vessel and in the reflector region we will concentrate on those areas.

A great deal of detail about the irradiation environment was given in HIBALL-I and that will not change in HIBALL-II. However, two more nuclear materials issues have arisen during the design of HIBALL-II. They are:

1. Compatibility of SiC with high temperature LiPb alloys.
2. Corrosion rate of HT-9 in $Li_{17}Pb_{83}$.

It has also been discovered that since HIBALL-I was published in 1981, new information on the radiation damage resistance of SiC and HT-9 has become available. We will briefly review the new non-nuclear and nuclear materials issues in the remainder of this chapter.

7.2 Compatibility of SiC at High Temperature

There have been three independent but rather qualitative experiments on the compatibility of SiC in Li-Pb alloys.[1-3] All of the experiments indicate that above 600°C, there seems to be little corrosion of SiC by Li-Pb alloys. A summary of the experimental information is given below.

SiC Material	Corrosive Fluid	Temp.-°C	Time-hr	Ref.
Not stated	Static Li	815	100	1
	Static Pb	815	100	1
Beta SiC Fibers	Static $Li_{17}Pb_{83}$	600	4500	2
Alpha SiC-Sintered	Static $Li_{17}Pb_{83}$	300-700	100	3

The first experiment[1] was performed in 1960 and showed that in pure Li, more than a 3 mill (or 6% wt change) or a 3% dimensional change occurred at 815°C for 100 hours. However, the same material showed essentially no penetration, weight change or dimensional change after 100 hours in pure lead at the same temperature. Since the activity of Li in $Li_{17}Pb_{83}$ is about 10^{-4}, the potential for corrosion of $Li_{17}Pb_{83}$ would be significantly less than for pure Li and probably more like the case for pure lead.

The second experiment[2] involved beta SiC fibers, marketed under the trade name of Nicalon®, inserted in $Li_{17}Pb_{83}$ for 4500 hours at 600°C. It was found that the $Li_{17}Pb_{83}$ completely wet the fibers and no dimensional changes were observed. This behavior may have been unique to the fibers because the pyrolytic treatment used to prepare the fibers introduces excess carbon and oxygen into the matrix. Consequently, the stoichiometry of the fibers is approximately $SiC_{1.3}O_{0.4}$. The excess C and O may increase the resistance of the fibers to corrosion by lead-lithium alloys and further work is required to quantify the information.

The third experiment[3] was performed by scientists at Interatom. They subjected large pieces of sintered alpha SiC to a static $Li_{17}Pb_{83}$ corrosion test at 300, 400, 500, 600 and 700°C. They found significant interaction between the alpha SiC and the LiPb alloy between 300 and 500°C, very little attack at 600°C and almost no attack at 700°C after 100 hours. It is not clear whether there is a difference in the behavior of alpha and beta SiC and future studies should examine this possibility.

In summary, the meager data which is available indicates that at 600°C and above, there should be no problem with corrosion on beta SiC fibers. However, there is some concern for the abnormal behavior of alpha SiC at lower temperatures and this needs to be investigated further.

References for Section 7.2

1. Oak Ridge National Lab Report, ORNL-2391, June, 1960, p. 14.

2. D.K. Sze and V. Coen, Abstract in the Third Topical Meeting on Fusion Technology, Albuquerque, NM, Sept. 19-22, 1983.

3. H. Runge, "Tritium-Bilanz und Verträglichkeit von SiC mit $Li_{17}Pb_{83}$ für Fusionsreaktorsystem Hiball", Interatom Report INTAT 55.06775.6, Feb., 1984.

7.3 Corrosion of HT-9 with $Li_{17}Pb_{83}$

Since the HIBALL-I report a few data points have been generated with respect to HT-9 and flowing (3 cm/s) $Li_{17}Pb_{83}$.[1] The two data points are shown in Fig. 7.3-1 and a straight line has been drawn through the data points to extrapolate to other temperatures. The corrosion rate, $\dot{C}$, can be approximated by the following equation;

$$\ln \dot{C} = 17.95 - \frac{11475}{T(^0K)} \quad (mg\ m^{-2}hr^{-1}) \quad .$$

The maximum corrosion rate at 500°C is approximately 20 microns/y per m^2. This is obviously not a thinning problem in the outlet tubes because after 21 FPY's, this would only amount to a loss of 0.4 mm and the tube is expected to be several cm thick. However, there is some concern about the plugging of heat exchanger tubes with the corrosion products generated. A detailed analysis of a similar HT-9/LiPb system in MARS[2] showed that even with far more HT-9 surface area, the plating out of the corrosion product was not severe. Furthermore, inhibitors such as Al or Mg can be used to lower the corrosion rate further.

In summary, excessive corrosion of the HT-9 heat transfer tubes is not found to be a problem. Future experiments at higher temperatures and with inhibitors or impurity cleanup systems need to be performed to develop more quantitative information.

References for Section 7.3

1. "Blanket Comparison and Selection Study, Final Report," Argonne National Laboratory Report ANL/FPP-84-1, September 1984.

2. "MARS - Mirror Advanced Reactor Study," Lawrence Livermore Report UCRL-53480, July 1984.

7.4 Irradiation Effects to SiC

The effects of irradiation on swelling of SiC were reviewed in HIBALL-I. No new information was found up to the publication of HIBALL-II. However, there is some new data on the effect of neutron irradiation on the thermal conductivity of SiC and that is included below.

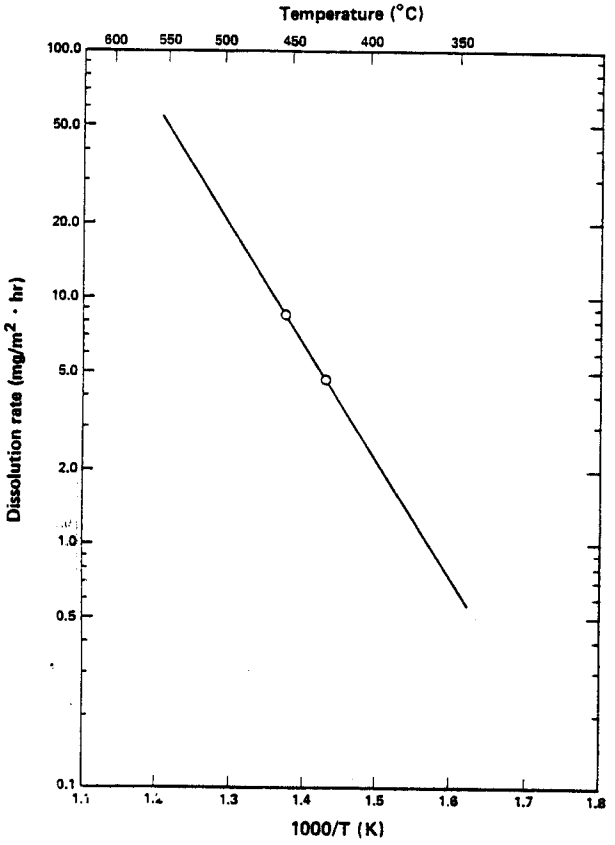

Fig. 7.3-1 Extrapolation of ANL corrosion data for the HT-9/$Li_{17}Pb_{83}$ system.

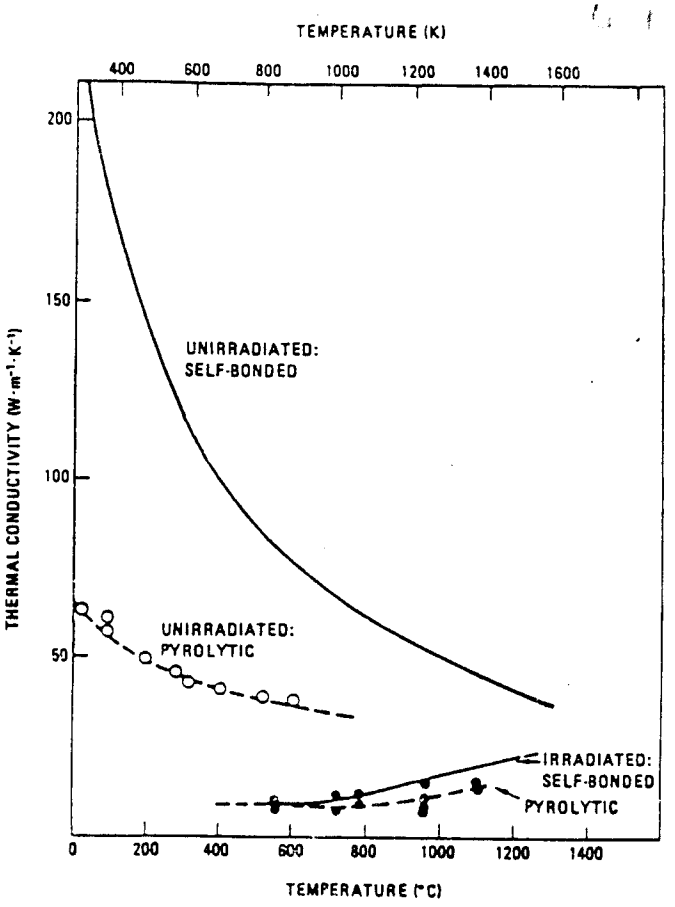

Fig. 7.4-1 Thermal conductivity of unirradiated SiC and irradiated SiC at the irradiation temperature as a function of temperature (fluences between 10^{25} and 10^{26} $n \cdot m^{-2}$). (1)

It is well known that irradiation tends to reduce the thermal conductivity of ceramic materials like SiC and it is important to factor this into any heat transfer calculations within the INPORT units. A further complication is the fact that the thermal conductivity of SiC is reduced as the temperature is raised. Figure 7.4-1 illustrates the temperature effect on pyrolytic and self-bonded SiC.[1] The unirradiated values can vary from 40 to 90 W $m^{-1}K^{-1}$ at 500°C.

When either the high or lower conductivity material is irradiated to 10^{26} n m^{-2}, the thermal conductivity drops to 10-20 W $m^{-1}K^{-1}$. This level of irradiation corresponds to roughly 10 dpa or 1 MW-y/m^2. Hence, a value of 15 W $m^{-1}K^{-1}$ will be used for the HIBALL-II study.

References for Section 7.4

1. "INTOR - International Tokamak Reactor", Phase 2A, Part 1, IAEA, Vienna, 1983, p. 251.

7.5 Radiation Effects to HT-9 Structure

There has been a considerable body of data reported on irradiated HT-9 since the analysis for HIBALL-I in 1981. The most recent summary of that data appears in Reference 1. In general, the favorable properties of HT-9 have been substantiated and the original choice of this alloy is still valid. The purpose of this section is to briefly quote information which has become available since the HIBALL-I report.

The anticipated damage environment for the HT-9 structural material in the chamber reflector region is given in Fig. 7.5-1 as a function of the effective tube thickness. Since the HIBALL-II designs calls for a gross tube thickness of 2 meters at a 33% packing density, there is 66 cm of effective material (LiPb/SiC) between the target and the structural material. The maximum damage rate at the HT-9 wall behind the INPORT units is then:

	Per FPY	Per 21 FPY's
dpa	2.7	56.7
appm He	0.4	8.4

The HT-9 wall is expected to operate in the 350 to 520°C range. It is therefore reasonable to examine the expected performance of HT-9 under such conditions with respect to swelling or the shift in the ductile to brittle transition temperature (DBTT). The conversion of 5 dpa per 10^{22} fission neutrons will be used in the following analysis.

7.5.1 Void Swelling

Considerable data on swelling of HT-9 has been reported in the past few years. Generally, the overall swelling is reported as

$$\frac{\Delta V}{V_o} = S_o - D$$

where S_o is the void induced swelling

D is the densification due to phase transformations.

The swelling due to void formation in HT-9 can be expressed as[2]

$$S_o = R \left\{d + \frac{1}{2} \ln \left[\frac{1 + \exp[\alpha(c-d)]}{1 + \exp(\alpha\tau)}\right]\right\}$$

where R = swelling rate in 0.0625% per dpa

d = dpa

α = curvature parameter, 0.014 per dpa

τ = incubation parameter

$$\tau = C_1 \exp \left\{C_2 [T-C_3]^2\right\}$$

C_1 = 72 dpa

C_2 = 3×10^{-4} per $°K^2$

C_3 = 673 °K .

The volume due to phase changes is

$$D = D^* \left[1 - \exp (-\lambda d)\right]$$

where D* = densification saturation parameter = - 0.15%

λ = densification time constant = 0.0625 per dpa.

The maximum swelling will occur at the 520°C, 57 dpa level. Since this is still below the incubation dose for swelling in HT-9 (75 dpa at 520°C) no void induced swelling is expected. However, there will be some densification due to precipitate formation and that is predicted to be ~ 0.15%.

A note in added proof of the superior resistance of HT-9 to void induced swelling is shown in Fig. 7.5-2. The swelling of simple and commercial austenitic alloys reveals that greater than 10% volume change is observed by damage levels of 20 or 60 dpa respectively. Simple ferritics extend the incubation dose to 50 dpa or more and no significant swelling is observed between 30 and 60 dpa, depending on the particular heat treatment. Even more advanced alloys such as PCA (not shown in Fig. 7.5-2) are expected to reach the 1% per dpa value at damage levels exceeding 70 to 100 dpa. In contrast, commercial ferritic steels have not exhibited more than 1% swelling in experiments conducted up to 100 dpa. When ferritics do pass beyond the transition fluence, they are not expected to swell faster than 0.1% per dpa. Based on breeder reactor experience, it appears that the reflector components exposed to the highest neutron flux for the lifetime of HIBALL-II would swell about 10 to 20% if made of 20% CW type 316 stainless steel. Although the reflector designs contemplated for HIBALL-II could accommodate a linear expansion of a few percent due to swelling, it is doubted that a significantly larger expansion could be accommodated in a power-producing fusion reactor. Therefore, the ferritic stainless steels were chosen for HIBALL-II.

The conclusion to be drawn from this analysis is that there should be no problem from dimensional changes in the HT-9 wall behind the INPORT units during the full reactor lifetime.

7.5.2 Irradiation Induced Shift in the Ductile to Brittle Transition Temperature

The ductile to brittle transition temperature (DBTT) can be defined as the intersection of the fracture and yield stresses when each is plotted as a function of temperature. At temperatures lower than the DBTT, the material will fracture in a brittle fashion before it reaches its yield point. Irradiation tends to raise the DBTT by introducing vacancy and interstitial dislocation loops as well as precipitates which may harden the alloy. An example of the upward shift in the DBTT with neutron irradiation is shown in Fig. 7.5-3.[3] After irradiation at 427°C to approximately 5 dpa the DBTT is increased from 0°C to 100°C.

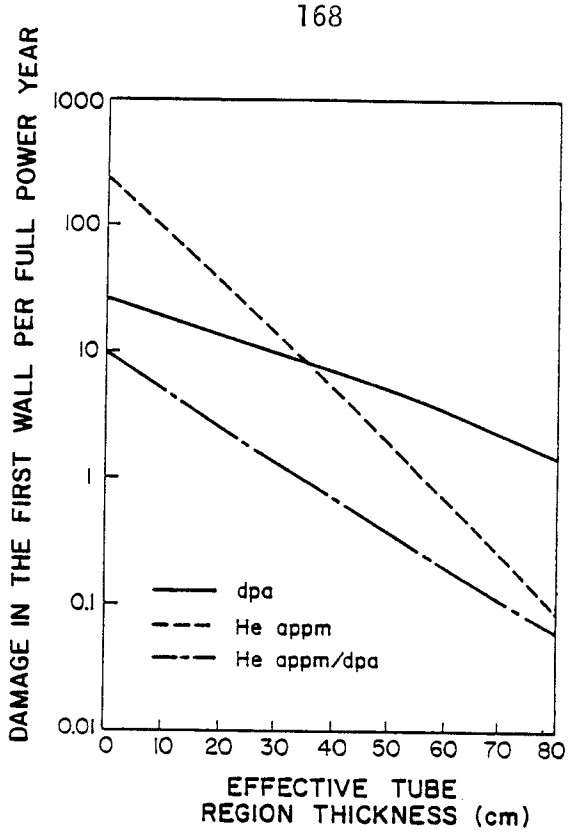

Fig. 7.5-1 Variation in damage parameters for HT-9 in the reflector region of HIBALL.

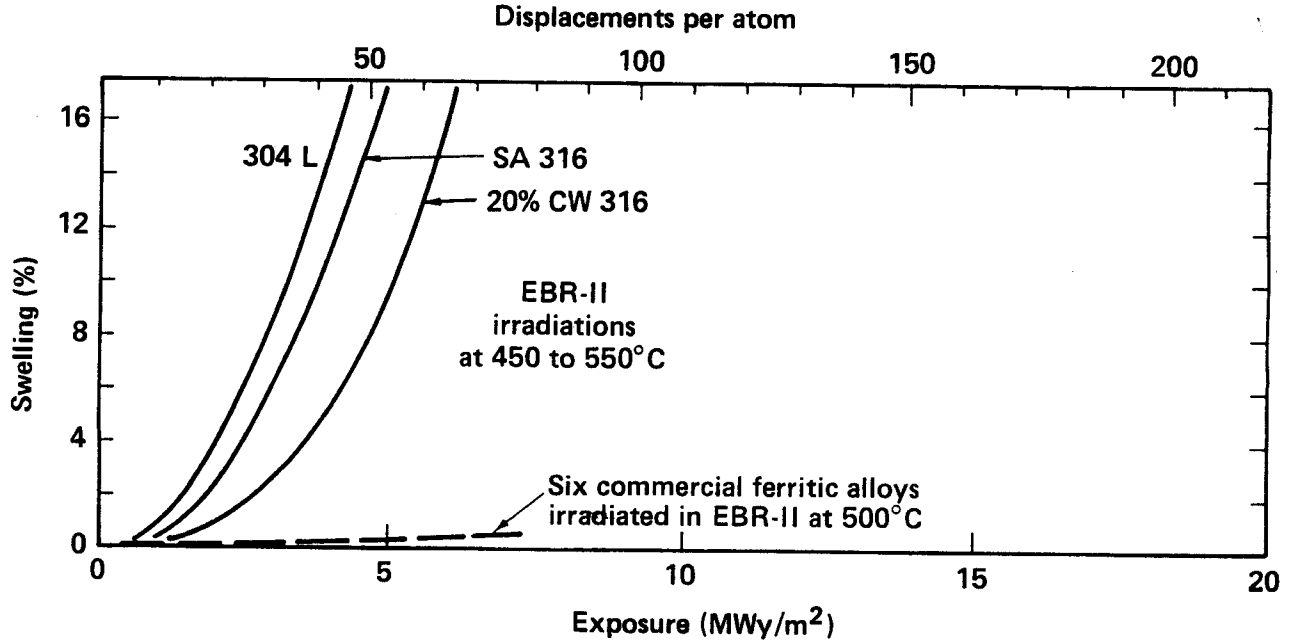

Fig. 7.5-2 Summary of recent swelling results for stainless steels irradiated with neutrons. Both austenitic and ferritic alloys show an incubation period before swelling starts, but the steady-state swelling rate is ~ 1% per year for austenitic alloys and 0.1% per dpa for ferritic alloys.

Another recent study by Laurtzen and Vaidyanathan[4] showed that at 13 dpa, the shift in the DBTT ranges from 140°C (at 390°C) to 50°C (at 450 and 500°C) (see Fig. 7.5-4). Above 500°C the ΔDBTT increases again to about 75°C. These results suggest that irradiation in the 350 to 500°C temperature range to 57 dpa might raise the DBTT to 150 to 200°C at the cold end (350°C) of the blanket and to 50 or 100°C in the hot end (520°C).

In either case severe consequences are not expected because the melting point of the $Li_{17}Pb_{83}$ is 235°C and the blanket temperature never reaches this point. If the Li-Pb alloy was drained out of the blanket for some reason hot He gas (~ 500°C) could be circulated in order to anneal out much of the damage which caused the upward shift in the DBTT.

References for Section 7.5

1. J.W. Davis and D.J. Michel, eds., "Proceedings of Topical Conference on Ferritic Alloys for Use in Nuclear Energy Technologies", AIME, Warrendale, Penn, 1984.

2. Proposed equation for Stress Free Swelling of HT-9 in Fusion Materials Handbook, to be published.

3. F.A. Smidt, J.R. Hawthorne and V. Provenzano, ASTM Special Technical Publication No. 725, 1981, p. 269.

4. T. Laurtzen, W.L. Bell and S. Vaidyanathan, p. 623 in "Proceedings of Topical Conference on Ferritic Alloys for Use in Nuclear Energy Technologies", Ed. J.W. Davis and D.J. Michel, AIME, 1984.

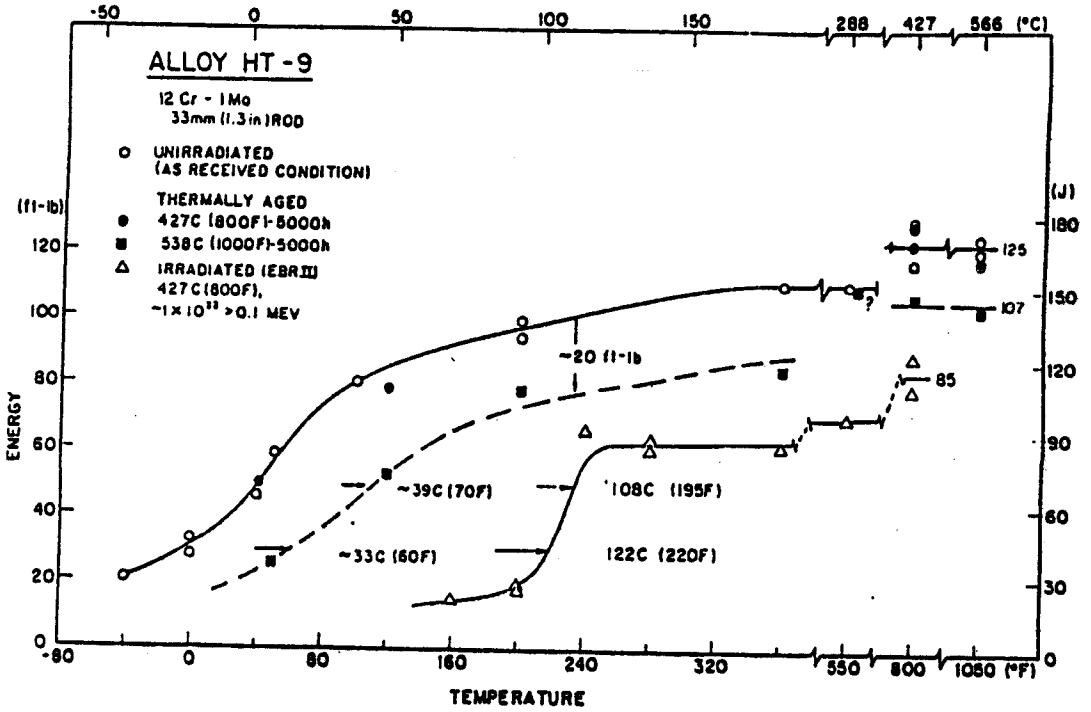

Fig. 7.5-3 Charpy-V energy values as a function of test temperature for HT-9 in the as-received condition, after 5000 hr aging at 427°C, after 5000 hr aging at 538°C, and after irradiation to a neutron fluence of 1.1×10^{22} n/cm^2 (E > 0.1 MeV) at an irradiation temperature of 419°C ± 15°C in the EBR-II reactor. From F. Smidt and scientists at Naval Research Laboratory.(3)

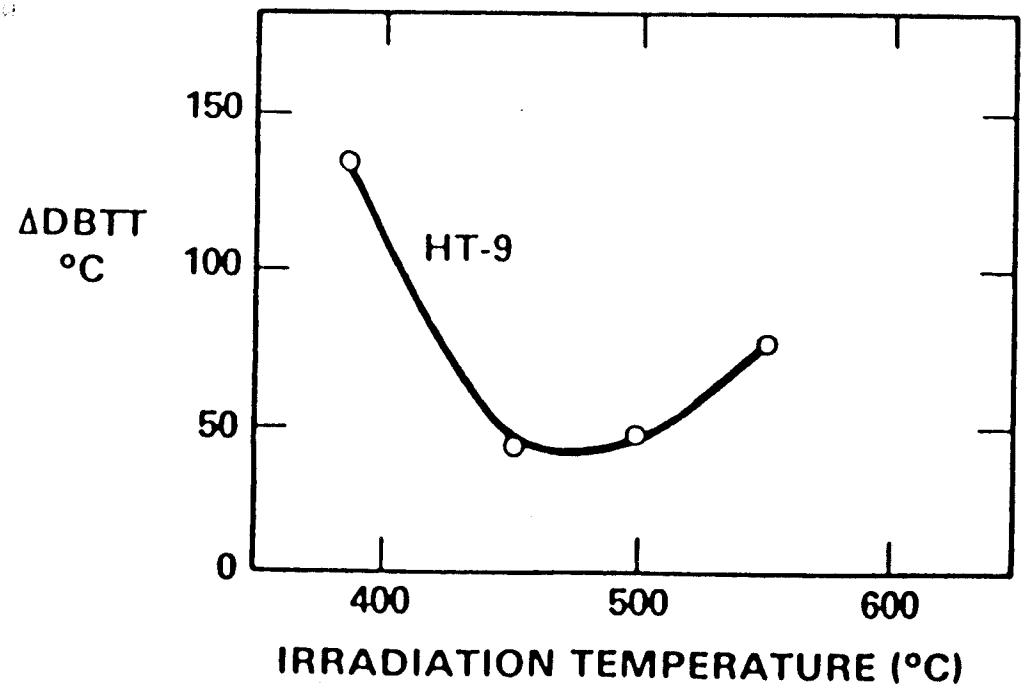

Fig. 7.5-4 Effect of neutron irradiation on the shift in the DBTT-15 dpa.(4)

8. HEAT TRANSFER CONCEPTS

8.1 Double Walled Steam Generator Concept

8.1.1 Heat Exchanger Arrangement and Power Cycle

The power cycle for the LiPb blanket is presented in Fig. 8.1-1. The MW_t heat input is split in two places to increase the effectiveness of heat transfer. The steam system is 16.6 MPa/482°C reheat. The heat transfer temperature diagram, Fig. 8.1-2, illustrates the effectiveness of the cycle over a system where the first stage reheat and economizer do not share the blanket heat. The evaporator pinch point is moved from 23.5 to 30% of the total heat transferred and the ΔT is raised from 15 to 25°C. This causes a larger log mean temperature difference (LMTD) in the evaporator, first stage reheater and the economizer which reduces heating surface requirements and LiPb inventory. A larger pinch point ΔT also encourages investigation of a higher steam cycle pressure with potential improvements in steam cycle efficiency over that which can be achieved at 16.6 MPa.

8.1.2 Double Walled Steam Generator

Heat exchange equipment for the HIBALL power cycle must fulfill exacting requirements while at the same time retain design features acceptable to the utility industry. The design requirements of liquid metal to water heat exchangers are complicated by:

- The component must provide a tritium diffusion barrier between blanket coolant and steam cycle.
- The component design must permit practical inspection and maintenance procedures in spite of radiation levels produced by activated corrosion products present in the blanket coolant.

The design described in Figs. 8.1-3 through 8.1-6[1] was created to meet the above requirements. It provides the following features:

1. Provision of an adequate tritium diffusion barrier.
2. Detection of potential tube defects that could lead to metal/water reactions.
3. Avoidance of size limitation problems typical of double walled heat exchangers.
4. Detection, location and repair of leaks by conventional methods (eddy current).
5. Compact construction.
6. Conventional component assembly.

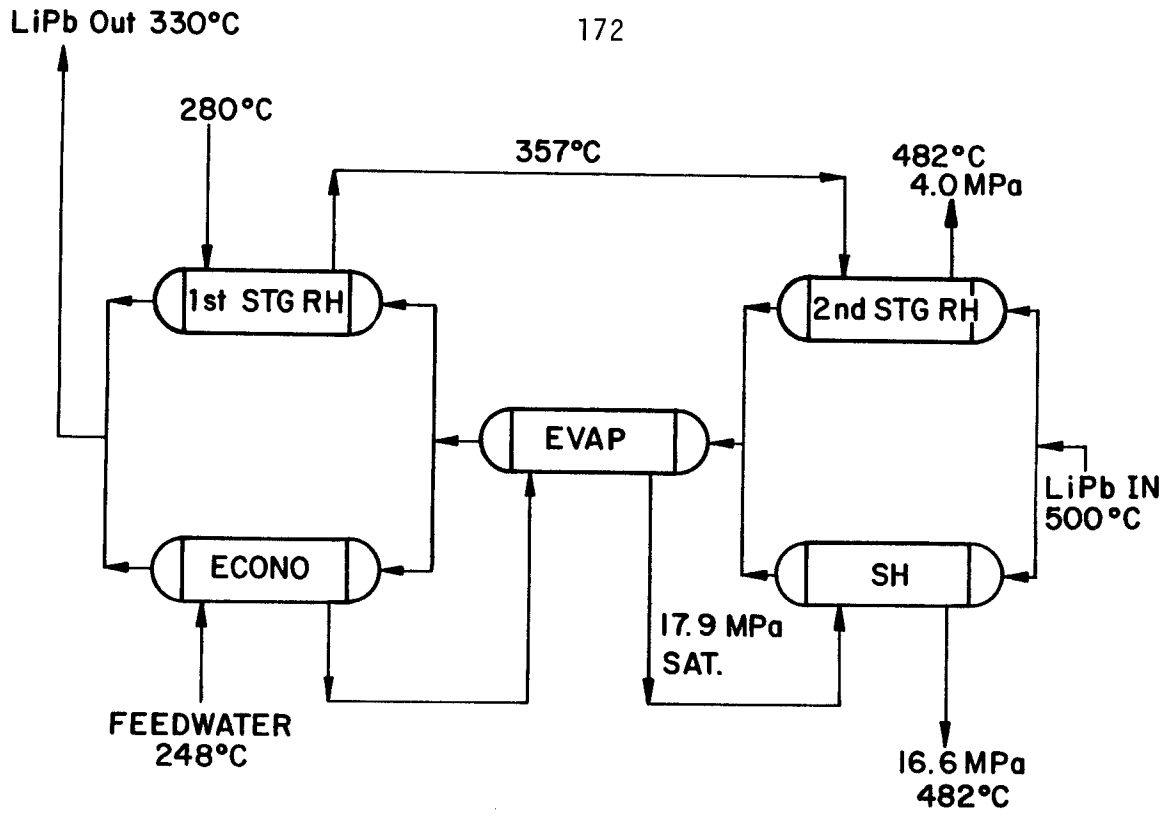

Fig. 8.1-1. Heat exchanger arrangement.

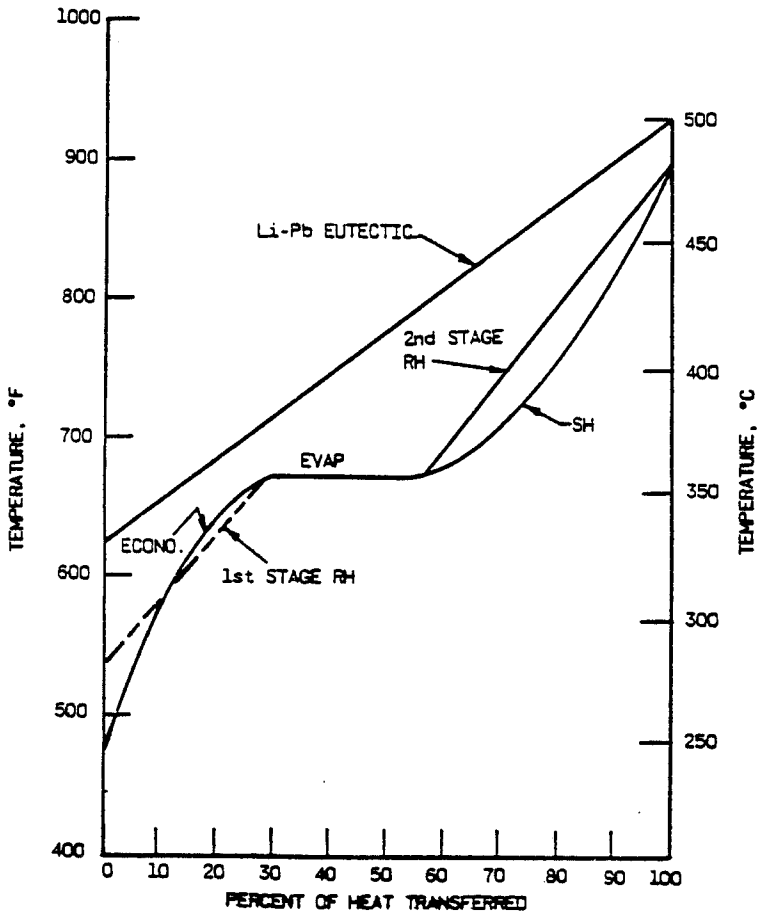

Fig. 8.1-2. HIBALL temperature diagram for 16.6 MPa 482°C/482°C steam cycle.

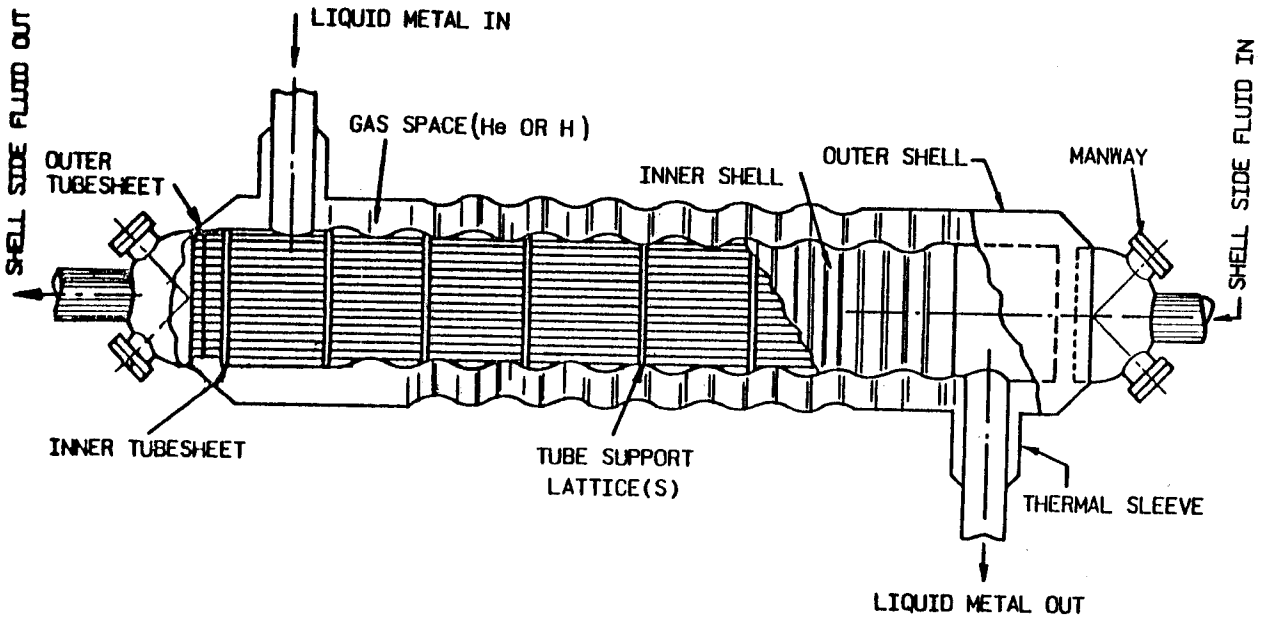

Fig. 8.1-3. Conceptual arrangement of steam generator.

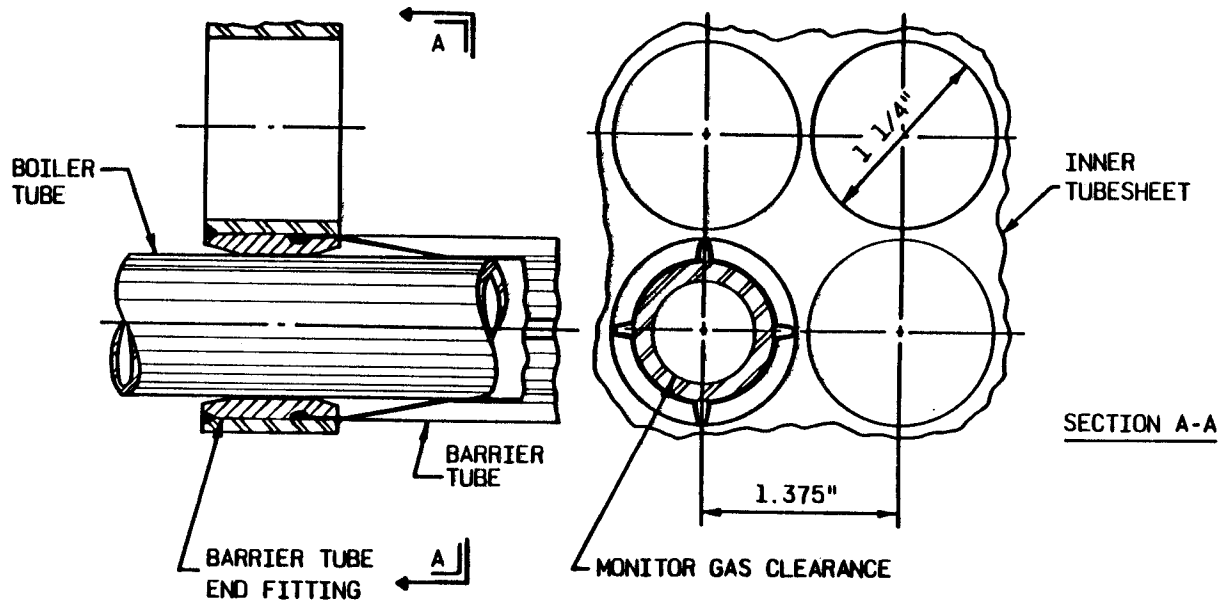

Fig. 8.1-4. Barrier tube to inner tubesheet detail.

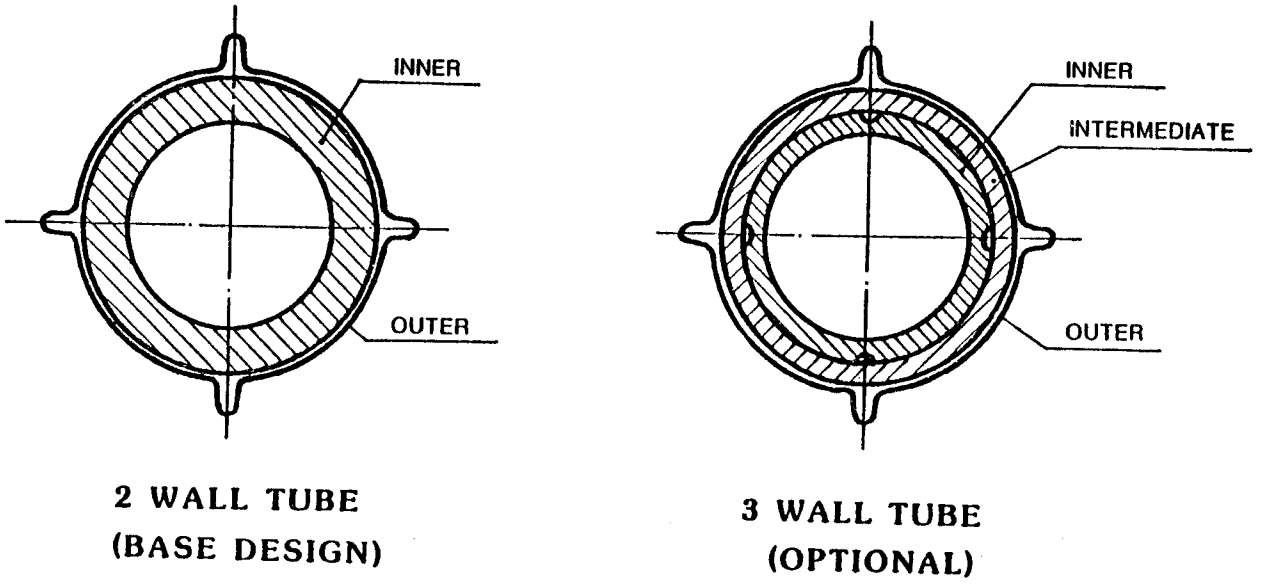

Fig. 8.1-5. Double walled tube structure.

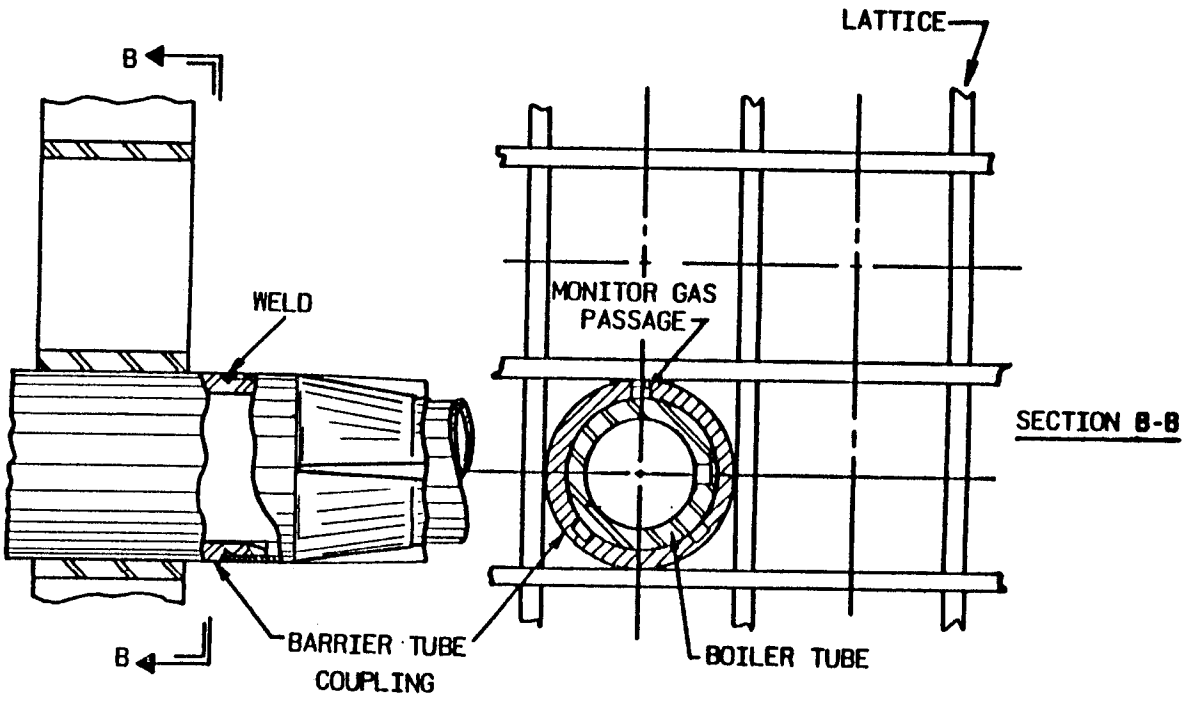

Fig. 8.1-6. Tube support detail.

The space between inner and outer shells and between inner and outer walls of each tube assembly is filled with helium at 1 atm containing oxygen at a partial pressure of one torr. A pumping system (not shown) is used to circulate this gas longitudinally through each tube wall gap as a sweep (or monitor) gas to detect water vapor.

The hemispherical heads shown in Fig. 8.1-3 are similar in configuration to those used for "once through" PWR steam generators. Thus the tube inspection and repair equipment developed for this equipment is applicable to the design shown in the above figure. This equipment has been used satisfactorily to perform inspection and maintenance work in radiation levels up to about 15 rem at the hemispherical head tube face.

To cope with higher radiation levels, the manways can be replaced by full opening closures, which in turn will permit use of rotating plugs and other equipment developed in the past for hot maintenance. The effect of activated corrosion product radiation on inspection and maintenance tends to be minimized by the following:

1. Vertical (instead of horizontal) tube sheet faces which reduce collection of corrosion particles on the surfaces.
2. Inner and outer tube sheets with a space in between which attenuates streaming of gamma rays through tube ID's.
3. Corrosion products will tend to collect at the top of the inner shell. Radiation from this location will not be in line with tube sheet holes.

8.1.3 Tritium Isolation

One of the most difficult problems associated with using $Li_{17}Pb_{83}$ is tritium confinement. The very low tritium solubility in $Li_{17}Pb_{83}$ results in a very high tritium partial pressure. The most vulnerable region in the primary loop for tritium leakage is the primary heat exchanger. To improve heat transfer, the surface of the heat exchanger is large and with thin-walled tube construction. Therefore, an effective tritium diffusion barrier is required between the primary loop and the steam cycle to reduce the tritium leakage to an acceptable level.

The tritium permeation through a single surface steam generator has been discussed in Section 6.4.1 and was shown to result in a release of 33 g/day, i.e. 3.3×10^5 curies per day. To reduce this release to an acceptable level, a tritium diffusion barrier of 10^5 is needed.

In the HIBALL design, a double walled heat exchanger is used to provide the required tritium diffusion barrier. The construction, with two tubes in close contact, was shown in Fig. 8.1-5. A helium purge with 1 torr of oxygen pressure passes through the channels to provide an oxidizing atmosphere between the two tubes. The oxide films formed between the two tubes, as well as the oxide film on the water side, provide an effective diffusion barrier.

Figure 8.1-7 shows two tritium diffusion paths through the double-walled steam generator. This is an enlarged figure around one contact point between the tubes.

Path 1: Through wall 1, across the gap and through wall 2.

Path 2: Through the contact point.

Path 1

The resistance to diffusion across the gap is the product of the resistance due to the oxide films and resistance due to the gap. The resistance of the gap was calculated using diffusion theory with the removal of tritium represented by an effective mean free path based on simple kinetic theory. Thus, each collision of a tritium molecule results in its removal. Figure 8.1-8 shows the attenuation factor due to the gap as a function of the gap width while Fig. 8.1-9 shows the attenuation factor due to the combined effect of three oxide coatings as a function of the single oxide coating layer factor. If the gap width is 10^{-3} cm, the attenuation factor due to the gap is 3×10^{-3}. To obtain a total attenuation factor of 10^{-5}, an attenuation factor of 3×10^{-3} is needed from the oxide coatings, which corresponds to a single layer factor of 20. Experiments have indicated that a single layer factor of a few hundred is available for ferritic steel. It can be concluded, therefore, that the attenuation factor of $<< 10^{-5}$ is available for tritium leakage across the gap.

Path 2

A two-dimensional, finite difference tritium diffusion calculation was performed for tritium leakage along path 2. The result shows that an attenuation of 10^{-5} is also available along this path. The total attenuation is the sum of the attenuation along those two paths and is, therefore, $\leq 10^{-5}$.

Numerous questions and uncertainties remain to be investigated with respect to these double-walled heat exchangers. In the previous calculations it was assumed that the tritium oxygen reactions occurred essentially instantaneously. Whether this actually is the case remains to be seen. However, recent

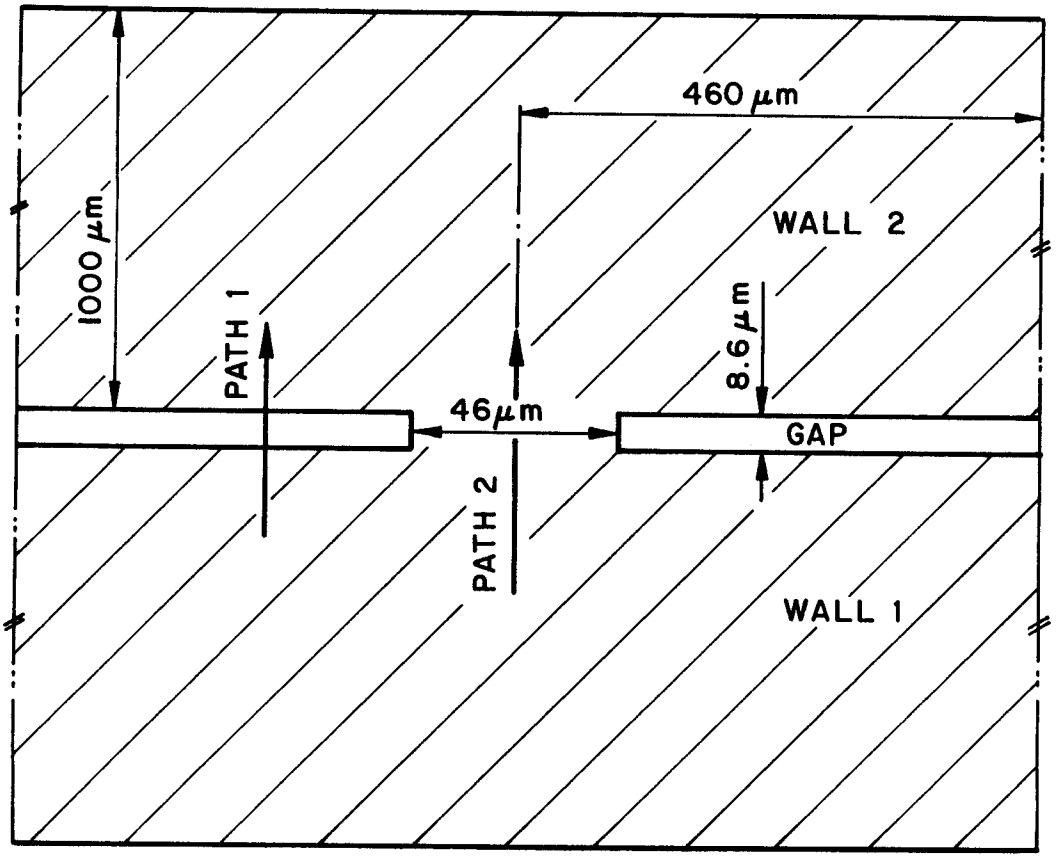

Fig. 8.1-7. Tritium diffusion path.

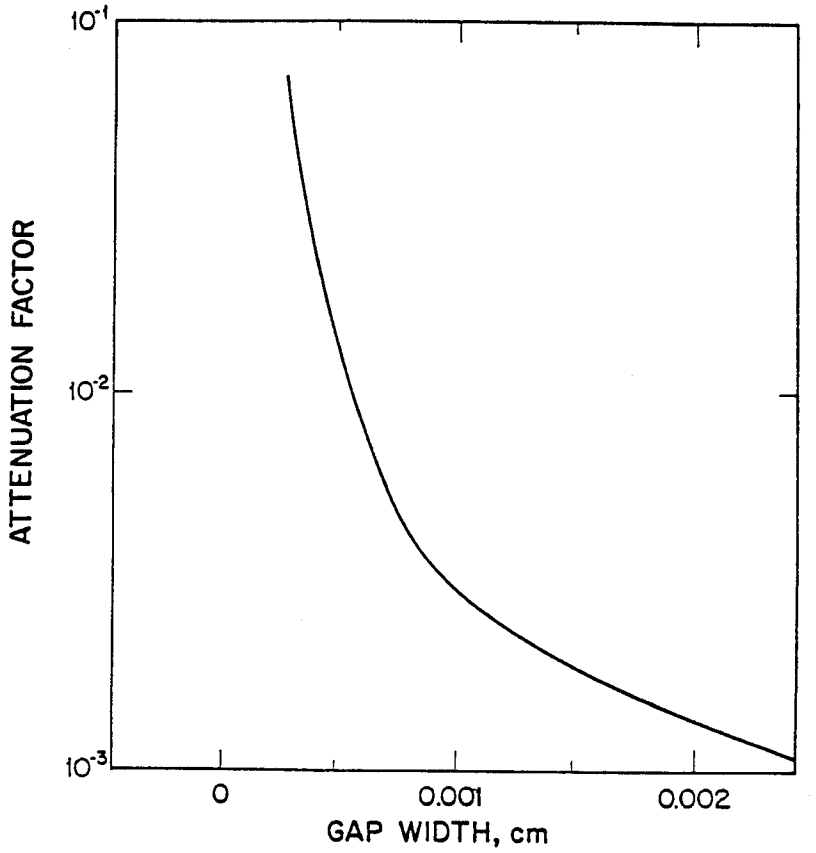

Fig. 8.1-8. Attenuation factor due to gap.

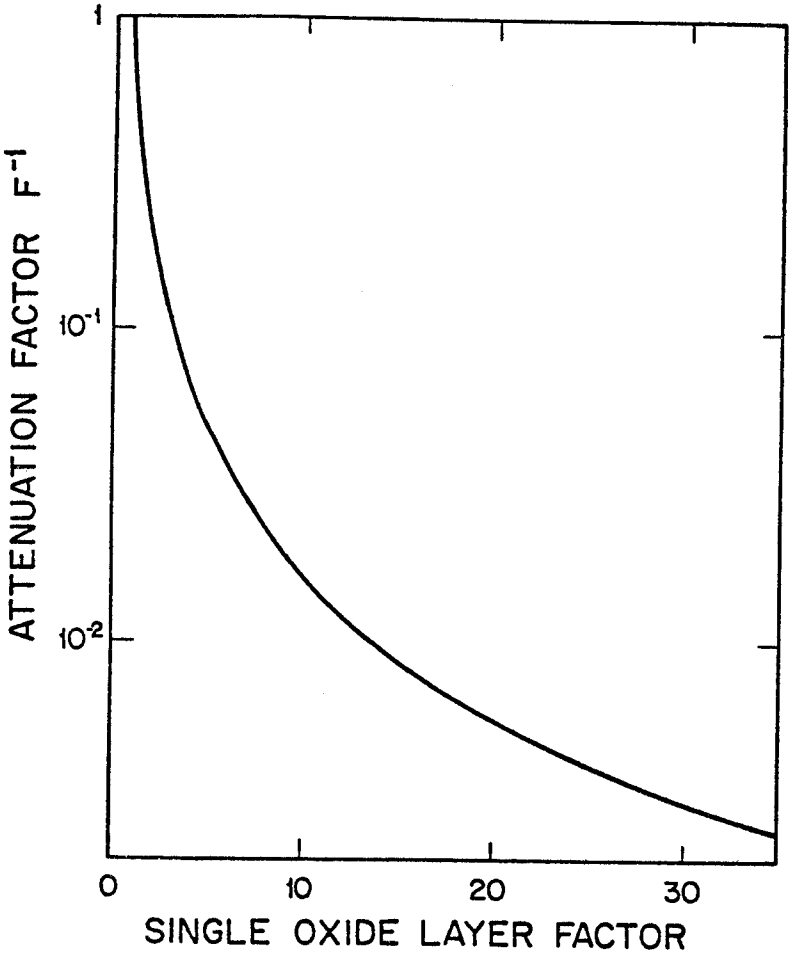

Fig. 8.1-9. Attenuation factor due to three oxide coatings.

experiments being performed at INEL[2] indicate even if that is not the case the tritium is still converted. These experiments appear to show that the reaction takes place not in the gap but with the oxygen in the surface oxide layer of the tubes. If this is so, then the oxygen in the gap need only be present at a level to maintain the oxide layer on the tubes. If the tritium penetrated the first walls of the steam generators at the previously mentioned rate, i.e. 3.3×10^5 Ci/day, in the form HT, only 176 grams of oxygen per day would have to be introduced into the system to maintain the oxide layer. Since the oxide layer need not be thick and can be controlled, concerns regarding the growth of the oxide layer to the point where it fills the gap may be alleviated. Only an experimental program can answer these concerns satisfactorily. The presence of the gap - any gap - is going to have a deleterious effect on heat transfer. A very preliminary estimate is that this effect may increase the steam generator surface area by about 25%. As above, an experimental program with systems with spacing satisfactory for tritium retention is required to assess this question fully.

8.2 Sodium Intermediate Loop Concept

8.2.1 Introduction

The double-walled steam generator presented in Section 8.1 is a very attractive concept, and it has been chosen as the reference concept from the considerations of plant power flow, cost, etc., for this report. Since, however, its feasibility is not fully established we briefly discuss an alternative, more conventional system[3] of the kind used in present-day liquid metal fast breeder reactors.

8.2.2 Design

For reasons of component size, it is considered to use two $Li_{17}Pb_{83}$ primary circuits, intermediate heat exchangers (IHX) and sodium secondary circuits per reactor chamber and three steam generators (SG) per secondary circuit. Some parameters are given in Table 8.2-1.

8.2.3 Tritium Isolation

Apart from tritium permeation barriers in the form of oxide layers, the mechanism for reducing tritium losses to the water/steam side differs from the one used in the double-walled SG concept. There, the tritium is oxidized into HTO by the purge gas; in the sodium secondary circuit, tritium would accumulate as NaT in the cold trap of the sodium purification bypass. The tritium

Table 8.2-1. Parameters for Intermediate Loop System

Total no. of primary circuits	8
No. of IHX & secondary circuits per primary circuit	1
Per secondary circuit:	
Power (MW_{th})	1279
IHX surface area (m^2)	4430
IHX material	austenitic
Na inventory (tonnes)	130
Na flow rate (m^3/s)	6
IHX sodium temperature, inlet (°C)	290
IHX sodium temperature, outlet (°C)	480
Cold trap temperature (°C)	115
No. of SG	3
Per SG:	
Power (MW_{th})	426
SG surface area (m^2)	1894
SG material	austenitic
Water inlet temperature (°C)	190
Steam temperature (°C)	460

concentration in the sodium is determined by the total hydrogen solubility by the cold trap temperature and by the isotopic ratio of the hydrogen. Corrosion on the water/steam side of the SG produces protium which permeates into the sodium, thus limiting the tritium concentration to about 6×10^{-4} wppm. Tritium losses to the water/steam side were found[3] to be 1 Ci/d for the HIBALL plant. It should be noted that austenitic steel was assumed for the IHX and SG which has advantages with respect to oxide barrier formation but may cause corrosion (mass transfer) problems with the ferritic steel used in the primary circuit.

References for Chapter 8

1. D.C. Schluderberg, J.H. Huang, L. Pong and D.K. Sze, "Thermal and Mechanical Design of a Double-Walled Steam Generator," Nuclear Tech./Fusion 4, 1509-1513 (1983).

2. D. Holland - private communication.

3. H. Runge, "Tritium-Bilanz und Verträglichkeit von SiC mit $Li_{17}Pb_{83}$ für Fusionsreaktorsystem HIBALL," Interatom Report INTAT 55.06775.6, 1984.

9. ENVIRONMENTAL AND SAFETY ASPECTS

9.1 Introduction

Potential releases to the environment of radioactive materials contained in the HIBALL plant must be prevented by safety design measures similar to those that are applied at present to fission converter (e.g. LWR's) and breeder reactors (e.g. LMFBR's). This means that a HIBALL type reactor plant must have safety components incorporated as plant protection systems. Examples are:

- plant shutdown system,
- control system,
- emergency cooling,
- decay heat removal system,
- multiple containment barriers between the radioactive materials and the environment.

Safety regulations and siting criteria for commercial fusion power plants will probably be very similar to those for present fission reactors.

Before addressing the nuclear environmental and safety issues of any fission or fusion power plant it is necessary to list its inventory of radioactive materials.

9.2. Radioactive Inventory

Radioactive materials as they exist or are generated in the different parts of the HIBALL reactor plant are:

- tritium in the entire fuel cycle of the plant (target fabrication facility, breeding blanket, reactor cavity, vacuum pumps, cleanup and isotope separation systems),
- activated debris material from burned pellets within the reactor cavity and in the vacuum system,
- activated structural and shielding material around the reactor cavity (blanket, reflector and radiation shield),
- activated coolant,
- activated structural and shielding material in the beam channels and at the focusing magnets.

In the following subsections the quantities of the different radioactive materials are discussed and listed. For tritium we assume a closed cycle with constant inventory (see Chapter 6). For the other species, activities at shutdown after two years operation are given (see Section 5.3.5).

9.2.1 Tritium Inventory

Table 9.2-1 summarizes the tritium inventories per GWe at different places within the power plant. By far the highest tritium inventory will occur in the target factory, where a one day supply of cryogenic targets to fuel the reactor and a one day tritium supply in uranium beds (prior to target filling) have been assumed (Chapter 6).

As explained in Chapter 6 the tritium inventory within the coolant and breeder material $Li_{17}Pb_{83}$ will be very small, only about 1 g/GWe. A similar small inventory of 3 g/GWe was originally assumed for the INPORT structures in HIBALL. However, the tritium solubility in SiC at 500°C and below is uncertain (Section 6.3.3), and the corresponding inventory might be as high as 250 g/GWe.[1]

9.2.2 Radioactivity in Coolant and Breeder Material

Neutron induced activation of the coolant and breeding material leads to the buildup of radioactive nuclides. The coolant and breeder material $Li_{17}Pb_{83}$ will be activated and the activation of lead will result in a considerable inventory as shown by Table 9.2-2. The highest activity of 0.6×10^8 Ci/GWe is due to ^{203}Pb having a half-life of 52 h.

No data are listed for the activity arising from corrosion products in the coolant and from impurities, with the exception of bismuth, a common natural impurity in lead. Additional bismuth is brought in by the Bi ion beams. This amounts, however, to only 1 ppm in 30 full power years.

In addition, ^6He and ^8Li are produced from lithium. They contribute to the radioactive inventory of the operating plant but not to the "releasable" inventory because of their short half-lives of 0.8 s.

9.2.3 Radioactivity Built Up in the Burning Target

The HIBALL target contains, besides DT, only materials that are also present in the coolant (Li and Pb) and thus produces the same radioactive nuclides. Quantitatively, the target radioactivity adds a negligible amount to the coolant radioactivity.

9.2.4 Radioactive Inventory in the Chamber Structures, Reflector and Shield

Radioactivity will be induced by neutron capture in the structural material of the blanket, the first steel wall, the reflector and the shield of the reactor cavity. The total radioactive inventory built up in the blanket structures, steel wall and reflector was estimated to be about 1.6×10^9 Ci/GWe (Section 5.3.5). The bulk of this activity is due to neutron activa-

Table 9.2-1. Tritium Inventory per GWe in HIBALL Reactor Plant
(1 kg has an activity of 0.96×10^7 Ci)

Plant component	Tritium inventory, kg/GWe
Blanket	
$Li_{17}Pb_{83}$ (coolant and breeder material)	0.001
Coolant guide tubes (INPORT, SiC)	0.003-0.25
Tritium Cycle	
Cryopumps	0.1
Cleanup unit	0.01
Isotope separation	0.02
Target Fabrication Facility	
Targets (one full power day supply)	1
Storage in uranium beds	1
Targets in fabrication[a]	1-3

[a] Depends on target filling process; 1 kg/GWe per day of diffusion filling duration is required.

Table 9.2-2. Radioactive Inventory per GWe in HIBALL $Li_{17}Pb_{83}$ Coolant After Two-Year Operation

Nuclide	Half Life	Activity (Ci/GWe)
^{203}Hg	47 d	1.2×10^6
^{205}Hg	5.2 min	1.1×10^6
^{204}Tl	3.78 y	0.4×10^5
^{203}Pb	52 h	0.6×10^8
^{205}Pb	1.5×10^7 y	0.5×10^2
^{210}Po	138 d	1.6×10^2
(from 40 atom-ppm Bi impurity)		
Total		6.2×10^8

tion of steel. The radioactivity in the outer concrete shield is much lower, 1.6×10^7 Ci/GWe, but still significant (Section 5.3.5).

9.2.5 Radioactivity Built Up in the Beam Lines

The final focusing layout for HIBALL-II with its smaller beam ports and a final neutron dump about 40 m from the chamber wall constitutes an important improvement over the HIBALL-I design also with respect to activation. The total activity per beam line of the new design was estimated in Section 4.3.6 at 66 Ci which corresponds to 1.4×10^3 Ci/GWe. While these activity levels are low compared with those of a reactor chamber they may be high enough to produce an unacceptable biological dose rate for certain manual maintenance operations.

9.3 Releases of Radioactivity Into the Environment During Normal Operation

9.3.1 Introduction

The permeation of tritium through the walls of steam generators, fuel cycle or target factory components represents the most important and most difficult environmental problem of the HIBALL plant. Gaseous ^{6}He has such a short half life that it does not play a role for radioactive release during normal operation. All other radioactive materials present in the plant are in either liquid or solid form. Their release to the environment under normal operation can therefore be excluded.

An assessment of the total releases of tritium from the power plant during normal operation requires estimates of release and permeability rates for each plant component containing tritium.

9.3.2 Permeability of Tritium Into the Steam Cycle

The permeation of tritium from the coolant through the walls of the steam generators causes a difficult technical problem, as the permeability of tritium through steel is relatively high and the heat transfer areas of steam generators are large so that considerable quantities of tritium may reach the steam cycle and the environment. As described in Chapter 6, simple steam generators would imply a leakage rate of 3×10^5 Ci/d, at least 10^4 times higher than can be allowed. Therefore, a diffusion barrier of 10^{-4}-10^{-5} for tritium is needed, which can be achieved either by double walled steam generators as they are developed presently for LMFBR applications or by an intermediate liquid metal loop.

Estimates have shown that a duplex tube steam generator diffusion barrier concept as described in Sections 6.4.2 and 8.1.3 may be sufficient to keep the permeation of tritium into the steam cycle below about 1 Ci/GWe/d.

If an intermediate liquid sodium loop (Section 8.2) is used instead of the duplex steam generator, diffusion barriers of 10^{-2} to 10^{-3} for leakage of tritium into the intermediate loop are required. The total losses of tritium from the intermediate circuits would be only about 2 Ci/d, only 1 Ci/d being released through the water path of the steam generators.[1] The total tritium inventory of the intermediate coolant circuits would be less than 1 g.

However, the primary coolant circuits consisting of pumps, valves, pipings, flow meters, storage or holdup tanks, purification systems etc. will probably have to be designed with aluminum sleeving or jacketing and in some cases with glove boxes to provide a secondary containment barrier against tritium permeation and to keep leakages low.

Table 9.3-1 summarizes the tritium losses from the HIBALL reactor plant. The total losses are estimated to be 20 Ci/GWe/d. Out of these total losses 80% are expected to go into the atmosphere and 20% into water.

9.3.3 Cumulative Doses from Normal Operation

With a given release rate as estimated in Table 9.3-1 radiation doses due to normal operation can be calculated for a given distance from the reactor plant. Assumptions must be made for the exhaust stack height, the atmospheric dispersion of the radioactivity and the population density around the plant. On the basis of a 100 or 200 m high exhaust stack, average meteorological conditions as measured at Hannover, FRG, and a population density of 250 persons/km^2 the cumulative doses were calculated following the international guidelines of ICRF 26 (1976) and ICRF 30 (1979), as well as the German guidelines GMBI-21.[2] Figure 9.3-1 shows the local effective dose equivalent commitment due to gaseous and liquid effluents. The figure compares the doses on a 1 GWe•y basis for a pressurized water reactor (PWR) and its respective reprocessing plant with HIBALL. The higher stack of 200 m of the latter strongly influences the doses in the immediate vicinity of the plant. Whereas HIBALL will release only tritium, additional radioactive nuclides, e.g., radioactive noble gases (krypton, xenon) and β- or α-emitting aerosols (fission products and actinides) must be accounted for[3] in the case of the PWR and its reprocessing plant. All dose data decrease strongly with distance and are in the range of 0.1 μSv/GWe/y (0.01 mrem/GWe/y) at a distance of 10 km from the

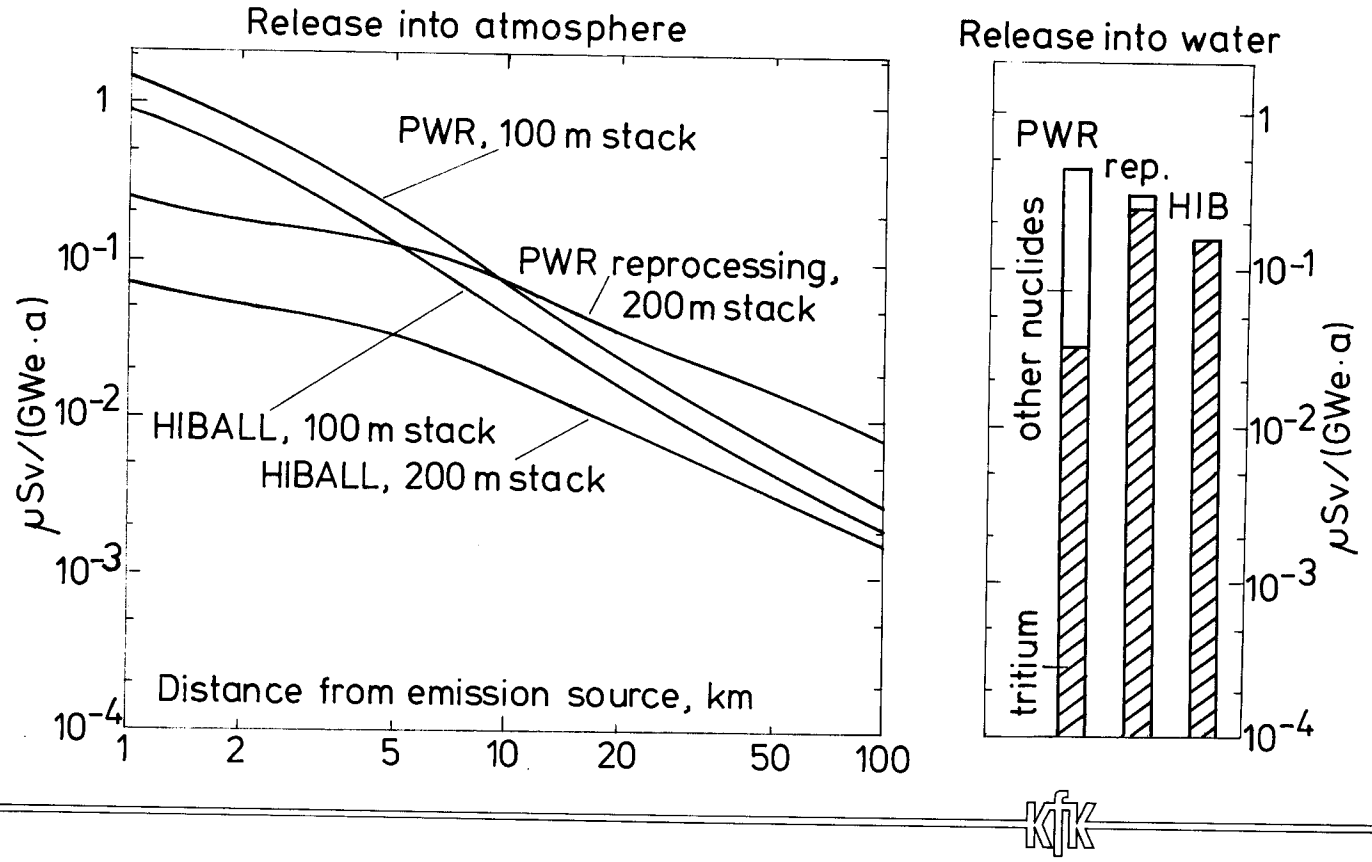

Fig. 9.3-1. Local effective dose equivalent commitments due to releases during normal operation.

Table 9.3-1. Tritium Released from HIBALL Reactor
(1 GWe basis)

	Ci/GWe/d
Intermediate coolant circuits, steam generators Double walled steam generators	1
Water coolant circuits of shield	1
Cryopump system	3
Fuel cleanup unit	2
Isotope separation unit	1
Target factory	5
Buildings and tritium recovery system	2

plant. This is well below the present limits imposed by radiation protection ordinances.

When considering these data is should be recalled that the results for a PWR and its associated reprocessing plant are based on realistic data whereas the estimates for HIBALL depend upon the above assumptions made for the diffusion barrier in the steam generator tubes and other permeation rates of tritium in different parts of the plant.

A comparison with tritium release rates from fission reactors and their fuel cycle shows that, under the present assumptions, heavy ion beam or magnetic fusion reactors would have similar release rates on a GWe•y basis as reprocessing plants and heavy water reactors (Table 9.3-2). Again it must be emphasized that the releases of tritium from fusion reactor plants are only preliminary estimates which can give an indication for confinement measures to be designed into such future plants. In this sense the difference in release rates between HIBALL and STARFIRE[8] stems only from differences in assumptions.

9.4 Accident Analysis

9.4.1 Introduction

In many respects an accident analysis for the HIBALL plant can only be very preliminary. As guidelines for the safety design and analysis of fusion reactors do not presently exist, one can only draw on the experience gained in fission reactor safety analysis and follow guidelines developed there.

Table 9.3-2. Tritium Release Rates from Fission and Fusion Reactor Plants on a GWe•y basis[7,8]

	Gaseous Ci/GWe/y	Liquid Ci/GWe/y
Pressurized Light Water Reactor (PWR)	45	400
Reprocessing for PWR	1100	3300
Heavy Water Reactor (HWR)	15000	7500
HIBALL	5800	1500
STARFIRE (Tokamak)	3200	800

The focus of the safety analysis must be on system or component failures which may lead to a major release of radioactivity to the environment. Following these lines, one has to distinguish between

- external events and
- internal accident sequences

leading either to containment failure or to failure of beam channels with large enough leaks for the release of radioactivity.

9.4.2 External Events

The reactor containment, the target factory and the beam channels must be designed according to safety standards usually determined by licensing authorities for a specific site to withstand:

- earthquakes,
- tornados and floods,
- airplane crash and gas cloud explosions.

These design requirements can be accommodated by a containment with an inner steel shell with high leak tightness and an outer 1.5 m thick concrete shell.

9.4.3 Internal Incidents

Plant internal incidents which may lead to accident sequences (listed without regard to probability of occurrence or possible countermeasures) are:

- power-cooling mismatch conditions, when the reactor plant is operating at full or partial load. Possible initiators are, e.g.
  - loss of off-site power
  - pump failures, leaks in coolant piping.

- failure to remove the decay heat after reactor shutdown due to loss of heat sinks (earthquake, loss of emergency power supply, component failure). The decay heat power of radioactive isotopes right at shutdown is about 1% of the full plant power.
- overpressurization of the containment as a consequence of chemical reactions, e.g., coolant-water reactions, coolant-concrete reactions generating hydrogen, coolant fires (lithium), combustion of hydrogen isotopes,
- power-cooling mismatch in the final focusing magnet or vacuum pumping systems, e.g., magnet quench or loss of cryogenic heat sinks,
- ion beams damaging the chamber wall, initiated by failure of pellet injection,
- stress induced failure of the vacuum system integrity leading to large leaks in beam channels or their connections to the reactor containment,
- failure of cryogenic cooling in the pellet manufacture and transport system, overpressurization of T_2 and D_2 containers.

This list of incidents potentially leading to severe accident sequences is certainly not complete. However, a conceptual plant design at this early stage does not warrant a detailed, quantitative safety and risk analysis. In addition, some of the physical processes, e.g. reactions of $Li_{17}Pb_{83}$ with air, water and concrete, are not yet fully understood. Only the results of small-scale experiments are available at present.[4,5] Although these experiments show rather mild chemical reactions of $Li_{17}Pb_{83}$ with water and air, much more information must become available on, e.g., the thermal interaction of hot coolant with water (vapor explosions) or aerosol generation during coolant-air reactions.

9.4.4 Accidental Releases of Radioactivity

Licensing regulations will require a consequence analysis of radioactivity releases from the reactor plant to the environment. This analysis will have to be performed following through all possible accident sequences which can lead to major radioactivity releases from the plant. As an example two such accident sequences are briefly described:

- As a consequence of an earthquake a stress induced leak in one or several beam channels close to the reactor could develop. Air could flow into the cavity and through chemical reaction of oxygen with $Li_{17}Pb_{83}$ a certain amount of aerosol would be generated. The cryopumps may heat up and release their tritium inventory. Both lead-lithium oxide aerosols and triti-

um would flow into the outer containment of the reactor or directly into the environment, depending upon where the leak develops.

- Loss of cryogenic heat sinks in the target manufacturing and storage facility may occur as a consequence of fire which also may damage the containment. Tritium may be released and penetrate through leaks to the environment.

As a detailed follow-up of a whole spectrum of accidents is not possible at the present stage of conceptual plant design, we consider a single example case instead. We assume that 0.5 kg of tritium (5×10^6 Ci) and 1% of the coolant activity in aerosol form would be suddenly released during an undefined severe accident. This assumption is not based on a deterministic analysis but rather represents a postulated conservative upper bound source term for radioactivity entering the environment. More realistic analysis may lead to substantially lower releases.

This puff release of radioactivity is assumed to occur from one of the four reactor containments of HIBALL each having about 1 GWe net output.

9.4.5 Cumulative Doses from Accidental Radioactivity Releases

The cumulative radiation dose a person receives at a certain distance from the reactor plant from a puff release of radioactivity depends on the release height and on the meteorological conditions, e.g., wind speed, wind direction and atmospheric dispersion rate. Cumulative dose equivalents were calculated[6] for the above activity released at a height of 100 m in two different weather situations. The exposure pathways considered were external exposure from the plume, external exposure from the ground, internal exposure via inhalation and internal exposure via ingestion of agricultural products harvested and consumed immediately after the accident. For dispersion category C (slightly unstable atmospheric conditions, $v = 3$ m/s at $H = 10$ m, no rain) the maximum dose is received at a distance of 500 m downwind from the exhaust stack and amounts to 105 mSv (10.5 rem). For dispersion category F (inversion, $v = 2$ m/s at $H = 10$ m, no rain) the maximum is found 8 km from the plant and amounts to 2.1 mSv.

Calculations for this 0.5 kg tritium release were also made assuming zero release height, i.e. direct leakage from a building. In this case, the maximum dose is received very close to the plant. The dose equivalent at a distance of 1 km is 360 mSv in inversion-type weather but only 40 mSv with a slightly unstable atmosphere.

It can be concluded that for these releases the dose equivalent would remain below 250 mSv (25 rem) at a distance of 2 km from the plant even in unfavorable weather conditions. A 2 km exclusion area boundary is roughly consistent with the extension of the HIBALL plant including the driver. The assumed releases thus stay below the 25 rem limit of Chapter 10 Part 100 of the U.S. Code of Federal Regulations and below the TFTR dose criterion for an accident with a probability of occurrence of 10^{-7} per year which is also defined as 25 rem at the plant exclusion area boundary.

References for Chapter 9

1. H. Runge, "Tritium-Bilanz und Verträglichkeit von SiC mit $Li_{17}Pb_{83}$ für Fusionsreaktorsystem HIBALL," Interatom Report INTAT 55.067756, February 1984.

2. Bundesministerium des Innern, Bundesrepublik Deutschland, Allgemeine Berechnungsgrundlage für die Strahlenexposition bei radioaktiven Ableitungen mit der Abluft oder in Oberflächengewässer, Gemeinsames Ministerialblatt 21, 369-436 (August 1979).

3. C. Halbritter and E. Lessmann, "Vergleich der Strahlenexposition aus Emissionen von Modell-Brennstoffkreisläufen für den Druckwasserreaktor und den Schnellen Brutreaktor," Kernforschungszentrum Karlsruhe Report KfK 3315 (1982).

4. L.D. Muhlestein, D.W. Jeppson and J.R. Barreca, "Summary of HEDL Fusion Reactor Safety Support Studies," Hanford Engineering Development Laboratory Report HEDL-SA-2360 (1980).

5. D.W. Jeppson and R.F. Keough, "Fusion Reactor Blanket and Coolant Material Compatibility," Hanford Engineering Development Laboratory Report HEDL-SA-2356 FP (1981).

6. A. Bayer and M. Bär, personal communication (1983).

7. International Tokamak Reactor, Phase One, Report of the International Tokamak Reactor Workshop, International Atomic Energy Agency, Vienna (1982).

8. "STARFIRE, A Commercial Tokamak Fusion Power Plant Study," Argonne National Laboratory Report ANL/FPP-80-1, September 1980.

10. COSTS

10.1 Capital Costs

The difference in the costs of the HIBALL-I and HIBALL-II power reactor systems is only in the driver. The cost of the new driver scenario utilizing B^{+1} ions has been determined by the GSI group. These costs include all the beam line elements leading all the way to the reactor chamber, including the final focusing magnets. Since the reactor chambers and the balance of plant have remained essentially unchanged, the original costs for those systems are used. These costs, however, were inflated to 1984 values at 3.6% which is the average annual inflation rate as given by the U.S. producer price index for special industry, machinery and equipment. An exchange rate of 2.897 DM per US$ is used to obtain the driver cost in dollars.

The costing methodology adopted is that provided in the U.S. DOE "Fusion Reactor Design Studies - Standard Accounts for Cost Estimates," PNL 2648. Most of the unit costs were taken from the US-INTOR study. The costs given are in constant dollars, that is no escalation due to inflation is used. Finally, the cost of the target factory is amortized over 30 years and is accounted for in the target costs. For a breakdown of chamber and balance of plant costs, the reader is referred to the HIBALL-I report.

Table 10.1-1 gives the new linac costs in DM and Table 10.1-2 the costs of the rings and beam transport. Table 10.1-3 gives the breakdown of the direct costs and Table 10.1-4, the indirect costs, interest during construction and the total costs in 1984 dollars. Since the analysis is in constant dollars, the interest during construction is based on a 5% annual deflated cost of capital. An 8 year construction period is used on the assumption that the driver, reactor plant and balance of plant construction can proceed in parallel. The interest during construction factor of 0.17 is taken from PNL 2648 for this set of conditions.

As is customary in conceptual design studies, costs of plant decommissioning have not been considered.

Table 10.1-1. Linac Cost (in MDM)

Source and injection	2 MDM x 8	16	
RFQ Linac	0.1 MDM/m x 320 m	32	
20 MHz Wideröe	0.15 MDM/m x 240 m	36	
40 MHz Wideröe	0.15 MDM/m x 416 m	62	
80 MHz Alvarez	0.1 MDM/m x 640 m	64	
320 MHz Alvarez	0.06 MDM/m x 5000 m	300	
Funnel section	2 MDM x 7	14	
Debuncher, energy + emit. meas., beam dump		6	
			530
RF < 80 MHz	0.75 MDM/MW x (40 + 52)	69	
RF 80 MHz	0.75 MDM/MW x (26 + 144)	128	
RF 320 MHz	0.53 MDM/MW x (500 + 1300)	954	
			1149
Controls		30	
Software		25	
			55
Cooling		150	
Air condition		50	
Electric power distribution		70	
Safety + communications		10	
			280
Injection building	200 DM/m^3 x 60 x 60 x 20 m	14	
Linac - low energy	9 kDM/m x 1200 m	11	
- high energy	13 kDM/m x 5000 m	66	
Equipment building	130 DM/m^3 x 15 x 15 x 6000 m	176	
Operation building		28	
Workshop and stores		40	
			335
			2,349

Table 10.1-2. Rings and Beam Transport Cost (in MDM)

Transfer rings, normal conducting	7.5 km		
0.1* MDM/m, incl. magnets, power suppl. vacuum, diagnostics, controls		750	
Storage and buncher rings, super cond.	15 km		
0.1 MDM/m, incl. magnets, refrigerator vacuum, diagnostics, controls		1,500	
Beam Lines, super cond.	24 km		
0.05 MDM/m, incl. magnets, refrigerator vacuum, diagnostics, controls		1,200	
Kickers and septa	5 MDM x 35	175	
Switching magnets	1 MDM x 20	20	
Beam combiner	1.5 MDM x 5	7.5	
RF system in storage rings	5 MDM x 10	50	
Timing and controls		35	
Correction dipoles	0.7 MDM x 80	56	
Final focusing	3.5 MDM x 80	280	
Remote handling equipment		10	
Cooling plant + distribution		130	
			4,214
Ring tunnels	10 kDM/m x 15 km	150	
Transport tunnels	8 kDM/m x 24 km	192	
Utility buildings for rings	10 MDM x 4	40	
Refrigerator + power supply buildings	3 MDM x 20	40	
			482
			4,696

*Unit prices taken from recent GSI and CERN research accelerator projects

Table 10.1-3. Breakdown of Direct Costs

	$ x 10^6 (1984)	
Reactor Plant		
Reactor cavities (4)	873	
Pellet injectors (4)	13	
Main heat transfer system	623	
RF linac	811	
Rings and beam transport	1621	3941
Balance of Plant		
Land and land rights	6	
Structures and site facilities	311	
Turbine plant and heat rejection	478	
Electric plant equipment	306	
Miscellaneous plant equipment	56	1157
		5098

Table 10.1-4. Indirect Costs and Interest During Construction

		$ x 10^6 (1984)
Total Direct Costs		5098
Indirect Costs		
Construction Facilities (15% of TDC)	765	
Engineering & Cost Management (15% of TDC)	765	
Owners' Costs (5% of TDC)	255	1785
Interest During Construction		1170
5%/yr Deflated Interest, 8 year Construction Period		
Grand Total Cost		8053

The net electrical power output of HIBALL is 3784 MWe. Thus the capital cost is:

$$\text{Capital Cost} = \frac{8053 \times 10^6}{3784 \times 10^3 \text{ kW}} = \$2128/\text{kWe} \ .$$

This can be compared with other recent fusion designs (adjusted at 3.6% per year to 1984$):

STARFIRE	2304 $/kWe
NUWMAK	2410
WITAMIR	2454
UWTOR-M	2183
MARS	2558

10.2 Busbar Costs

The busbar costs are given in Table 10.2-2. The breakdown is as follows.

10.2.1 Target Costs

The cost of the target factory was amortized in the target costs and thus does not appear as a direct cost. We assumed a $\$222 \times 10^6$ target factory cost which, after the indirect costs and interest during construction were added, became $\$350 \times 10^6$. The target cost breakdown is given in Table 10.2-1. At a 70% availability, the number of targets needed for all four cavities is 4.4×10^8/yr. The annual target cost is thus $\$74 \times 10^6$.

10.2.2 Operation and Maintenance

As provided in PNL 2648, the operation and maintenance was taken as 2% per year of the total capital cost, or $\$161 \times 10^6$.

10.2.3 Component Replacement

A two year lifetime was taken for the INPORT tubes and the upper blanket modules. The annual component replacement cost is thus $\$71 \times 10^6$.

10.2.4 Fixed Charge Rate on Capital

A straight 10% annual fixed charge rate on capital was used.

Table 10.2-1. Target Costs

	cents/target
30 year amortization of target factory	2.7
Operation and maintenance (2% p.a. of capital cost)	1.6
Fixed charge rate (10% annual)	8.0
Material (D_2, plastic, etc.)	2.2
Profit	2.2
	16.7

Table 10.2-2. HIBALL-II Busbar Costs

Assumptions: 70% availability
10% fixed charge rate
3784 MWe net power output = 2.32×10^{10} kWh per year

$$\text{Busbar costs} = \$ \frac{(74 \times 10^6 + 161 \times 10^6 + 71 \times 10^6 + 805 \times 10^6)\ 1000\ \text{mills/\$}}{2.32 \times 10^{10}\ \text{kWh}}$$

$$= 47.9\ \text{mills/kWh} .$$

Some of the other recently designed fusion power systems have the following busbar costs (adjusted at 3.6% annual inflation rate to \$1984):

STARFIRE	40.4 mills/kWh
NUWMAK	40.9
WITAMIR	41.6
UWTOR-M	38.6
MARS	47.9

10.3 Comparison of HIBALL-I and HIBALL-II Costs

The only difference in the costs of HIBALL-I and HIBALL-II is in the driver. The unit costs used in HIBALL-II are more recent, better verified and therefore more reliable. The cost of the HIBALL-I driver was 4718 MDM (1981) and the HIBALL-II driver 7045 MDM (1984) or 49% higher. When HIBALL-I is escalated at 3.6% to 1984, the difference is only 34%.

To gain a perspective on the different driver scenarios, two cost comparisons have been made. In the first case, the original cost of the HIBALL-I driver was escalated at 3.6% to 1984 using the 1984 rate of exchange. Table 10.3-1 shows that in this case, the capital cost for HIBALL-II was 14% and the busbar cost, 11% higher than in HIBALL-I. In the second case, shown in Table 10.3-2, the new HIBALL-II driver unit costs were applied to the HIBALL-I driver. It is interesting to note that the difference in the driver cost is only 4.8% higher for HIBALL-II. Further, the capital cost and busbar cost is higher by 1.7% and 1.3%, respectively.

Of the two comparisons the second one is more realistic. Table 10.3-2 shows that the more credible HIBALL-II driver scenario, evaluated using current unit costs does not increase the total capital and busbar costs over the HIBALL-I case when the same unit costs are applied to both systems.

Table 10.3-1. Comparison of HIBALL-I and HIBALL-II Costs (Case 1)
(Original unit costs applied to HIBALL-I driver)

	HIBALL-I $ x 10^6 (1984)	HIBALL-II $ x 10^6 (1984)	% Difference
Driver 1981 MDM	4718		
Driver 1984 MDM	5244	7045	
Driver 1984 US$	1810.3	2432	34
Reactor Plant Incl. Driver	3319	3941	19
Balance of Plant	1157	1157	0
Indirect Costs	1567	1785	14
Interest Dur. Const.	1027	1170	14
Total Capital Costs	7070	8053	14
Unit Cap. Cost $/kWe	1868	2128	14
Busbar Cost mills/kWh	43.7	47.9	11

Table 10.3-2. Comparison of HIBALL-I and HIBALL-II Costs (Case 2)

(HIBALL-II unit costs applied to both drivers)

	HIBALL-I $ x 10^6 (1984)	HIBALL-II $ x 10^6 (1984)	% Difference
Driver MDM	6725	7045	
Driver US$	2321	2432	4.7
Reactor Plant Incl. Driver	3834	3941	2.8
Balance of Plant	1157	1157	0
Indirect Costs	1748	1785	2.1
Interest During Const.	1149	1170	1.8
Total Capital Costs	7888	8053	2.1
Unit Capital Costs $/kWe	2093	2128	1.7
Busbar Cost, mills/kWh	47.3	47.9	1.3

APPENDIX A. TECHNICAL PARAMETER LIST

Contents

I. GENERAL PARAMETERS

	HIBALL-I	HIBALL-II
Average DT power - 17.6 MeV/fusion (MW)	8000	8000
Target power (MW)	7920	7920
Target multiplication	0.99	0.99
Target yield (MJ)	396	396
Driver pulse energy (MJ)	5.0	5.0
Target energy requirement (MJ)	4.8	4.6
Overall driver efficiency (%)	26.5	26.5
Target gain	83	87
Fusion gain nG	22	23
Blanket multiplication	1.274	1.274
Total nuclear thermal power (MW)	10193	10193
Gross power	10272	10272
Gross thermal efficiency (%)	42	42
Gross electrical output (MW)	4278	4314
Recirculating power fraction	0.12	0.12
Net electrical output (MW)	3768	3784
# of chambers	4	4
Chamber repetition rate (Hz)	5	5
Chamber geometry	cylindrical	cylindrical
Chamber diameter (m)	14	14
Chamber height (m) (at vacuum wall)	10	10
Chamber alloy	HT-9	HT-9
# of beam ports per chamber	20	20
Breeding material	$Li_{17}Pb_{83}$	$Li_{17}Pb_{83}$
Breeding ratio	1.25	1.25

II. TARGET PARAMETERS

	HIBALL-I	HIBALL-II
Composition		
D (mg)	1.6	1.6
T (mg)	2.4	2.4

II. TARGET PARAMETERS (continued)

	HIBALL-I	HIBALL-II
DT load (mg)	4.0	4.0
Material #1 (mg)	LiPb 67.1	Li 54.5
Material #2 (mg)	Pb 288	Pb 330
Burnup (%)	30	30
Total mass (mg)	359	388.5
Configuration (# of layers)	3	5
Target diameter (cm)	0.6	0.796
Absorbed ion energy (MJ)	4.8	4.56
No burn ignition temperature (keV)	5	1
Fuel ρR at ignition (g/cm^2)	2	2
Hot spot ρR at ignition (g/cm^2)	0.4	0.4
Pusher ρR at ignition (g/cm^2)	1	2.7
DT yield (MJ)	400	400
Target yield (MJ)	396	396
Target energy multiplication	0.99	0.99
Average DT power (MW)	8000	8000
Target power (MW)	7920	7920
Target gain	83	87
Neutron yield (MJ)	284.8	284.8
Neutron spectrum, $\bar{E}$ (MeV)	11.98	11.98
Neutron multiplication	1.046	1.046
Gamma yield (MJ)	0.6	0.6
Gamma spectrum, $\bar{E}$ (MeV)	1.53	1.53
X-ray yield (MJ)	89.5	89.5
X-ray spectrum - blackbody (keV)	see histogram	see histogram
Debris yield (MJ)	21.0	21.0
Debris spectrum (keV/amu)	0.6	0.6
Radioactivity production (Ci/target @ t = 0)	1.2×10^6	1.2×10^6
Target injection velocity (m/s)	200	200
Target injector type	gas gun	gas gun
Target tracking	optical	optical
Target cost	15¢	16.7¢

III. TARGET DELIVERY PARAMETERS

	HIBALL-I	HIBALL-II
Target delivery		
Longitudinal positioning tolerance (mm).....	0.5	0.5
Lateral positioning tolerance (mm).....	0.7	0.7
Target velocity (m/s).....	200	200
Repetition Frequency (Hz).....	5	5
Injection:		
Type.....	gas gun	gas gun
Projectile (sabot+target) mass (g).....	2	2
Propellant gas amount (torr liters/shot).....	608	608
Propellant gas.....	D_2	D_2
Total prop. gas handled (mg/shot).....	141	141
Buffer cavity pressure, min, (torr).....	1	1
max, (torr).....	2	2
Buffer cavity volume (m^3).....	0.88	0.88
Injection channel diameter (mm).....	10	10
Prop. gas entering reactor cavity (mg/shot)..	1.6	1.6
Gas gun total efficiency.....	0.5	0.5
Gun barrel diameter (mm).....	10	10
Pressure of prop. gas reservoir (Bar).....	5	5
Acceleration distance (m).....	2	2
Acceleration (m/s^2).....	10^4	10^4
Acceleration time (ms).....	20	20
Total target travel time (ms).....	80	80
Tolerance on total travel time (ms).....	±5	±5
Distance muzzle to focus (m).....	12	12
Tracking:		
Lateral tracking.....	none	none
Longitudinal tracking, type.....	light-beam interception	light-beam interception
Tracking position 1, distance from focus (m)	5.5	5.5
Tracking position 2, distance from focus (m)	3.0	3.0
Light beam diameter (mm).....	0.2	0.2
Precision of arrival time prediction (μs)....	±1	±1
Duration of processing tracking results (ms)	1	1

IV. DRIVER PARAMETERS

	HIBALL-I	HIBALL-II
Ion		
Type	Bi	Bi
Charge state	+2	+1
Energy (GeV)	10	10
Velocity v (m/s)	9.25×10^7	9.25×10^7
Beta, $\beta = v/c$	0.30875	0.30875
Gamma, $\gamma = (1 - \beta^2)^{-1/2}$	1.051	1.051
Magnetic stiffness (tesla • meters)	107.7	210.7
Mass number	209	209
Driver System		
Ion pulse energy (MJ)	5.0	5.0
Repetition rate (Hz)	20	20
Effective main pulse width (ns)	20	20
Number of final beams	20	20
Electric current per final beam (kA)	2.5	1.25
Driver efficiency (%)	26.5	26.5
Max. storage time (ms)	40	4
Ion source		
Type	"Elsire"	"HORDIS"
Ion electric current per source (mA)	20	21
Number of sources	8	8
Normalized source emittance (m)	2×10^{-7}	2×10^{-7}
Accelerator		
Type	RF Linac	RF Linac
Efficiency (%)	33.3	33.5
Length (km)	3.0	5
Effective voltage drop, U_Σ (GV)	5	10
Beam current during single pulse (mA)	160	165
Average beam current in pulse train (mA)	144	132
Single pulse length (μs)	15	1.6
Length of pulse train (ms)	7.5	3.84
Pulses per train	450	1920
Repetition rate of pulse trains (Hz)	20	20

IV. DRIVER PARAMETERS (continued)

	HIBALL-I	HIBALL-II
RF duty cycle	0.16	0.08
Momentum width, $\Delta p/p$	$\pm 5 \times 10^{-5}$	$\pm 1 \times 10^{-4}$
Linac emittance, normalized (m)	6×10^{-7}	3×10^{-7}
Beam power (GW)	0.8	1.32
RF power (GW)		2.6
RF power/length (MW/m)		0.52
Mains power (MW)	300	300
First section		
Type	RFQ	RFQ
No. of branches	8	8
Frequency (MHz)	13.5	10
Type of amplifier		Tetrode
Last section		
Type	Alvarez	Alvarez
Frequency (MHz)	324	320
Type of amplifier	Klystron	Klystron
Debuncher frequency (MHz)	108	80
Chopper between linac and TR	no	yes
Transfer rings		
Number of rings	1	5
Average radius (m)	663	236
Average dipole field (T)	0.16	0.89
Revolution time (μs)	45	16
Injection, radial stacking		
# turns	3	3 (first 2 rings) 1 (other rings)
Maximum dilution factor	2	2.7
Maximum beam current (A)	0.46	0.5 (first ring) 3.2 (last ring)
Tune depression		
Horizontal	0.36	0.09 ... 0.41
Vertical	0.87	0.26 ... 0.32
Momentum width, $\Delta p/p$	$\pm 5 \times 10^{-5}$	$\pm 1 \times 10^{-4}$

IV. DRIVER PARAMETERS (continued)

	HIBALL-I	HIBALL-II
Beam emittance		
Horizontal (m)	12×10^{-6}	7.5×10^{-6}
Vertical (mm-mrad)	2×10^{-6}	12.5×10^{-6}
Betatron oscillations per turn		
ν_{Ho}	59.85 (?)	9.85
ν_{Vo}	59.85 (?)	$< \nu_{Ho}$
Vacuum pressure (torr)	10^{-9}	10^{-9}
Ejection kicker		
Flat top time (μs)	45	45
Rise time (μs)	< 1	< 2
Reset time (μs)	< 15	< 15
Kicking angle (mrad)	2.5	2.5
Stored energy per shot (kJ)	0.05	0.05
# kicks per shot	50	80 (first) 10 (last)
Power (kW) (η = 0.2)	50	50
Beam rotator	yes	no
Condenser rings		
# of rings	5	none
Injection radial stacking		
# of turns	3	3
Maximum dilution factor	1.67	1.67
Beam emittance		
Horizontal (m)	10×10^{-6}	10×10^{-6}
Vertical (m)	12×10^{-6}	12×10^{-6}
Average dipole field, $\overline{B}$ (tesla)	0.477	0.477
Average radius (m)	221.1	221.1
Revolution time (μs)	15	15
Coasting beam current (A)	1.38	1.38
Vacuum pressure (torr)	$< 10^{-10}$	$< 10^{-10}$
Ejection kickers (1 per ring)		
Flat top time (μs)	> 15	> 15
Rise time (μs)	< 1	< 1

IV. DRIVER PARAMETERS (continued)

	HIBALL-I	HIBALL-II
Reset time (μs)	≤ 100	≤ 100
Kicking angle (mrad)	2.5	2.5
Stored energy per shot (kJ)	0.1	0.1
Average frequency of shots (s^{-1})	40	40
Power per CR, η = 0.2 (kW)	20	20
Storage rings		
# of rings	10	10
Injection, radial stacking		
# of turns	3	2
Maximum dilution factor	1.5	2
Beam emittance		
Horizontal (m)	4.5×10^{-5}	3.0×10^{-5}
Vertical (m)	9.0×10^{-5}	3.0×10^{-5}
Average dipole field, $\overline{B}$ (tesla)	1.431	1.78
Average radius (m)	73.7	118
Tune depression		
Horizontal	0.3 ... 3.3	0.24
Vertical	0.2 ... 2.3	0.24
Momentum width, Δp/p	$\pm 8 \times 10^{-5}$	$\pm 1 \times 10^{-4}$
Revolution time (μs)	5	8
Maximum beam current (A)	21	12.5
Betatron oscillations per turn	40 (?)	40 (?)
ν_{Ho}	9.85 (?)	9.85 (?)
ν_{Vo}	$\leq \nu H_o$	$\leq \nu H_o$
Vacuum pressure (torr)	10^{-10}-10^{-11}	10^{-10}-10^{-11}
RF 1 (MHz)	0.4	0.25
RF 2 (MHz)	---	0.75
RF 3 (MHz)	---	1.0
Power for ferrite RF cavities (kW/ring)		10
Adiabatic compression	yes	no
Harmonic number	2	2
Initial volts per turn (kV)	2	2
Final volts per turn (kV)	200	200

IV. DRIVER PARAMETERS (continued)

	HIBALL-I	HIBALL-II
Rise time (ms)	10	10
Initial $\Delta p/p$	$\pm 3 \times 10^{-5}$	$\pm 3 \times 10^{-5}$
Final $\Delta p/p$	$\pm 5 \times 10^{-4}$	$\pm 5 \times 10^{-4}$
Final $\Delta\Phi$	$\pm 15°$	$\pm 15°$
Final Δt (ns)	± 100	± 100
Separatrix $\Delta p/p$	$\pm 3 \times 10^{-3}$	$\pm 3 \times 10^{-3}$
Synchrotron freq/revolution freq	1/350	1/350
Ejection kickers		
# of kickers per ring	1	1
Kicking angle (mrad)	6*	6*
Rise time (μs)	1.5	≤ 2
Flat top time (ns)	≥ 500	1200
Stored energy per shot (kJ)	2	2
Average frequency of shots (s^{-1})	20	20
Power per kicker, $\eta = 0.2$ (kW)	40	40
Fast compression induction linacs (space charge effects included)		
# of compressors	20	none
Length per compressor (m)	200	
Voltage (MV)	300	
Pulse shape	sawtooth	
Pulse length (ns)	200	
Focal length (km)	0.8	
$\Delta p/p$	$\pm 5 \times 10^{-3}$	
Buncher rings		
# of rings	none	10
Ave. radius, dipole field, rev. time, betatron osc		as storage rings
Injection, # turns		1
Beam emittances		
Horizontal (m)		3×10^{-5}
Vertical (m)		3×10^{-5}

*For 4 cm hor. beam width (space charge).

IV. DRIVER PARAMETERS (continued)

	HIBALL-I	HIBALL-II
Tune depression at ejection		~ 3
Momentum width, $\Delta p/p$ at ejection	3×10^{-5}	$\pm 1.3 \times 10^{-2}$
# of bunches per ring		2
Beam current at ejection (A)		~ 165
Bunch length		
Injection (μs)		2.0
Ejection (μs)		~ 0.15
# of turns		~ 20
RF		
f_1 (MHz)		0.25
U_1 (MV)		12.5
f_2 (MHz)		0.5
U_2 (MV)		-1.3
Ejection kickers		
# per ring		2
Rise time (μs)		≤ 3
Vacuum pressure (torr)		10^{-10}
Beam lines		
Total number	20	20
Length (km) per long beam line	1.2	?
# into each chamber (short)	20	20
Length (km)	0.3	?
Total length of all beam lines (km)	48	?
Lattice period (m)	> 2.8	≤ 5.6
Phase advance	$\pi/3$	$\pi/3$
Beam tube inner diameter (cm)	8	8
Beam chamber entry		
Final focusing magnets	quadrupoles	Q's + dipoles
Maximum field at beam envelope (T)	5.4	1.8
Distance from FFM to target (m)	8.5	8.5
Clearance for cavity-beam line vacuum pump (m)	2	2
Cavity pump down time between shots (ms)	150	150

IV. DRIVER PARAMETERS (continued)

	HIBALL-I	HIBALL-II
Beam port dimensions (cm)		
Vertical	103	21.6
Horizontal	34.3	16.6
Distance from beam port to target (m)	7.27	7.27
Final Beams		
Eff. width of main pulse (ns)	20	20
Momentum width, $\Delta p/p$	$\pm 5 \times 10^{-3}$	$\pm 1 \times 10^{-2}$
Electric peak current per beam (A)	2500	1250
Pulse energy (MJ)	5.0	5.0
Maximum power (TW)	250	250
Pulse repetition rate (Hz)	20	20
Focused spot diameter (mm)	6	8
Fraction of ions within spot (%)	80	79
Unnormalized emittance per beam (m)		
Vertical	1.2×10^{-4}	3×10^{-5}
Horizontal	4.5×10^{-5}	3×10^{-5}

V. CHAMBER PARAMETERS

	HIBALL-I	HIBALL-II
Coolant and breeding material	$Li_{17}Pb_{83}$	$Li_{17}Pb_{83}$
Li-6 enrichment, %	natural	natural
INPORT tube Region		
Inport tube structural material and v/o	SiC-2	SiC-2
Inport tube coolant v/o	97.3	97.3
Tube region support structure v/o	HT-9-0.7	HT-9-0.7
First surface radius (m)	5	5
Region thickness (m)	2	2
Region density factor	0.33	0.33
Effective coolant thickness (m)	0.66	0.66
Mass of coolant in tubes/cavity (tonnes)	2295	2295
Tubes		

V. CHAMBER PARAMETERS (continued)

	HIBALL-I	HIBALL-II
Length (m)	10	10
Diameter (cm)		
First two rows	3	3
Wall thickness (mm) [100% density factor]	0.8	0.8
Remaining rows	10	10
Wall thickness (mm)	2	2
Number		
First two rows	1230	1230
Remainder	3060	3060
Number of penetrations in region	20	20
Total area of beam penetrations at first surface (m^2)	3.6	0.37
Pb at. density - ($atom/cm^3$)*	4×10^{10}	4×10^{10}
Noncondensable at. density @ 500°C		
- $atoms/cm^3$	0.13×10^{10}	0.13×10^{10}
Pressure - torr	$< 10^{-4}$	$< 10^{-4}$
Chamber top		
Structural material (v/o)	HT-9 (1)	HT-9 (1)
Tube material (v/o)	SiC (2)	SiC (2)
Coolant v/o	97	97
Height at chamber centerline (m)	6.5	6.5
Region thickness (m)	0.5	0.5
Mass of coolant in top region (tonnes)	717	717
Number of penetrations in top	1	1
Total area of penetrations at chamber inner surface (m^2)	3.1×10^{-4}	3.1×10^{-4}
Chamber bottom pool		
Structural material and v/o	---	---
Coolant v/o	100	100
Minimum distance from pool to target (m)	5	5
Region thickness (m)	1.0	1.0

*Just before shot.

V. CHAMBER PARAMETERS (continued)

	HIBALL-I	HIBALL-II
Mass of coolant in bottom pool per chamber (tonnes)	1448	1448
Maximum 1st surface neutron energy current - at chamber midplane (MW/m^2)	4.54	4.54
Neutrons passing through each beam line penetration per shot	8.14×10^{16}	1.63×10^{16}
Maximum total 1st surface X-ray and debris heat flux (J/cm^2)	34.5	34.5
DT power per cavity (MW)	2000	2000
Total n & γ power in cavity (MW)	1667.4	1667.4
Tube region	1097.1	1097.1
Cavity top	293.1	293.1
Cavity bottom	277.2	277.2
Total power in cavity, including X-rays and debris (MW)	2208.7	2208.7
Energy multiplication[1]	1.1	1.1
n & γ energy multiplication[2]	1.17	1.17
Average power density (W/cm^3)	3.44	3.44
Tube region	4.41	4.41
Top region	3.51	3.51
Bottom region	1.80	1.80
Peak/average spatial power density in tube region	4.87	4.87
Impulse on first row of tubes ($dyne\text{-}s/cm^2$)	600	600
Amount of coolant blown off per shot (kg)	13	13
Maximum DPA/FPY in SiC		
Tube region	118	118
Top region	70	70
Maximum He production in SiC (appm/FPY)		
Tube region	3705	3705
Top region	2192	2192
Bottom region	---	---

[1] Total energy deposited in region/DT yield

[2] Total n & γ energy deposited in region/n & γ energy incident on 1st surface.

V. CHAMBER PARAMETERS (continued)

	HIBALL-I	HIBALL-II
Tritium breeding ratio	1.216	1.216
^{6}Li	1.190	1.190
Tube region	0.729	0.729
Top region	0.226	0.226
Bottom region	0.235	0.235
^{7}Li	0.026	0.026
Tube region	0.081	0.081
Top region	0.004	0.004
Bottom region	0.004	0.004
Coolant		
Inlet temperature (°C) first row & other tubes	330	330
Outlet temperature (°C) first row & other tubes	500	500
Flow rate/cavity (kg/hr)	2.94×10^{8}	2.94×10^{8}
Maximum velocity within tubes in first two rows (m/s)	5	5
Maximum velocity within tubes not in the first two rows (m/s)	1.3	1.3
Pressure @ rear INPORT tube entrance (MPa)	0.2	0.139
ΔP for entire loop (MPa)	2.0	2.0
Pumping power delivered to coolant per cavity (MW)	17.9	17.9

VI. CHAMBER, REFLECTOR AND SHIELD REGION PARAMETERS

	HIBALL-I	HIBALL-II
A. Vacuum Boundary Wall		
Structural material	HT-9	HT-9
Side wall		
Inside diameter (m)	14	14
Thickness (m)	0.01	0.01
Height (m)	12.0	12.0

VI. CHAMBER, REFLECTOR AND SHIELD REGION PARAMETERS (continued)

	HIBALL-I	HIBALL-II
Average power density (W/cm^3)	1.65	1.65
Side wall	1.22	1.22
Power deposited in vacuum wall per cavity (MW)	11.0	11.0
Maximum DPA/FPY		
Side wall	2.69	2.69
Peak instantaneous dpa rate (dpa/s) - side wall at midplane	0.009	0.009
Maximum He production (appm/FPY)		
Side wall	0.364	0.364
Peak instantaneous He production rate (appm/s) - side wall at midplane	0.11	0.11
Maximum temperature (°C)	520	520
Expected lifetime (FPY)	24	24
B. Reflector		
Structural material	HT-9	HT-9
Coolant	$Li_{17}Pb_{83}$	$Li_{17}Pb_{83}$
Side reflector		
Inside diameter (m)	14.02	14.02
Thickness (m)	0.4	0.4
Mass of structure (tonnes)	1530	1530
Mass of coolant (tonnes)	205	205
v/o of structure	90	90
v/o of coolant	10	10
Top reflector		
Thickness (m)	0.4	0.4
Mass of structure (tonnes)	432	432
Mass of coolant (tonnes)	58	58
v/o of structure	90	90
v/o of coolant	10	10
Bottom reflector (splash plate)		
Thickness (m)	0.4	0.4
Mass of structure (tonnes)	484	484
Mass of coolant (tonnes)	65	65
v/o of structure	90	90

VI. CHAMBER, REFLECTOR AND SHIELD REGION PARAMETERS (continued)

	HIBALL-I	HIBALL-II
v/o of coolant	10	10
Total mass of structural material in reflector per chamber (tonnes)	2446	2446
Total mass of coolant in reflector per chamber (tonnes)	328	328
Average power density (W/cm^3)	0.941	0.941
Side reflector	0.939	0.939
Top reflector	1.465	1.465
Bottom reflector (splash plate)	0.257	0.257
Radial + axial peak/average spatial power density - in side reflector	4.577	4.577
Power deposited in reflector per chamber (MW)	318.3	318.3
Side	211.1	211.1
Top	91.4	91.4
Bottom	15.8	15.8
Maximum DPA/FPY		
Side reflector	2.43	2.43
Top reflector	4.50	4.50
Bottom reflector	1.36	1.36
Maximum He production in structural material (appm/FPY)		
Side reflector	0.300	0.300
Top reflector	0.715	0.715
Bottom reflector	0.006	0.006
Tritium breeding ratio	0.034	0.034
^6Li	0.034	0.034
Side	0.022	0.022
Top	0.010	0.010
Bottom	0.002	0.002
^7Li	4×10^{-6}	4×10^{-6}
Side	2×10^{-6}	2×10^{-6}
Top	2×10^{-6}	2×10^{-6}
Bottom	0	0

VI. CHAMBER, REFLECTOR AND SHIELD REGION PARAMETERS (continued)

	HIBALL-I	HIBALL-II
Coolant		
Mass of coolant within reflector per chamber (tonnes)	328	328
Flow rate/chamber (kg/hr)	4.4×10^7	4.4×10^7
Inlet temperature (°C)	330	330
Outlet temperature (°C)	500	500
Maximum coolant velocity (m/s)	1	1
Pressure (MPa)	2	2
ΔP for entire loop (MPa)	0.7	0.7
Pumping power delivered to coolant per chamber (MW)	1	1
Maximum structure temperature (°C)	550	550
Radioactivity (Ci)	1.2×10^9	1.2×10^9
C. Shield		
Material (v/o)	concrete (95)	reinforced concrete (95)
Coolant (v/o)	H_2O (5)	H_2O (5)
Side shield		
Inside diameter (m)	14.82	14.82
Thickness (m)	3.5	2.9
Top shield		
Height above midplane at centerline (m)	7.41	7.41
Thickness (m)	3.5	2.9
Bottom shield		
Height below midplane (m)	6.40	6.40
Thickness (m)	3.5	2.9
Maximum power density at midplane (W/cm^3)	0.045	0.045
Average power density (W/cm^3)	0.0018	0.0022
Power deposited in shield/chamber (MW)	6.82	6.82
Dose rate at outer surface of shield at midplane (mrem/hr)	2.64	2.2
neutron	1.4×10^{-5}	10^{-4}
gamma	2.64	2.2
Peak DPA rate in F.F. magnet stabilizer (DPA/FPY)	4.48×10^{-6}	1.8×10^{-5}

VI. CHAMBER, REFLECTOR AND SHIELD REGION PARAMETERS (continued)

	HIBALL-I	HIBALL-II
Peak radiation dose rate in F.F. magnet insulator (Rad/FPY)	7.2×10^{6}	3×10^{7}
Peak power density in F.F. magnets (W/cm^3)	5.35×10^{-7}	7.6×10^{-6}
Coolant		
Inlet temperature (°C)	45	45
Outlet temperature (°C)	60	60
Flow rate per cavity (kg/hr)	3.6×10^{5}	3.6×10^{5}
Maximum velocity (m/s)	1	1
Pressure (MPa)	0.5	0.5
ΔP in entire loop (MPa)	0.2	0.2
Pumping power delivered to coolant/chamber (MW)	1.4	1.4
Peak structure temperature (°C)	60	60

VII. BALANCE OF PLANT

	HIBALL-I	HIBALL-II
Steam temperature (°C)	482	482
Steam pressure (MPa)	15.5	15.5
Steam flow rate (kg/hr)	1.8×10^{7}	1.8×10^{7}
Feedwater temperature (°C)	300	248
Reheat temperature (°C)	482	482
Steam generator surface area (m^2)	5.2×10^{4}	5.2×10^{4}
Steam generator		
Material composition	HT-9	HT-9
Wall thickness (mm)	1.0	1.0
Primary inlet temperature (°C)	330	330
Primary outlet temperature (°C)	500	500
Tritium permeation rate to H_2O (Ci/d)	0.38	0.02

VIII. SYSTEM POWER FLOW PARAMETERS

	HIBALL-I	HIBALL-II
Average DT power per cavity (MW)	2000	2000
Total power recoverable per cavity (MW)	2548	2548
Blanket & reflector energy multiplication	1.274	1.274
Total pumping power delivered to coolant per cavity (MW)	20	20
Gross power per cavity (MW)	2568	2568
Gross power per 4 cavities (MW)	10272	10272
Gross thermal efficiency (%)	42	42
Gross plant output (MWe)	4298	4314
Recirculating power (MWe)	530	530
Driver system	375	375
Linac	300	300
Rings, beam handling & transport, final focus	75	75
Target manufacture and delivery (MW)	?	?
Coolant pumps	110	110
Vacuum pumps	5	5
Plant auxiliaries	40	40
Net plant output (MWe)	3768	3784
Net plant efficiency (%)	36.7	36.8

IX. MATERIAL BALANCE IN CHAMBER GAS

	HIBALL-I	HIBALL-II
Material inserted per shot		
D - target (mg)	1.6	1.6
(# of atoms)	4.8×10^{20}	4.8×10^{20}
T - target (mg)	2.4	2.4
(# of atoms)	4.8×10^{20}	4.8×10^{20}
Li - target (mg)	26.5	26.5
(# of atoms)	2.37×10^{21}	2.30×10^{21}
Pb - target (mg)	329	329
(# of atoms)	9.56×10^{20}	9.85×10^{20}

IX. MATERIAL BALANCE IN CHAMBER GAS (continued)

	HIBALL-I	HIBALL-II
Bi - ion beam (mg)	1.0×10^{-3}	1.0×10^{-3}
(# of atoms)	3.0×10^{15}	3.0×10^{15}
Li - INPORT blowoff (g)	79	79
(# of atoms)	6.85×10^{24}	7.1×10^{24}
Pb - INPORT blowoff (g)	13×10^{3}	13×10^{3}
(# of atoms)	3.8×10^{25}	3.9×10^{25}
Nonvolatiles (g)	1.4×10^{4}	1.3×10^{4}
(# of atoms)	4.52×10^{25}	4.6×10^{25}
D_2 (target injector) mg/shot	1.6	1.6
# of atoms	4.8×10^{20}	4.8×10^{20}
Total D, T, D_2 (mg)	5.6	5.6
(# of atoms)	1.44×10^{21}	1.44×10^{21}
Fractional burnup, $f_b = T_b/(T_b + T_p)$	0.29	0.29
Material evacuated per shot		
D - target, unburned (mg)	1.1	1.14
(# of atoms)	3.4×10^{20}	3.53×10^{20}
T - target, unburned (mg)	1.7	1.7
(# of atoms)	3.4×10^{20}	3.52×10^{20}
D_2 (target injector) - mg/shot	1.6	1.6
- # atoms	4.8×10^{20}	4.8×10^{20}
T - lost from coolant (mg)	0.88	0.87
(# of atoms)	1.76×10^{20}	1.8×10^{20}
He-DT fusion reaction (mg)	0.94	0.90
(# of atoms)	1.4×10^{20}	1.4×10^{20}
He-breeder production (mg)	1.17	1.13
(# of atoms)	1.76×10^{20}	1.75×10^{20}
He - total (mg)	2.11	2.03
(# of atoms)	3.17×10^{20}	3.15×10^{20}
Total (D, T, He, D_2/Target inj.) (mg)	7.39	7.36
Total # of atoms	1.65×10^{21}	1.68×10^{21}
# of shots per chamber per second	5	5
# of chambers	4	4
Total condensables pump rate/chamber (g/s)	0	0

IX. MATERIAL BALANCE IN CHAMBER GAS (continued)

	HIBALL-I	HIBALL-II
Total noncondensables pump rate/chamber (g/s)..	0.037	0.037
Cavity pressure (torr @ 0°C).....	10^{-4}	10^{-4}

X. BREEDING PARAMETERS

	HIBALL-I	HIBALL-II
Coolant breeding region		
Breeding material.....	$Li_{17}Pb_{83}$	$Li_{17}Pb_{83}$
Flow rate for one chamber (kg/hr).....	3.38×10^{8}	3.38×10^{8}
Breeder mass within one chamber (kg).....	4.46×10^{6}	4.46×10^{6}
Total breeder mass for all chambers (kg).....	1.78×10^{7}	1.78×10^{7}
Inlet temperature (°C).....	330	330
Outlet temperature (°C).....	500	500
Breeding ratio.....	1.25	1.25
Steady state tritium concentration (wppm)....	6.1×10^{-4}	1.4×10^{-4}
Tritium pressure (torr @ 0°C).....	10^{-4}	10^{-4}
Tritium extraction method.....	In situ extraction	In situ vacuum degassing
Tritium inventory - steady state - 4 chambers		
Reactor chamber (SiC + LiPb) (kg).....	0.026	0.015
Pipes/steam generator (kg).....	0.033	0.007
Cryopumps (2 hr on-line) - kg.....	0.37	0.37
Cryogenic distillation columns (kg).....	0.16	0.083
Fuel cleanup (kg).....	0.042	0.031
Target fabrication.....	4.1	4.1
Storage - 2 days fuel supply (kg).....	8.4	8.2
Total (kg).....	13.1	12.8
Total active inventory (kg).....	4.7	4.6
Total vulnerable inventory (Ci).....	4.7×10^{7}	4.6×10^{7}

APPENDIX B. COST OPTIMIZATION FOR HIBALL

B.1 Introduction

The HIBALL-I heavy ion beam fusion reactor design[1] completed in July 1981 is a self-consistent detailed point design. Upon completion of a point design such as HIBALL, the next step is to determine whether the specific parameters chosen for the point design represent an optimum set.

The optimization criterion used for this analysis is the true "bottom line," the busbar cost. However, to vary every major parameter in HIBALL-I to test its cost sensitivity is a task requiring a "systems analysis" computer model. Such an effort is beyond the scope of this project. Instead, only a single parameter was varied, the ion energy between three specific values, 5 GeV, 10 GeV and 20 GeV. The 10 GeV value represents the base case and all parameters for this case are taken from the HIBALL-I study. The 5 GeV and 20 GeV cases clearly represent an attempt to determine the economic penalties or payoffs associated with lower and higher ion energies. The variation in ion energy cannot be made while holding everything else fixed. For instance, the target gain will change with changing ion energy, hence the yield will change, leading to a change in the cavity size. Therefore it was tried to construct a self-consistent set of parameters for the 5 and 20 GeV cases by scaling from the 10 GeV HIBALL-I values. In this way systems can be compared at three different ion energies without repeating a complete conceptual design for each.

B.2 Accelerator, Storage Rings and Beam Lines

Varying the ion energy has a great effect on the design and cost of the accelerator, storage rings, and beam lines (i.e., the driver). Higher energies increase the accelerator length and its cost. However, space charge limits are reduced, hence the storage rings and beam lines are modified. The opposite is true for lower energies. All relevant driver costs are reproduced in Table B-1.

B.3 Target

The target does not figure directly into the cost but it plays a very important role in this analysis because different ion energies produce different target gains and hence different yields. Therefore we must have a general model of target performance that will include these effects. For this we used the target design analysis of J. Meyer-ter-Vehn and N. Metzler[1] and the gain model of Bodner.[2] The coupling efficiency versus ion energy taken from the Meyer-ter-Vehn/Metzler work is plotted in Fig. B-1.

Table B-1. Driver Parameters and Relative Costs for 5, 10 and 20 GeV Ions

		5 GeV		10 GeV	20 GeV
E_{ion}		5 GeV		10 GeV	20 GeV
Q_{pulse}		2.5 MJ		5 MJ	10 MJ
τ_{full}*		15 ns		15 ns	15 ns
τ_{eff}*		10 ns		10 ns	10 ns
P_{max}		250 TW		500 TW	1000 TW
Ion		Bi^{2+}	Bi^{1+}	Bi^{2+}	Bi^{2+}
No. of Storage Rings		20	5	10	5
No. of Beam Lines per SR		4	4	2	1 2**
No. of Beam Lines		80	20	20	5 10**
Size of Final Lenses (lin)***		0.7	1.4	"1"	1.4
Size of Final Buncher		0.5	1	"1"	2
Length of Beam Lines		0.7	0.7	"1"	1.4
Period Length in Beam Lines		0.7	1.4	"1"	1.4
Space Charge Param. in BL's		0.5	0.5	"1"	2 → 1
Rep. Rate		1.8	1.1	"1"	0.55
	Weight Factor for Cost	Relative Costs			
Linac	"1"	0.5	1	"1"	2
TR	0.05	0.7	1.4	"1"	1.4
CR's	0.1	0.7	1.4	"1"	1.4
SR's	0.7	1.4	0.7	"1"	0.7
Ext. Bunchers	0.6	2	1	"1"	0.5
Beam Lines	0.4	2.8	0.7	"1"	0.7
Final Lenses, Ports	0.2	2	2	"1"	1
Site	?	1	1	"1"	> 1 (Left Out)
Buildings	0.25	1	1	"1"	1.5
Cost Factor Relative to HIBALL-I		1.38	0.98	"1"	1.17

* A parabolic pulse shape is assumed, corresponding to a 10 ns rectangular pulse.

** From longitudinal emittance considerations.

*** Costs of final lenses are roughly estimated to be the square of this number.

Bodner's target performance model is not reproduced here. It is described in Refs. 1 and 2. It is based on seven parameters: coupling efficiency, cold fuel isentrope, implosion symmetry, compression, shell aspect ratio, ignitor temperature, and hot spot ρR value. This, of course, is the quantity plotted in Fig. B-1. We fix the other parameters in the Bodner model to produce a gain of 80 with 5 MJ of input energy at 10 GeV. A summary of this analysis is given in Table B-2. For the 10 GeV case the given set of parameters produces a gain of 80 for 5 MJ of input energy. The final density is varied until an optimum is found. This density variation is done for each of the other two cases as well. The coupling efficiency of 6.5% is taken from Fig. B-1. The symmetry, aspect ratio, ignitor temperature, and hot spot ρR value are chosen to be representative of typical successful implosions.

The 5 and 20 GeV cases require some further explanation. The driver analysis assumes pulse energies of 2.5 MJ at 5 GeV, 5 MJ at 10 GeV and 10 MJ at 20 GeV. These input energies at 5 and 20 GeV do not correspond to a gain of 80. Therefore two separate analyses were done each for the 5 and 20 GeV cases. First, these values of input energy were used to compute the gain. This gives values of G = 130 at 5 GeV and G = 15 at 20 GeV. Next is asked, using the Bodner model, what input energy will give a gain of 80? At 5 GeV the answer is 1 MJ. At 20 GeV the input energy is in excess of 100 MJ because the coupling efficiency is so low (1.5%). This absurd value is not used. Instead, it's postulated that a gain of 80 can be achieved with 10 MJ of 20 GeV ions using an alternative target design. These five values of input energy and yield are used to determine the driver and chamber costs.

B.4 Reactor Chamber

The cost of the chamber is determined by its size and the size is determined by the yield of the target. The required chamber radius as a function of yield has been established for two limiting parameters, the temperature rise limit on the first row of INPORT tubes and the condensation time limit. It is required that the surface temperature not exceed 500°C so that the vapor pressure of the $Li_{17}Pb_{83}$ does not exceed 10^{-4} torr. The "free parameters" in this analysis are the coolant velocity and the radius to the first surface of INPORT tubes (and hence the heat flux upon them).

The assumptions that go into this analysis are the following:

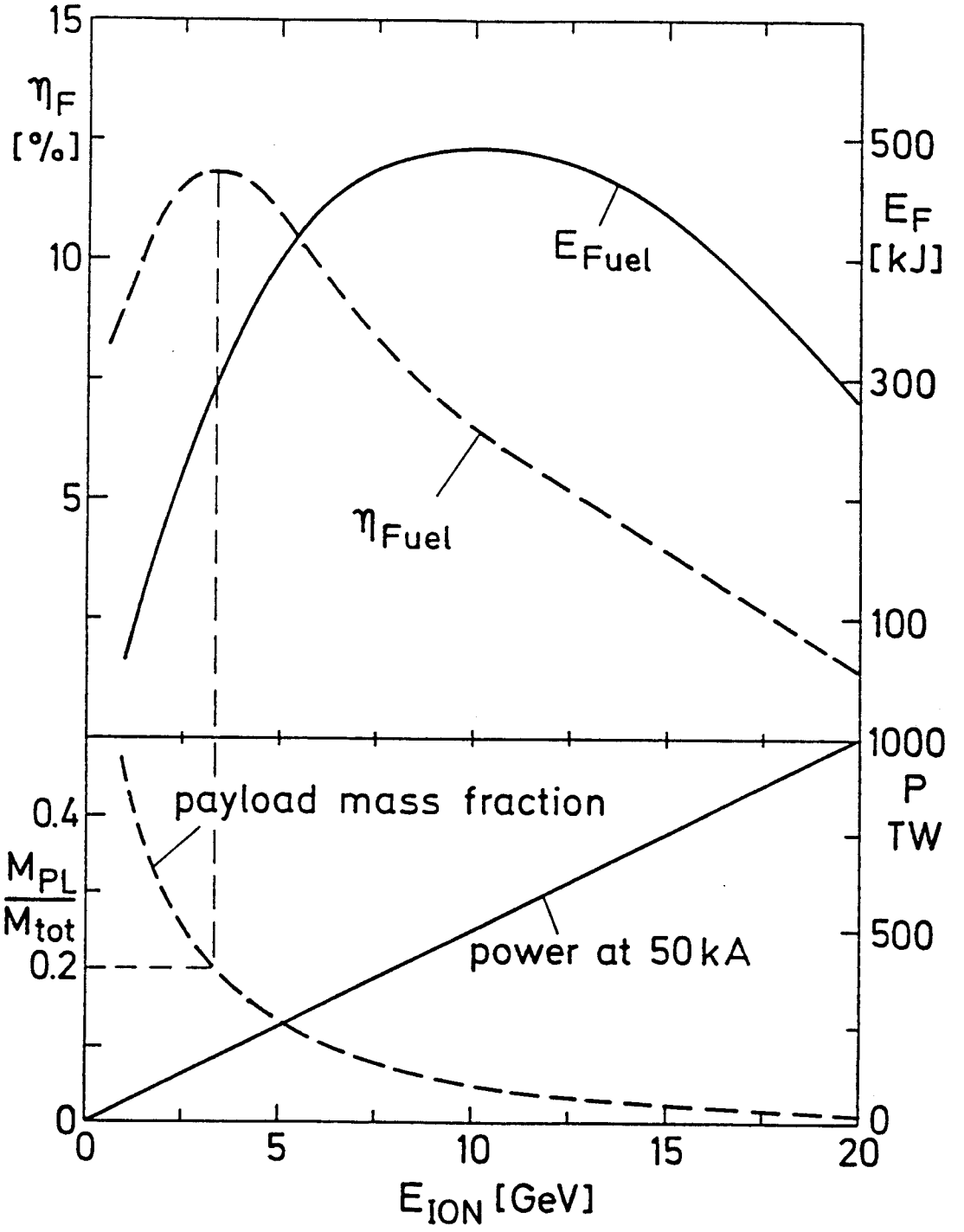

Fig. B-1. Coupling efficiency vs. ion energy for constant current (50 kA).

Table B-2. Results of Bodner Target Gain Model for 5, 10 and 20 GeV Ions

Parameters	5 GeV		10 GeV	20 GeV	
Input Energy	1 MJ	2.5 MJ	5 MJ	10 MJ	10 MJ
Target Gain	80	130	80	15	80
Yield (MJ)	80	325	400	150	800
Coupling Eff. (MtV calcs.)	0.11	0.11	0.065	0.015	0.015
Isentrope/Fermi	7.5	7.5	7.5	7.5	7.5
Symmetry	0.03	0.03	0.03	0.03	0.03
Final Density (g/cm^3)	75	75	50	85	85
Aspect Ratio	10	10	10	10	10
Ignitor Temp. (keV)	5	5	5	5	5
Hot Spot ρR (g/cm^2)	0.5	0.5	0.5	0.5	0.5

1. The fraction of energy in the form of surface heating and volumetric heating of the first row of INPORT tubes are the same as in HIBALL (i.e., independent of yield).
2. The repetition rate is held fixed at 5 Hz.
3. As mentioned above, the calculations are based only on heat transfer through the $Li_{17}Pb_{83}$ film and SiC wall.
4. The layer through which heat must be transferred is 1.5 mm thick and consists of 20% SiC and 80% $Li_{17}Pb_{83}$.

Given a chamber size we compute:

1. the coolant velocity required to keep the maximum surface temperature below 500°,
2. the coolant temperature rise, and
3. the allowed neutron wall loading and the DT yield.

The calculations are plotted parametrically in Fig. B-2. The allowable yield is plotted as a function of the cavity radius for different coolant velocities. We have chosen a velocity of 7.5 m/s to serve as the reference value for this parameter study.

A model has been developed for the condensation of the vaporized Li-Pb in the cavity, which leads to scaling of the time for condensation (t_c) in the cavity with radius (R) and target yield (Y). In this model, the effects of

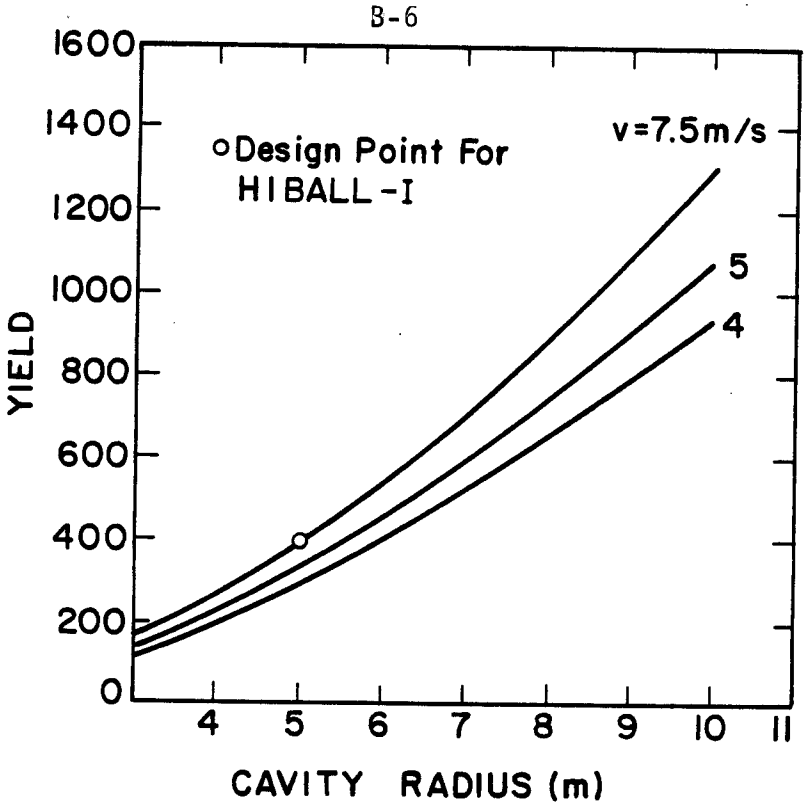

Fig. B-2. Yield as a function of cavity radius and coolant velocity.

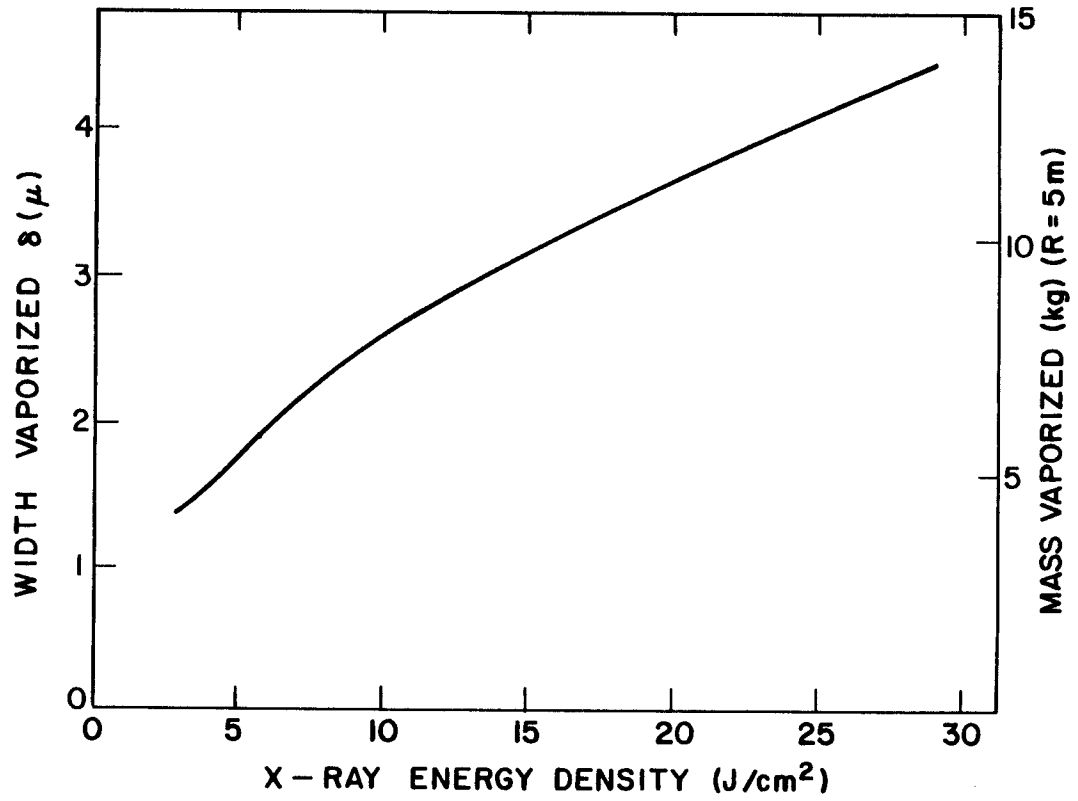

Fig. B-3. X-ray vaporization of $Li_{17}Pb_{83}$ for HIBALL target spectrum.

radiation and additional evaporation of Li-Pb from the surfaces of the tubes are ignored. The vapor is assumed to be an ideal gas but the latent heat of fusion of Li-Pb is taken into account.

Assuming that the vapor is an ideal gas, the temperature of the vapor (T_{gas}) may be written as

$$T_{gas} = \frac{C_1}{M_{gas}} (0.3\ Y - M_{gas} \Delta H_v) \ . \tag{B.1}$$

Here, C_1 is a constant, ΔH_v is the heat of fusion of Li-Pb, and M_{gas} is the amount of Li-Pb put into the cavity through vaporization of target x-rays. The 0.3 is the result of assuming that 30% of the yield is non-neutronic. Figure B-3 shows the results of a series of computer calculations[3] of M_{gas} for the target x-ray spectrum particular to the HIBALL target[1] and for various specific x-ray energy depositions (energy/area). From Fig. B-3, M_{gas} has been approximated as

$$M_{gas} = C_2 \sqrt{Y}\ R \ , \tag{B.2}$$

where C_2 is another constant. Neglecting evaporation of additional Li-Pb, the condensation time has been assumed to be proportional to the dimensions of the cavity and inversely proportional to the thermal velocity of the gas atoms; that is,

$$\frac{1}{t_c} = \frac{C_3}{R} \sqrt{T_{gas}} \tag{B.3}$$

where C_3 is yet another constant.

Combining Eqs. (1), (2) and (3), the condensation time is expressed as

$$t_c^{-1} = \frac{C_3}{R} \left(\frac{C_1}{C_2} \left(\frac{0.3\ \sqrt{Y}}{R} - C_2 \Delta H_v\right)\right)^{1/2} \ . \tag{B.4}$$

$C_2 \Delta H_v$ has been determined to be 2.62 $\sqrt{J}$/cm so that when $\sqrt{Y}/R \gg 10\ \sqrt{J}$/cm,

$$t_c \propto \frac{R^{3/2}}{Y^{1/4}} \ . \tag{B.5}$$

For the HIBALL reference case (Y = 400 MJ; R = 500 cm), $\sqrt{Y}/R = 40\ \sqrt{J}$/cm so that Eq. (5) clearly holds.

Figure B-4 shows these two limiting curves (i.e., temperature rise and condensation time) for a repetition rate of 5 Hz; it can be seen that the optimum point for HIBALL is at 5 m cavity radius. The curve shows the excluded parameter space to the right of the intersection point. The temperature limit curve can be used for a repetition rate different from 5 Hz, provided the "equivalent yield" is obtained for the new repetition rate. Thus the equivalent yield for HIBALL at 4 Hz is

$$(\frac{5}{4})(400) = 500 \ .$$

Using Fig. B-4 we can estimate the cavity size for the five cases described in Section B.2. The results of this analysis are given in Table B-3. Analyzing the first case where the yield is 80 MJ it is found that for the repetition rates of 8 Hz and 9 Hz, the following are the limiting cavity radii:

	8 Hz	9 Hz
For condensation, radius (m) must be less than:	2.79	2.58
For temperature limit, radius (m) must be greater than:	2.6	2.75

Obviously the 9 Hz case will not work. The 8 Hz case is selected with a cavity radius of 2.60 m.

In arriving at the number of cavities, the important criterion is the full utilization of the driver. At 5 GeV note that if the driver can deliver 36 pulses per second (pps) at 2.5 MJ, it then should be capable of delivering 1 MJ at 90 pps. At a repetition rate of 8 Hz, this means 11 cavities can be driven with a single accelerator. Such a procedure is followed in obtaining the parameters in Table B-3.

B.5 Cost Analysis

The costing was performed with 1981 dollars and conforms to the U.S. DOE "Fusion Reactor Studies - Standard Accounts for Cost Estimates," PNL 2648.

Costing was done for the five cases given below:

Case	1	2	3	4	5
Ion Energy (GeV)	5	5	10	20	20
Energy on Target (MJ)	1	2.5	5	10	10
Assumed Gain	80	130	80	15	80

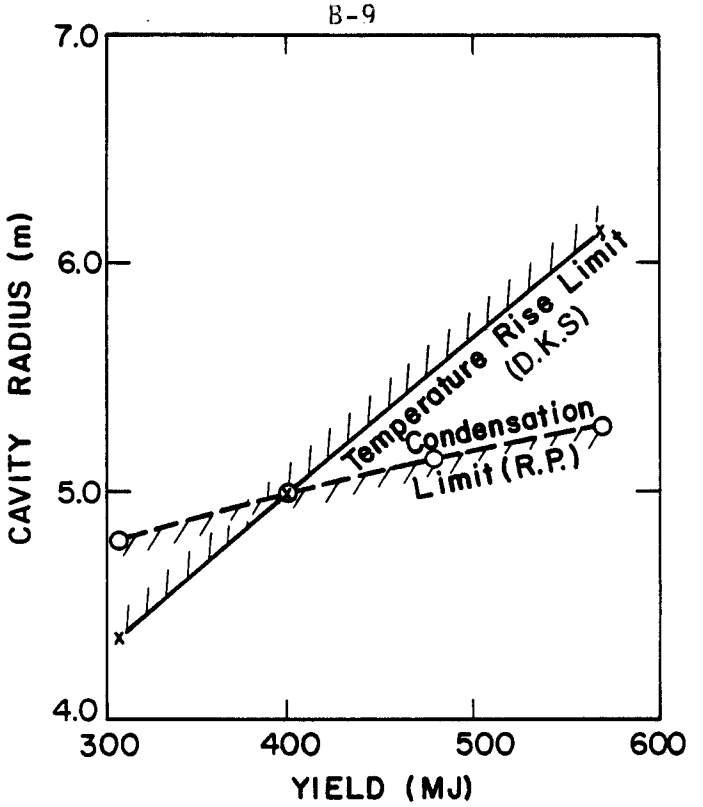

Fig. B-4. Allowable parameter space for 5 Hz.

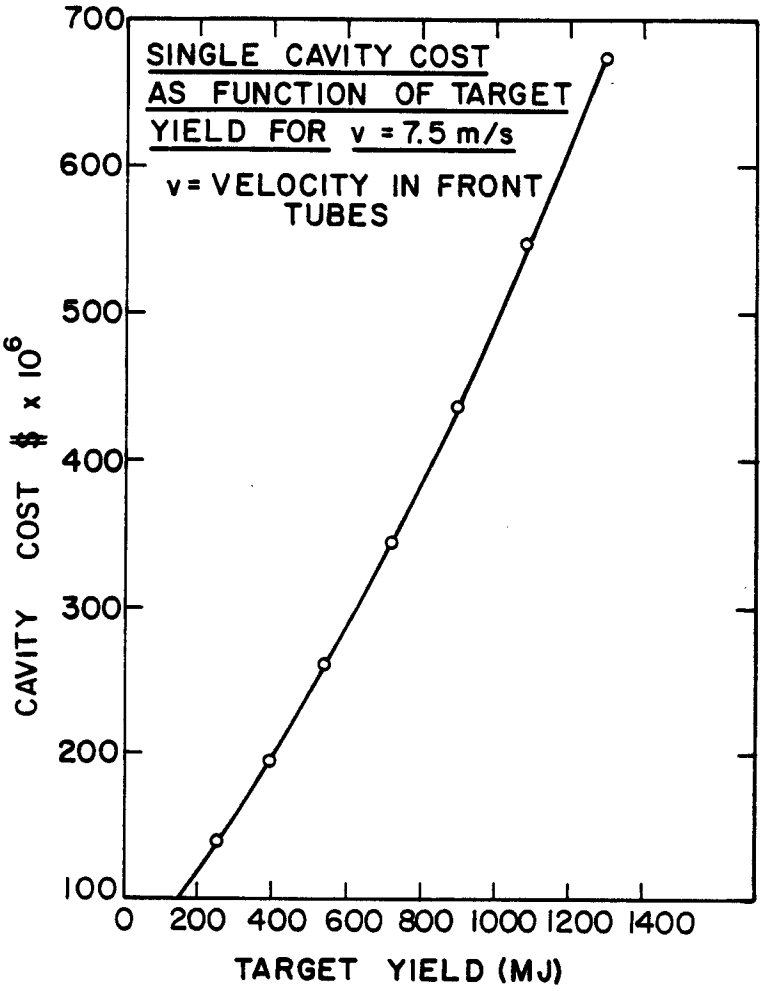

Fig. B-5. Single chamber cost as a function of target yield for $v_{coolant}$ = 7.5 m/s.

Table B-3. Parameters for the Five Accelerator Cases Considered

	Case 1	2	3	4	5
Ion Energy (GeV)	5	5	10	20	20
Energy on Target (MJ)	1	2.5	5	10	10
Gain (from MPQ)	80	130	80	15	80
Yield	80	325	400	150	800
Cavity Radius (m)	2.60	4.5	5.0	3.0	6.3
Rep. Rate (HZ)	8	5	5	5.5	3.66
No. of Cavities	11	7	4	2	3
Beams/Cavity (from GSI)	32	80	20	10	10
DT Power (MW_{th})	7040	11,375	8000	1650	8784

The first step in the costing procedure is to determine the optimum cavity radius and the repetition rate. Once these are known, the number of cavities is obtained, always taking the maximum output of the driver.

Direct Costs

a) Driver: The costs in Table B-1 were used, making an adjustment to the cost of the beam lines depending on the number of chambers.

In the first case, for example, the cost obtained in Table B-1 was for 4 chambers with 80 beams each. This is adjusted for 11 chambers with 32 beams each, an increase of 10%. The relative cost of the beam lines is thus increased from 2.8 to 3.1. Since the weighting factor for the beam lines is 0.4, the overall cost factor for the driver goes from 1.38 to 1.416. This means the cost of the driver is 1887 x 1.416 = 2672 million dollars.

b) Chambers: Figure B-5 gives the single chamber costs as a function of target yield for a rep. rate of 5 Hz. The effective yield for a different rep. rate as explained earlier can be used to obtain the cost for any case. Extrapolating the curve slightly gives a cost of \$80 x 10^6 for an effective yield of 128 MJ.

c) Main Heat Transfer and Transport: This account is broken up into 3 basic parts: the liquid metal pumps, the steam generator and the pipes. The scaling for the pumps (which for HIBALL-I amounted to 40% of the entire account) is scaled as $(P_{th})^{0.8}$. The steam generator, amounting to 31% of the system cost, also scales as $(P_{th})^{0.8}$. The pipes scale as $(P_{th})^{0.8}$ x (No. of chambers)$^{0.4}$.

d) Pellet Injector: the pellet injector scales as $(Hz)^{0.4}$ x (No. of chambers).

e) Land and Land Rights: These were taken as 5×10^6 for all five cases.

f) Structures and Site Facilities: The reactor buildings in HIBALL-I accounted for ~ 30% of the direct cost. This account scales as chamber radius)$^{0.8}$ x (No. of chambers)$^{0.4}$. The turbine building was 25% of the structures cost and it scales as $(P_{th})^{0.8}$. The remaining structures are assumed to cost the same for all five cases.

g) Turbine Plant Equipment: Scales as $(P_{th})^{0.7}$.

h) Electric Plant Equipment: Scales as $(P_e)^{0.9}$.

i) Miscellaneous Plant Equipment: Scales as $(P_{th})^{0.9}$.

Indirect Costs

j) Construction Facilities: Taken as 15% of total direct costs.

k) Engineering Cost Management: This is also taken as 15% of the total direct costs.

l) Owners' Cost: Taken as 5% of total direct costs.

m) Interest During Construction: 5% per annum deflated interest for an 8 year construction period. This amounts to 17% of direct and indirect costs.

The net power output in each case is arrived at by taking the thermal efficiency in HIBALL-I, then subtracting the driver power and the needed auxiliary power. Table B-4 lists the direct costs, indirect costs, total capital costs, net power output, and unit capital costs for the five cases.

Busbar Costs

The annual operating cost is made up of the fuel cost (target cost), operation and maintenance, component replacement and the fixed charge on capital.

As in HIBALL-I the target cost is taken at 15¢ per target and has the target factory amortized in the cost. Thus, for each case, this amounts to the targets used per year at 70% availability multiplied by 15¢.

Operation and maintenance is taken as 2% of the total capital cost.

Table B-4. Capital Costs of HIBALL-I Options

	Millions of 1981 Dollars				
	Case				
	1	2	3	4	5
Driver	2672	3085.2	1887	2124.8	2164.4
Cavities	880	1165	785	192	846
Main Heat Transfer	577.1	795.3	560	147.4	584.8
Pellet Injector	39.8	21	12	6.2	7.9
Total Reactor Plant Eq.	4168.9	5066.5	3244	2470.4	3603.1
Land & Land Rights	5	5	5	5	5
Structures & Site Facil.	323.2	354.2	280	173.5	277.4
Turbine Plant Equip.	393.2	550.1	430	142	459.1
Electric Plant Equip.	245.1	377.5	275	66.4	299.1
Miscellaneous Plant Equip.	42.5	68.5	50	12	54.5
Total Direct Costs	5177.9	6421.8	4284	2869.3	4698.2
Construction Facilities	776.7	963.3	642.6	430.4	704.7
Engineering Cost Management	776.7	963.3	642.6	430.4	704.7
Owners' Cost	258.9	321.1	214.2	143.5	234.9
Total Dir. & Indir. Costs	6990.2	8669.5	5783.4	3873.6	6342.5
Interest During Const.	1188.3	1473.3	983.2	658.5	1078.2
Total Capital Cost	8178.5	10143.3	6766.6	4532.1	7420.7
Net Power Output (MW_e)	3308.8	5564	3760	418	4128.5
Unit Capital Cost ($\$/kW_e$)	2472	1823	1799	10842	1797

Component replacement is based on a 2 year lifetime of the SiC INPORT blanket.

Fixed charge on capital is taken at 10% per annum.

Table B-5 gives the annual operating expenses, the energy sold per year in kWh and the busbar cost in mills/kWh.

Figure B-6 gives the graphic representation of the unit capital cost as a function of ion energy, energy on target and gain. The percentages relative to HIBALL-I are given in brackets. Figure B-7 does the same thing for the busbar costs.

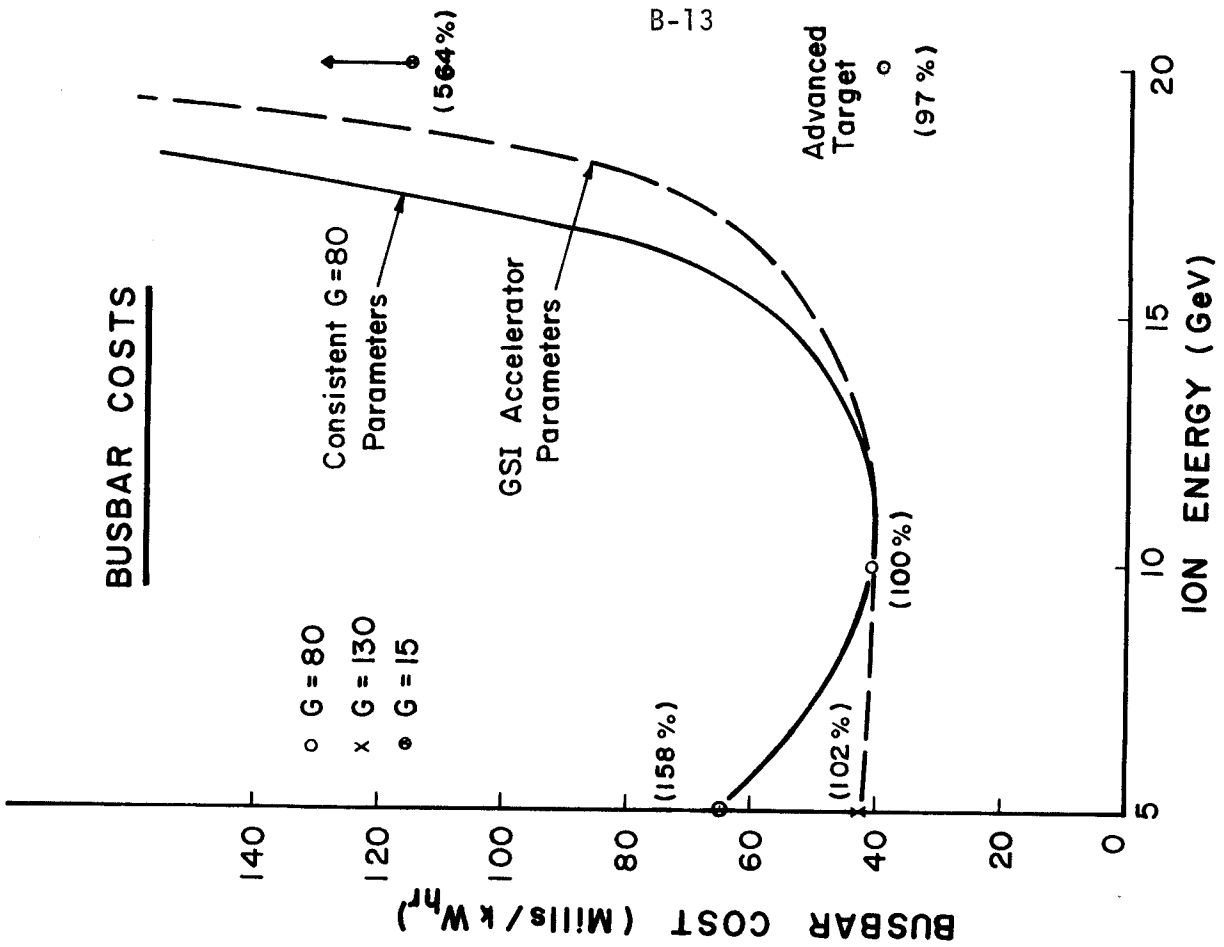

Fig. B-7. Busbar costs.

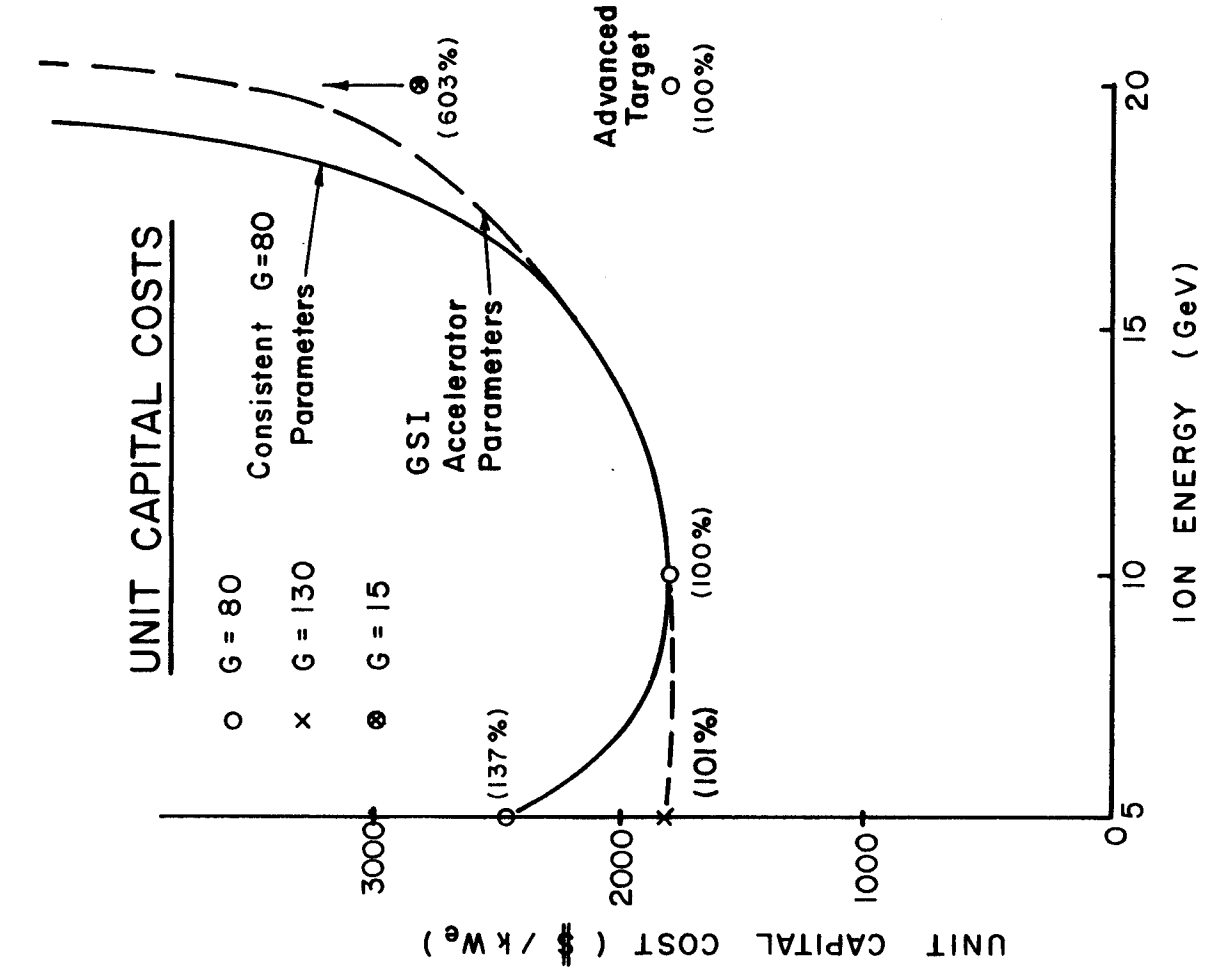

Fig. B-6. Unit capital costs.

Table B-5. Annual Operating and Busbar Costs

	Millions of 1981 Dollars Per Year				
	Case				
	1	2	3	4	5
Pellet Costs	290.4	115.5	66.	36.3	36.3
Operating & Maint.	163.6	202.9	135.3	90.6	148.4
Component Replacement	38.5	90.1	64.	10.	80.25
Interest on Capital	817.9	1014.3	676.6	453.2	742.1
Total Annual Operating Costs \$ x 10^6	1310.4	1422.8	941.9	590.1	1007.1
Net Power Sold (70% Avail.) kWh x 10^{10}/yr	2.03	3.40	2.31	0.256	2.536
Busbar Costs (mills/kWh)	64.5	41.8	40.8	230	39.7

B.6 Conclusions

The plot of busbar cost vs. ion energy, Fig. B-7, clearly shows that the optimum point in our parameter study is near the original HIBALL-I case. This is true for both the consistent gain = 80 parametric study and the study that follows the GSI accelerator parameters listed in Table B-1. It must be noted that the features of this cost dependence on ion energy are strongly influenced by the target gain predictions. Using the coupling efficiencies of MPQ and the Bodner gain model greatly penalizes the 20 GeV case. We observe that if an advanced target design could give a gain of 80 for 10 MJ of 20 GeV ions, significant cost advantages could be obtained. The cost, based on this observation, is also plotted on Fig. B-7. From this it is seen that there is a very broad optimum over the range of 10-20 GeV if alternative targets capable of utilizing high energy ions can be designed. Confirmation of this is beyond the scope of this work. Therefore, based upon the "G = 80 curve" it is concluded that 10 GeV is about the optimum energy for the HIBALL-I heavy ion beam fusion reactor concept. The conclusion allowed consideration of 10 GeV ions for HIBALL-II and directed our efforts toward improving the analysis of the critical components of the design concept.

References for Appendix B

1. B. Badger et al., "HIBALL, A Conceptual Heavy Ion Beam Driven Fusion Reactor Study," University of Wisconsin Fusion Technology Institute Report UWFDM-450 (June 1981), Kernforschungszentrum Karlsruhe Report KfK-3202.

2. S. Bodner, "Critical Elements of High Gain Laser Fusion," Naval Research Laboratory Report NRL MR-4453 (January 1981).

3. R. Peterson, D.K. Sze, A. Hassanein and L. Pong, "Gas Dynamics and Heat Transfer Phenomena in Liquid metal ICF Reactor First Surfaces," University of Wisconsin Fusion Technology Institute Report UWFDM-443 (October 1981).